Author:
Khodr, Codor

Title:
Three-dimensional infrasonic wave propagation above irregular boundaries

Three-dimensional infrasonic wave propagation above irregular boundaries

Codor Khodr

A dissertation submitted to the University of Bristol in accordance with the requirements for award of the degree of Doctor of Philosophy in the Faculty of Engineering

School of Civil, Aerospace and Mechanical Engineering

October 2019

40.600 words

Abstract

This thesis deals with the propagation of infrasonic waves above irregular boundaries using a numerical approach based on the parabolic equation (PE) method. The first part of the thesis is dedicated to the development of a two-dimensional parabolic equation (2DPE) method, based on the well-known Beilis-Tappert coordinate shift map. While the original theory was limited to a narrow-angle formulation, it is here extended to wide-angle propagation by using higher-order Padé series to approximate the pseudo-differential square-root operator. The equation is numerically solved using the implicit Crank-Nicolson finite-difference scheme and validated against both analytical solutions (in the case of propagation above a flat impedance surface) and a COMSOL Finite-Element model (in the case of propagation above an irregular Gaussian surface). Simulations show a good agreement between the analytical models and the 2DPE. The wide-angle formulation allows for a more accurate representation of the pressure field at higher-altitude while maintaining the accuracy of the original first-order shift map.

A significant part of the thesis is dedicated to the derivation of a novel three-dimensional parabolic equation (3DPE) that takes into account both irregular boundaries and refraction from a layered atmosphere, with an effective sound speed profile. This development represents a first attempt at applying the PE method to three-dimensional surface scattering, in the context of atmospheric acoustics. Here, a coordinate transformation method is used on the Helmholtz equation to express the problem in a flattened domain, where simplified impedance boundary conditions can be easily enforced. Realistic propagation problems in infrasonic wave modeling typically involve large-scale simulations. As a result, the main focus of the proposed method is the derivation of an efficient numerical scheme, avoiding the inversion of a large sparse system. This has been achieved by a combination of a small-slope assumption and the use of an iterative gradient scheme, which involves the computation of tridiagonal matrices only. Another solution, based on the Alternate

Direction Implicit (ADI) and the Split-Step Padé scheme, has also been proposed to extend the method to wide-angle propagation.

A parametric study has also been proposed to quantify the diffraction of infrasonic waves by a bivariate Gaussian surface of variable height. The frequency range considered spans from 0.5 Hz to 10 Hz, for a propagation range of 10 km and an obstacle size that varies between 0 and 300 m of height. The obstacle scale, which is simply the ratio of the Gaussian surface height to the wavelength (i.e h_0/λ) is proven to be the governing parameter of the existence of diffractive effects in the shadow zone, downstream of the obstacle. A comparison with the 2DPE shows a difference in Sound Pressure Level (SPL) between 3 dB and 10 dB in the shadow zone. More simulations have been performed to investigate the coupled effects of irregular boundaries and atmospheric refraction, for linear, logarithmic and jet atmospheric sound speed profiles. It is shown that in the presence of terrain, transversal scattering effects become significant, even for smooth profiles and low frequencies. The parametric study has confirmed the existence of three-dimensional topographic effects in the higher end of the infrasound spectrum ($f > 1$ Hz).

In order to check the novel 3DPE solver for a realistic propagation problem, a Wind-Turbine noise prediction is carried out in a three-dimensional environment. Numerical PE simulations are compared against the experimental pressure data, extracted from recordings made at the IS50 micro-barometer array, part of the International Monitoring System (IMS), located in the Ascension Island. Based on the results, it is highlighted that topography plays an important role in the correct prediction of the pressure field in a realistic environment, as three-dimensional modeling enabled us to correctly match experimental data at different receiver locations.

3

To my beloved parents,
Mounzer and Salma

À mes très chers parents,
Mounzer et Salma

Dedication and acknowledgements

I would like to begin by thanking my PhD supervisor, Professor Mahdi Azarpeyvand, without whom the present thesis would not have been possible. His precious advice and continuous support, throughout the four years of my PhD, allowed me to take on a very challenging subject. I would like to express my gratitude to my industrial supervisor, Dr. David Green, Principal Geophysicist at AWE Blacknest, for his insight and expertise on infrasound modeling. I am very grateful to him for inviting me to Blacknest in my second year and for introducing me to many people in the infrasound community. My gratitude also goes to my research sponsor, AWE, for the financial support and the opportunity to pursue such an exciting project.

During my time in Bristol, I have been able to explore several topics, such as wave propagation, scientific computing and the fascinating science of infrasound. The understanding I have reached today was largely enabled by the help I received from many people at the University of Bristol. In this respect, I am grateful to Dr. Anton Shterenlikht, from the Department of Mechanical Engineering, for his help with FORTRAN programming. He has given me valuable advice back when I had little experience on the subject, and helped me take a step in the right direction. I would also like to thank my reviewers Dr. Anthony Croxford and Dr. Alexander Velichko; my secondary supervisor, Dr. Alison Rust and my PGR tutor, Dr. Alberto Gambaruto.

I am also grateful to my examiners, Professor Fabrizio Scarpa and Dr. Olga Umnova (University of Salford), for their feedback, which certainly helped me improve my thesis.

This work is also dedicated to my friends and colleagues at the University of Bristol, especially fellow PhD students from the Fluids and Aerodynamics Research Group (FARG) and Offices 1.80/2.80. Your spirit and camaraderie was very valuable and appreciated. From the numerous activities we did together to the mutual support, I will forever have a very fond memory of my time in Bristol.

Last, but not least, I am grateful to my family for their unconditional support throughout the years.

Author's declaration

I declare that the work in this dissertation was carried out in accordance with the requirements of the University's Regulations and Code of Practice for Research Degree Programmes and that it has not been submitted for any other academic award. Except where indicated by specific reference in the text, the work is the candidate's own work. Work done in collaboration with, or with the assistance of, others, is indicated as such. Any views expressed in the dissertation are those of the author.

SIGNED: ..... DATE: .....

Contents

List of Figures

List of Tables

Nomenclature

Acronyms

ABL	Absorbing Boundary Layer
ADI	Alternate Direction Implicit
BEM	Boundary Element Method
BTPE	Beilis-Tappert Parabolic Equation
CFD	Computational Fluid Dynamics
CNPE	Cranck-Nicolson Parabolic Equation
EM	Electromagnetic
FEM	Finite Element Method
GFPE	Green Function Parabolic Equation
GTPE	Generalized Terrain Parabolic Equation
PE	Parabolic Equation
PML	Perfectly Matched Layer
RSPL	Relative Sound Pressure Level
SPL	Sound Pressure Level
SSF	Split-Step Fourier
SSP	Split-Step Padé

UA	Underwater Acoustics
WAPE	Wide-Angle Parabolic Equation

Greek letters

$\bar{\varphi}$	Maximum propagation angle
$\boldsymbol{\xi}$	Receiver location in the numerical coordinate system
$\Delta\xi$, $\Delta\nu$, $\Delta\eta$	Grid spacing in the numerical domain
Δx, Δy, Δz	Grid spacing in the physical domain
δ	Dirac impulse
γ	Adiabatic index of air, $\gamma = 1.4$
λ	Wavelength
$\mathbf{\Psi}^m$	Matrix of the discretized values of the pressure envelope at the step ξ_m
ω	Angular frequency, $\omega = 2\pi f$
ψ	Complex pressure envelope
ψ_i	Incident complex pressure envelope
ψ_r	Reflected complex pressure envelope
Ψ_j^m	Complex pressure envelope vector containing the column of points $\psi_{1,j}^m, \ldots, \psi_{N_z,j}^m$
$\psi_{n,j}^m$	Complex pressure envelope expressed at the grid point (ξ_m, ν_j, η_n)
ρ	Acoustic density fluctuation
ρ_0	Atmospheric mean density
σ_0	Perfectly Matched Layer (PML) absorbing coefficient
θ_i	Incident angle at the ground surface with respect to the normal
θ_r	Reflected angle at the ground surface with respect to the normal
θ_x	Boundary angle along x
θ_y	Boundary angle along y

φ	Elevation angle to the receiver
φ_r	Elevation angle of the reflected wave
ϱ	Atmospheric density
ζ_0	Characteristic impedance of air
ζ_g	Characteristic impedance of the ground

Operators

Δ	Scalar Laplacian operator
$\mathcal{L}$	One-way square-root operator
$\mathcal{Y}$	Transversal differential operator in the physical domain
$\mathcal{Y}^*$	Transversal differential operator in the transformed numerical domain
$\mathcal{Z}$	Altitude differential operator in the physical domain
$\mathcal{Z}^*$	Altitude differential operator in the transformed numerical domain
∇	Gradient operator

Latin letters

(ξ, ν, η)	Transformed (earth-flattened) Cartesian coordinates
(x, y, z)	Cartesian coordinates
$\hat{L}_p$	Relative sound pressure level (RSPL)
$\mathbf{D}_{l,\xi}$	Finite-difference matrix of the l-th order derivative with respect to ξ
$\mathbf{k}$	Wavevector
$\mathbf{M}^{\pm}$	Crank-Nicolson Parabolic Equation system matrices along η
$\mathbf{n}$	Ground surface normal vector
$\mathbf{P}^{\pm}$	Crank-Nicolson Parabolic Equation system matrices along ν

$\mathbf{u}$	Atmospheric fluid velocity amplitude
$\mathbf{v}$	Acoustic velocity fluctuation
$\mathbf{v}_0$	Mean atmospheric fluid velocity
$\mathbf{x}$	Receiver location in the physical coordinate system
$\mathbf{x}_s$	Source location
c	Sound speed
c_0	Sea level adiabatic sound speed
c_{eff}	Effective sound speed
E	Beilis-Tappert phase shift
f	Wave frequency
G	Three-dimensional Green function
g	Acceleration of gravity
h	Ground surface profile
h_0	Ground surface height
k	Wavenumber
k_0	Natural wavenumber
k_g	Wavenumber of the ground material
k_{eff}	Effective wavenumber
l_c	Creeping wave layer
L_p	Sound pressure level (SPL)
M	Mach number, $M = v_0/c_0$.
N_x, N_y, N_z	Number of grid points in x, y, z
P	Atmospheric pressure
p	Real acoustic pressure
P_0	Mean atmospheric pressure
p_c	Complex acoustic pressure
p_i	Real incident acoustic pressure
p_r	Real reflected acoustic pressure
p_{ref}	Reference acoustic pressure

p_{rms}	Root mean square acoustic pressure
$p_{c,i}$	Complex incident acoustic pressure
$p_{c,r}$	Complex reflected acoustic pressure
Q	Spherical reflection coefficient
R	Universal gas constant
R_0	Radius of curvature of sound rays, Radius of a curved surface
R_p	Plane reflection coefficient
S_0	Sound source amplitude
T	Atmospheric temperature
t	Time
T_0	Sea level atmospheric temperature
v	Acoustic velocity
v_c	Complex acoustic velocity
x_0, y_0	Location of the Gaussian hill
x_1, x_2	Obstacle limits along x
y_1, y_2	Obstacle limits along y
Y_g	Normalized admittance of the ground material
Z_g	Normalized impedance of the ground material
Z_s	Normalized impedance of the ground surface

Chapter 1

Introduction

This thesis explores the effect of the earth surface on infrasound propagation in the atmosphere through the implementation of a novel three-dimensional parabolic equation method. Low-frequency sound propagation in the atmosphere is complicated due to the presence of inhomogeneous atmosphere and irregular boundaries, *i.e.* the earth's surface. Over the past twenty years significant efforts have been made to improve our understanding of how atmospheric inhomogeneities affects infrasound propagation, and many of these effects have been successfully modeled using a range of numerical approaches. Less effort, however, has been made in understanding of the interaction of infrasound with irregular topographies, especially in three dimensions. This thesis identifies methodologies to fill this numerical modeling gap. As an introduction, this chapter provides some context on infrasound monitoring and the main motivations behind the proposed study. First, a brief history of infrasound monitoring up to the modern era and its role in the detection of nuclear explosions is presented in Sec. 1.1. Then, a brief description of the atmosphere as a propagation medium is provided, with a concise listing of all the issues that arise in infrasound modeling. An extensive review of all numerical methods for atmospheric acoustics is given in Sec. 1.2, with a particular focus on applications to infrasound prediction. Finally, the statement of the problem and the scope of the thesis are detailed in Sec. 1.3. The main intention of this introduction chapter is to provide a comprehensive review of the important works carried out on the numeri-

cal modeling of infrasonic waves propagation. The theoretical aspects related to the papers will be provided in chapters 2 to 4.

1.1 Studying infrasound: scope and challenges

Infrasound is a term used to describe low frequency acoustic waves, usually below a frequency of 20 Hz and above a frequency of 0.02 Hz [115]. Large scale natural events, such as earthquakes and volcanoes, are typical sources of infrasound in the atmosphere [101]. Similarly, nuclear explosions release enough energy to generate infrasound that can be recorded thousands of kilometers away from the epicenter. The study of infrasound is a rather recent field in geophysics, and has gained a great deal of interest after the second world war and during the early era of atmospheric nuclear weapons testing. A schematic of all four types of nuclear tests (underground, near-ground, atmospheric and underwater) is given in Fig. 1.1. Scientists started to examine both experimental and theoretical aspects of infrasound propagation as early as 1954, harnessing its potential in the detection of atmospheric nuclear tests [25]. Since 1963 and the ratification of the Limited Test-Ban Treaty (LTBT), atmospheric nuclear tests have been prohibited, which has driven nuclear powers to switch to underground nuclear tests, slowly reducing the interest of infrasound as a detection tool. Some of the research made has contributed to other military applications, like detection of sonic booms from fighter jets or underwater acoustics. Since then, the understanding of atmospheric infrasound has been largely improved by more theoretical results and the development of efficient simulation tools, starting in the late 70's and enabled by the increase of computational capabilities.

In 1996, the opening of the Comprehensive Nuclear-Test-Ban Treaty (CTBT), prohibiting all testing of nuclear weapons, renewed the interest of scientists towards infrasound. Indeed, the CTBT included the recording of infrasound in the atmosphere as part of the verification system, alongside seismic, hydro-acoustic and radionuclide monitoring. To achieve this, the Comprehensive Nuclear Test-Ban Treaty Organization (CTBTO) relies on the International Monitoring System (IMS), which

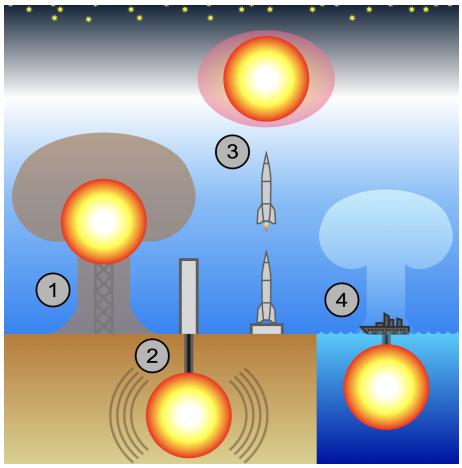

Figure 1.1: Illustration of different nuclear tests. (1): Near-ground atmospheric explosion, (2): Underground explosion, (3): High-altitude nuclear explosions, (4): Underwater nuclear tests. Credits: Wikimedia Commons.

is composed of 337 recording facilities spread across the globe, 60 of which are infrasound stations, spaced by a distance of 2000 km on average [46]. Signals recorded across the network of infrasound stations are analyzed to determine the origin time and location of the generation event. The number of infrasound stations have been progressively increased through a global effort, with the objective of improving the probability of detection. A map of all the recording facilities of the IMS is shown in Fig. 1.2. An important issue concurrent to infrasound monitoring is the treatment of background noise and the correct discrimination of recorded events, which has been achieved by the design of noise-canceling micro-barographs [6].

Prediction of infrasound signal arrival times and waveform structure is extremely challenging due to the uncertainties associated with the varying propagation medium and the wide variety of signal source mechanisms. This raises an important question: how accurate are the current modeling techniques, knowing the large number of parameters that influence both the source and propagation medium? While great progress has been made since the opening of the CTBT for signature, some issues in infrasound propagation are yet to be understood. We begin by outlining the several aspects of infrasound propagation in the atmosphere before presenting the scope and purpose of the thesis.

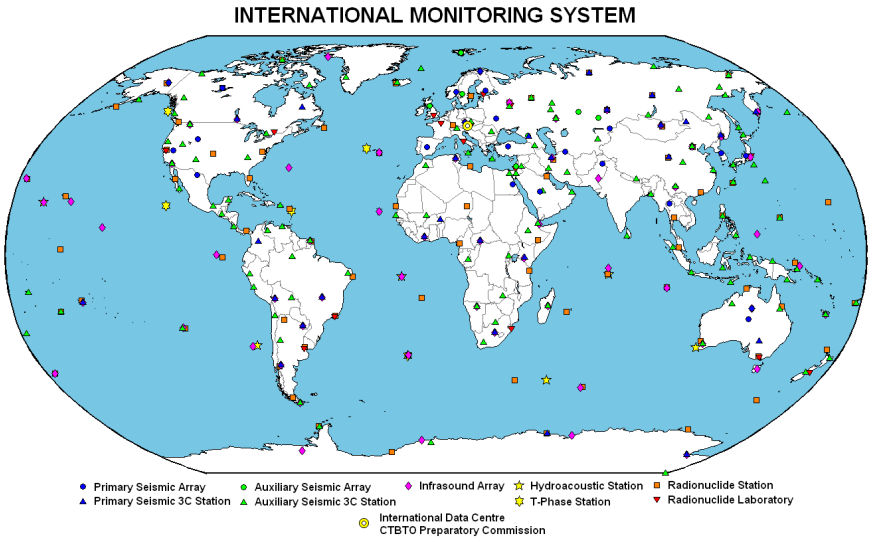

Figure 1.2: Geographical location of the 337 recording facilities of the International Monitoring System (IMS). Credits: Government of Canada.

1.1.1 Sources of Infrasound

Infrasonic waves differ in strength, duration and waveform depending on the source type. While nuclear explosions do have an clear infrasound signature, they are not the most common source of infrasound in the atmosphere. Among the possible natural or man-made sources are earthquakes, tsunamis, meteorites and sonic booms from supersonic planes [31, 46]. Most importantly, the propagation distance varies greatly as a function of the typical wavelength. Infrasonic waves with a frequency close to 10 Hz are on the higher end of the infrasound spectrum, and will propagate over a distance of a few kilometers before being attenuated, while those with lower frequencies, i.e. $0.01\,\text{Hz} < f < 0.1\,\text{Hz}$, can propagate over larger distances and even circle around the earth [219]. A brief summary of the common infrasound sources is provided in Table 1.1, where we also specify the frequency range, amplitude and maximum propagation distance associated with each one. In the case of nuclear explosions, the resulting sound source can be accurately described as a localized impulse of short duration and high acoustic intensity. Typically, both atmospheric and underground nuclear explosions occur "close" to the ground, i.e. at an altitude

or depth that is small in comparison with the propagation distance.

Source	Frequency (Hz)	Max. Amplitude (Pa)	Max. distance (km)
Artificial events			
Nuclear explosion			
Underground	$1 - 20$	~ 1	~ 1000
Atmospheric	$0.002 - 20$	> 20	> 20000
Chemical explosion	$0.05 - 20$	~ 10	> 5000
Mine firing	$0.05 - 20$	~ 10	> 5000
Supersonic jet	$0.3 - 20$	~ 10	~ 5000
Space shuttle	$0.01 - 20$	~ 5	~ 5000
Natural events			
Earthquakes	$0.005 - 20$	~ 4	≥ 10000
Meteorite	$0.01 - 20$	> 10	> 20000
Volcanic eruption	$0.002 - 20$	> 20	> 20000
Tornado	$0.5 - 20$	~ 0.5	~ 300
Thunder	$0.5 - 20$	~ 0.5	~ 300

Table 1.1: A brief summary of observed infrasound sources in the atmosphere and their properties. The data is extracted from Christie and Campus [46].

Underground tests can also generate infrasound in the atmosphere, although the amplitudes recorded are less significant and therefore more difficult to identify than for atmospheric explosions. The infrasonic waves from underground explosions are generated by the oscillation of the near-ground features under the effect of seismic waves propagating from the source location. In this case, signals must be interpreted using a seismo-acoustic model, which includes an explicit description of the ground medium [10, 183]. Two notable examples of infrasound recorded from an underground nuclear explosion are the 2016 North Korean tests, which took place on the 6th of January and 9th of September [154]. Strong signals were recorded at regional seismo-acoustic arrays in South Korea, but the number of recordings was strongly influenced by the stratospheric wind conditions. In the specific case of the modern nuclear tests carried out in North Korea, the infrasound stations IS30

and IS45, located in Japan and East Russia, respectively, have been able to record infrasound arrivals between 2009 and 2016 [13, 109].

The analysis of infrasound associated with a particular event recorded by the IMS is achieved through a combination of data inversion and forward modeling. The source properties are generally unknown but can be derived from recorded signals [84]. The physical values of interest are the azimuth, phase velocity, correlation and signal-to-noise ratio (SNR), which are estimated by using inversion algorithms like the Bayesian Infrasonic Source Localization (BISL) [34, 138] or the progressive multichannel correlation technique (PMCC) [42]. The accuracy of data inversion depends on the number of infrasound arrivals detected and the uncertainty of the atmospheric medium. In some cases, the exact source properties are deducted by experimental recordings, which is referred to as the ground-truth events [91, 140]. These type of sources are of great importance in infrasound monitoring as they allow a clear validation of infrasound modeling tools [159]. A review of available analytical and numerical methods for the forward modeling of atmospheric infrasound will be provided in Sec. 1.2.

1.1.2 Basic structure of the atmosphere

In this section, we provide a general description of the earth atmosphere as a propagation medium. The earth atmosphere can be divided into a succession of layers up to an altitude of 140 km in most standard models, which are, from the lowest to the highest: (i) the Troposphere (below 30 km), (ii) the Stratosphere (between 30 km and 60 km), (iii) the Mesosphere (between 60 km and 100 km) and (iv) the Thermosphere (above 100 km) [79], as seen in Fig. 1.3. Theoretically, the atmosphere extends up to an altitude of 500 km, beyond which the atmospheric density becomes negligible. The stratification of gas in the atmosphere plays a major role in the propagation of infrasound, it has an effect on both the wave-field direction and amplitude. The typical earth atmosphere is composed of 78.1% of Nitrogen (N_2), 20.1% of Oxygen (O_2) and less than 1% of Argon (Ar). Up to a 100km of altitude, the balance of elements is constant, which implies an average molar masse of air

close to $M_{\text{air}} \approx 28.96\,\text{kg} \cdot \text{mol}^{-1}$. Many databases, built on both empirical observations and theoretical models, provide a time dependent description of atmospheric parameters such as composition, density, temperature or pressure as a function of altitude [221]. Among the most popular atmospheric models is the European Center for Medium Range Weather Forecasting (ECMWF) Infrasound propagation and the Ground-to-Space (G2S) database. A more generic description of the atmospheric temperature as a function of altitude is known as the U.S. Standard Atmosphere [188], but it does not account for regional variations of the atmospheric composition or time-dependent temperature fluctuations.

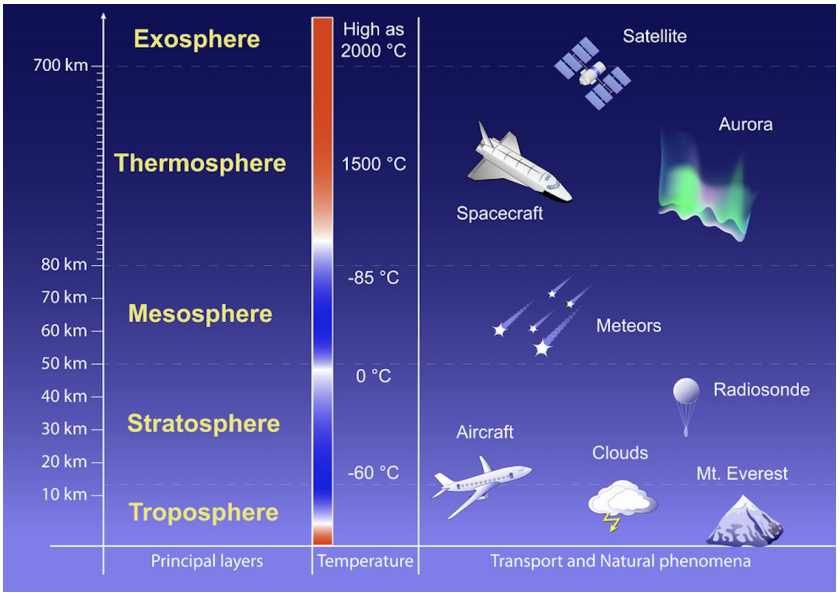

Figure 1.3: Structure of the atmosphere and atmospheric temperature variation as a function of altitude, between 0 km and 700 km.

1.1.3 Infrasound propagation

The behavior of infrasonic waves in the atmosphere is governed by large scale atmospheric structures, such as the stratification of gas, and small scale localized inhomogeneities, such as turbulence and wind jets. It is also influenced by the ground

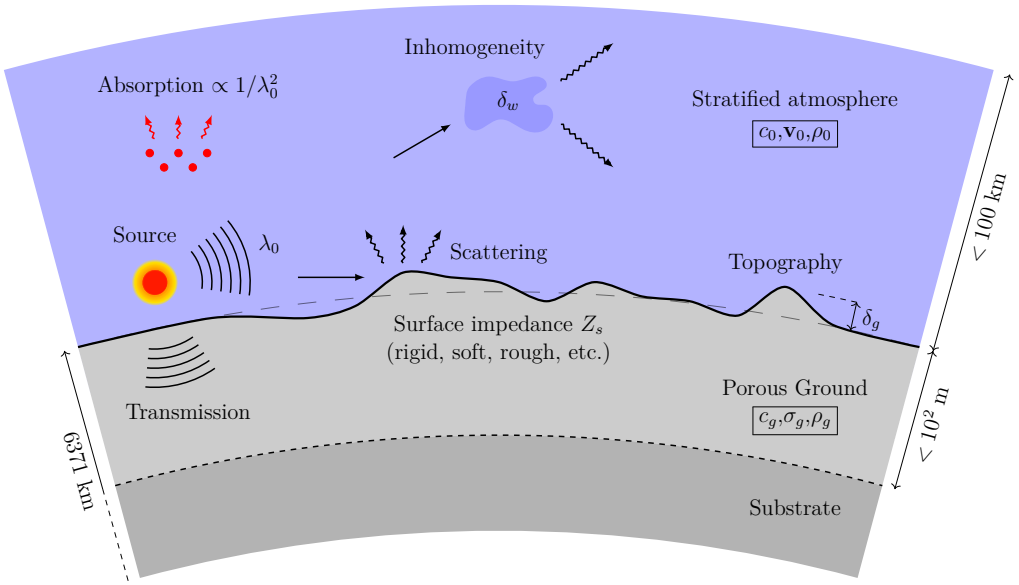

Figure 1.4: Schematic of the environmental parameters impacting infrasound propagation. λ_0 is the wavelength. The scales δ_w and δ_g represent the size of the atmospheric inhomogeneities and the topographic obstacles, respectively. Information about the ground material and surface properties is contained in the surface impedance Z_s. The ground material can be considered to be layered (*extended reacting model*) or semi-infinite (*locally reacting model*).

boundary, which can be geometrically irregular due to topographic obstacles, surface material type or roughness. A summary of all physical effects on infrasound are given in Fig. 1.4. The propagation of infrasound over long distances is enhanced by the existence of atmospheric waveguides resulting from the variation of the sound speed with altitude. The most substantial group of atmospheric effects can be grouped under the term of *refraction*, which describes the "slow" variation of the wave direction according to the Snell principle [38]. Smaller effects include *diffraction*, which arise from discontinuities in the medium mean state, and *tunneling* effects due to the presence of sharp variations in the atmospheric properties, such as wind jets. Finally, air friction mechanisms can cause atmospheric absorption, which is a dissipative effect that reduces the wave amplitude with distance [197].

1.2 Current state-of-the-art in infrasound modeling

In this section, we present the current state-of-the-art in numerical modeling of acoustic waves in the atmosphere. Many methods used in infrasound modeling are related to past and contemporary approaches used in Underwater Acoustics, Optics and Electromagnetic propagation. Realistic infrasound propagation involve several environmental parameters (medium inhomogeneity, topography) that are beyond the remit of analytical solutions. This has encouraged the development of various numerical methods to account for an increasing amount of physical effects. Early contributions (in the 60's and 70's) focused on simplified models for infrasound propagation, such as parabolic equations or normal modes, but the rapid improvement in computational power has shifted the focus of infrasound modeling towards more practical considerations, such as fast solvers and higher-order models. The current simulation tools can be split into several families of methods, which are namely normal modes (NM), boundary integral/element methods (BIM/BEM), ray tracing (RT), parabolic equations (PE) and direct time-domain methods. A brief summary and a literature review for each type of method is provided below.

1.2.1 Normal Modes (NM)

Analytical methods for infrasound propagation are available only in some cases, where the pressure field is given explicitly as a function of the medium parameters. Among the first analytical methods developed for long range sound propagation are the normal modes, which seeks a solution by expressing the pressure field as a superposition of modal contributions. Each mode shape is a height-dependent function that is fully determined by an eigenvalue problem, where each eigenvalue corresponds to a wavenumber in altitude [100]. The number of terms in the expansion physically represents the number of propagating modes in the atmospheric waveguide. Normal modes and associated methods are very accurate when dealing with a refracting atmosphere, and it has been used extensively to model the tro-

pospheric ducting of infrasound [215, 213, 214]. Other works have also considered propagation over a complex impedance plane for specific effective sound speed profiles [166], establishing an important equivalence between normal modes and ray tracing solutions. Normal mode solutions have also been developed for propagation above curved surfaces [29, 177], but no generic result is available for scattering by arbitrarily shaped and irregular boundaries.

Improvements on the original normal mode formulation have been achieved by Bertin et al. [30], who developed a reduced-order model by using a wavelet expansion of atmospheric variations. This allows one to simplify the computation of the pressure field by only considering the most critical eigenvalues (modes). This approach was later used to model propagation over irregular topography, including the effect of ground-induced disturbances on the effective sound speed profile [77]. Other contributions have investigated the applicability of normal mode methods for propagation in three-dimensional varying waveguides [100]. Specifically, Luo and Schmidt [130] have derived a normal mode solution for propagation above a three-dimensional conical seamount, in the context of underwater acoustics. The normal mode solution requires the computation of mode shapes in altitude and, in the case of a three-dimensional environment, along the azimuthal/transversal direction as well (which is referred to as azimuthal refraction). The normal mode is, therefore, rather inefficient in terms of implementation, and its use for three-dimensional atmospheric propagation above irregular boundaries is limited.

1.2.2 Boundary methods (BEM)

Another notable class of numerical methods for wave scattering by irregular surfaces can be grouped under the name of "boundary" methods. This approach differs from other methods in acoustics by its expression of the solution field using the Helmholtz-Kirchhoff integral [45]. The pressure field is first determined at the surface by enforcing a boundary condition and an initial condition (i.e. incident field). Then, the solution over the whole domain is calculated as a sum of all scattered fields generated by every boundary point. Extensive research has been carried out over

the past decades and applied to problems in Optics, Electromagnetics and Acoustics [65, 64, 190]. Similarly, it is possible to discretize the Helmholtz-Kirchhoff integral using Finite-Elements (FE) at the boundary, which leads to the Boundary Element Method (BEM). In the context of atmospheric acoustics, the main advantage of BEM over regular FEM is that there is no need to mesh the entire propagation domain, which can lead to drastic improvement in memory requirements. However, boundary methods involve the derivation of the Green function of the problem at hand [99, **?**]. The Green function for acoustic scattering is known in free-field, but not for a general inhomogeneous atmosphere [167]. In 3D, the computation of the Green function largely dominates the total computation time, which makes BEM impractical for large-scale problems.

A common approach to compensate for the limitations of BEM is to couple it with another method for sound propagation, such as the Normal Modes or Parabolic Equations. A rather old but well acknowledged work is the Meteo-BEM method introduced by Premat et al. [162], who coupled BEM with normal modes in order to model sound propagation in an inhomogeneous atmosphere over a rigid sound barrier. A significant advantage of this method is that it proposes a general framework for coupling the BEM with any numerical method. Another study [161], from the same author, used the same approach to develop a hybrid method, relying on both the BEM and the very efficient Green Function Parabolic Equation (GFPE). This method, called Meteo-BEM, was proven to be accurate and efficient, taking advantage of both the BEM and a more efficient propagation tool. However, it only allowed propagation over generic obstacles (arcs, slopes, barriers, ...) and extending the method to realistic topography seems beyond the capabilities of the model. While the diffracted part is correctly estimated, computational issues become critical in 3D, constraining boundary formulations to propagation at short ranges only. Therefore, boundary methods have not attracted much interest as a method for infrasound propagation in the atmosphere, which usually involves computations up to thousands of wavelengths.

1.2.3 Geometrical methods (Ray Tracing, GTD)

Ray tracing (RT) usually refers to all method that address wave propagation from a geometrical perspective rather than through a continuum mechanics formulation of fundamental acoustics. In this case, the wave is modeled by considering the trajectory of a wavefront normal (or ray), which is subject to the Snell law when traveling through a medium of varying refractive index n. The trajectories are determined by solving an Eikonal equation, and the pressure field is deduced by solving a transport equation involving the computation of a Jacobian matrix. An early ray tracing solver for atmospheric acoustics is known under the name HARPA [102] and was capable of modeling propagation over irregular topography. A more recent solver called GeoAc has been developed by Blom et al. [35] at the Los Alamos National Laboratory (LANL). The GeoAc solver includes both two-dimensional and three-dimensional propagation in an inhomogeneous atmosphere, and is considered as the standard ray tracing tool for infrasound modeling. Recently, GeoAc has been included in NCPAprop, a software package from the University of Mississippi's NCPA (National Center for Physical Acoustics) [128, 216]. Although ray tracing methods are computationally advantageous, their validity is limited to large scale variation of the refractive index and cannot accurately model diffraction effects from small scale inhomogeneities. Furthermore, including irregular surfaces in ray tracing algorithms poses a large number of challenges both in terms of the implementation of boundary conditions and physical accuracy in shadow zones.

While ray tracing involves the computation of individual ray paths, the geometrical theory of diffraction (GTD) [157] provides a more physical description of the wave field. An early contribution to the use of the GTD in the context of atmospheric acoustics is due to Rasmussen [164], who provided an analytical solution for propagation over a perfectly reflecting wedge. Later, Salomons [179] compared the GTD to the Parabolic Equation (PE), the Boundary Element Method (BEM) and experimental data for propagation over a variety of noise barriers, including ground impedance discontinuities. It was shown that the GTD performs well in most cases, except at low frequencies. Another contribution was made by Robertson [168], who used the GTD as a benchmark for the validation of the Parabolic Equation (PE).

Since the GTD relies on an analytical description of the diffracted field, it is not possible to use it as a simulation tool for realistic topography.

1.2.4 Finite-Difference Time Domain (FDTD)

While most numerical methods used in infrasound modeling rely on a physical approximation, it is also possible to model wave propagation from a Fluid Mechanics perspective by solving the Navier-Stokes equation [132]. In a three-dimensional propagation space, the time-dependent pressure fluctuation is a function of four dimensions (*i.e.* spatial variables (x, y, z) and time t), which can lead to a very large linear system. The propagation distances in infrasound propagation would make any standard aero-acoustics solver too slow, so the Navier-Stokes equation is solved using fast Finite-Difference Time-Domain (FDTD) schemes [60, 61, 146]. The main advantage of such a direct modeling is that all non-linear effects are enabled, leading to high-fidelity models of infrasound propagation in inhomogeneous media. More recently, significant improvements have been achieved thanks to parallel computing, leading to highly accurate three-dimensional solvers. Notably, Sabatini et al. [173, 172] have developed a GPU-accelerated code for the unsteady three-dimensional Navier-Stokes equation.

Hybrid models relying on FDTD have also attracted a lot of attention, especially FDTD-PE coupled models [204], allowing for both an accurate near-field description of the acoustic source and efficient computation of the scattered field over long distances. An interesting study has been carried out by Cotte et al. [56], who used a FDTD-PE method to compute sound propagation from a wind turbine. This approach seems more reasonable than complete direct modeling but raises an important problem, namely the conversion of the time-domain solution to a frequency-domain starter, particularly for three-dimensional propagation. The FDTD has become increasingly popular for infrasound propagation in the atmosphere, including for the modeling of topographic effects. Among the significant contributions made in this perspective, Heimann [93] applied a curvilinear coordinate transformation on the FDTD equations and compared it to the "natural" inclusion of the

terrain profile. More recently, Dragna and Blanc-Benon [73, 71] have developed a FDTD method, based on Linearized Euler Equations (LEE) and optimized finite-differences, and validated against outdoors experiments [**?**]. Finally, time-domain impedance boundary conditions have been derived by Dragna et al. [72] in order to account for physical causality in the FDTD numerical scheme, which is not possible with frequency-domain methods such as the Parabolic Equation of the Normal Modes.

1.2.5 Parabolic Equations (PE)

One of the oldest and most popular simulation techniques for long-range infrasound is the so-called Parabolic Equation (PE) method [118]. The PE method consists of applying a paraxial approximation to the Helmholtz equation, which leads to a simplified solution that is accurate only within a small angle around a preferred direction of propagation. This method has been originally derived for Underwater Acoustics [117, 116, 184, 199] before being used in Atmospheric Acoustics [217, 177]. Parabolic equations can be solved using marching schemes and are very efficient for predictions at long ranges and within the atmospheric boundary layer. In order to overcome the angle limitation of the PE and enable propagation at higher altitudes, higher-order paraxial approximations have been introduced by considering Padé expansions of the square-root operator [50, 131, 143]. Wide-angle models have lead to the development of more accurate forms of the PE, taking into account atmospheric velocity and turbulence [32, 59, 146] while standard models, *e.g.* the original PE derived by Tappert [199], were constrained to the effective sound speed approximation.

The PE method has also been adapted to wave scattering by irregular boundaries. One of the first attempts at modeling the effects of rough boundaries with the PE was made by Beilis and Tappert [26] in the context of Electromagnetic wave propagation, who proposed a coordinate transformation to express the PE in a flattened numerical domain, where the solution can be computed efficiently. This method is referred to as the Beilis-Tappert Parabolic Equation (BTPE). The Beilis-Tappert coordi-

nate transformation has been extensively used to model propagation over wedges, hills and realistic terrains [121]. The most attractive feature of the BTPE is that range-dependence is included in a phase shift at every marching step [68, 95, 152]. In atmospheric acoustics, Sack and West [174] used the Beilis-Tappert coordinate transformation to derive the Generalized-Terrain Parabolic Equation (GTPE), which included a novel a wide-angle formulation. The GTPE has become a reference for low frequency sound propagation over irregular boundaries, but included an important limitation, namely it does not take into account atmospheric inhomogeneities. Another important contribution is the Rotated Parabolic Equation, developed by Collins [53], who proposed to model propagation as a succession of titled, flat numerical domains. Another method, known as the Polar-PE and derived by Parakkal et al. [153], relied on the modeling of irregular boundaries as a continuous succession of circles, using a conformal mapping formulation from Aero-Acoustics. The Polar-PE was proven to be accurate but the conformal mapping used limits its applicability to smooth profiles. More recently, Parakkal et al. [152] have proposed an improved version of the BTPE, with inclusion of simplified boundary conditions, but was limited to narrow-angle propagation.

Another major focus of the PE research has been the extension of the original theory to three-dimensional propagation in cylindrical and Cartesian coordinates. The driving argument behind the development of three-dimensional parabolic equations (3DPE) has been the existence of significant transversal effects that were not accounted for by the two-dimensional parabolic equations (2DPE). Indeed, the 2DPE assumes the propagation domain to be axisymmetric, which is not true in the case of realistic three-dimensional environments. The phenomenon of out-of-plane scattering is known as *horizontal refraction* [202], and was first investigated in Underwater Acoustics. An early 3DPE was derived by Lee et al. [116], who used a wide-angle expansion of the square-root operator with an Alternate Direction Implicit (ADI) numerical scheme. This method has been further generalized into the Split-Step Padé (SSP) method [192, 193, 126], based on finite-differences, and the Split-Step Fourier (SSF) method [127], based on Fourier Transforms. Both the SSP and the SSF numerical schemes have been popular as they allow to solve each direction separately, reducing the computational costs. Another approach has been adopted by Cheng et al. [44], who did not make use of direction splitting and solved a large

sparse system instead. It was pointed out that this approach requires very high computational resources, and that an iterative solver, like the Generalized Minimal Residual Method (GMRES) [170], must be used.

More recently, in October 2019, a series of contributions to the three-dimensional parabolic equation (3DPE) was published in the Journal of the Acoustical Society of America (JASA). One of the most recent developments in this field is that of Lin et al. [125], who developed a wide-angle boundary-fitted 3DPE using non-uniform Galerkin finite-differences. This method allows for an accurate treatment of irregular boundaries but have only been applied to pressure-release interfaces. In atmospheric acoustics, the earth surface is usually modeled as an impedance boundary condition, which involves a directional derivative. As a result, boundary-fitted grids would require an interpolation at every boundary point, which makes the implementation of the PE method more challenging for arbitrarily shaped boundaries. However, this highlights the interest of the research community in the development of an efficient 3DPE that take into account scattering by irregular boundaries. The technical and theoretical aspects of the PE method will be detailed in chapters 3 and 4.

1.3 Statement of the problem

Numerical simulations play a crucial role in the modeling of ground-truth events, and many efforts have been dedicated to the application of existing models to realistic infrasound problems. The literature review provided in Sec. 1.2 demonstrates that every numerical method has its own limitations and no standard model can allow a full description of propagation effects in a complex environment without trade-offs. The current common approach consist of implementations that combine different prediction tools to perform a forward infrasound modeling. Typically, parabolic equations and ray tracing simulations are overlaid to provide a dual geometrical and physical interpretation of infrasound arrivals [159]. While simulations have successfully matched experimental observations, an important modeling issue remains: numerical methods are subject to several medium uncertainties, such as temperature

variation, wind conditions and ground effects. Meteorological effects on infrasound propagation are well understood, but little effort has been made towards a proper study of infrasound interaction with the earth surface. Therefore, this thesis aims at studying the effects of realistic ground conditions on infrasound propagation. The proposed study will attempt to fill the following gaps in the current literature,

- **Issue 1:** Quantify the effects of irregular boundaries on grazing infrasound propagation. What are the physical phenomena involved and which parameters are the key contributors to three-dimensional propagation effects?

- **Issue 2:** Derive an efficient three-dimensional parabolic equation (3DPE) that takes into account both atmospheric refraction and topographic effects for irregular boundaries.

- **Issue 3:** Determine to what extent are topographic effects relevant in realistic infrasound propagation in a complex three-dimensional environment.

1.3.1 Research hypotheses

The effects of topography on infrasound are theoretically described by the theory of acoustic diffraction [157]. Several scattering mechanisms are involved, depending on the type and size of the obstacle (trees, hills, mountains, etc.) in comparison with the wavelength λ_0. It is possible to classify topographic obstacles into three general scales, depending on the ratio δ_g/λ_0, where δ_g is the obstacle size (height or width) and λ_0 the wavelength. As such, any realistic topography can be described by a superposition of: (i) boundary roughness ($\delta_g/\lambda_0 \ll 1$), (ii) diffractive obstacles and sound barriers ($\delta_g/\lambda_0 \simeq 1$) and (iii) long-range variations ($\delta_g/\lambda_0 \gg 1$). However, the importance of these effects in practice has long been unknown or not clearly identified. As a result, the literature on the subject is very scarce, since it is assumed that topography has a limited influence on low-frequency sound.

Recent studies of infrasound propagation [134, 107] have led researchers to reexamine

this assumption, speculating on the existence of significant topographic effects in some situations. Kim and Lees [108, 107] performed FDTD simulations of volcanic infrasound and showed that topography plays a crucial role on local infrasound propagation (*i.e* for ranges of a few kilometers), as terrain barriers close to the source cause strong anisotropic effects. Such effects have been associated with discrepancies in infrasound observations by McKenna et al. [134], who proved that terrain leads to an underestimation of the waveform amplitude. Generally, the literature suggest that the local maxima (or minima) of the terrain elevation is the key factor in anticipating the effect of topography. In order to address the issue of topographic effects, it is necessary to establish a clear framework for the proposed study. From the existing literature, it is reasonable to assume that:

- **Hypothesis 1:** At infrasonic frequencies of interest ($0.1 < f < 10\,\text{Hz}$), all scales of the earth surface can be reasonably described by a smooth and continuous surface. This is justified by the fact that obstacles that are negligible in size compared to the wavelength can be ignored.

- **Hypothesis 2:** The ground is assumed to be made of a porous material which acoustic properties are fully contained in the surface impedance Z_s. The ground can be either semi-infinite (*i.e. locally reacting*) or layered (*i.e. extended reacting*).

- **Hypothesis 3:** Interaction of low-frequency acoustic waves with topography can be divided into two main mechanisms: (i) grazing-angle scattering between the direct wave and the terrain obstacle, (ii) ground-bounce scattering of tropospheric and stratospheric infrasound arrivals.

- **Hypothesis 4:** As suggested by the literature, terrain interacts with infrasound locally, and is of relevance only when the source, or the receiver, are close to topographic obstacles. Therefore, only regionals distances (*i.e* less than 100 km) are considered in this thesis.

- **Hypothesis 5:** The earth curvature is generally negligible, with little to no effect on the wave amplitude, except when considering very high altitudes, in

which case it leads to a difference of a few seconds in arrival time estimations for a propagation distance of 1000 km [66]. This is verified geometrically by comparing the absolute distance d with the arc-length d' between two points on earth (source A and receiver B). By definition,

$$\begin{aligned} d &= R_0 \sin\theta_0, \\ d' &= R_0\theta_0, \end{aligned}$$

where $R_0 = 6371$ km is the earth radius and θ_0 is the sector angle between A and B. According to Hypothesis 4, local infrasonic propagation occurs over distances less than $d' = 100$ km, which leads to $\theta_0 = 100/6371 \approx 0.015$ and $\sin\theta_0 \approx 0.0149$. Therefore, $d' \approx d$ and the earth sphericity is locally negligible.

- **Hypothesis 6:** The atmosphere is assumed to be layered and modeled by the effective sound speed approximation (ESSA) [87]. The physical quantities of interest for the modeling of the atmosphere are the adiabatic sound speed c_0 (which is deduced from the temperature T) , the wind flow $\mathbf{v}_0$ and the atmospheric density ρ_0. All of these quantities depend on the altitude z only.

Unlike atmospheric parameters, topographic data are not subject to uncertainties and can be easily extracted from satellite imagery. One of the most common gridded databases for global topography is the ETOPO1 model, which was developed in 2008 by the National Oceanic and Atmospheric Administration (NOAA) [8], with a scale of 3 arc-seconds in latitude and longitude. This leads to a grid resolution of about 90 meters, which is an accurate format for infrasound applications. Another notable dataset has been created by the NASA Shuttle Radar Topography Mission [78], which has a 1 arc-second sampling (i.e. 30 meters grid resolution) and is the highest open-source resolution model available for global topography. The main challenge behind modeling infrasound above irregular terrain is less related to data variability and more to the capabilities of the numerical method used.

1.3.2 Proposed methodology

In this thesis, we will focus on the Parabolic Equation (PE) and its suitability for modeling propagation over three-dimensional irregular boundaries. The choice for this method over the others is motivated by a number of reasons. Firstly, the Parabolic Equation method is well suited for low-frequency propagation over long distances. The theory is well documented and the number of successful results over the past decades [118] provide enough confidence in the PE as a prediction tool. Moreover, the Parabolic Equation method is versatile and can be easily implemented to solve large three-dimensional problems without reaching prohibitive calculation times. Finally, it is the only numerical method that has been extensively applied to propagation over irregular terrains in two-dimensions, and most technical details related to numerical implementation are available in the literature, namely boundary conditions [117, 40], wide-angle capability [59], terrain mapping [153, 152], three-dimensional schemes [232, 192]. The main purpose of the thesis will be devoted to the extension of the existing theory to accommodate three-dimensional terrain. The main objectives of the thesis can be summarized as:

- **Objective 1:** Propose and validate a novel and efficient Parabolic Equation (PE) method to model propagation over irregular three-dimensional boundaries in a refractive atmosphere.

- **Objective 2:** Demonstrate the existence of three-dimensional propagation effects quantify the scattered field through a parametric study for a range of irregular surfaces

- **Objective 3:** Apply three-dimensional modeling to a realistic infrasound modeling problem and compare numerical results against experimental measurements.

1.3.3 Thesis structure

The remainder of the thesis is structured as follows: Chapter 2 will contain the basic theory of linear acoustics and propagation in a refractive medium, in particular, retrieving the wave equation for a layered atmosphere with variable density. In Chapter 3, the parabolic equation in two-dimensions is derived. Additionally, a minor contribution to the existing theory is made by coupling the wide-angle finite-difference solution of the Beilis-Tappert Parabolic Equation (BTPE) with first-order terrain terms. In Chapter 4, the Beilis-Tappert transform is extended to the three-dimensional PE with two numerical schemes based on finite-differences. We implement and validate a narrow-angle version of the three-dimensional BTPE and lay the ground for a wide-angle solution based on the well known Split-Step Padé approach. In Chapter 5, the PE solver will be used to model propagation in homogeneous and inhomogeneous atmospheres, over a generic irregular boundary defined by a Gaussian hill. In, Chapter 6 will present a realistic case of infrasound propagation in a mountainous region, with comparisons between PE modeling and amplitude ratios derived from IMS data. Finally, conclusions and suggestions for future work will be given in Chapter 7.

Chapter 2

Wave propagation in a layered media

A study of infrasound propagation in the atmosphere requires the use of an appropriate form of the wave equation, including medium inhomogeneities as well as realistic boundary conditions. The development of a wave equation that takes into account all effects influencing propagation remains an open problem. As a result, the best approach has been to derive the wave equation with a reasonable amount of assumptions, tailored to the problem at hand. For example, a common hypothesis is that the atmosphere can be treated as a layered medium, meaning that all its state variables, such as temperature, density or pressure, vary in altitude only, allowing us to remove range-dependence. In other scenarios, the atmosphere can be modeled as a moving or turbulent medium, increasing the level of complexity of the model for a more accurate physical representation. However, the choice of the model must be motivated by the real features of the atmosphere as a propagation medium and their importance in the intended study.

In the present thesis, the atmosphere is assumed to be layered and the motion of the atmosphere (wind flows) is incorporated in the wave equation through the effective sound speed approximation. The general theory of sound propagation in the atmosphere will be presented in Sec. 2.1, with the purpose of obtaining an

appropriate form of the wave equation for a layered effective medium. The specific issues related to the interaction of sound with the earth surface are given in Sec. 2.2. Finally, the definition of sound sources and physical quantities of interest are given in Sec. 2.3.

2.1 Theory of sound propagation

2.1.1 Linear acoustics equations

In this subsection, we present one of the several possible derivations of the standard wave equation in a compressible fluid, as explained in numerous references such as Dowling and Ffowcs-Williams [70] or Pierce [157]. We constrain ourselves, in the rest of the present thesis, to linear acoustics while pointing out that for some specific sound mechanisms, such as explosions or very loud shockwaves, non-linear terms are large and a more complete theory (non-linear acoustics) should be selected. Sound as a physical mechanism can be represented as a local pressure fluctuation that travels in a fluid, which generates corresponding velocity and density fluctuations. The fundamental assumption behind linear acoustics is that the pressure fluctuation caused by sound waves are small in comparison with the mean pressure of the medium. This allows to write the total pressure P, density ϱ and velocity $\mathbf{u}$ of the fluid, at a location $\mathbf{x}$ and time t, as

$$P(\mathbf{x},t) = p_0(\mathbf{x},t) + p(\mathbf{x},t), \tag{2.1a}$$

$$\varrho(\mathbf{x},t) = \rho_0(\mathbf{x},t) + \rho(\mathbf{x},t), \tag{2.1b}$$

$$\mathbf{u}(\mathbf{x},t) = \mathbf{v}_0(\mathbf{x},t) + \mathbf{v}(\mathbf{x},t), \tag{2.1c}$$

where p_0, ρ_0 and $\mathbf{v}_0$ are the mean pressure, density and velocity of the fluid medium, respectively, and p, ρ and $\mathbf{v}$ are the pressure, density and velocity fluctuations associated with the sound wave. The expressions in Eq. (2.1) can be seen as a first-order expansion, such that the acoustic variables are an order of magnitude lower than the

mean variables. It is possible to derive the equations of linear acoustics by starting from the fundamental equations of fluid mechanics, which are the conservation of mass and conservation of momentum, respectively written as

$$\frac{\partial \varrho}{\partial t} + \nabla \cdot (\varrho \mathbf{u}) = 0, \tag{2.2a}$$

$$\frac{\partial \mathbf{u}}{\partial t} + \mathbf{u} \cdot \nabla \mathbf{u} + \frac{1}{\varrho} \nabla P = 0. \tag{2.2b}$$

Equations (2.2a) and (2.2b) are obtained by considering an infinitesimal volume of fluid subject to a pressure gradient. The details of the derivations can be found in fluid or continuum mechanics reference books [89]. Furthermore, sound propagation is an adiabatic process, and the atmosphere, mostly composed of air, is a perfect gas, so the state variables P and ϱ are linked by the Laplace law of thermodynamics

$$P = C\varrho^{\gamma}, \tag{2.3}$$

where $\gamma = 1.4$ for air and C is a constant. Equation (2.3) suggests that the amplitude of fluctuations in sound propagation are small enough to generate no heat flow. When subjected to a density fluctuation from a traveling sound wave, the total pressure P can be expressed using the first-order Taylor expansion,

$$P \simeq p_0 + \left(\frac{\partial P}{\partial \rho}\right) \rho. \tag{2.4}$$

Hence, using Eq. (2.1), we identify the last term in Eq. (2.4) as the acoustic pressure fluctuation p. Using Eq. (2.3) to express the derivative in Eq. (2.4), we obtain

$$p = \left(\frac{\partial P}{\partial \varrho}\right) \rho = \gamma \left(\frac{P}{\varrho}\right) \rho, \tag{2.5}$$

and using the law of perfect gases, we have

$$P = \rho R T, \tag{2.6}$$

where R is the universal gas constant and T is the temperature. Using Eq. (2.6) to replace P in Eq. (2.5), the following equation is obtained

$$p = c^2 \rho, \tag{2.7}$$

where $c = \sqrt{\gamma RT}$ is the sound speed. The relation in Eq. (2.7) accounts for the thermodynamic properties of sound propagation in air. Next, the wave equation is derived by combining the fundamental equations of linear acoustics given in Eq. (2.2a) (conservation of mass) and Eq. (2.2b) (conservation of momentum) with the constitutive model of the medium given in Eq. (2.7). In order to derive the wave equation, the expressions of P, $\mathbf{u}$ and ϱ in Eq. (2.1) are inserted in Eq. (2.2a) and Eq. (2.2b) which, after neglecting the time and space derivatives of the zeroth-order mean variables p_0, ρ_0 and $\mathbf{v}_0$, leads to the following first-order equations

$$\frac{D\rho}{Dt} + \rho_0 \nabla \cdot \mathbf{v} = 0, \tag{2.8a}$$

$$\frac{D\mathbf{v}}{Dt} + \frac{1}{\rho_0} \nabla p = 0, \tag{2.8b}$$

where $\nabla \mathbf{v}$ is a tensor and D/Dt is the Lagrangian derivative of the medium, i.e. the rate of change expressed locally for a moving fluid element. Since the atmosphere is subjected to a mean velocity field $\mathbf{v}_0$, the Lagrangian derivative is defined as

$$\frac{D}{Dt} = \frac{\partial}{\partial t} + \mathbf{v}_0 \cdot \nabla. \tag{2.9}$$

The Lagrangian derivative inherits the linearity properties of Eulerian time derivatives and can be used without loss of generality. Taking the Lagrangian derivative of the equation of mass conservation given in Eq. (2.8a) leads to

$$\frac{D^2\rho}{D^2t} + \rho_0 \nabla \cdot \frac{D\mathbf{v}}{Dt} = 0, \tag{2.10}$$

and, using the equation of momentum conservation in Eq. (2.8b) to express the

term $D\mathbf{v}/Dt$ in Eq. (2.10), the following equation is obtained

$$\frac{D^2\rho}{D^2t} - \rho_0 \nabla \cdot \left(\frac{1}{\rho_0} \nabla p \right) = 0, \tag{2.11}$$

Finally, Eq. (2.7) is used to express the density fluctuation ρ in Eq. (2.11). This leads to the wave equation for an atmosphere with a mean density ρ_0 and a mean fluid velocity $\mathbf{v}_0$,

$$\boxed{\frac{1}{c^2}\frac{D^2p}{Dt^2} - \rho_0 \nabla \cdot \left(\frac{1}{\rho_0} \nabla p \right) = 0.} \tag{2.12}$$

This form of the wave equation is one of the most general possible, although some other formulations have been developed to include a turbulent field [158]. For a medium at rest, i.e. for $\mathbf{v}_0 = \mathbf{0}$, the Lagrangian derivative D/Dt in Eq. (2.9) reduces to the Eulerian derivative $\partial/\partial t$. Furthermore, assuming the medium to be homogeneous, the mean density ρ_0 is constant everywhere in space and Eq. (2.12) reduces to

$$\Delta p - \frac{1}{c^2}\frac{\partial^2 p}{\partial t^2} = 0. \tag{2.13}$$

where $\Delta = \nabla^2$ is the scalar Laplacian operator. Equation (2.13) is known as the homogeneous wave equation and describes sound radiation in free-field, i.e in the absence of a source term or medium inhomogeneities.

The right-hand side of Eq. (2.13) can be defined according to the type of sound source. A monopole source emitting from a location $\mathbf{x}_s$ is mathematically represented as a term of the form $S_0(t)\delta(\mathbf{x} - \mathbf{x}_s)$, where S_0 is the time-dependent amplitude and δ the Dirac function. Other formulations specific to certain applications will use different types of sources, like the Lighthill tensor in Aero-acoustics [123, 139].

In the general case, it is possible to factor the pressure field p and separate the spatial variable $\mathbf{x}$ from the time variable t. For a monochromatic harmonic, time-

dependence is contained in a factor $e^{-i\omega t}$, and the pressure fluctuation p is given by

$$p(\mathbf{x}, t) = \mathrm{Re}\{p_c(\mathbf{x}, \omega)e^{-i\omega t}\}, \tag{2.14}$$

where $\omega = 2\pi f$ is the angular frequency of the wave and p_c is the complex pressure amplitude. Equation (2.14) implies that the pressure field has an oscillatory behavior with respect to time and the wave-field can be entirely solved in the frequency domain. Substituting Eq. (2.14) into the homogeneous wave equation, given by Eq. (2.13), leads to the Helmholtz equation for the pressure amplitude p_c

$$\boxed{\frac{\partial^2 p_c}{\partial x^2} + \frac{\partial^2 p_c}{\partial y^2} + \frac{\partial^2 p_c}{\partial z^2} + k^2 p_c = 0.} \tag{2.15}$$

where $k = \omega/c$ is the wavenumber. After solving Eq. (2.15) for p_c, the real pressure fluctuation p is obtained by using Eq. (2.14). The sound speed c can be generalized to situations where the atmosphere is not isothermal, while still maintaining the adiabatic property of sound propagation. Realistic atmospheres are usually described by a variation of temperature with altitude, which leads to equivalent disturbances in the medium velocity, pressure and density. Starting from the previous definition in Eq. (2.7), the adiabatic sound speed c can be defined as

$$c(z) = c_0\sqrt{\frac{T(z)}{T_0}} \tag{2.16}$$

where $c_0 = \sqrt{\gamma R T_0}$ is the isothermal sound speed and $T_0 = 283\,\mathrm{K}$ is the standard isothermal atmosphere temperature. The perfect gas law states that variations in temperature implies concurrent variations in mean atmospheric density ρ_0 and pressure p_0. For an isothermal atmosphere at $T = T_0$, we have $\rho_0 = 1.29\,\mathrm{kg}^3 \cdot \mathrm{m}^{-1}$.

2.1.2 The effective sound speed approximation

In this section, we will present a common approximation of the wave equation in a moving medium that was derived in Eq. (2.12). For many applications, the

homogeneous Helmholtz equation, given by Eq. (2.15), provides a sufficiently accurate model. But, in atmospheric acoustics, medium inhomogeneities can become substantial and affect the sound propagation over large distances. Using a general model, such as Eq. (2.12), can pose a large number of challenges when deriving a numerical solution. A simplification can be reached by assuming the medium to be at rest (independent of time) and layered, i.e. spatially varying along the altitude z only. In this case, the total pressure, density and sound velocity fields given in Eq. (2.1) can be written as

$$P(\mathbf{x}) = p_0(z) + p(\mathbf{x}), \tag{2.17a}$$

$$\varrho(\mathbf{x}) = \rho_0(z) + \rho(\mathbf{x}), \tag{2.17b}$$

$$\mathbf{u}(\mathbf{x}) = \mathbf{v}_0(z) + \mathbf{v}(\mathbf{x}), \tag{2.17c}$$

where $\mathbf{v}_0 = (\mathbf{v}_{0,h}, 0)^T = v_0(z)(\cos\theta_w, \sin\theta_w, 0)^T$ is the medium velocity and $\mathbf{v}_{0,h}$ is the horizontal wind velocity, i.e. the projection of $\mathbf{v}_0$ in the (x, y) plane. After replacing p by the complex pressure p_c using Eq. (2.14), the inhomogeneous wave equation Eq. (2.12) becomes

$$\frac{1}{c^2}\left\{-i\omega + \mathbf{v}_{0,h}\cdot\nabla_h\right\}^2 p_c - \Delta_\perp p_c - \rho_0 \frac{\partial}{\partial z}\left(\frac{1}{\rho_0}\frac{\partial p_c}{\partial z}\right) = 0, \tag{2.18}$$

where Δ_h is the Laplacian operator in the horizontal plane (x, y). The purpose of the effective sound speed approximation is to simplify the term $\mathbf{v}_{0,h}\cdot\nabla_h$ in Eq. (2.18), which can be achieved by considering a plane wave behavior in the horizontal plane. We begin by writing p_c as the spatial Fourier transform of $\tilde{p}_c$, which can be expressed as

$$p_c(\mathbf{x}, \omega) = \frac{1}{4\pi^2}\iint_{\mathbb{R}^2} \tilde{p}_c(\mathbf{k}_h, z, \omega) e^{i\mathbf{k}_h\cdot\mathbf{x}} \mathrm{d}\mathbf{k}_h, \tag{2.19}$$

where $\mathbf{k}_h = (k_x, k_y)^T$ is the horizontal wave-vector and $\mathbf{x}$ is the receiver location. The wave-vector $\mathbf{k}_h$ gives the propagation direction of the plane wave solution, so for a wave of angular frequency ω, it can be written as $\mathbf{k}_h = (\omega/c(z))\boldsymbol{\nu}_h$, where $\boldsymbol{\nu}_h$ is the unit vector giving the propagation direction in the (x, y) plane and $c(z)$ is the

adiabatic sound speed. Substituting Eq. (2.19) in $\mathbf{v}_{0,h} \cdot \nabla_h$, leads to the following equation for $\tilde{p}_c$ in the wavenumber domain,

$$\mathbf{v}_{0,h} \cdot \nabla_h p_c = \frac{\omega v_0(z)}{c(z)} (\mathbf{e}_0 \cdot \boldsymbol{\nu}_h) \tilde{p}_c. \tag{2.20}$$

where $\mathbf{e}_0$ is the direction of the horizontal wind $\mathbf{v}_{0,h}$. After inspecting Eq. (2.20), it appears that the effective sound speed approximation has modified the refractive term k^2 to an effective quantity, as

$$k_{\text{eff}}^2 = \frac{(-i\omega + i\mathbf{v}_{0,h} \cdot \mathbf{k}_h)^2}{c^2} \approx \frac{\omega^2}{c_{\text{eff}}^2} + \mathcal{O}(M^2), \tag{2.21}$$

where $M = v_0/c$ is the Mach number and c_{eff} is the effective sound speed, defined as $c_{\text{eff}}(z) = v_0(z) + c(z)$. Using Eq. (2.21) to replace the first term in Eq. (2.18), we obtain a common version of the wave equation used in Atmospheric and Underwater Acoustics [100, 38] that includes both density variation in altitude and atmospheric refraction from a layered media and horizontal atmospheric winds,

$$\boxed{\rho_0 \frac{\partial}{\partial z} \left(\frac{1}{\rho_0} \frac{\partial p_c}{\partial z} \right) + \Delta_h p_c + k_{\text{eff}}^2(z) p_c = 0.} \tag{2.22}$$

Therefore, the effective sound speed approximation made in Eq. (2.21) accounts for the atmospheric stratification by the means of an effective wavenumber, and the final wave equation derived in Eq. (2.22) can be seen as a modified version of the homogeneous Helmholtz equation given by Eq. (2.15). Physically, atmospheric refraction is described as the change of the acoustic velocity field $\mathbf{v}$ due to a variation of c. By including the medium velocity terms $\mathbf{v}_0$ into the sound speed, the approximation made in Eq. (2.21) has converted the convective terms into refractive terms, resulting in a much simpler form of the wave equation.

A further investigation of the effective sound speed approximation and its limitations can be achieved through a geometrical acoustics approach. From Eq. (2.17c), we see that the total velocity can be written as the sum of the sound velocity $\mathbf{v}$ and the mean medium velocity $\mathbf{v}_0$. For a specific sound ray traveling along a direction

described by a unit vector $\boldsymbol{\nu}$, the acoustic velocity can be written as $\mathbf{v} = c(z)\boldsymbol{\nu}$, where $c(z)$ is the adiabatic sound speed defined in Eq. (2.16). Therefore, the total velocity field is

$$\mathbf{u}(z) = v_0(z)\mathbf{e}_0 + c(z)\boldsymbol{\nu}, \tag{2.23}$$

where $v_0(z) = ||\mathbf{v}_0(z)||$ is the medium mean velocity and $\mathbf{e}_0$ is the unit vector in the direction of $\mathbf{v}_0(z)$. This is achieved by assuming that the medium moves in the same direction as the wave is propagating, i.e. $\mathbf{e}_0 \simeq \boldsymbol{\nu}$, so the total wavefront speed is approximately $||\mathbf{u}(\mathbf{x})|| \simeq v_0(z) + c(z)$, which provides a justification for the form of c_{eff} introduced in Eq. (2.21). This assumption is valid as long as transversal winds are negligible, which is an important limitation that can lead to an error in the interference locations at long range and shifted infrasound arrivals [87].

In practice, the atmosphere wind profile $\mathbf{v}_0$ depends largely on atmospheric conditions as well as the boundary properties, which has been extensively studied in the literature [223, 200]. For low altitude problems, a popular expression for the effective sound speed is the logarithmic profile

$$c_{\text{eff}}(z) = c_0 + b \ln\left(1 + \frac{z}{z_0}\right), \tag{2.24}$$

where $b = v_f/k_v$, with v_f the friction speed and k_v the Von Karman constant associated with the boundary material, and z_0 is the height of the material roughness. The Von Karman k_v constant is universal, its experimental values range from 0.36 to 0.44, with a generic value of 0.40 in the fluid mechanics literature [182]. The physical meaning of k_v remains uncertain, as it is a mathematical constant that arise from fitting flow measurements with the logarithmic law in Eq. (2.24). It accounts for the turbulent behavior of the flow at the vicinity of the wall. The height z_0 can be changed according to the type of boundary, *e.g.* $z_0 \approx 1$ m for propagation over plain land, and $z_0 \approx 10^{-3}$ m above sea. The effective sound speed profile defined in Eq. (2.24) is valid only in the atmospheric boundary layer (i.e. for $0 < z < 10\,\text{km}$), where realistic wind conditions are reasonably well approximated by a logarithmic profile [177].

2.2 Interaction of sound with the ground

Prior research has proven that the ground has a very important effect on outdoor sound propagation, even at low frequencies . In most cases, the ground is modeled as an absorbing porous material, and the surface between the ground and the atmosphere is represented by an impedance plane, with a normalized surface impedance Z_s [15, 177]. This surface impedance accounts for a medium discontinuity, in such a way that when sound interacts with the earth surface, one part of the wave is transmitted to the ground while another is reflected back into the atmosphere, following the Huygens-Fresnel principle [157]. The reflected wave is composed of *specular* and *diffuse* reflections, whose amplitude depends on the value of the surface impedance Z_s. The specular reflection component describes the part of the wave that "bounces" off the impedance surface, and contains a major part of the energy. The diffuse reflection component involves small amplitude reflections occurring in all directions, arising from the microstructure of the impedance plane and is relevant at high frequencies (in comparison with the roughness size).

2.2.1 Reflection by the ground surface

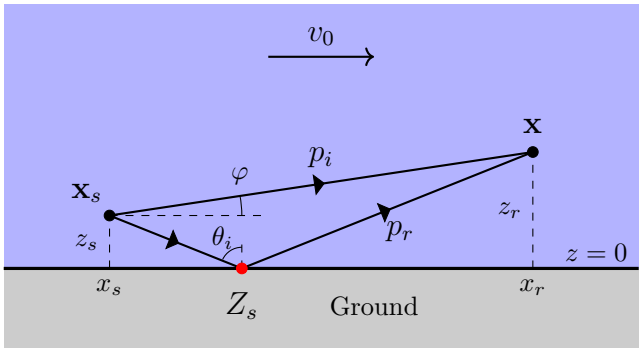

Figure 2.1: Propagation over a flat ground surface of impedance Z_s, from a source located at $\mathbf{x}_s$ and a receiver located at $\mathbf{x}$, in a uniform atmospheric flow v_0 in the direction $+x$. The red dot represents the only reflection point between the source and the receiver, the angle φ is the elevation angle and θ_i the angle of incidence with the ground surface.

In this section, the analytical solution of a wave propagating above a flat impedance surface is presented. When a wave interacts with an obstacle of any sort, the pressure field is scattered following several mechanisms. All these effects can be accounted for by the generation of a scattered pressure field p_s, which is superposed to the incident (direct) wave p_i to create a total complex pressure $p_c = p_i + p_s$. When the boundary is flat, $p_s = p_r$, where p_r is the reflected wave, obtained using the method of image sources [28, 177], in which the reflected field is equal to the field emitted by an image source located below the surface. Fig. 2.1 provides a schematic of a point source located close to an impedance surface, at a location $\mathbf{x}_s$, emitting sound towards a receiver located at $\mathbf{x}$. For a monopole source located at $\mathbf{x}_s = (x_s, y_s, z_s)$ and radiating a spherical wave above a plane located at $z = 0$, the reflected field is equal to a wave radiated by an image source at $\mathbf{x}'_s = (x_s, y_s, -z_s)$. Hence, the total pressure field p at a point $\mathbf{x}$ in space can be written as

$$\boxed{p_c(\mathbf{x}) = S_0 \left(\frac{e^{ik_0 R_i}}{R_i} + Q(\varphi) \frac{e^{ik_0 R_r}}{R_r} \right),} \tag{2.25}$$

where S_0 is the amplitude, $R_i = |\mathbf{x}_s - \mathbf{x}|$ is the distance between the source and the receiver, $R_r = |\mathbf{x}'_s - \mathbf{x}|$ is the distance between the image source and the receiver and $Q(\varphi)$ is the spherical reflection coefficient, which depends on the propagation angle φ. The complex pressure p_c in Eq. (2.25) is solution of the homogeneous Helmholtz equation given in Eq. (2.15). The spherical reflection coefficient is given by

$$Q(\varphi) = R_p(\varphi) + (1 - R_p(\varphi))F(w), \tag{2.26}$$

where R_p is the plane wave reflection coefficient, given by

$$R_p(\varphi) = \frac{Z_s \cos\varphi - \chi}{Z_s \cos\varphi + \chi}, \tag{2.27}$$

and w, χ and F are given by [28]

$$F(w) = 1 + iw\sqrt{\pi}e^{-w^2}\operatorname{erfc}(-iw), \tag{2.28a}$$

$$w = \frac{1}{1 - R_p}\sqrt{\frac{2ik_0R_r}{Z_s}}, \tag{2.28b}$$

$$\chi = \sqrt{1 - \frac{k_0}{k_g}\sin^2\varphi}, \tag{2.28c}$$

where k_g is the wavenumber in the ground material and erfc is the complex error function. When the ground is perfectly reflecting, we have $Z_s = \infty$, which leads to $Q = 1$. Small scale irregularities of the ground surface are usually accounted for by setting an appropriate model of the ground material. Usually, the ground material is defined as a porous medium, which is entirely defined by the surface impedance Z_s in Eqs. (2.27) and (2.28b). The most common models for the impedance of porous materials are the Zwikker-Kosten model [234] and the empirical Delany-Bazley model [63]. More recently, extensive research on the characterization of the effect of rough surfaces on grazing acoustic waves has been carried out by Attenborough [15, 18, 198]. The standard approach consists of deriving an effective impedance Z^* that includes roughness corrections. This method has allowed the derivation of corrected reflection coefficients for outdoor sound propagation in different types of geographical conditions: forests, deserts, grasslands, oceans [177]. Equation (2.25) has been extended to take into account the ground effects with varying impedance [28], but does not hold for cases when the ground surface is not flat.

Finally, we introduce a generalization of Eq. (2.25) for the case of a uniform medium flow. The solution given by Eq. (2.25) relies on the existence of a Green function for the homogeneous Helmholtz equation derived in Eq. (2.15). However, the Green function of a general propagation problem in an inhomogeneous medium is not explicitly known, so the method of images cannot be used for a layered atmosphere with an arbitrary sound speed profile $c(z)$. One of the only exceptions is when the atmosphere is subjected to a constant uniform wind profile v_0 in the propagation direction x. In this case the three-dimensional Green function is given by [167]

$$G(\mathbf{x}, \mathbf{x}_s) = \frac{e^{ik_0\tilde{R}_i/\beta^2}}{4\pi\tilde{R}_i}, \tag{2.29}$$

where $M = v_0/c_0$ is the Mach number, $\beta^2 = 1 - M^2$ is a constant and the (convected) distance $\tilde{R}_i$ of the direct wave between the source and the receiver (and the associated reflected wave distance $\tilde{R}_r$) is given by

$$\tilde{R}_i = \sqrt{(x - x_s)^2 + \beta^2((y - y_s)^2 + (z - z_s^2))} - M(x - x_s), \tag{2.30a}$$

$$\tilde{R}_r = \sqrt{(x - x_s)^2 + \beta^2((y - y_s)^2 + (z + z_s^2))} - M(x - x_s). \tag{2.30b}$$

The convected Green function in Eq. (2.29) is very common in Aero-acoustics, where it is used to calculate the scattering of aerodynamic sound from irregular shapes in presence of a uniform fluid flow (e.g. in a wind tunnel). In the case of radiation over an impedance surface, the method of images can be used again, and the complex pressure amplitude can be expressed as

$$p_c(\mathbf{x}) = S_0\left(\frac{e^{ik_0\tilde{R}_i/\beta^2}}{\tilde{R}_i} + Q(\varphi)\frac{e^{ik_0\tilde{R}_r/\beta^2}}{\tilde{R}_r}\right), \tag{2.31}$$

where S_0 is the source strength, $Q(\varphi)$ is identical to the reflection coefficient given by Eq. (2.26) and the convected distances $\tilde{R}_i$ and $\tilde{R}_r$ are given by Eq. (2.30a) and Eq. (2.30b), respectively. In Chapters 3 and 4, the analytical solution given by Eq. (2.25) will be used to validate the Crank-Nicolson Parabolic Equation codes in 2D and 3D for propagation in a homogeneous atmosphere, above a flat impedance surface.

2.2.2 Diffraction by irregular terrain and barriers

In this section, the phenomenon of acoustic diffraction is investigated and the expression of pressure for propagation over an idealized wedge is presented. The idealized wedge obstacle, illustrated in Fig. 2.2, has been of interest in underwater acoustics

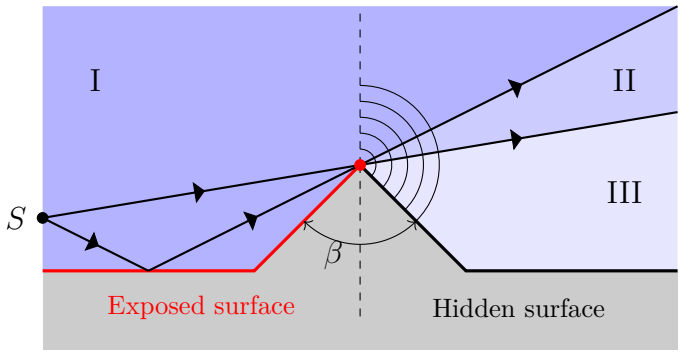

Figure 2.2: Diffraction of sound by a wedge. The zone (I) is subject to direct and reflected waves, zone (II) is dominated by direct waves and zone (III) is the shadow zone, which is below the line of sight.

and outdoor sound propagation since it is one of the few cases for which an analytical solution, based on the geometrical theory of diffraction (GTD), is available [164, 168]. It is known, from the theory of diffraction [157], that the pressure field at any receiving point in space is expressed a sum of a geometrical pressure $p_{g,0}$ and a diffracted pressure p_{diff}, i.e $p_c = p_{g,0} + p_{\text{diff}}$. The geometrical part $p_{g,0}$ of the wave stems from the direct wave and reflections on boundaries, while the diffracted part is generated by corners and wedges (see Fig. 2.2). As a result, the total pressure is written as

$$p_c = p_i + p_r + p_{\text{diff}}, \tag{2.32}$$

where p_i is the incident pressure, p_r the reflected pressure and p_{diff} the diffracted pressure. The expression of p_r can be deduced using the method of images, as in Sec. 2.2.1, which can be generalized to tilted flat boundaries. However, the diffracted pressure p_d, generated by a wedge of aperture β, is expressed using Fresnel integrals [164], i.e.

$$\boxed{p_{\text{diff}}(\mathbf{x}) = \frac{e^{ik_0\mathcal{R}}}{\mathcal{R}}\left(V\left(\frac{r_0 r_1}{\mathcal{R}}, 1, \varphi_1 - \varphi_0\right) + V\left(\frac{r_0 r_1}{\mathcal{R}}, 1, \varphi_1 + \varphi_0\right)\right),} \tag{2.33}$$

where $k_0 = \omega/c_0$ is the wavenumber, r_0 is the distance between the source and the wedge, r_1 is the distance between the wedge and the receiver, and $\mathcal{R} = r_0 + r_1$ is the

total travelled distance. The angle φ_0 (φ_1) is the angle between the exposed face of the wedge and the incident (diffracted) ray, as shown in Fig. 2.2. The quantity V is defined by $V(A,B,\varphi) = V^+(A,B,\varphi) + V^-(A,B,\varphi)$, where A, B are dummy variables and $V^\pm$ are given by [164]

$$V^\pm = -\frac{e^{i\pi/4}}{2\nu\sqrt{2\pi k_0 AB}} \cot\left(\frac{\pi \pm \varphi}{2\nu}\right) F'(BX^\pm(\varphi, A)), \tag{2.34a}$$

where $\nu = 2 - \beta/\pi$. The function F in Eq. (2.34a) is the Fresnel integral [164], and its derivative satisfies $F'(x) = -2i\sqrt{x}e^{-ix}F(\sqrt{x})$. The function $X^\pm$ in Eq. (2.34a) is defined as

$$X^\pm(\varphi, A) = 2k_0 A \cos^2\left(\frac{2N^\pm\nu\pi - \varphi}{2}\right), \tag{2.35}$$

where A is, again, a dummy variable, and $N^\pm$ are the Fresnel numbers associated with the rigid wedge,

$$N^+ = \begin{cases} 0 & , \quad \varphi \leq \pi - \beta, \\ 1 & , \quad \varphi > \pi - \beta \end{cases} \tag{2.36}$$

and

$$N^- = \begin{cases} -1 & , \quad \varphi < \beta - \pi, \\ 0 & , \quad \beta - \pi \geq \varphi \leq 3\pi - \beta, \\ 0 & , \quad \varphi > 3\pi - \beta \end{cases} \tag{2.37}$$

A more general understanding of sound scattering can be reached by considering an incident plane wave $p_i = Ae^{i\mathbf{k}\cdot\mathbf{x}}$ hitting an arbitrary rigid boundary. Hence, we have $\partial p/\partial \mathbf{n} = 0$ as a boundary condition, which allows us to establish a relation for the scattered field,

$$\nabla p_s \cdot \mathbf{n} = -i(\mathbf{k}\cdot\mathbf{n})Ae^{i\mathbf{k}\cdot\mathbf{x}}. \tag{2.38}$$

It leads to the interesting equivalency, established by Pierce [157], that reduces scattering from a body as the field generated by the same body but with a vibrating outer interface. Physically, Eq. (2.38) means that the obstacle acts like another source, which can be decomposed into a series of terms if we approximate the exponential to a certain order n_s, which leads to

$$\nabla p_s \cdot \mathbf{n} = -iA(\mathbf{k} \cdot \mathbf{n}) \sum_{j=0}^{n_s} \frac{(i\mathbf{k} \cdot \mathbf{x})^j}{j!}, \tag{2.39}$$

The first term in the right-hand side of Eq. (2.39) represents a monopole source while the second term is a dipole source, etc. In the two-dimensional case, if we consider an incident plane wave with a wavevector defined as $\mathbf{k} = k_0(\cos\varphi, \sin\varphi)$ and assume a grazing angle $\varphi \ll 1$ in the far-field, we have $\sin\varphi \approx \varphi$ and $\cos\varphi \approx 1$. Then, Eq. (2.39) becomes

$$\mathbf{v}_s \cdot \mathbf{n} = -A \frac{(\mathbf{k} \cdot \mathbf{n})}{\omega\rho} \sum_{j=0}^{n_s} \frac{(ik_0\varphi)^j}{j!}. \tag{2.40}$$

However, the expansion in Eq. (2.40) is valid only within the limitations of Rayleigh Scattering, for which the wavelength is large in front of the obstacle size. When we are dealing with propagation above an irregular surface, Eq. (2.40) provide an insight into the effect of a small irregularity on an incident wave. This approach has been used by Collins [48] to derive "rough" boundary conditions in the 3DPE. Indeed, a simple derivation based on Eq. (2.40) allows us to write the plane reflection coefficient, $R_p(\varphi)$, as a sum of angle contributions, *i.e.*

$$R_p(\varphi) = \sum_{j=0}^{n_s} a_j \varphi^j \tag{2.41}$$

which can be readily implemented in any numerical or analytical method involving the use of a reflection coefficient.

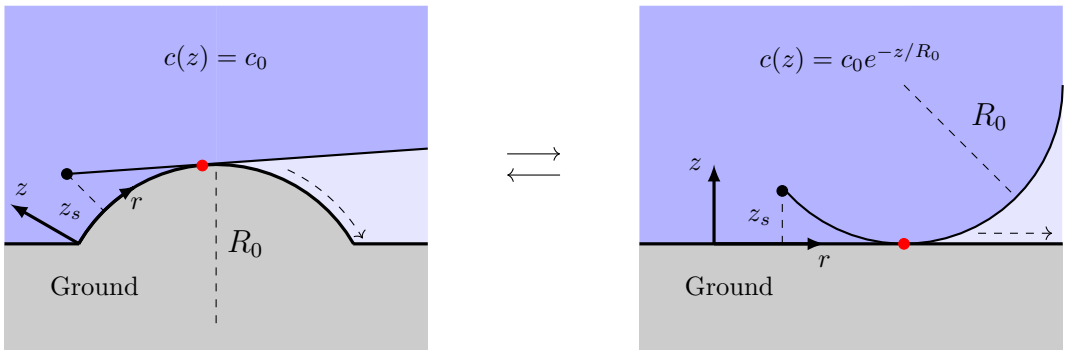

Figure 2.3: Analogy between propagation above a convex curved surface of radius R_0 in a homogeneous atmosphere of sound speed c_0 (left), and propagation above a flat surface in an upward refractive atmosphere with an exponential sound speed profile $c(z) = c_0 e^{-z/R_0}$ (right). The dashed arrows show the trajectory of creeping waves within a layer of thickness l and the light blue regions denote the shadow zone. The red dots are the diffraction points.

2.2.3 Curved surfaces and creeping waves

Another class of geometrical obstacles that have been extensively investigated are curved surfaces, mainly for validation purposes. In the context of atmospheric acoustics, propagation over both concave and convex boundaries had been first studied in 1959 by Seckler and Keller [180, 181]. A schematic of the scattering by a circular, convex surface is given in Fig. 2.3. Later, an important result was obtained by Berry and Daigle [29] and Wang and Li [212], who established an analogy between propagation over curved surfaces and propagation over a flat surface with an exponential sound speed profile c, which has the form

$$c(z) = c_0 \exp\left(\frac{\sigma z}{R_0}\right) \simeq c_0 \left(1 + \frac{\sigma z}{R_0}\right) + \mathcal{O}\left(\frac{z^2}{R_0^2}\right) \tag{2.42}$$

where R_0 is the curved surface radius, with $\sigma = -1$ for a convex surface and $\sigma = +1$ for a concave surface. This result is also known as the "exponential analogy" and has been validated against scaled experiments in a laboratory environment [29, 212]. The analytical solution for the linear profile Eq. (2.42), which is valid for a small altitude z, is based on the so-called Von der Pol-Bremmer diffraction formula [80]. However, when $\sigma = -1$, the analytical solution fails in the shadow zone, where

the pressure field has to be evaluated by the means of residue series [157]. The shadow zone is the area located downstream of the curved surface and below the line of sight, where no ray can reach and the pressure field is purely diffracted. For a source located at a perpendicular distance z_s above the curved surface, the points (r, z) located in the shadow zone are defined by the expression $r > \sqrt{2R_0 z_s} + \sqrt{2R_0 z}$, where r is the distance along the surface, as seen in Fig. 2.3. Following Pierce [157], the pressure field above a convex curved surface, in the curved coordinate system, can be expressed as

$$\boxed{p_c(r, z) = S_0 \frac{e^{ik_0 r}}{r} V(r, z),} \tag{2.43}$$

where S_0 is the monopole source strength and the quantity V is the diffraction integral expressed as a residue series, as

$$V(r, z) = \sqrt{4\pi\xi} e^{i\pi/4} \times \sum_n \frac{e^{i\tau_n \xi} \mathrm{Ai}((\tau_n - z_s/l_c)e^{2i\pi/3}) \mathrm{Ai}((\tau_n - z/l_c)e^{2i\pi/3})}{(\tau_n - q^2)(\mathrm{Ai}(\tau_n e^{2i\pi/3}))^2}, \tag{2.44}$$

where Ai is the Airy function [1] and τ_n are the zeros of the functional equation $\mathrm{Ai}'(\tau_n) - q\mathrm{Ai}(\tau_n)$. The values τ_n are related to the propagating modes k_n by $\tau_n = 2k_0 l_c^2 (k_n - k_0)$ and the coefficients l_c, ξ and q are defined as

$$l_c = \left(\frac{R_0}{2k_0^2} \right)^{1/3}, \tag{2.45a}$$

$$\xi = \frac{r}{2k_0^2 l_c^2}, \tag{2.45b}$$

$$q = \frac{ik_0 l_c \rho_0 c_0}{Z_s}, \tag{2.45c}$$

where Z_s is the ground surface impedance, ρ_0 is the air density and c_0 is the isothermal sound speed.

Another key aspect of propagation above a curved surface is that it is an ideal scenario for the analysis of creeping waves in the shadow zone. Creeping waves do

not stem from the sound source itself but from a secondary source, located at the diffraction point, which is the intersection between the surface and the line of sight. Creeping waves travel along the curved surface, following an ordinary ray path, and are contained within a layer of thickness $l_c = (R_0/2k_0^2)^{1/3}$. Specifically, pressure decay of the diffracted field in the shadow zone is proportional to $e^{-\alpha r}/\sqrt{r}$ where α is an absorption coefficient. The residue series solution, given by Eq. (2.44), has been used by Attenborough et al. [17] as a benchmark to validate the Crank-Nicolson Parabolic Equation (CNPE) and the Green Function Parabolic Equation (GFPE) [177]. Following the same procedure, the formula given by Eq. (2.44) will be used in Chapter 3 to validate a 2D finite-difference Parabolic Equation for propagation in a refracting atmosphere.

2.2.4 Impedance ground condition

We begin by assuming a flat bottom surface located at $z = 0$ separating the atmosphere form the ground. According to Snell's law, when an incident wave reaches the interface between the ground and the atmosphere at an angle θ_i, part of the wave will be reflected back with an angle θ_r while the other will be transmitted to the ground, with an angle θ_t. The key parameter governing the amplitude of the reflected and transmitted waves is the ground characteristic impedance ζ_g, which can be understood as the resistance of the ground medium to the propagation of sound. It is defined by the ratio of pressure to the particle velocity and depends on the frequency ω of the incident wave, *i.e.*

$$\zeta_g(\omega) = \left\{ \frac{p_c}{v_c} \right\}_{z<0}, \tag{2.46}$$

where $v_c = ||\mathbf{v}_c||$ is the norm of the sound velocity. In the case of air, it is simply given by $\zeta_0 = \rho_0 c_0 = 427\,\mathrm{kg}\cdot\mathrm{m}^{-2}\cdot\mathrm{s}^{-1}$ [177]. This value will be used as a reference for a new variable, the normalized impedance the ground medium Z_g, which is defined as the ratio of the characteristic impedance of the ground to the characteristic impedance of air, hence

$$Z_g = \frac{\zeta_g}{\zeta_0}. \tag{2.47}$$

In order to set a boundary condition, it is necessary to evaluate impedance at the surface $z = 0$. Hence, we are interested in the value of Z_g at the limit $z \longrightarrow 0$, which is also called the surface impedance and is defined by

$$Z_s(\omega) = \frac{1}{\rho_0 c_0} \left\{ \frac{p_c}{v_c} \right\}_{z=0}. \tag{2.48}$$

A useful simplification for calculating Z_s is to assume that the ground is locally reacting, meaning that the sound interacts with the surface along the normal direction only. In that case, we have $v_c \simeq v_n$, where $v_n = \mathbf{v}_c \cdot \mathbf{n}$ is the normal component of velocity. However, for a porous material, such an approximation is not always true and a full plane wave analysis is required. Following a lengthy derivation, Salomons (2001) [177] gives the following relationship between Z_g and Z_s,

$$\boxed{Z_s = \frac{Z_g}{\sqrt{1 - (k_0/k_g)\sin^2\theta_i}}}, \tag{2.49}$$

where θ_i is the angle between the incident wave and the normal to the surface and k_g is the wavenumber in the ground material. For a locally reacting surface, the wave propagates normally to the surface, *i.e.* $\theta_i = 0$, and, consequently, $Z_g = Z_s$ and angle dependence is removed. The case $\theta_i = \pi/2$ represents a grazing wave, for which $Z_s \longrightarrow \infty$. The dependance on the angle of incidence is an important limitation that can be overcome by assuming $|k/k_g| \ll 1$, which holds for most realistic cases, giving $Z_s = Z_g$. Following a simple plane wave analysis as in Salomons [177], the locally reacting assumption introduced above raises $\theta_t = 0$ and $\theta_i = \theta_r = \theta$, i.e. the incident and reflected angles are equal. This gives a reflection coefficient

$$R = \frac{Z_s \cos\theta - 1}{Z_s \cos\theta + 1}. \tag{2.50}$$

If the incident wave is normal to the ground, it reduces to $R = (Z_s - 1)/(Z_s + 1)$. Above the ground surface, the total field is then $\psi = \psi_i + \psi_r = \psi_i + R\psi_i$. If the

surface is perfectly reflecting (rigid boundary condition), then $R = 1$ with no angle dependance.

A review of numerous outdoor ground impedance models is given by Attenborough (1985) [15], which usually assume the ground to be a rigid-framed porous material. Among the many models available, there is the one proposed by Zwikker and Kosten [234]. The Zwikker-Kosten model provides an analytical expression for the ground impedance and wavenumber Z_g and k_g from the equations of wave propagation in a porous media. The key parameter to be considered are the ground porosity Ω_g, the sound speed c_g, the density of the ground material ρ_g and the medium the flow resistivity σ_g, leading to the formulas

$$k_g = \frac{\omega}{c_g}\sqrt{q_c \Omega_g}, \tag{2.51a}$$

$$Z_g = \sqrt{\frac{q_c}{\Omega_g}}, \tag{2.51b}$$

where ω is the natural angular frequency $q_c = c_s/\Omega_g + i\sigma_g/(\rho_g\omega_0)$. The constant c_s is experimentally obtained and has a value ranging from 3 to 7 in most practical cases. The real and imaginary parts of Z_s as a function of the incident angle θ_i are plotted in Fig. 2.4 for the values $c_g = 1500\,\mathrm{m}\cdot\mathrm{s}^{-1}$, $\rho_g = 1.5\,\mathrm{kg}\cdot\mathrm{m}^{-3}$ and a flow resistivity $\sigma_g = 200 \times 10^3$ Pa. From inspecting Fig. 2.4, it appears that the real part of the surface impedance, $\Re(Z_s)$, peaks for $\theta_i \approx 45°$ and lower frequencies (*i.e.* $f < 0.01\,\mathrm{Hz}$). The imaginary part $\Im(Z_s)$ shows a similar behavior, which suggests that the absolute norm of the impedance is higher for lower-frequencies. At higher frequencies, the angle of incidence θ_i have significantly less influence on the value of the surface impedance Z_s. Once the surface impedance Z_s is determined, the amplitude of the reflected wave (or reflection coefficient) can be estimated using Eq. (2.50).

For a stratified heterogeneous ground, composed of N_l layers of thickness d_j and normalized impedances $Z_j =$ ($Z_0 = 1$ is for the atmosphere), the surface impedance Z_s will contain information about the thicknesses and physical properties of the subsequent layer. The theory of sound propagation in a multilayered medium can be

found in Brekhovskikh and Godin (1990) [39], where the following recursive formula is obtained for the impedance of the j-th interface between layer j and $j+1$,

$$\hat{Z}_{(n)} = Z_n \left(\frac{Z_{n-1} - iZ_n \tan \phi_j}{Z_n - iZ_{n-1} \tan \phi_j} \right), \tag{2.52}$$

where $\phi_j = d_j c_j \cos\theta_j$ where θ_j is the incident angle inside the layer (j). It is important to note that there is a major difference between seismic waves and acoustic waves transmitted from atmospheric sources to the ground medium. While seismic waves travel in the ground material (*i.e* in the solid part of the ground), sound can only travel in the air contained in the ground pores and usually penetrates the ground on a few centimeters only. In practice, there are only a few cases in which a multilayered must be considered, like snow or grass. In that case, the ground is modeled as a porous layer sitting on a hard bed and the surface impedance Z_s in Eq. (2.49) is replaced by an effective impedance Z_s^* given by [16],

$$\boxed{Z_s^* = \frac{Z_s}{\tan(k_0 d_g \sqrt{1 - (k_0/k_g)\sin\theta_i})}}, \tag{2.53}$$

where d_g is the porous layer thickness. After inspecting Eq. (2.53), it appears that $Z_s^* \to \infty$, meaning that the surface becomes rigid, as the upper porous layer thickness decreases ($d_g \to 0$). On the other hand, some porous grounds (grass, forests, crops) can be qualified as ground roughness, which is described as a randomly varying surface of an RMS height $\delta_g \ll \lambda_0$. The effects of such grounds can be taken into account via the so-called boss model [18, 37], which provides alternative values for the effective surface impedance Z_s^*.

2.3 Sound generation and loudness

In this section, we discuss the mechanisms through which low frequency sound is generated and introduce several essential concepts for the quantification of sound propagation in the atmosphere. Sound generation can be the result of many physical processes, such as vibrating bodies, combustion (thermo-acoustics), turbulence

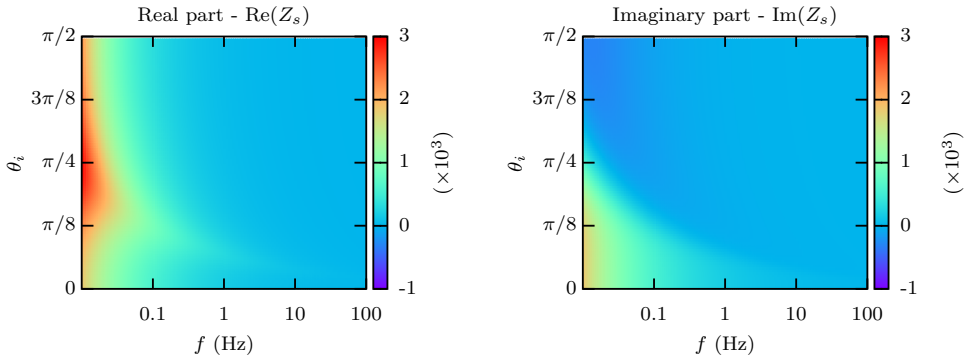

Figure 2.4: Spectrum of the real and imaginary parts of the surface impedance Z_s in function of the incident angle θ_i for a porous ground defined by the Zwikker-Kosten model with $c_g = 1500\,\mathrm{m}\cdot\mathrm{s}^{-1}$, $\rho_g = 1.5\,\mathrm{kg}\cdot\mathrm{m}^{-3}$

(aero-acoustics) or non-linear processes like impacts and shockwaves. These processes correspond to forcing terms in the otherwise homogeneous wave equation, Eq. (2.13), so energy is radiated from the source region and the medium goes back to equilibrium. We now consider an arbitrary source term $q(\mathbf{x}, t)$, located in at $\mathbf{x}_s$ and within a region V, so the homogeneous wave equation in Eq. (2.13) becomes

$$\Delta p - \frac{1}{c^2}\frac{\partial^2 p}{\partial t^2} = q(\mathbf{x}, t). \tag{2.54}$$

Unlike Eq. (2.13), the solution of Eq. (2.54) is unique, and using the properties of the Dirac function δ, the source term can be written as

$$q(\mathbf{x}, t) = \iiint_V q(\mathbf{x}', t)\delta(\mathbf{x} - \mathbf{x}')\mathrm{d}\mathbf{x}'. \tag{2.55}$$

Equation (2.55) establishes an equivalency between any source and a vibrating body, which is a continuous set of monopole sources at locations $\mathbf{x}'$ on ∂V, the exterior surface enclosing the region V. An important property of the homogeneous wave in Eq. (2.13), is that its solution depends on the radial distance $r = |\mathbf{x} - \mathbf{x}'|$ only and can be written in the form $f(t - r/c)/r$ [70], which has a singularity at $r = 0$. This leads to the following result,

$$\left\{\Delta - \frac{1}{c^2}\frac{\partial^2}{\partial t^2}\right\}\frac{q(\mathbf{x}', t - r/c)}{r} = 4\pi q(\mathbf{x}', t)\delta(\mathbf{x}' - \mathbf{x}). \tag{2.56}$$

Integrating both sides over the whole volume V and using Eq. (2.55) to replace the right-hand side, we obtain

$$\left\{\Delta - \frac{1}{c^2}\frac{\partial^2}{\partial t^2}\right\}\iiint_V \frac{q(\mathbf{x}', t - r/c)}{4\pi r}\mathrm{d}\mathbf{x}' = q(\mathbf{x}, t). \tag{2.57}$$

In most applications, we are often interested in the far-field solution, i.e. $|k_0\mathbf{x}| \gg 1$, which satisfies the radiation condition at infinity. It is possible to show that every fundamental source solution p, satisfying Eq. (2.54), will have an asymptotic behavior governed by the Sommerfeld condition [58], which is given by

$$r\left(\frac{\partial p}{\partial r} - ik_0 p\right) \xrightarrow[r\to\infty]{} 0 \tag{2.58}$$

Substituting Eq. (2.57) into the original wave equation in Eq. (2.54) yields the general solution of the homogeneous wave equation in free field,

$$p(\mathbf{x}, t) \sim \frac{1}{4\pi|\mathbf{x}|}\iiint_V q(\mathbf{x}', t - r/c)\mathrm{d}\mathbf{x}'. \tag{2.59}$$

For a monopole source, the function q is given by $S_0(t)\delta(\mathbf{x} - \mathbf{x}_s)$, where S_0 is the source strength as a function of time. As a result, the pressure field radiated by a monopole source can be written as

$$p_{\text{mono}}(\mathbf{x}, t) \sim \frac{S_0(t - |\mathbf{x} - \mathbf{x}_s|/c)}{4\pi|\mathbf{x} - \mathbf{x}_s|}. \tag{2.60}$$

With no loss of generality, we consider a broadband source emitting a set of N frequencies $\omega_n = 2\pi f_n$. The source amplitude function S_0 can then be written as a sum of N modal contributions,

$$S_0(t) = \sum_{n=0}^{N-1} S_{0,n} e^{-i\omega_n t}, \tag{2.61}$$

where $S_{0,n}$ are the modal amplitudes, which corresponds to the discrete counterpart of the power spectral density of the source. Hence, the monopole source in Eq. (2.60) becomes

$$\begin{aligned} p_{\text{mono}}(\mathbf{x}, t) &\sim \frac{1}{4\pi|\mathbf{x}-\mathbf{x}_s|} \sum_{n=0}^{N-1} S_{0,n} e^{-i\omega_n (t-|\mathbf{x}-\mathbf{x}_s|/c)}, \\ &= \frac{1}{4\pi|\mathbf{x}-\mathbf{x}_s|} \sum_{n=1}^{N-1} S_{0,n} e^{-i\omega_n t} e^{ik_n|\mathbf{x}-\mathbf{x}_s|}, \\ &= \sum_{n=0}^{N-1} p_{c,n}(\mathbf{x}) e^{-i\omega_n t}, \end{aligned}$$

where $k_n = \omega_n/c$ is the wavenumber associated with the n-th frequency and $p_{c,n}$ the modal complex pressure, defined by

$$p_{c,n}(\mathbf{x}) = \frac{S_{0,n} e^{ik_n|\mathbf{x}-\mathbf{x}_s|}}{4\pi|\mathbf{x}-\mathbf{x}_s|}, \tag{2.62}$$

In the case of a monochromatic wave (single frequency), we simply have $N = 1$ in Eq. (2.61) and $p_c = p_{c,0}$ and the wave contains only the fundamental frequency ω_0. Real-world examples of monopole sources are rare and large-scale events, like explosions and other infrasound sources, are some of the closest illustrations of the theoretical monopole. While loud noises generate large pressure disturbances, sound fluctuations are usually very small compared to atmospheric pressure p_0, and are typically of the order of 10^{-5} Pa. As a result, wave propagation cannot be well understood, unless compared to a given reference of sound amplitude. In order to quantify sound perception, it is then necessary to introduce a better measure than the pressure p, which is achieved by the sound pressure level (SPL), defined from p as

$$\boxed{L_p(\mathbf{x}) = 10 \log_{10} \left(\frac{p^2_{\text{rms}}(\mathbf{x})}{p^2_{\text{ref}}} \right),} \tag{2.63}$$

where p_{rms} is the root-mean square (RMS) or average pressure fluctuation and p_{ref} the reference pressure, which may be taken as a fixed value or as equal to the SPL at

a given reference point $\mathbf{x}_{\text{ref}}$. The average pressure p_{rms} is calculated from the pressure fluctuation by $p_{\text{rms}} = |p|/\sqrt{2}$ and the reference pressure p_{ref} is usually taken as the threshold of hearing, which is 20 µPa. The Sound Pressure Level (SPL) L_p in Eq. (2.63) is given in decibels (dB) and quantifies the "loudness" of the sound field, as perceived by the human ear. In other scenarios, especially involving loud sound sources, it is more convenient to define the sound amplitude relative to a reference point, in which case we rather refer to L_p as the Relative Sound Pressure Level (RSPL). In order to differentiate the SPL from the RSPL, we name the latter as $\hat{L}_p$ and we define it as

$$\hat{L}_p(\mathbf{x}) = L_p(\mathbf{x}) - L_p(\mathbf{x}_{\text{ref}}). \tag{2.64}$$

The RSPL defined in Eq. (2.64) will be used in the future chapters. The RSPL is also referred to as the Transmission Loss (TL) in the literature, since it accounts for the decay of sound between a point (usually close to the source), and the far-field. The acoustic intensity vector is defined as $\mathbf{I}(t, \mathbf{x}) = p(t, \mathbf{x})\mathbf{v}(t, \mathbf{x})$ and the acoustic power $W(t, \mathbf{x})$ of the sound source is defined as

$$W(t) = \iint_{\Sigma} \mathbf{I}(t, \mathbf{x}) \cdot \mathbf{n} \mathrm{d}\Sigma, \tag{2.65}$$

where Σ is an arbitrary surface enclosing the source and $\mathbf{n}$ is the normal to the surface Σ at an elementary point $\mathbf{x}$. Inserting Eq. (2.62) into Eq. (2.65), we obtain the average sound intensity level for the n-th harmonic of the source $\bar{I}_n = \bar{W}_n/4\pi r^2$, where $r = |\mathbf{x} - \mathbf{x}_s|$ is the radial distance between the source and receiver and $\bar{W}_n$ is the average sound power. From the definition of the acoustic intensity, we can write $\bar{I}_n = p_{\text{rms}}/\rho c$, which leads to $\bar{W}_n = 2\pi S_{0,n}/\rho c$. Adding the effect of absorption on sound propagation, the relative sound pressure level in Eq. (2.64) can be written as

$$\hat{L}_{\text{mono},n}(r) = 10 \log_{10}\left(\frac{\bar{W}_n}{W_{\text{ref}}}\right) - 10 \log_{10}(4\pi r^2) - \alpha r, \tag{2.66}$$

where α is the absorption coefficient and W_{ref} is the power at the reference location. The first term in Eq. (2.66) represents the sound pressure level amplitude, the second term accounts for the geometrical spreading and the last term for atmospheric

absorption due to fluid viscosity. Changing the source amplitude $S_{0,n}$ will simply shift the sound pressure level by a constant value without affecting the pressure decay with distance. An important feature of Eq. (2.66) is that the asymptotic spreading of a monopole source defined by Eq. (2.60) is frequency-independent.

2.4 Conclusions

In this chapter, we have exposed the general theory of sound propagation in the atmosphere and made a review of the propagation effects of importance in the appropriate derivation of an efficient simulation tools for acoustic scattering by irregular surfaces. The wave equation derived in Eq. (2.22) is restricted to the effective atmosphere approximation for a layered medium and variation of density as a function of altitude. This form of wave equation is very common in infrasound propagation and atmospheric acoustics, it has been used as the starting point of many parabolic equation derivations [177, 118]. Other notable formulations of the wave equation that have been developed for long range sound propagation include a full description of the medium velocity $\mathbf{v}_0$ in Eq. (2.12) and a turbulence field, leading to an accurate description for a moving inhomogeneous media [87, 145] in two dimensions. In the present thesis, Eq. (2.22) will be used to derive a three-dimensional parabolic equation in Chap. 4 in presence of irregular topography.

Chapter 3

Two-dimensional Parabolic Equation (2DPE) for propagation over irregular boundaries

In the previous Chapter, the general theory of wave propagation in a layered medium was presented. In this respect, a wave equation for an effective atmosphere was derived and several analytical solutions, for propagation above the ground surface, were reviewed. In this Chapter, the theoretical foundations of the parabolic equation (PE) method in two-dimensional space will be presented, with the objective of modeling infrasound propagation above irregular boundaries.

The Parabolic Equation (PE) is an accurate method for wave propagation which relies on a small-angle approximation. The method is well-adapted to physical problems where propagation is expected to occur within a small aperture around a preferred direction. The main advantage of the PE lies in the reduction of the elliptic Helmholtz equation to a parabolic equation, which can be easily solved numerically. Its efficiency has made it a method of choice in many research areas focusing on long range wave phenomena, such as Underwater Acoustics (UA) [199] or Electromagnetic (EM) propagation, before being later applied to Atmospheric

Acoustics (AA) and Infrasound Monitoring. Over the past decades, the PE has been extensively studied and improved to cover an increasing number of realistic propagation problems [118]. Numerous studies have highlighted the flexibility of the PE and its advantages over other methods, such as ray tracing and Boundary Elements (BEM). In particular, the PE is able to accommodate a large number of atmospheric parameters, like refraction, density variation, mean sound speed and turbulence. Several numerical schemes have been derived in order to solve the PE, namely the Split-Step Fourier [199], Finite-Differences [220], Green functions [85, 176] and Finite-Elements [86].

Early developments [199] have only considered propagation above a flat surface with variable impedance, but were followed by several successful attempts at generalizing the PE to irregular boundaries and interfaces [117, 174]. The term "irregular" refers to any boundary that is not flat, but within the constraints of continuity implied by Hypothesis 1 in Sec. 1.3.1. The simplest method consists of dividing any irregular boundary as a succession of range-independent regions, where the ground surface is flat. This approach is also referred to as the "staircase" approximation and was implemented in two-dimensional ocean acoustics by Collins [49] and earlier works. A more accurate treatment of irregular boundaries and interfaces involves the use of a sloping impedance boundary condition [117, 40], which overcomes the energy conservation issues in the staircase approximation, as highlighted by Porter *et al.* [160]. Indeed, for a staircase approximation, the PE does not account for back-scattering from vertical interfaces. This issue can be overlooked for slowly varying boundary if the numerical step size is smaller than $\lambda/30$ [62].

Another category of methods for irregular boundaries in the PE is based on terrain-following coordinate transforms, aimed at rewriting the PE in a flat numerical domain where the boundary conditions are simplified. Notable methods developed in this perspective are the rotated parabolic equation [53] and the Generalized-Terrain Parabolic Equation (GTPE) [174]. A more recent method has been developed by Parakkal et al. [152], who has used the so-called Beilis-Tappert Parabolic equation (BTPE) [26] and derived an equivalent impedance boundary condition.

This Chapter deals with the derivation of a two-dimensional parabolic equation

(2DPE) for propagation above iiregular boundaries. In Sec. 3.1, the theory of the two-dimensional PE will be presented for an effective stratified atmosphere. Next, the Generalized Terrain Parabolic Equation (GTPE) and Beilis-Tappert Parabolic Equation (BTPE) will be presented in Sec.3.2. In particular, the BTPE will be extended to wide-angle while retaining first-order terrain terms. In Sec. 3.3, a Crank-Nicolson finite-difference scheme of the BTPE is derived. Finally, in Sec. 3.4, the BTPE code is validated against frequency-domain Finite Element simulations carried out using COMSOL Multiphysics.

3.1 Paraxial approximation of the Helmholtz equation

The prior research in this area has shown that the PE is an accurate method for the modeling of sound propagation in complex environments with both atmospheric and topographic parameters. The PE theory dates back to 1977, when Tappert [199] investigated the possibility to transform the reduced Helmholtz equation to a parabolic form. The general idea was to propose a model for propagation in a shallow water environment, where most of the energy is propagated in one geometrical direction in space. In this section, the mathematical foundations of the PE will be presented for a propagation in free field. The concept of wide-angle capability will also be discussed as it is a crucial parameter in the development of an accurate solution in presence of terrain.

3.1.1 Parabolic equations in a stratified media

The two-dimensional PE can be derived from the frequency-domain Helmholtz equation, Eq. (2.15), in a stratified atmosphere with an effective sound speed. In a three-dimensional Cylindrical coordinate system $\mathbf{r} = (r, \theta, z)$, the Helmholtz equation can be written as

$$\left\{\frac{1}{r}\frac{\partial}{\partial r}\left(r\frac{\partial}{\partial r}\right)+\frac{1}{r^2}\frac{\partial^2}{\partial\theta^2}+\rho\frac{\partial}{\partial z}\left(\frac{1}{\rho}\frac{\partial}{\partial z}\right)+k_{\text{eff}}^2\right\}p_c(\mathbf{r})=0, \tag{3.1}$$

where $k_{\text{eff}}(z)=\omega/c_{\text{eff}}(z)$ is the wavenumber, $\omega=2\pi f$ is the angular frequency and $c_{\text{eff}}(z)$ is the effective sound speed. The complex pressure amplitude p_c is related to the time-domain pressure p through the relation

$$p(\mathbf{r},t)=\text{Re}\{p_c(\mathbf{r})e^{-i\omega t}\}, \tag{3.2}$$

where t is the time variable. In order to reduce Eq. (3.1) to a two-dimensional space, we assume the propagation domain to be invariant in the azimuthal direction θ and write the problem in a single plane (r,z). Furthermore, spherical spreading is taken into account by replacing p_c with $q_c/\sqrt{r}$, where q_c is the axisymmetric complex pressure. So, Eq. (3.1) becomes

$$\left\{\frac{\partial^2}{\partial r^2}+\rho\frac{\partial}{\partial z}\left(\frac{1}{\rho}\frac{\partial}{\partial z}\right)+k_{\text{eff}}^2(z)+\frac{1}{4r^2}\right\}q_c(r,z)=0, \tag{3.3}$$

and, utilizing the far-field approximation $|k_0 r|\gg 1$, the last term on the left-hand side of Eq. (3.3) is dropped, which leads to the following two-dimensional Helmholtz equation

$$\left\{\frac{\partial^2}{\partial r^2}+\rho\frac{\partial}{\partial z}\left(\frac{1}{\rho}\frac{\partial}{\partial z}\right)+k_{\text{eff}}^2(z)\right\}q_c(r,z)=0. \tag{3.4}$$

In the remainder of this chapter, the variable r will be replaced by x. Then, Eq. (3.4) can be factorized into two wave components, a progressive term p_c^+ propagating along $+x$ and a regressive term q_c^- propagating along $-x$. Hence, Eq. (3.4) can be now expressed as

$$\left\{\frac{\partial}{\partial x}-ik_0\mathcal{L}\right\}\left\{\frac{\partial}{\partial x}+ik_0\mathcal{L}\right\}q_c(x,z)=0, \tag{3.5}$$

where the operator $\mathcal{L}$ is defined as

$$\mathcal{L}=\sqrt{1+\mathcal{Z}}, \tag{3.6}$$

and the differential operator $\mathcal{Z}$ is given by

$$\mathcal{Z} = \frac{1}{k_0^2}\left(\rho\frac{\partial}{\partial z}\left(\frac{1}{\rho}\frac{\partial}{\partial z}\right) + k^2(z) - k_0^2\right). \tag{3.7}$$

Equation (3.5) holds as long as the terms $\partial/\partial x$ and $\mathcal{L}$ permute, i.e. if $\partial/\partial x\,(\mathcal{L}) = \mathcal{L}(\partial/\partial x)$, which is true for a stratified atmosphere since $\mathcal{L}$ does not depend on x in a range-independent atmosphere. Therefore, Eq. (3.5) becomes an exact representation of the Helmholtz equation. From there, Eq. (3.5) can be written as a set of uncoupled equations for q_c^+ and q_c^-

$$\left\{\frac{\partial}{\partial x} - ik_0\mathcal{L}\right\} q_c^+(x,z) = 0, \tag{3.8a}$$

$$\left\{\frac{\partial}{\partial x} + ik_0\mathcal{L}\right\} q_c^-(x,z) = 0, \tag{3.8b}$$

and the total complex pressure is simply the sum of these two contributions, i.e. $q_c = q_c^+ + q_c^-$, where q_c^- is generated through backscattering, which arises from sharp variations of the propagation domain along x. We retain only the progressive wave, so $q_c \simeq q_c^+$ and ignore backscattering, which is also called the one-way approximation [203, 22] and is valid for a receiver placed downstream of the scattering region. Then, the complex pressure q_c is expressed under the following form,

$$q_c(x,z) = \psi(x,z)e^{ik_0x}, \tag{3.9}$$

where ψ is now the slowly varying envelope of q_c, and e^{ik_0x} a factor including fast oscillations along the paraxial direction x. Substituting Eq. (3.9) into Eq. (3.8a), we finally have

$$\left\{\frac{\partial}{\partial x} - ik_0(\mathcal{L}-1)\right\}\psi(x,z) = 0. \tag{3.10}$$

The main issue underlying the PE is the choice of an appropriate expansion for the square-root term $\mathcal{L} = \sqrt{1+\mathcal{Z}}$, which is necessary to make Eq. (3.10) linear. It

is possible to approximate the operator $\mathcal{L}$ for a small variation of $\mathcal{Z}$, or $k_z \gg k_x$, which can be physically interpreted as a small propagation angle with respect to x. The most natural choice would be to use Taylor approximation of the form

$$\mathcal{L} \simeq 1 + \sum_{j=1}^{N} l_j \mathcal{Z}^j + \mathcal{O}(\mathcal{Z}^{N+1}). \tag{3.11}$$

where N is the order of the expansion and l_j are real coefficients. The accuracy of the approximation depends on the expansion order N, which leads to a higher propagation angle. The accuracy of the expansion, and the associated angle capability will be investigated in Sec. 3.1.2. The first-order Taylor expansion is obtained for $N = 1$ and $\mathcal{L}(\mathcal{Z}) = 1 + \mathcal{Z}/2$, which gives rise to the standard PE

$$\boxed{\left\{\frac{\partial}{\partial x} - ik_0\frac{\mathcal{Z}}{2}\right\}\psi(x,z) = 0.} \tag{3.12}$$

A higher value of N would lead to a more accurate parabolic solution, at the expense of additional terms. Other mathematical derivations [22, 50, 59] have introduced higher-order approximations for $\mathcal{L}$ by using a rational Padé expansion, so $\mathcal{L} \approx \mathcal{P}/\mathcal{Q}$, where $\mathcal{P}$ and $\mathcal{Q}$ are polynomials of orders N_p and N_q, respectively. According to Trefethen and Halpern [203], the PE is well-posed and has a unique solution if $N_p = N_q = N$, so the general Padé approximation can take the form

$$\mathcal{L}(\mathcal{Z}) = 1 + \sum_{j=1}^{N} \frac{a_j \mathcal{Z}}{1 + b_j \mathcal{Z}} + \mathcal{O}(\mathcal{Z}^{N+1}), \tag{3.13}$$

where a_j, b_j are defined by

$$a_j = \frac{2}{2N+1} \sin^2\left(\frac{j\pi}{2N+1}\right), \tag{3.14a}$$

$$b_j = \cos^2\left(\frac{j\pi}{2N+1}\right). \tag{3.14b}$$

The so-called wide-angle PE has been introduced by Claerbout [47] and usually referred to as the first-order Padé approximation, obtained using $N = 1$ in Eq. (3.13).

The corresponding coefficients are given by $a_1 = 1/2$, $b_1 = 1/4$, and Eq. (3.10) can be written as

$$\boxed{\left\{\left(1+\frac{\mathcal{Z}}{4}\right)\frac{\partial}{\partial x} - ik_0\frac{\mathcal{Z}}{2}\right\}\psi(x,z) = 0.} \tag{3.15}$$

The terms "narrow" and "wide" angle to describe different types of PE are related to the physical propagation angle of the wave with respect to x. For a relative solution error of 10^{-3}, the maximum propagation angle associated with Eq. (3.12) is 17.5° and Eq. (3.15) is 32.5°.

3.1.2 Wide-angle capability

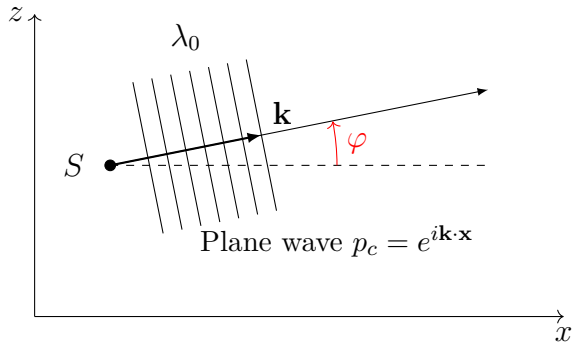

Figure 3.1: Paraxial propagation of sound along direction x

In this section, the accuracy of the narrow-angle and wide-angle PE, given by Eq. (3.12) and Eq. (3.15), respectively, will be estimated. The total error of the PE solution can be divided into three main parts: the error due to the one-way propagation assumption made in Eq. (3.10), the dispersion error of the Taylor expansion defined in Eq. (3.11) (or Padé expansion defined in Eq. (3.13)) and the error associated with the numerical scheme. The latter is unavoidable, even for a full-wave model, and can only be reduced by using finer numerical grids in exchange of an increased computational cost. In order to circumvent the one-way limitation, some

models have implemented coupled and uncoupled solutions of Eq. (3.5), taking into account backscattering from sound barriers in range-dependent media [49, 97]. This is known as the "two-way PE" and can provide an accurate solution for capturing reverberation effects in Ocean Acoustics but also of less interest in atmospheric sound propagation. Subsequently, the accuracy of the PE is mostly a function of the order of the Padé expansion, which governs the maximum propagation angle. In order to estimate the accuracy of the PE, we first consider the plane wave solution of the Helmholtz equation in a homogenous atmosphere, which is

$$p_c(x,z) = e^{i\mathbf{k}\cdot\mathbf{x}}, \tag{3.16}$$

where $\mathbf{k} = (k_x, k_z) = k_0(\cos\varphi, \sin\varphi)$ is the wavevector, φ is the propagation angle with respect to x and $\mathbf{x} = (x, z)$, as shown in Fig. 3.1. The corresponding complex envelope $\psi(x,z) = p_c(x,z)e^{-ik_0x}$ is given by

$$\psi(x,z) = e^{ik_0(x(\cos\varphi - 1) + z\sin\varphi)}. \tag{3.17}$$

Next, the plane wave solution ψ' of Eq. (3.10) is considered, which can be expressed as

$$\psi'(x,z) = e^{i\mathbf{k}'\cdot\mathbf{x}}, \tag{3.18}$$

where $\mathbf{k}' = (k'_x, k'_z)$ is the wavevector associated with the parabolic plane wave solution. In order to estimate the accuracy of the PE, we compare the difference in phase between the fields ψ and ψ'. Following Salomons [177], the z-component k'_z of the parabolic plane wave ψ' satisfies $k'_z = k_z$, so that a condition on k'_x can be obtained. After replacing the square root operator in Eq. (3.10) by the N-th order expansion defined in Eq. (3.13), the following N^{th}-order Padé PE is obtained,

$$\frac{\partial\psi'}{\partial x} = ik_0\left\{\sum_{j=1}^{N}\frac{a_j\mathcal{Z}}{1+b_j\mathcal{Z}}\right\}\psi'. \tag{3.19}$$

After noticing that $\mathcal{Z}\psi' = -(k_z/k_0)^2\psi'$ and $\partial\psi'/\partial x = ik'_x\psi'$, Eq. (3.19) leads to the

parabolic dispersion relation

$$\frac{k_x'}{k_0} = -\sum_{j=1}^{N} \frac{a_j k_z^2}{k_0^2 - b_j k_z^2}. \tag{3.20}$$

The error of the PE solution can be examined by evaluating the phase difference between ψ and ψ', i.e.

$$\epsilon_p = |\Delta\mathbf{k} \cdot \mathbf{x}|, \tag{3.21}$$

where $\Delta\mathbf{k} = \mathbf{k} - \mathbf{k}'$. In order to remove the frequency dependency, the propagation of the phase error can be treated in terms of the wavelength by writing $|\mathbf{x}| = n\lambda_0$ in Eq. (3.21). Here n is the number of wavelengths separating the source from the receiver. Since $k_z' = k_z$, Eq. (3.21) can be written as

$$\epsilon_p = 2\pi n \epsilon_d, \tag{3.22}$$

where $\epsilon_d = |k_x' - k_x|/k_0$ is the dispersion error. It follows from Eq. 3.22 that the phase error ϵ_p linearly increases with distance with a rate of change proportional to the dispersion error ϵ_d, which contains all information about the expansion order used in Eq. (3.19). In order to evaluate ϵ_d, we need to compute k_x' using Eq (3.20). The plane wave component along x is given by $k_x = k_0 \sin\varphi$ and the plane wave component along z is $k_z = k_0 \cos\varphi$, so the dispersion error ϵ_d can be found from

$$\boxed{\epsilon_d = \left| \sum_{j=1}^{N} \frac{a_j \cos^2\varphi}{1 - b_j \cos^2\varphi} - \sin\varphi \right|.} \tag{3.23}$$

The dispersion error ϵ_d is plotted in Fig. 3.2 for several values of N and for the original Tappert (narrow-angle) PE, which corresponds to a special case of Eq. (3.13), where $N = 1$, $a_1 = 1/2$ and $b_1 = 0$. The maximum angles of propagation for an error level of $\epsilon_d = 10^{-4}$ are given in Table 3.1. If the expansion order in Eq. (3.19) becomes large ($N \longrightarrow \infty$), then the Padé expansion is equal to the square-root operator $\mathcal{L}$ in Eq. (3.6). Using the same approach, it follows that $\epsilon_d = 0$

when $N \longrightarrow \infty$, so the dispersion error converges to zero as the expansion order N increases.

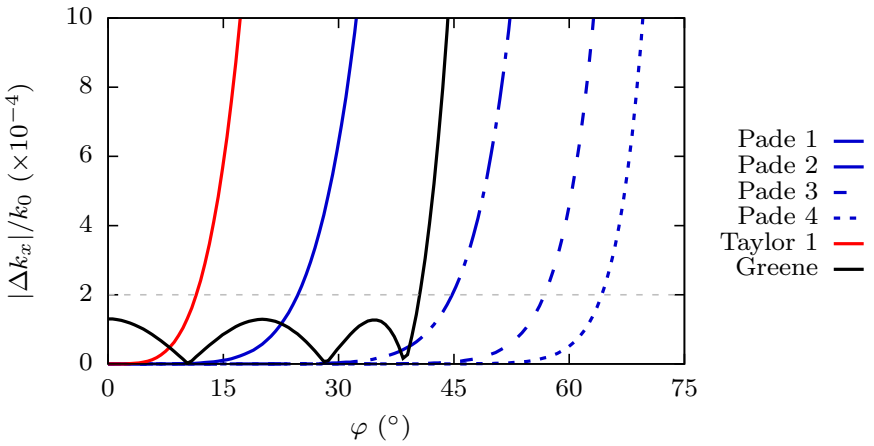

Figure 3.2: Dispersion relation error ϵ_d (Eq. (3.23)) in function of the paraxial propagation angle φ for several square-root approximations.

Operator expansion	Maximum angle $\bar{\varphi}$ (°)
No expansion (3.6)	90.0
Taylor expansion (3.11)	
First-order Taylor, $N = 1$	17.5
Second-order Taylor, $N = 2$	25.8
Padé expansion (3.13)	
First-order Padé, $N = 1$	32.2
Second-order Padé, $N = 2$	53.0
Third-order Padé, $N = 3$	63.6
Fourth-order Padé, $N = 4$	70.1

Table 3.1: Maximum propagation angle $\bar{\varphi}$ of Taylor and Padé expansions of the operator $\mathcal{L}$ for a dispersion error of $\epsilon_d = 10^{-3}$

3.1.3 Source definition

The uniqueness of the solution in Eq. (3.10) is enforced by an initial condition along the parabolic direction of the problem, which corresponds to the paraxial direction x. This initial condition must produce a solution that is physically consistent with the expected analytical result from a full wave model. The pressure field solution p_H of a point source located at $x_s = 0$ and $z = z_s$ is given by the inhomogeneous Helmholtz equation,

$$\Delta p_H(x,z) + k_0^2 p_H(x,z) = 2\pi S_0 \delta(z - z_s)\delta(x - x_s), \tag{3.24}$$

where δ is the Dirac impulse, S_0 is the monopole source amplitude and $\mathbf{x}_s = (x_s, z_s)$ is the source location. The right hand side of Eq. (3.24) cannot be readily implemented in a numerical scheme and must be written in a PE compatible form. According to Jensen et al. [100], it is possible to derive an analytical or a numerical starting field as an approximation of a monopole source in an unbounded free-field. One of the simplest ways is to represent ψ_0 as a Gaussian source,

$$\psi_0(z) = A \exp\left(-\frac{(z - z_s)^2}{2w^2}\right), \tag{3.25}$$

where A and w are, respectively, the amplitude and beamwidth of the source. In order to demonstrate that this choice is compatible with the expected behavior of the PE, we first derive the analytical solution ψ of Eq. (3.12) with the condition $\psi(0,z) = \delta(z - z_s)$, and deduce the complex pressure p_c using Eq. (3.9). According to Tappert [199] and Jensen et al. [100], the complex pressure p_c is given by

$$p_c(x,z) = \frac{Aw}{\sqrt{x(w^2 + 2ix/k_0)}} \exp\left(-ik_0 x + \frac{(z - z_s)^2}{w^2 + 2ix/k_0}\right). \tag{3.26}$$

On the other hand, the solution of Eq. (3.24) is given by

$$p_H(x,z) = S_0 \frac{e^{ik_0 R}}{4\pi R}, \tag{3.27}$$

where $R = \sqrt{(x-x_s)^2 + (z-z_s)^2}$ is the distance between the source and the receiver. Hence, the PE and Helmholtz solutions are asymptotically equivalent since they both decay proportionally to $1/\sqrt{x}$ when $x \longrightarrow \infty$, but do not match in the near field, as a consequence of the paraxial approximation. The remaining task is to determine the coefficients A and w in Eq. (3.25) by matching the local energy of the PE solution, given by Eq. (3.26), with the local energy of the Helmholtz solution, given by Eq. (3.27). The acoustic energy of the PE solution p_c and the Helmholtz solution p_H are expressed as

$$|p_c(x,z)|^2 = \frac{A^2 w^2}{x\sqrt{(4x^2/k_0^2 + w^4)}} \exp\left(\frac{-(z-z_s)^2 w^2}{4x^2/k_0^2 + w^4}\right), \tag{3.28a}$$

$$|p_H(x,z)|^2 = \frac{S_0^2}{8\pi R^2}. \tag{3.28b}$$

In the far-field, i.e. when $k_0 R \gg 1$, it is possible to assume that $(z-z_s)/x \gg 1$ and use a first-order Taylor expansion to approximate the exponentials in Eqs. (3.28a) and (3.28b). Therefore, the far-field acoustic energy associated with the parabolic solution p_c and the Helmholtz solution p_H become

$$|p_c(x,z)|^2 = \frac{A^2 w^2 k_0}{2x^2}\left(1 - \frac{(z-z_s)^2 w^2 k_0^2}{2x^2}\right), \tag{3.29a}$$

$$|p_H(x,z)|^2 = \frac{S_0^2}{8\pi x^2}\left(1 - \frac{(z-z_s)^2}{x^2}\right). \tag{3.29b}$$

It is possible to normalize the monopole source p_H by taking $S_0 = 4\pi$, which yields values of $A = \sqrt{k_0}$ and $w = \sqrt{2}/k_0$, and the Gaussian source is given by

$$\boxed{\psi_0(z) = \sqrt{k_0}\exp\left(-\frac{(z-z_s)^2}{k_0^2}\right).} \tag{3.30}$$

In an attempt to increase the maximum angle of propagation of the PE, Greene [92] followed a similar procedure to derive a wide-angle Gaussian source, by using

a first-order Padé expansion to express the energy $|p_c|^2$ in the far-field. It has been shown that the improvement from a higher-order Gaussian source to approximate a monopole Dirac impulse δ is marginal and the paraxial condition of the PE approximation remains the limiting factor. Salomons [177] has advocated the use of the Greene source with $N = 1$ for the first-order wide-angle 2DPE, defined in Eq. (3.15). For $N = 0$, $a_0 = 1$ and $b_N = 2$, the Greene source is similar to the Gaussian source obtained in Eq. (3.30).

3.2 Terrain inclusion in the parabolic equation

Following the source definition explained above, the parabolic equation (PE) method can be straightforwardly implemented for propagation over a flat impedance surface, as it is equivalent to having two "mirror" sources (with respect to surface location) in free-field. However, taking into account an irregular bottom surface (or terrain) is necessary to obtain a full representation of a realistic environment. Terrain inclusion techniques fall within three different categories, each relying on a different physical representation of the terrain

- Boundary masking, and related interface methods, which are mainly used in Underwater Acoustics [117, 68, 100].
- Conformal mappings, which rely on an angle-preserving transformation of the propagation domain [177, 153].
- Shift maps, which are based on the Beilis-Tappert method [26, 152]. Related approaches include the curvilinear shift map [98], Piecewise-Linear Shift Map (PLSM) [95].

While boundary masking methods treat the ground as part of the numerical domain, conformal mappings and shift maps rely on a terrain-following coordinate transform. Conformal mappings are defined as angle-preserving transformation from the phys-

ical domain to a rectangular numerical domain. Among the available methods are the rotated parabolic equation [53] or the exponential analogy [153], which treat realistic terrain profiles as a succession of analytically defined functions. We can also mention the high-fidelity summation-by-parts method (SBP) introduced by Almquist et al. [7], who used an efficient and scalable finite-difference scheme to overcome the difficulty of using a curvilinear transform.

The other major type of coordinate transforms is referred to as the shift maps, which are all related to the so-called "Beilis-Tappert" method, first introduced by Beilis and Tappert [26]. This method has been applied to outdoor sound propagation, which has led to the Generalized Terrain Parabolic Equation (GTPE), developed by Sack and West [174]. Similar methods have been applied to Electromagnetic propagation [68, 111]. A slight variation of the Beilis-Tappert method involves approximating the bottom boundary as a piecewise-linear profile [95, 75]. Another variant involves the use of a curvilinear map [93, 98], which slightly improves the accuracy of the Beilis-Tappert map. The piecewise-linear, curvilinear and standard Beilis-Tappert coordinate transforms are represented in Fig. 3.3. Unlike conformal mappings, these transforms are not angle-preserving but are well adapted to propagation over irregular boundaries with smooth variations and can accommodate a large array of problems without loss of generality.

In this section, we begin by writing the physical boundary condition for pressure at a terrain interface, which is most generally described by an impedance surface. Then, we will present a general theory of the Beilis-Tappert shift map applied to the two-dimensional parabolic equation, based on the works of Beilis and Tappert [26], Sack and West [174] and Parakkal et al. [152]. We develop a Crank-Nicolson marching scheme and discretize the resulting system using finite-differences, unlike previous formulations which have used Fourier transforms. In particular, we extend the first-order phase shift to the Padé PE with an arbitrary order.

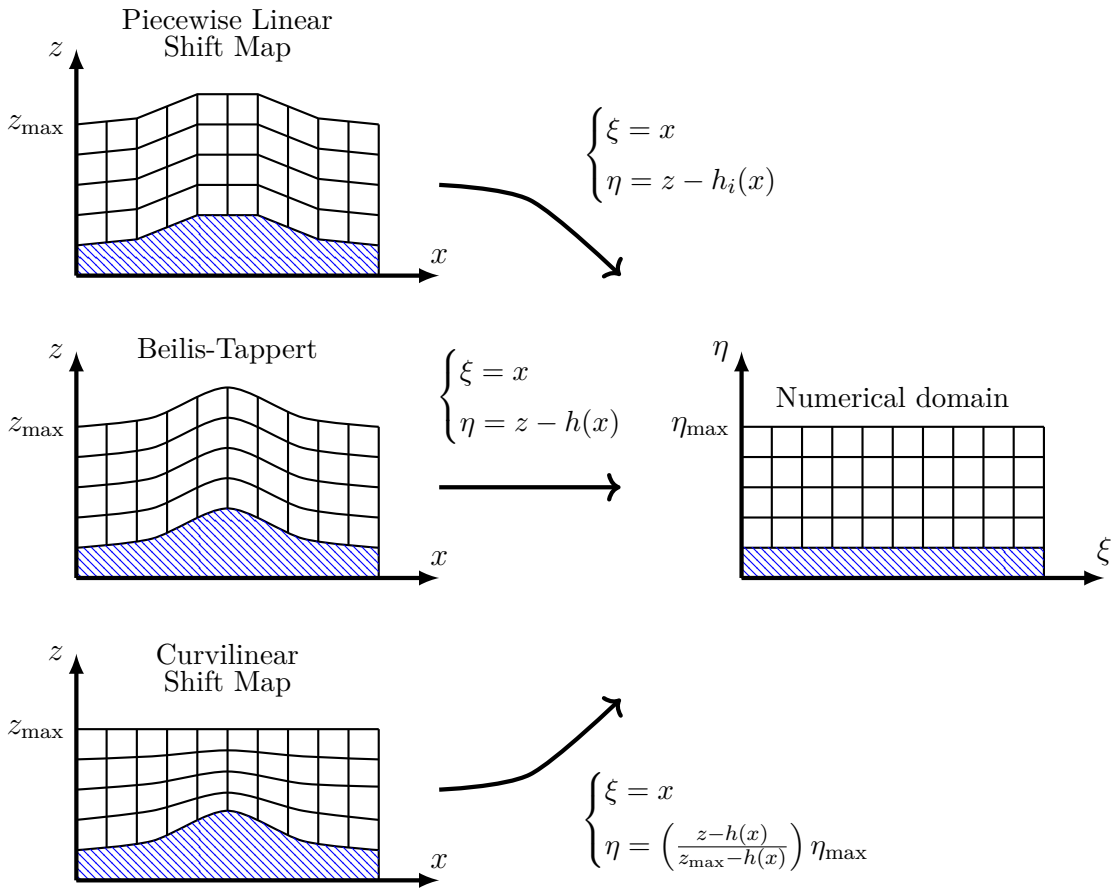

Figure 3.3: Coordinate transforms of the physical domain above an irregular boundary associated with the (i) Piecewise Linear, (ii) Beilis-Tappert and (iii) Curvilinear Shift Maps.

3.2.1 Sloping impedance boundary condition

We consider a propagation domain delimited by an irregular bottom boundary, described by a profile $z = h(x)$ along the propagating direction (cf. Fig 3.4). The pressure value at the vicinity of the surface is governed by a boundary condition, usually enforcing a value on p_c or its rate of change. In atmospheric acoustics, the ground can be a soft boundary (Dirichlet boundary condition), hard boundary (Neu-

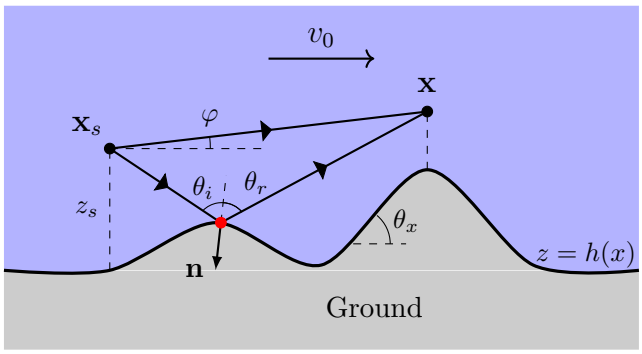

Figure 3.4: Schematic of a wave propagating above an irregular boundary, defined by the profile function $z = h(x)$, with a sloping angle θ_x. The source is located at $\mathbf{x}_s$ and the receiver at $\mathbf{x}$. The atmosphere is subject to a horizontal speed $\mathbf{v}_0$ in the direction of propagation.

mann boundary condition) or an impedance surface (Robin boundary condition). These three conditions have the following forms,

$$p_c \quad =0, \tag{3.31a}$$

$$\partial p_c/\partial \mathbf{n}=0, \tag{3.31b}$$

$$\partial p_c/\partial \mathbf{n}=ik_0 Y_g p_c, , \tag{3.31c}$$

where $Y_g = 1/Z_g$ is the ground admittance and $\mathbf{n}$ is the unit normal to the ground surface. In the most general case, an accurate treatment of the ground surface is possible if the impedance boundary condition in Eq. (3.31c) is used. When the surface is rigid, impedance becomes infinite and the boundary condition is of the Neumann type, as defined in Eq. (3.31b), hence the term of "hard" boundary. If the ground surface is flat, the normal derivatives simply reduces to the derivatives along z, and a simple finite-difference discretization can be used, as in [177]. When the ground is sloping, a term $\partial p_c/\partial x$ appears in the directional derivative $\partial p_c/\partial \mathbf{n} = \nabla p_c \cdot \mathbf{n}$ where $\mathbf{n}$ is the normal to the ground. In order to make the boundary condition consistent with the PE, the term $\partial p_c/\partial x$ must be replaced by its expression in Eq. (3.12), as shown in Abrahamsson and Kreiss [4]. Starting from Eq. (3.31c), and considering a sloping terrain angle $\tan\theta_x = \partial h/\partial x$, the impedance boundary condition (IBC) becomes

$$\cos\theta_x \left(\frac{\partial p_c}{\partial z}\right) - \sin\theta_x \left(\frac{\partial p_c}{\partial x}\right) = ik_0 Y_g p_c. \tag{3.32}$$

Then, we recall that $p_c = \psi e^{ik_0 x}$, where ψ is the complex pressure envelope, so Eq. (3.32) becomes

$$\cos\theta_x \left(\frac{\partial \psi}{\partial z}\right) - \sin\theta_x \left(\frac{\partial \psi}{\partial x}\right) - ik_0 \sin\theta_x \psi = ik_0 Y_g \psi. \tag{3.33}$$

Using the narrow-angle approximation, defined in Eq. (3.12), to express $\partial\psi/\partial x$, a new form of the IBC can be obtained. Furthermore, using $k = k_0$ at the ground level (*i.e.* at z = h(x)) leads to

$$\boxed{\sin\theta_x \left(\frac{\partial^2 \psi}{\partial z^2}\right) + 2ik_0 \cos\theta_x \left(\frac{\partial \psi}{\partial z}\right) + 2k_0^2 \left(\frac{1}{Z_g} + \sin\theta_x\right)\psi = 0.} \tag{3.34}$$

It is possible to retrieve the IBC for a flat surface by stating $\theta_x = 0$ in Eq. (3.34). Several ground properties can be represented by varying the impedance Z_g. As mentioned above, the rigid (or Neumann) boundary condition is obtained by setting $Z_g \to \infty$ and accounts for a perfectly reflecting ground surface. While the assumption of a rigid ground surface is common, some scenarios in the literature have explored the conditions associated with a penetrable terrain. In this case, the ground is a (fluid) medium defined by a density ρ_g, a sound velocity c_g, an absorption coefficient α_g and it is necessary to derive a PE scheme that takes into account more than one medium. One of the most notable early contributions to this area is due to Lee and McDaniel [117], who introduced interface conditions in the Implicit Finite Difference (IFD) code and an extension to sloping interfaces in oceanic bottoms is developed by Brooke [40].

3.2.2 Generalized terrain method (GTPE)

The Generalized Terrain Parabolic Equation (GTPE) was derived by Sack and West [174]. It is one of the first models of irregular terrain inclusion in atmospheric acoustics and it has been implemented in the present thesis for the purpose of benchmarking. The derivation of the GTPE is based on a physical approach of the PE theory

rather than the operator-based development presented in Sec. 3.1. First, the complex pressure p_c is expressed as

$$p_c(\mathbf{x}) = \psi(\mathbf{x}) e^{ik_0 x}, \tag{3.35}$$

where ψ is the slowly varying complex pressure envelope. Using Eq. (3.35) straight into the Helmholtz equation, Eq. (3.4), gives

$$\frac{\partial^2 \psi}{\partial z^2} + \frac{\partial^2 \psi}{\partial x^2} + 2ik_0 \frac{\partial \psi}{\partial x} + (k(z)^2 - k_0^2)\psi = 0. \tag{3.36}$$

This equation differs from the narrow-angle PE given in Eq. (3.12) only by the additional term $\partial^2\psi/\partial x^2$, so the paraxial approximation is equivalent to neglecting second-order terms in comparison to the first-order terms in x, *i.e.*

$$\left|\frac{\partial^2 \psi}{\partial x^2}\right| \ll \left|2ik_0 \frac{\partial \psi}{\partial x}\right|, \tag{3.37}$$

Physically, Eq. (3.37) stipulates that the pressure variation along x is slow, and that second order fluctuations can be neglected. Sack and West [174] proposed to postpone the use of the paraxial approximation, defined in Eq. (3.37), into Eq. (3.36) to the later stages of the derivation in order to limit the physical error. In the presence of an irregular boundary, an earth-flattening coordinate transform similar to the one used in Beilis and Tappert [26] was introduced. It is defined as

$$\begin{aligned} \xi &= x, \\ \eta &= z - h(x). \end{aligned} \tag{3.38}$$

After applying Eq. (3.38) into Eq. (3.36), the Helmholtz equation in the new coordinate system (ξ, η) is obtained,

$$\begin{aligned} \frac{\partial^2 \psi}{\partial \xi^2} + 2ik_0 \frac{\partial \psi}{\partial \xi} - 2\frac{dh}{d\xi}\left(\frac{\partial^2 \psi}{\partial \xi \partial \eta} + ik_0 \frac{\partial \psi}{\partial \eta}\right) - \frac{d^2 h}{d\xi^2}\frac{\partial \psi}{\partial \eta} \\ + \left(\left(\frac{dh}{d\xi}\right)^2 + 1\right)\frac{\partial \psi}{\partial \eta^2} + (k(z)^2 - k_0^2)\psi = 0. \end{aligned} \tag{3.39}$$

This equation is strongly elliptic due to the cross-term $\partial^2/\partial\xi\partial\eta$. Following the paraxial approximation made in Eq. (3.37), the terms $\partial^2/\partial\xi\partial\eta$ and $\partial^2/\partial\xi^2$, which are second order derivatives in range in the (ξ, η) coordinate system, can be neglected. Therefore Eq. (3.39) becomes the so-called first-order (*i.e* narrow-angle) GTPE,

$$\frac{\partial\psi}{\partial\xi} = \frac{i}{2k_0}\mathcal{Q}_1\psi, \tag{3.40}$$

$$\mathcal{Q}_1 = A_2\frac{\partial^2}{\partial\eta^2} + A_1\frac{\partial}{\partial\eta} + A_0, \tag{3.41}$$

where the coefficients A_0, A_1 and A_2 are defined as,

$$A_0 = k^2 - k_0^2, \tag{3.42a}$$

$$A_1 = \left(\frac{dh}{d\xi}\right)^2 + 1, \tag{3.42b}$$

$$A_2 = 2ik_0\frac{dh}{d\xi} + \frac{d^2h}{d\xi^2}. \tag{3.42c}$$

The second-order GTPE can be obtained by integrating Eq.(3.39) between ξ and $\xi + \Delta\xi$ and integrating the cross-term by parts. Furthermore, the first-order expression obtained in Eq. (3.40) is used to express the integral of $\partial^2/\partial\eta^2$ between ξ and $\xi + \Delta\xi$, so we have

$$\int_{\delta I}\frac{\partial^2\psi}{\partial\xi^2} = \left[\frac{i}{2k_0}\mathcal{Q}_1\right]_{\xi}^{\xi+\Delta\xi},$$

$$\int_{\delta I}\frac{dh}{d\xi}\frac{\partial^2\psi}{\partial\xi\partial\eta} = \left[\frac{dh}{d\xi}\frac{\partial\psi}{\partial\eta}\right]_{\xi}^{\xi+\Delta\xi} - \int_{\delta I}\frac{d^2h}{d\xi^2}\frac{\partial\psi}{\partial\eta}.$$

The solution field ψ and its derivatives are assumed to be linear on $\delta I = [\xi, \xi + \Delta\xi]$.

After a lengthy but straightforward derivation, detailed in Salomons [177], the following semi-discretized second-order GTPE can be obtained

$$\left(a_2^- \frac{\partial^2}{\partial \eta^2} + a_1^- \frac{\partial}{\partial \eta} + a_0^-\right) \psi(\xi + \Delta\xi) = \left(a_2^+ \frac{\partial^2}{\partial \eta^2} + a_1^+ \frac{\partial}{\partial \eta} + a_0^+\right) \psi(\xi). \tag{3.43}$$

For the sake of simplicity, the new quantity

$$B_1 = \frac{d^2 h}{d\xi^2} - 2ik_0 \frac{dh}{d\xi}, \tag{3.44}$$

is introduced, and we state that the terms with a superscript "+" are evaluated at ξ_{m+1} and the ones with a superscript "−" at ξ_m. We also introduce the average $F^+(A) = \Delta\xi(A^+/3 + A^-/6)$ and $F^-(A) = \Delta\xi(A^+/6 + A^-/3)$, which arise from the integrals in Eqs. (3.2.2) and (3.2.2). So, the coefficients in Eq. (3.43) are given by

$$a_2^\pm = \frac{1}{2ik_0}\left(\frac{i}{2k_0} A_2^\pm \pm F^\pm(A_2)\right), \tag{3.45}$$

$$a_1^\pm = \frac{-1}{2ik_0}\left(\frac{i}{2k_0} B_1^\pm \pm F^\pm(B_1)\right), \tag{3.46}$$

$$a_0^\pm = 1 + \frac{1}{4k_0}\left(\frac{1}{k_0} \pm \frac{\Delta\xi}{i}\right) A_0. \tag{3.47}$$

The marching scheme in Eq. (3.43), and the coefficients given by Eqs. (3.45), (3.46) and (3.47), are readily discretized using the finite-difference method. The boundary conditions at the surface $\eta = 0$ and at the top $\eta = z_{\max}$ are implemented in the same way as the flat case, except that the sloping impedance boundary condition (3.34) is taken into account. This implies that the boundary condition at the step $\xi + \Delta\xi$ depends on the field at the previous step ξ. The details of the derivations are detailed in Salomons [177]. Next, solution ψ is discretized as ψ_n^m at every grid point (ξ_m, η_n) in the numerical domain. After naming $\Psi_m = (\psi_1^m, \ldots, \psi_{N_z}^m)$ the vector containing all the solution points at a specific step ξ_m, the following tridiagonal system is obtained

$$\mathbf{M}^- \Psi^{m+1} = \mathbf{M}^+ \Psi^m, \tag{3.48}$$

where the system matrices $\mathbf{M}^{\pm}$ are given by

$$\mathbf{M}^{\pm} = a_2^{\pm}\mathbf{D}_2 + a_1^{\pm}\mathbf{D}_1 + \mathbf{A}_0^{\pm}. \tag{3.49}$$

The tridiagonal matrices $\mathbf{D}_l$ are the central finite-difference matrices for the derivative of order l and $\mathbf{A}_0^{\pm} = \mathrm{diag}_n(a_{0,n}^{\pm})$ is the diagonal refractive term. This method presents numerous advantages compared to methods developed previously [28]. Unlike conformal mapping techniques, the GFPE is not limited to the boundaries defined by analytical profiles and can be used to model propagation above realistic terrain. Moreover, this method is accurate up to the sloping angles of 30°, which is satisfactory for a wide range of practical problems.

3.2.3 Beilis-Tappert method (BTPE)

In this section, a variation of the method presented in Sec. 3.2.2 is presented. Instead of using a terrain-following coordinate change on the Helmholtz equation, the Beilis-Tappert Parabolic Equation (BTPE) is derived by using a coordinate transformation on the PE defined in Eq. (3.10). This method was originally introduced by Parakkal *et al.* [152], who has shown that its domain of validity is similar to the GTPE and has derived simplified boundary conditions. First, the Beilis-Tappert coordinate transform, defined in Eq. (3.38) is applied to the parabolic equation defined in Eq. (3.10). The resulting equation is expressed in the flattened numerical domain, defined by coordinates (ξ, η) and contains additional terms, specifically a first-order derivative in η. Parakkal *et al.* [152] has shown that this derivative can be canceled by introducing an appropriate wave modulation of the form

$$p_c(x, z) = \psi(\xi, \eta)e^{i(k_0 x + E(\xi,\eta))}, \tag{3.50}$$

where E is a real-valued function, that can be interpreted as a terrain-induced phase shift in the complex envelope ψ. A possible expression of E that satisfies $\partial\psi/\partial\eta = 0$ is

$$E(\xi,\eta) = k_0\eta + \frac{k_0}{2}\int_0^{\xi}\left(\frac{dh}{d\xi}\right)^2 d\xi, \tag{3.51}$$

and the new narrow-angle PE in the (ξ,η) coordinate system becomes

$$\frac{\partial\psi}{\partial\xi} = \frac{i}{2k_0}\left(\frac{\partial^2\psi}{\partial\eta^2} + (k^2-k_0^2)\psi\right) - ik_0\eta\frac{dh}{d\xi}\psi. \tag{3.52}$$

An inspection of Eq. (3.52) shows that the Beilis-Tappert map, given by Eq. (3.38), has introduced an additional range-dependent refractive term $ik_0\eta dh/d\xi$ in the PE. As mentioned earlier, the density variation of the atmosphere can be incorporated by changing the second-order derivative in η, leading to a new form of the BTPE

$$\boxed{\frac{\partial\psi}{\partial\xi} = \frac{i}{2k_0}\left(\rho\frac{\partial}{\partial\eta}\left(\frac{1}{\rho}\frac{\partial\psi}{\partial\eta}\right) + (k^2-k_0^2)\psi\right) - ik_0\eta\frac{dh}{d\xi}\psi.} \tag{3.53}$$

Next, the accuracy of the Beilis-Tappert coordinate transform, given by Eq. (3.38), is investigated. From the wide-angle capability estimation performed in Table 3.1 the maximum narrow-angle propagation angle is $\bar{\varphi} \approx 17.5°$. A simple geometrical analysis can help us understand why this rather acceptable limitation for propagation over a flat surface may become an issue for an irregular bottom. Considering an incoming wave interacting with an inclined interface tilted at an angle of θ_x, the reflected wave will have an elevation angle of $\varphi_r = 2\theta_x - \varphi$. Within the paraxial approximation, it is possible to assume that the incident propagation angle φ is almost zero. As a result, elevation of the reflected wave satisfies $\varphi_r > \bar{\varphi}$ as soon as $\theta_x > 8.75°$, restricting the method to small terrain slopes. The accuracy can be improved by considering a wide-angle version of the BTPE. Applying the coordinate change $p_c = \psi e^{iE}$ to Eq. (3.10) leads to

$$\left\{\left(\frac{\partial}{\partial\xi} + i\frac{\partial E}{\partial\xi}\right) - \frac{dh}{d\xi}\left(\frac{\partial}{\partial\eta} + i\frac{\partial E}{\partial\eta}\right) - ik_0(-1+\sqrt{1+\mathcal{Z}+Q})\right\}\psi = 0, \tag{3.54}$$

which is a modified parabolic equation governing the phase shifted complex wave field ψ, where the operator Q is a differential operator introduced by the phase shift

and is given by

$$Q = \frac{2i}{k_0^2}\frac{\partial E}{\partial \eta}\frac{\partial}{\partial \eta} + \frac{1}{k_0^2}\left(i\frac{\partial^2 E}{\partial \eta^2} - \left(\frac{\partial E}{\partial \eta}\right)^2\right). \tag{3.55}$$

The square root operator in Eq. (3.54) is split assuming that terrain scattering term $\mathcal{Q}$ is small in front of the diffractive operator $\mathcal{Z}$ [68], which leads to the firs-order splitting,

$$\sqrt{1+\mathcal{Z}+Q} \approx \sqrt{1+\mathcal{Z}} + Q/2 + \mathcal{O}(Q). \tag{3.56}$$

The splitting given by Eq. (3.56) is consistent with the paraxial approximation, Eq. (3.37), since the refractive term Q is small in comparison with the diffractive term $\mathcal{Z}$ at low frequencies. This follows from the fact that for a smooth boundary, the scattered field is small in comparison with the incident field. As a result, the approximation in Eq. (3.56) is valid for boundaries with a sloping angle of about 20° [68]. It is then possible to cancel the first-order derivatives in η by enforcing the condition $\partial E/\partial \eta = k_0 dh/d\xi$, which gives a phase of the form

$$E(\xi,\eta) = k_0\frac{dh}{d\xi}\eta + C(\xi), \tag{3.57}$$

where C is a range-dependent refractive term. It is possible to choose an appropriate form for C, so that the modified wide-angle equation is identical to the PE for propagation above a flat surface, which is defined in Eq. (3.10). Recasting the phase E of Eq. (3.57) into Eq. (3.54), the following equation is obtained

$$\left\{\frac{\partial}{\partial \xi} + i\left(k_0\eta\frac{d^2h}{d\xi^2} + \frac{dC}{d\xi}\right) - \frac{ik_0}{2}\left(\frac{dh}{d\xi}\right)^2 - ik_0(-1+\sqrt{1+\mathcal{Z}})\right\}\psi = 0, \tag{3.58}$$

which can be simplified if $dC/d\xi = k_0(dh/d\xi)^2/2$. This leads to the exact same phase shift E as the narrow-angle BTPE defined in Eq. (3.51). The final modified wide-angle PE is then

$$\boxed{\frac{\partial \psi}{\partial \xi} = ik_0(-1+\sqrt{1+\mathcal{Z}})\psi - ik_0\eta\frac{d^2h}{d\xi^2}\psi.} \tag{3.59}$$

An important simplification is possible if the terrain profile h is assumed to be piecewise linear, which leads to $d^2h/d\xi^2 = 0$ locally. It reduces the BTPE to Eq. (3.10), leaving all terrain terms in the multiplicative factor $e^{i(k_0\xi+E(\xi,\eta))}$. This equation is related to the work carried out by Donohue and Kuttler [68] and Holm [95] for electromagnetic propagation. The piecewise linear approximation is useful for realistic terrains that cannot be described by analytical functions and its accuracy can be always maintained by taking a smaller step $\Delta\xi$.

3.3 Numerical Solution of the BTPE

In the present section, a finite-difference solution of Eq. (3.52) will be presented. This solution relies on a discretization of the numerical domain $\mathcal{D}$ into $(N_x+1)\times(N_z+1)$ regularly spaced points $\{\xi_0,\cdots,\xi_{N_x}\}\times\{\eta_0,\cdots,\eta_{N_z}\}$ where $\xi_m = \xi_0 + m\Delta\xi$ and $\eta_n = \eta_0 + n\Delta\eta$. The step $m = 0$ corresponds to the initial condition of the marching scheme, while $n = 0$ corresponds to the numerical domain bottom surface. As a result, the wave field at every grid point is written as $\psi_{n,m} = \psi(\xi_m, \eta_n)$ and the column of points at every step m in range is stored in a vector $\Psi_m = (\psi_{1,m},\cdots,\psi_{N_z,m})$. For finite-difference solvers, the value of the marching step $\Delta\xi$ must satisfy the Courant–Friedrichs–Lewy (CFL) condition

$$\Delta\xi \leq c_0\Delta t, \tag{3.60}$$

where Δt is the time step and c_0 is the sound speed. For a single-frequency problem, we can write $\Delta t = 1/\omega$, where $\omega = 2\pi f$ is the angular frequency, so the CFL condition (Eq. (3.60)) in frequency domain is given by

$$\Delta\xi \leq \frac{c_0}{2\pi f}. \tag{3.61}$$

Since $c_0/f = \lambda_0$, we set the numerical step to a value smaller or equal to $\sim \lambda_0/6$, with λ_0 the wavelength. On the other hand, Split-Step Fourier methods [131] are more

numerically efficient and result in an accurate result with a marching step $\Delta x = \lambda_0$ but do not allow as much flexibility for irregular bottom boundary conditions.

3.3.1 Crank-Nicolson marching scheme

In this section, Eq. (3.52) is solved numerically using finite-differences, which is an alternative formulation to the Split-Step Fourier method used in the original paper of Parakkal et al. [152]. We derive a method to compute the solution at a step $\xi + \Delta\xi$ from the solution at ξ. This operation is called a marching scheme and, when applied recursively, allows us to compute the solution vector Ψ_m at all points $\xi_m = m\Delta\xi$. Two successive field points $\psi(\xi + \Delta\xi, \eta)$ and $\psi(\xi, \eta)$ are related by the implicit Crank-Nicolson marching scheme [191]

$$\exp\left(-\frac{\Delta\xi}{2}\frac{\partial}{\partial\xi}\right)\psi(\xi + \Delta\xi, \eta) = \exp\left(\frac{\Delta\xi}{2}\frac{\partial}{\partial\xi}\right)\psi(\xi, \eta), \tag{3.62}$$

which is an implicit numerical scheme. According to Lee and McDaniel [117], implicit schemes present the advantage of being unconditionally stable and requiring knowledge from the previous step only to compute the following step. In exchange for stability, the Crank-Nicolson scheme, given in Eq. (3.62), requires the resolution of a linear system at every marching step. The exponential terms in Eq. (3.62) are approximated using a first-order Taylor expansion, leading to

$$\Psi_{m+1} - \frac{\Delta\xi}{2}\left(\frac{\partial\Psi}{\partial\xi}\right)_{m+1} = \Psi_m + \frac{\Delta\xi}{2}\left(\frac{\partial\Psi}{\partial\xi}\right)_m. \tag{3.63}$$

The range derivatives in Eq. (3.63) are expressed using the PE, given in Eq. (3.52). By introducing the coefficients $\mu^{\pm} = \pm ik_0\Delta\xi/4$, Eq. (3.63) becomes,

$$\left\{1 + \mu^{-}\mathcal{Z}^*\right\}\Psi_{m+1} = \left\{1 + \mu^{+}\mathcal{Z}^*\right\}\Psi_m, \tag{3.64}$$

where $\mathcal{Z}^*$ is the new form of the operator $\mathcal{Z}$ defined in Eq. (3.7), but with an additional terrain-related term, $\mathcal{Z}^* = \mathcal{Z} - 2\eta(d^2h/d\xi^2)$, which is a modified diffraction

operator in the (ξ, η) coordinate system. Equation (3.64) is then fully discretized, by evaluating $\mathcal{Z}^*$ at each grid point (ξ_m, η_n), which gives

$$\mathcal{Z}^*\psi_{m,n} = \frac{1}{k_0^2}\left(\rho_n \frac{\partial}{\partial \eta}\left(\frac{1}{\rho}\frac{\partial \psi}{\partial \eta}\right)_{m,n} + (k_n^2 - k_0^2)\psi_{m,n}\right) - 2\eta_n \left(\frac{d^2 h}{d\xi^2}\right)_m \psi_{m,n}, \tag{3.65}$$

The second-order derivative in η can be discretized using the finite-difference method, as proposed in Salomons [177], which leads to

$$\rho_n \frac{\partial}{\partial \eta}\left(\frac{1}{\rho}\frac{\partial \psi}{\partial \eta}\right)_{m,n} = \frac{\gamma_n^{+1}\psi_{m,n+1} - 2\gamma_n^0 \psi_{m,n} + \gamma_n^{-1}\psi_{m,n-1}}{\Delta\eta^2}, \tag{3.66}$$

$$\begin{aligned} \gamma_n^{+1} &= \frac{1}{2}\left(1 + \frac{\rho_n}{\rho_{n+1}}\right), \\ \gamma_n^{0} &= \frac{1}{4}\left(2 + \frac{\rho_n}{\rho_{n+1}} + \frac{\rho_n}{\rho_{n-1}}\right), \\ \gamma_n^{-1} &= \frac{1}{2}\left(1 + \frac{\rho_n}{\rho_{n-1}}\right). \end{aligned} \tag{3.67}$$

The discretization in Eq. (3.65) requires special care at the domain boundaries. At the domain limit points, *i.e.* $n = 1$ and $n = N_z$, the out-of-grid field values $\psi_{m,0}$, ψ_{m,N_z+1} have to be replaced using the boundary conditions. The bottom boundary is governed by the sloping impedance boundary condition Eq. (3.34), while the upper limit of the grid is a hard (perfectly reflecting) boundary. Since the BTPE is solved for the envelope ψ, before being translated back to complex pressure p_c in the original domain, it is necessary to derive the boundary conditions in the (ξ, η) system. This has been done by Parakkal [152], according to whom the boundary conditions can be written as

$$\psi_{m,0} = \alpha_m^1 \psi_{m,1} + \alpha_m^2 \psi_{m,2}, \tag{3.68}$$

$$\psi_{m,N_z+1} = \beta_m^1 \psi_{m,N_z} + \beta_m^2 \psi_{m,N_z-1}, \tag{3.69}$$

where α_m^n, β_m^n are range-dependent coefficients given in Parakkal et al. [152]. In

this same paper, it is pointed out that if the terrain slope θ_x is lower than 15° then the error from using a flat boundary condition is only about 0.04 and it can be for small terrain angles. Equation (3.64) can be expressed in a matrix form, as

$$\mathbf{M}^{-}\Psi_{m+1} = \mathbf{M}^{+}\Psi_{m}, \tag{3.70}$$

where the system matrices are given by

$$\mathbf{M}^{\pm} = \mathbf{I} + \mu^{\pm}(\mathbf{D}_2 + \mathbf{K}_m^*), \tag{3.71}$$

with $\mathbf{I} = \text{diag}_n(1)$ is the identity matrix of size N_z and $\mu^{\pm} = \pm ik_0\Delta\xi/4$, as before. The tridiagonal matrix $\mathbf{D}_2$ is the second-order finite-difference matrix and it represents the diffraction term, corresponding to the discretization of the second-order spatial derivative with respect to η. The diagonal matrix $\mathbf{K}_m^*$ is the range dependent refraction term in the flattened coordinate system (ξ, η), expressed as

$$\mathbf{K}_m^* = \mathbf{K} + \mathbf{B}_m, \tag{3.72}$$

where the diagonal matrices $\mathbf{K}$ and $\mathbf{B}_m$ are given by

$$\mathbf{K} = \text{diag}_n((k_n^2 - k_0^2)/k_0^2), \tag{3.73a}$$

$$\mathbf{B}_m = \text{diag}_n(-2\eta_n(d^2h/d\xi^2)_m), \tag{3.73b}$$

We can see that Eq. (3.70) differs from the GTPE, given in Eq. (3.48). The phase shift introduced in Eq. (3.51) has allowed us to transform a first-order finite-difference matrix $\mathbf{D}_1$ into a refracting term $\mathbf{B}_m$, which greatly simplifies computations and boundary condition incorporation.

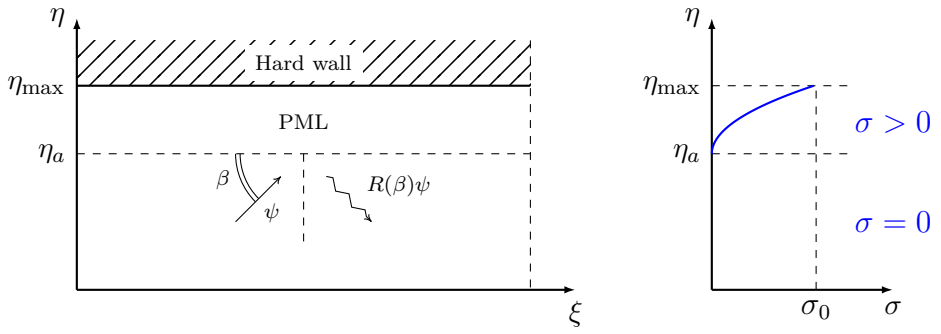

Figure 3.5: Schematic of the Perfectly Matched Layer (PML) the spurious reflection from the incident wave ψ at an angle β (left), plot of the associated quadratic absorption function σ (right).

3.3.2 Upper absorbing boundary condition

In theory, the physical domain is infinite and the behavior of the wave field away from the source (i.e. when $|k_0\mathbf{x}| \gg 1$) is governed by the Sommerfeld radiation condition [58]. This cannot be reasonably implemented numerically unless the numerical domain is made very large. After the problem is discretized into a finite domain, a truncation error appears due to reflections from the numerical boundary. In order to damp these reflections, a Perfectly Matched Layer (PML) of thickness H_a is introduced below the upper limit of the numerical domain, which is defined as $\eta = \eta_{\max}$ (cf. Fig. 3.5). This method was originally developed by Bérenger [27] and introduced to the PE method by Yevick and Thomson [229]. Here, a PML in the direction η is defined by making a complex change of variable $\eta \to \eta^*$, where the complex cooridnate η^* is defined by

$$\eta^* = \eta - i \int_{\eta_a}^{\eta} \sigma(s) ds, \tag{3.74}$$

where $\eta_a = \eta_{\max} - H_a$, is the starting altitude of the PML and σ_0 is an artificial absorbing coefficient that varies smoothly, typically under as quadratic function of η, *i.e.*

$$\sigma(\eta) = \sigma_0 \frac{(\eta - \eta_a)^2}{H_a^2}. \tag{3.75}$$

The absorbing coefficient σ_0 is the amplitude of the imaginary part of η^*, it can be physically interpreted as the rate of decay of the wave, which becomes evanescent inside the PML region $\eta > \eta_a$. A simple calculation based on the derivations of Yevick and Thomson [229] can help us determine the right absorbing coefficient for a PML of a given thickness, subject to an incident wave at an incident angle β:

$$\sigma_0 = -\frac{3}{2}\frac{\ln|R(\beta)|}{k_0 \sin(\beta) H_a}, \tag{3.76}$$

where $k_0 = 2\pi f$ is the natural wavenumber and $R(\beta)$ is the reflection coefficient, that has to be made as small as possible (e.g. $\sim 10^{-4}$) if we want to limit spurious numerical effects. We can further interpret this result in terms of the sound wavelength λ_0 instead of the frequency, so

$$k_0 = \frac{2\pi}{\lambda_0} \;,\; H_a = N\lambda_0 \quad \Longrightarrow \quad \boxed{\sigma_0 = -\frac{3}{4\pi}\frac{\ln|R(\beta)|}{N \sin(\beta)},} \tag{3.77}$$

where N gives the PML thickness in terms of wavelengths. In Fig. 3.6, the artificial absorbing coefficient σ_0 and the reflection loss $\ln|R|$ are plotted as a function of the incident angle β (*c.f.* Fig. 3.5), for different different values of the normalized layer thickness N (*i.e.* as a number of wavelengths). Critical reflection happens when $\beta = 0$, which corresponds to grazing incidence. It appears that a larger value of N allows the use of a smaller absorption coefficient σ_0, which presents the advantage of reducing spurious reflections from the interface $\eta = \eta_a$. Furthermore, a larger value of N significantly improves the damping of the wave, as seen in the right plot of Fig. 3.6.

Therefore, it is physically more advantageous to increase the size of the PML, as it would lower the coefficient σ_0 and allow a smoother damping. However, increasing the size of the PML too much creates a bigger domain and therefore longer computations, so the choice has to be made between the accuracy and efficiency of the modeling. The change of variables introduced in Eq. (3.38) leads to a modified derivative $\partial/\partial\eta \to 1/(1 + i\sigma(\eta)) \times \partial/\partial\eta$. In order to simplify the numerical solution, the density ρ and the effective sound speed c_{eff} in the PML are assumed to be

constant. After discretization, the rows of the tridiagonal matrix $\mathbf{M}_2$, corresponding to the points located at $\eta > \eta_a$, are modified according to

$$\left(\frac{\partial^2\psi}{\partial\eta^{*2}}\right)_{m,n} = \frac{1}{(1+i\sigma_n)^2}\left(\frac{d_n^{+1}\psi_{m,n+1} + d_n^0\psi_{m,n} + d_n^{-1}\psi_{m,n-1}}{\Delta\eta^2}\right) \tag{3.78}$$

$$\begin{aligned} d_n^{+1} &= \frac{1}{\Delta\eta^2} - i\frac{\sigma_{n+1}-\sigma_{n-1}}{2\Delta\eta}, \\ d_n^{0} &= \frac{-2}{\Delta\eta^2}, \\ d_n^{-1} &= \frac{1}{\Delta\eta^2} + i\frac{\sigma_{n+1}-\sigma_{n-1}}{2\Delta\eta}. \end{aligned}$$

In Yevick and Thomson [229], a comparison between the PML and more generic physical absorbers is made. It is proven that if the appropriate profile is chosen for σ, numerical reflections can be avoided after discretization. In this same paper, an equivalent absorbing layer is built by introducing a complex wavenumber in the lossy regions and it is shown that the discretization-induced error of the PML is orders of magnitude smaller. This can be interpreted physically by the fact that the PML creates loss in the diffractive term $\partial^2/\partial\eta^2$ instead of the wavenumber k.

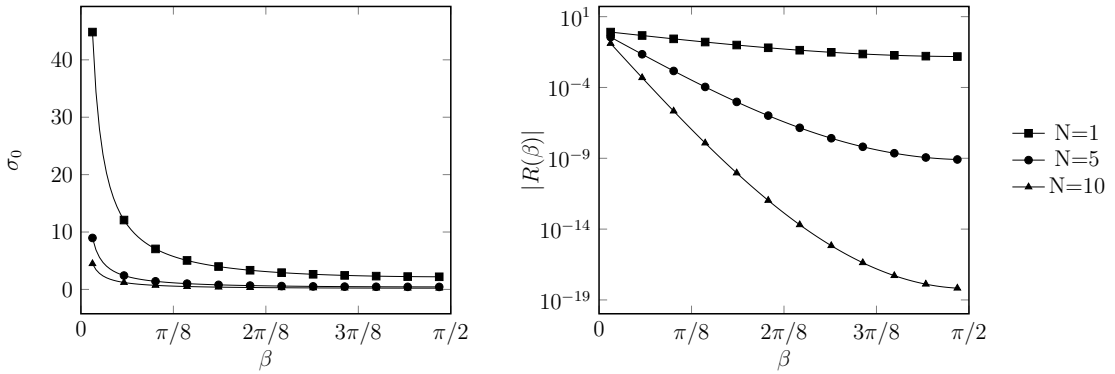

Figure 3.6: Dimensionless absorbing coefficient σ_0 for a reflection amplitude of 10^{-3}(left) and reflection amplitude $|R|$ for $\sigma_0 = 1$ (right) as a function of the incident angle β for a PML thickness $N = 1$, 5 and 10 wavelengths

3.4 Validation of the 2DPE

In this section, a set of simulations are presented in order to validate the two dimensional codes developed to implement the narrow-angle BTPE, given in Eq. (3.52), and the wide-angle BTPE, given in Eq. (3.59). The following configurations are considered: propagation above a flat rigid surface in a homogeneous atmosphere in Sec. 3.4.1, propagation over a flat rigid surface in a refracting atmosphere in Sec. 3.4.2, propagation over a flat rigid surface in a variable density atmosphere in Sec. 3.4.3, propagation over a gaussian hill of variable height in a homogeneous atmosphere in Sec. 3.4.4. Analytical solutions are used as benchmarks in Sec. 3.4.1 and Sec. 3.4.2, while a COMSOL FEM model is used in Sec. 3.4.4. Results will be presented for the Relative Sound Pressure Level (RSPL) across the propagation field, which is defined as

$$\hat{L}_p(x,z) = 10\log_{10}\left(\frac{p_c(x,z)}{\sqrt{2}p_{\text{ref}}}\right)^2, \tag{3.79}$$

where p_{ref} is the reference pressure, which will be taken one numerical step away from the source location, i.e. $p_{\text{ref}} = p_c(\Delta\xi, z_s)$. The RSPL is related to the Sound Pressure Level (SPL) L_p by $\hat{L}_p = L_p - L_{\text{ref}}$, where L_{ref} is the SPL at the reference location. A schematic of the validation cases is given in Fig. 3.7. The terrain obstacle is located between x_1 and x_2, in such a way that the RSPL at x_1 is only fully described by propagation over a flat impedance surface, while x_2 will be used to estimate the near post-obstacle solution.

3.4.1 Propagation over a flat ground in a homogeneous media

The simulations of the wave propagation from a point source above a rigid impedance plane have been carried out using the Parabolic Equation defined in Sec. 3.2.3. The source is located at $x_s = 0$ m, $z_s = 25$ m and the atmosphere is a rectangular domain

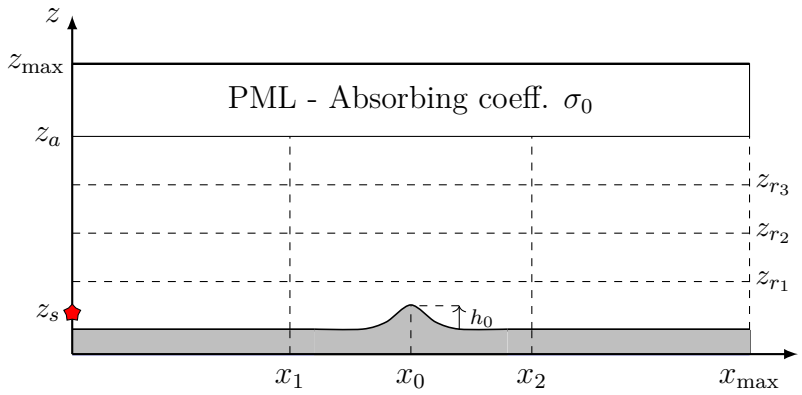

Figure 3.7: Schematic of the domain used for the validation cases of the PE in 2D. The red star represents the source, which is located at $x_s = 0$ m, $z_s = 25$ m, and the blue lines correspond to the receiver locations probed. The flat case corresponds to $h_0 = 0$.

of range $L = 10.0\,\text{km}$ and height $H = 5.0\,\text{km}$. The medium is assumed to be isothermal and homogeneous, with a constant effective sound speed $c(z) = c_0 = 343\,\text{m}\cdot\text{s}^{-1}$. The domain is truncated in altitude by an artificial PML layer of thickness $h_a = H/5$, defined in Sec. 3.3.2. Several monochromatic sources have been considered, with $f = 1$, 5, 10 and 20 Hz respectively. The relative sound pressure level $\hat{L}_p$ at several receiver altitudes, namely $z_r = 0$, 350, 1000 and 2000 m are plotted in Fig. 3.8. For propagation above a rigid flat surface, the analytical complex pressure is given by [27, 177]

$$p_c^{(a)}(x,z) = \frac{e^{ik_0 R_i}}{R_i} + \frac{e^{ik_0 R_r}}{R_r}, \tag{3.80}$$

where $R_i = \sqrt{(x-x_s)^2 + (z-z_s)^2}$ and $R_r = \sqrt{(x-x_s)^2 + (z+z_s)^2}$. The agreement between the PE and the analytical solution is verified at lower altitudes with near-field discrepancies appearing as the receiver height increases. This error is due to the intrinsic angle limitation of the PE, which results in a numerical error away from the source axis. In order to illustrate this fact quantitatively, we introduce the concept of parabolic aperture. For a given error $e = 10^{-4}$, the parabolic aperture is the set of physical points (x, z) within the angle limitation θ_p associated with e, which are defined by $|z - z_s| < x \tan\theta_p$. For example, for the narrow-angle approximation we have $\theta_p = 17.5°$, which leads to a minimum range of $x \approx 6.34\,\text{km}$ to be below the error threshold. This is graphically verifiable by reading the last row of

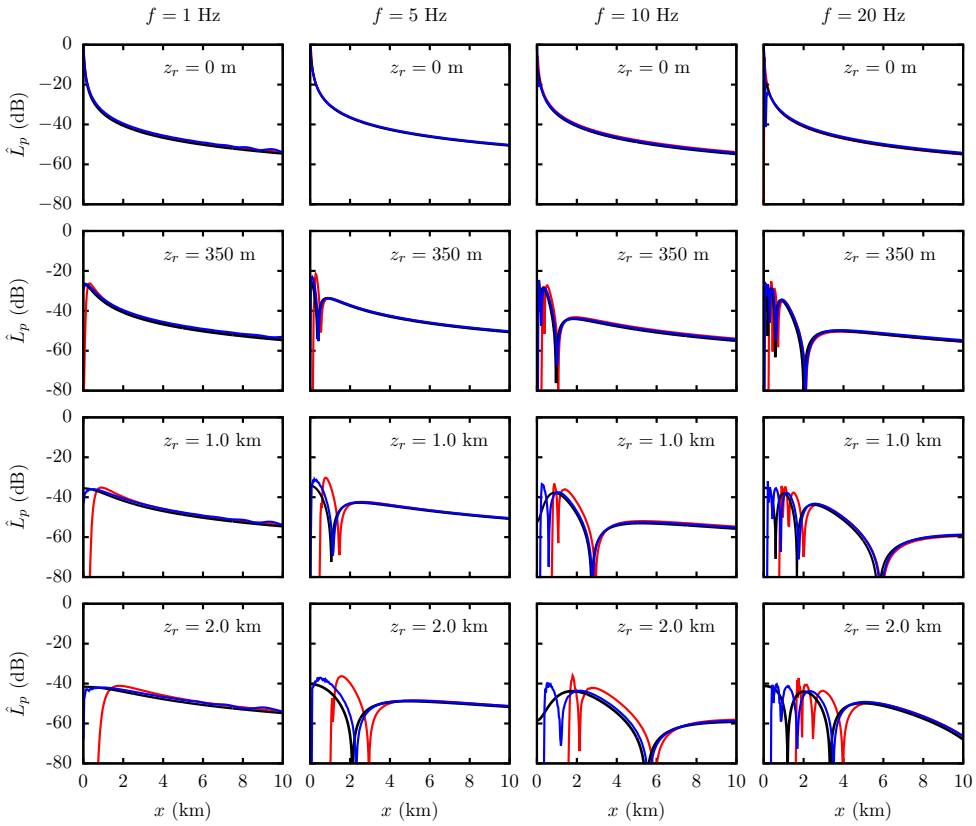

Figure 3.8: Validation of PE for a flat rigid surface, homogeneous atmosphere ($c = c_0 = 343\,\mathrm{m}\cdot\mathrm{s}^{-1}$), $f = [1, 5, 10, 20]$ Hz. Relative Sound Pressure Level (RSPL) $\hat{L}_p$ along distance at ground level (first row) and several altitudes $z_r = 350$ m (second row), 1.0 km (third row) and 2.0 km (fourth row), as computed by the narrow-angle BTPE (—), the wide-angle BTPE (—) and the analytical solution (—).

Fig. 3.8. Near $x = 0$, the PE solution diverges as this corresponds to the normal to the paraxial direction.

3.4.2 Propagation over a flat ground in a refracting atmosphere

In this section, a validation of the narrow and wide angle PE are presented for an upward and downward refracting atmosphere. Hence, we consider the effective

sound speed profiles $c_{\text{eff}} = c_0/\sqrt{1+a_w z}$, where a_w is a constant. If $a_w < 0$ the atmosphere is said to be downward refracting and if $a_w > 0$, the atmosphere is upward refracting. The coefficient a_w is expressed as $a_w = 2/R$, where R is the radius of curvature associated with the rays of the solution. If $z \ll R/2$, then the sound speed profile can be approximated by

$$c_{\text{eff}} = c_0 \left(1 \pm \frac{z}{R}\right), \tag{3.81}$$

which is known as the bilinear profile equivalency [166, 122]. The domain of validity of this approximation overlaps the paraxial region of interest, defined by $z \ll R$. This choice of effective sound speed is motivated by the fact that analytical solutions are available for these profiles, they were developed by Berry and Daigle [29], who proved the equivalency between propagation in an upward refracting atmosphere and diffraction by a curved surface, and Raspet et al. [166] for downward refraction. The upward and downward refracting solutions are based on residue series and normal modes solutions respectively, consisting of a a sum of a certain number N modal contributions, defined by wavenumbers k_n. For a source located at a height z_s above an impedance plane, the total pressure fields are written, in a two-dimensional cartesian space, as [17]

$$p_{\uparrow}(x,z) = \frac{\pi e^{i\pi/6}}{l_c} \sum_{n=1}^{N} H_0^{(1)}(k_n x) \left(\frac{\text{Ai}(b_n - (z_s/l_c)e^{2i\pi/3}))\text{Ai}(b_n - (z/l_c)e^{2i\pi/3})}{\text{Ai}'(b_n)^2 - b_n \text{Ai}(b_n)^2} \right) \tag{3.82a}$$

$$p_{\downarrow}(x,z) = \frac{\pi e^{i\pi/2}}{l_c} \sum_{n=1}^{N} H_0^{(1)}(k_n x) \left(\frac{\text{Ai}(\tau_n + z_s/l_c))\text{Ai}(\tau_n + z/l_c)}{\tau_n \text{Ai}(\tau_n)^2 - \text{Ai}'(\tau_n)^2} \right), \tag{3.82b}$$

where $\tau_n = (k_n^2 - k_0^2)l^2$, $b_n = \tau_n e^{2i\pi/3}$ and $l_c = (R/2k_0^2)^{1/3}$ is interpreted as the creeping wave layer thickness. The subscripts $\uparrow$ and $\downarrow$ denote upward and downward refraction, respectively. The quantities τ_n and b_n are the zeros of the so-called pole conditions [17]

$$\mathrm{Ai}'(\tau_n) + q\mathrm{Ai}(\tau_n) \quad = 0, \tag{3.83a}$$

$$\mathrm{Ai}'(b_n) + qe^{i\pi/3}\mathrm{Ai}(b_n) = 0, \tag{3.83b}$$

with $q = ik_0 l_c \rho_0 c_0 / Z_g$, and Z_g the ground impedance. For the sake of simplicity, we have assumed the ground to be perfectly reflecting in the following simulations, so the coefficient q in Eq. (3.83) is null and the pole conditions reduce to τ_n being equal to the zero of the derivative of the Airy function Ai'. One important parameter to be determined is the number of modes propagated to reach an accurate solution. In Raspet et al. [166], it is estimated to be $N \approx (2/3) \cdot f/|dc/dz|$ and using equation (3.81), it reduces to $N \approx (2/3) \cdot Rf/c_0$ in the case of the bilinear approximation. Furthermore, the maximum height of a given mode corresponds to the turning point of the associated ray and is approximated by $h_n \approx l_c(3\pi n/2)^{3/2}$. The take-off angle of the ray n is given by $\sin\theta_{0,n} = \mathrm{Re}(k_n)/k_0$, so the modes accurately propagated by the PE must verify the condition $\theta_{0,n} < \bar{\varphi}_p$.

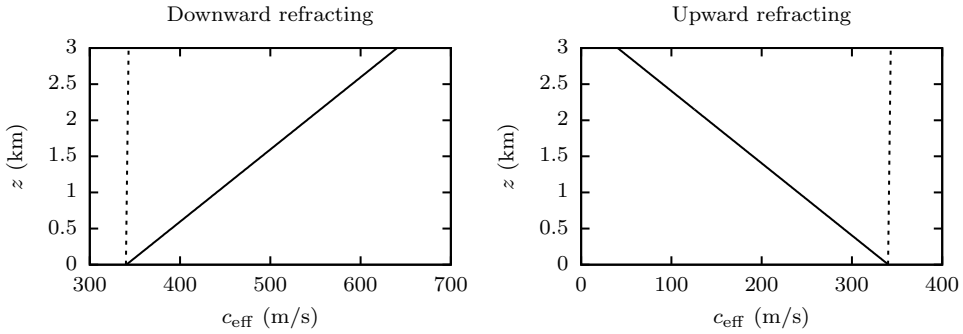

Figure 3.9: Effective sound speed profiles used for the validation of the PE in an upward refracting ($c_0/R = -0.1\,\mathrm{s}^{-1}$) and downward refracting atmosphere ($c_0/R = +0.1\,\mathrm{s}^{-1}$).

We are interested in the comparison of the PE with analytical pressures $p_\uparrow$ and $p_\downarrow$ in a region satisfying the accuracy of both models, i.e. near the ground. Attenborough (1995) provides benchmarks generated by PE and Fast Field Program methods and mentions a good agreement with analytical solutions in some scenarios only, but does not provide a comparison. Results of simulations for a downward refracting

atmosphere are presented in Fig. 3.10 for the sound speed gradient $c_0/R = +0.1\,\mathrm{s}^{-1}$ (cf. Fig. 3.9). The source is located at $z_s = 25\,\mathrm{m}$ as before. The number of modes necessary to compute the solution is 7, 34, 67 and 134 for $f = 1$, 5, 10 and 20 Hz respectively. The corresponding creeping wave layer thicknesses and maximum ray heights are given in table 3.2. We can readily see that the PE matches the normal modes solution for $f = 10\,\mathrm{Hz}$ while presenting some discrepancies at lower frequencies, where the PE fails to propagate all the necessary modes. Finally, an upward refractive atmosphere is considered, for which $c_0/R = -0.1\,\mathrm{s}^{-1}$ (*c.f.* Fig. 3.9), with all the other parameters remaining unchanged. The comparison is presented in Fig. 3.11 shows a very good agreement between the PE and the analytical solutions. Unlike the downward refracting case, the number of modes necessary to compute the solution is smaller, making the PE more accurate for these atmospheric conditions.

Frequency f (Hz)	Number of modes N_m	Creeping wave thickness $l_c(m)$	Maximum ray height $h_{N_m}(m)$
1	7	172.25	1771.68
5	34	58.91	1737.81
10	67	37.11	1720.69
20	134	23.38	1720.84

Table 3.2: Maximum ray height h_{N_m}, creeping layer wave thickness l and number of modes N_m associated with the downward refracting normal mode solution (3.82a) for frequencies $f = [1, 5, 10, 20]$ Hz.

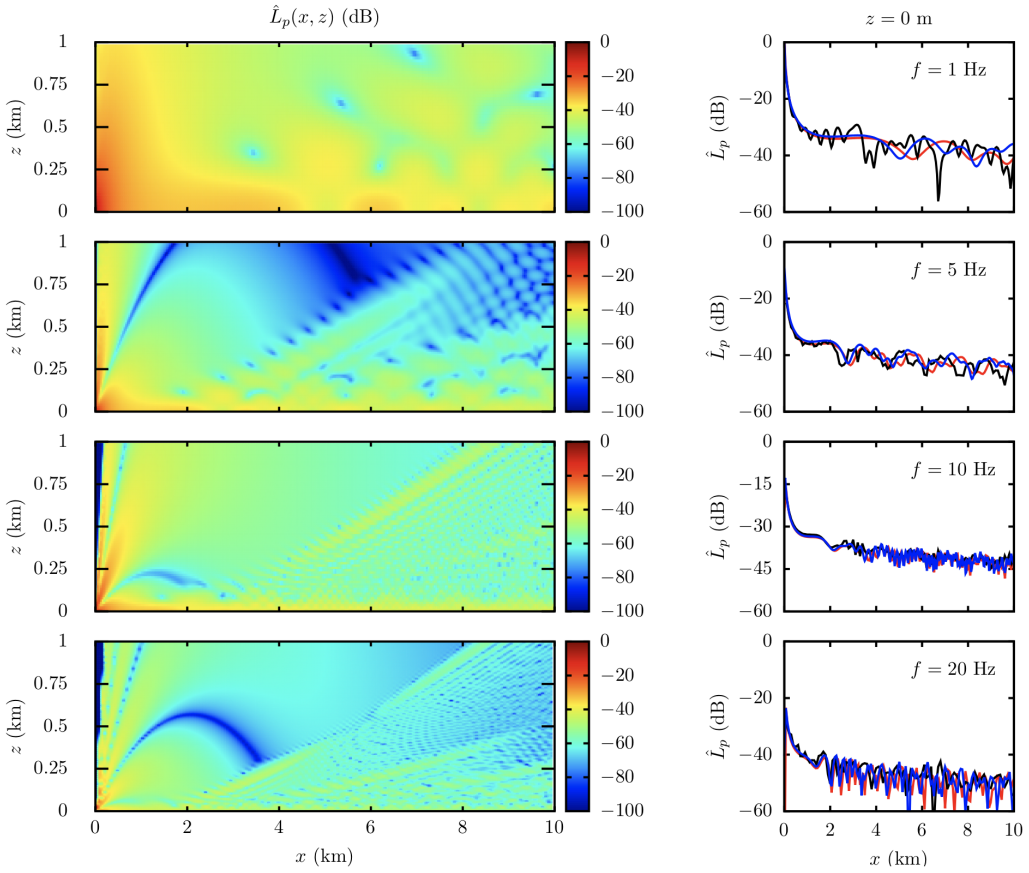

Figure 3.10: Validation of PE for a flat rigid surface, downward refracting atmosphere ($c_0/R = +0.1\,\mathrm{s}^{-1}$), $f = [1, 5, 10, 20]$ Hz. Left column: RSPL $\hat{L}_p$ contour plot in the (x, z) plane from the wide-angle BTPE. Right column: RSPL at ground level as computed by the narrow-angle BTPE (—), the wide-angle BTPE (—) and the analytical solution (—).

3.4.3 Propagation in a variable density atmosphere

In this section, the influence of the atmospheric density on infrasound propagation is investigated. The effective sound speed and density profiles considered are taken from Waxler et al. (2015) [216] and are plotted in Fig. 3.12. For an effective atmosphere, the medium density depends on altitude and becomes negligible for $z > 30$ km. As a result, taking into account density is relevant only at very low frequencies ($f < 1$ Hz) where the sound is likely to escape the tropospheric waveguide. Two frequencies are considered here, namely $f = 1$ Hz and $f = 0.1$ Hz, propagating on a

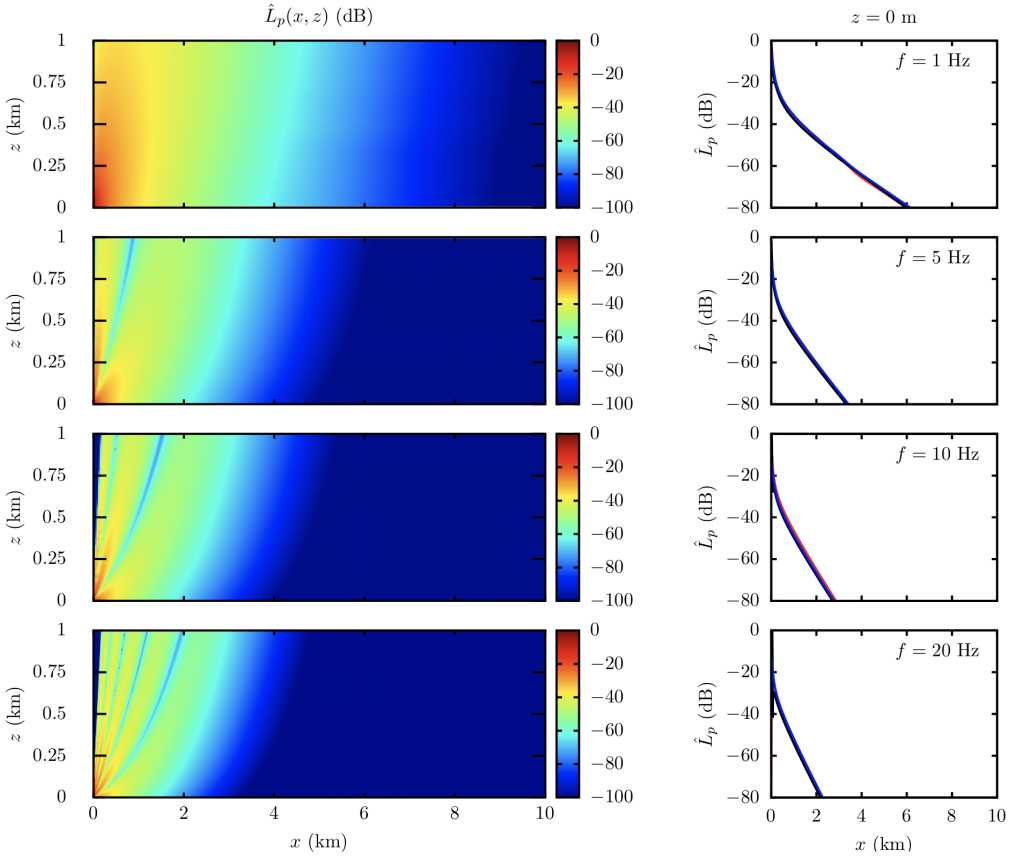

Figure 3.11: Validation of PE for a flat rigid surface, downward refracting atmosphere ($c_0/R = -0.1\,\mathrm{s}^{-1}$), $f = [1, 5, 10, 20]$ Hz. Left column: RSPL $\hat{L}_p$ contour plot in the (x, z) plane from the wide-angle BTPE. Right column: RSPL at ground level as computed by the narrow-angle BTPE (—), the wide-angle BTPE (—) and the analytical solution (—).

distance of 400 km. The source is located at $x_s = 0$ m and $z_s = 100$ m. The atmosphere has a maximum height of 100 km, and will be considered with and without density variation. The nominal value of the density at the ground level ($z = 0$ m) is $\rho_0 = 1.23$ kg/m^3.

Results are given in Fig. 3.13 for $f = 0.1$ Hz and Fig. 3.14 for $f = 1$ Hz. It appears that the decrease in density greatly reduces the amplitude at $z > 60$ km, as expected, with an RSPL lower than -100 dB. For both frequencies, the stratospheric jet generates infrasonic arrivals between $x = 200$ km and $x = 350$ km. At $x = 200$

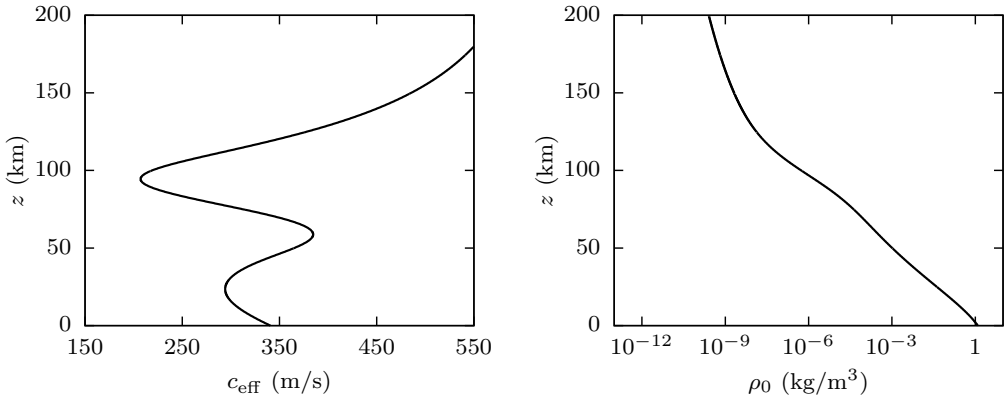

Figure 3.12: NCPA canonical profiles for the effective sound speed c_{eff} (left) and the medium density ρ_0 (right). The increase in effective sound speed at 60 km is a result of the stratospheric wind, which generates downward refraction.

km, there is an increase in RSPL of about 60 dB for $f = 0.1$ Hz and 70 dB for $f = 1$ Hz. The turning point of the ray paths is identified at $z \approx 42$ km of altitude, where the wavefront direction is tilted back to the ground. The turning point is independent of the frequency as it is a function of the effective sound speed and the shooting angle of the ray (see Appendix L, p. 246 of Salomons (2001) [177]).

The upward refracting condition for $z < 40$ km is due to the negative gradient of the effective sound speed in the troposphere, as seen in Fig. 3.12. This leads to a noticeable shadow zone between $x = 100$ km, up to $x = 200$ km. The difference between the RSPL for constant and variable densities is no more than 2 dB for $f = 0.1$ Hz and is indistinguishable at $f = 1$ Hz. Therefore, density variation leads to a reduction of the waveform amplitude at long ranges and very low frequencies, without any difference in the interference location. In particular, it appears that for a purely tropospheric propagation, when the altitude is below a few kilometers, density variation can be neglected without any significant loss in accuracy.

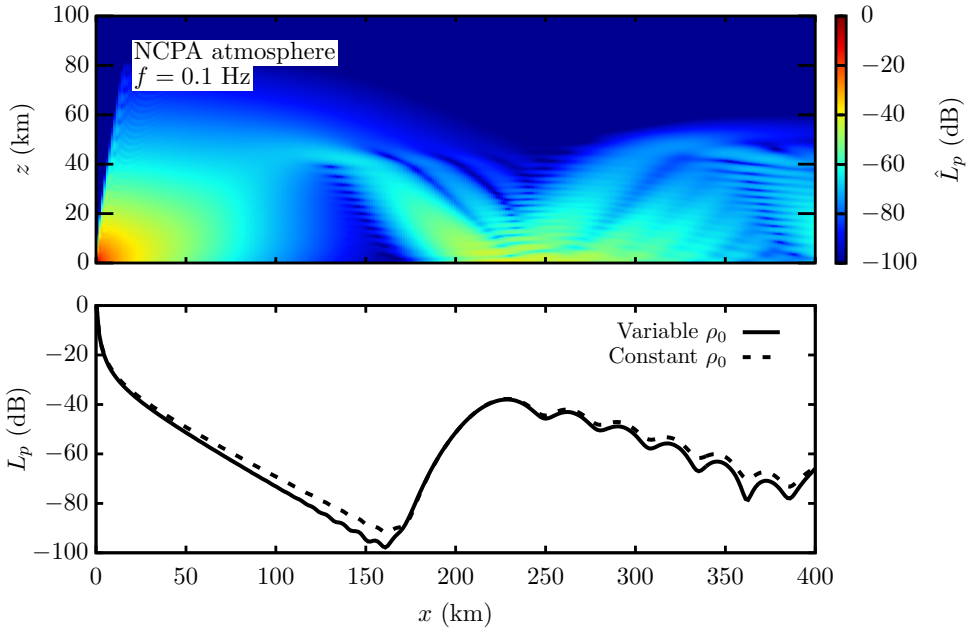

Figure 3.13: PE simulation of low-frequency propagation in an effective atmosphere with a density profile, for a frequency $f = 0.1$ Hz. Top: contour plot of the RSPL in the (x, z) plane. Bottom: comparison of the RSPL at the ground level ($z = 0$ m) for a variable and constant density profile.

3.4.4 Propagation over a gaussian hill in a homogeneous media

Next, several simple test cases were considered in order to assess the accuracy of the narrow-angle and wide-angle BTPE developed in Sec. 3.2.3. The input parameters of the simulations are identical to the previous section, but with an irregular bottom interface (or hill) described by the profile $h(x) = h_0 \exp\left(-(x - x_0)^2/2s^2\right)$, where $s = 500\,\text{m}$, $x_0 = 5.0\,\text{km}$ are constants and the maximum hill heights considered are $h_0 = 100$ (Case 1), 200 (Case 2) and 300 m (Case 3). A frequency domain finite element model was set for each value of the parameter h_0. The Relative Sound Pressure Level (RSPL) $\hat{L}_p$ at receiver heights $z_r = 0$, 350, 1000 and 2000 m are presented in Figs. 3.15, 3.20 and 3.25, which show a very good agreement between the BTPE and FEM at low altitudes. The argument previously made about accuracy in the

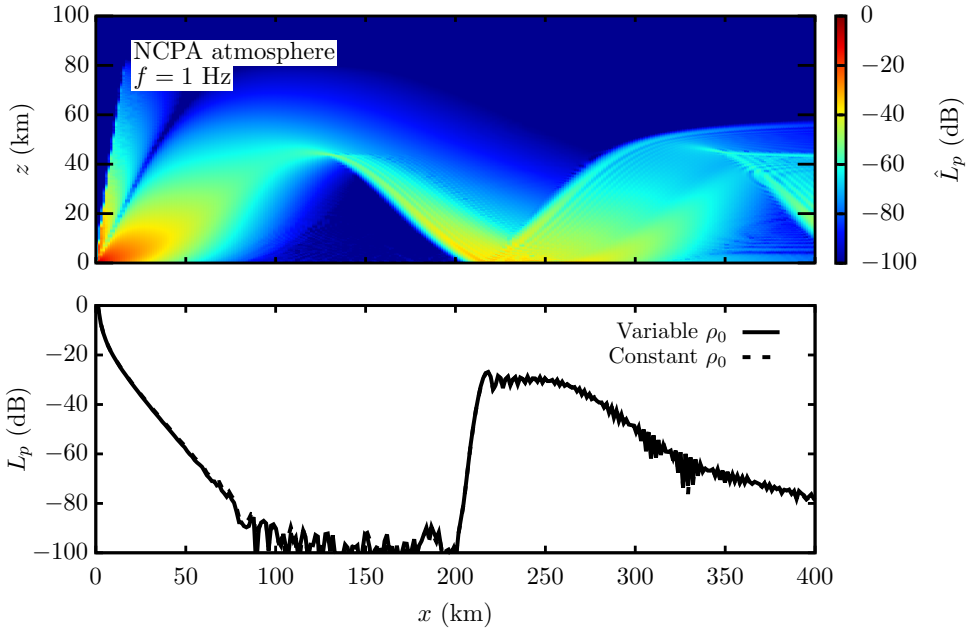

Figure 3.14: PE simulation of low-frequency propagation in an effective atmosphere with a density profile, for a frequency $f = 1$ Hz. Top: contour plot of the RSPL in the (x, z) plane. Bottom: comparison of the RSPL at the ground level ($z = 0$ m) for a variable and constant density profile.

near-filed still holds, as the wide-angle BTPE is significantly more accurate in this region, especially at $f = 1\,\text{Hz}$. A pressure increase appears at the left vicinity of the terrain peak $x = x_0^-$, which can be explained by concentration of incident waves on the exposed side. Past the obstacle, the SPL field is composed of two different structures, namely destructive interferences between direct and reflected waves that form in a caustic region, and a shadow zone bellow the "line of sight" (line between the source (S) and the peak $I_0 = (x_0, h_0)$), in which the total field is equal to the diffracted field only $p = p_d$. As the peak altitude h_0 and the frequency f increase, the number of these destructive interferences gets larger.

Figures 3.16 to 3.19 show the RSPL in the whole plane and the RSPL along altitude at several distances away from the source for $h_0 = 100\,\text{m}$. The narrow-angle BTPE and wide-angle PE both agree well with the FEM model. Before the obstacle (at

$x_r = 3.0\,\text{km}$), the sound pressure level field is the same as in the flat case. Past the obstacle (at $x_r = 7.0\,\text{km}$), we notice that destructive interferences stem from the first (horizontal) pressure lobe interaction with the ground. The two wave structures described earlier suggest that diffraction of sound by the terrain peak separates the wave field into a set of tangent destructive interferences in the upper waveguide and a shadow zone parallel to the ground. This is clearly noticeable for $h_0 = 200\,\text{m}$ in Figs. 3.21 to 3.24. For $f = 20\,\text{Hz}$, we see an additional scattered field from a creeping wave along the terrain obstacle. This effect generates oscillations in the plane $x_r = 7.0\,\text{km}$ at higher altitudes ($z > 1\,\text{km}$), where the BTPE fails to properly match the FEM. At $x_r = 10.0\,\text{km}$, we are far enough from the source to be well within the domain of validity of the PE, which explains the close agreement between the PE and FEM. Simulations performed for Case 3 (Figs. 3.26 to 3.29) show that while the wide-angle BTPE is more accurate at $x_r = 3.0\,\text{km}$, its improvement is marginal past the obstacle. Hence, we can see that the first-order approximation for terrain terms made in Eq. (3.56) prevails on the angle limitation when it comes to the scattered field contribution to the total pressure level.

3.4.5 Conclusions

In this section, several models for sound propagation over irregular boundaries have been presented and validated against analytical results. The wide-angle Beilis-Tappert PE extends the narrow-angle version of Parakkal et al. [152] in terms of atmospheric propagation while retaining the first-order terrain terms only. This formulation presents a number of advantages in comparison with the previously developed Generalized Terrain PE, which also relies on a terrain-following coordinate transform. First, the boundary conditions is simplified due to the phase shift introduced, so the sloping impedance is handled locally through an effective admittance of the form $Y_{\text{eff}} = C_1 Y + C_2$. Then, the piecewise linear approximation allows the method to accommodate realistic terrain data and cancel the second-order derivatives of the bottom profile. This approximation is satisfactory in a wide range of practical cases, as long as the boundary slope is within 30°. Moreover, refraction and density variation have been implemented in the Beilis-Tappert PE,

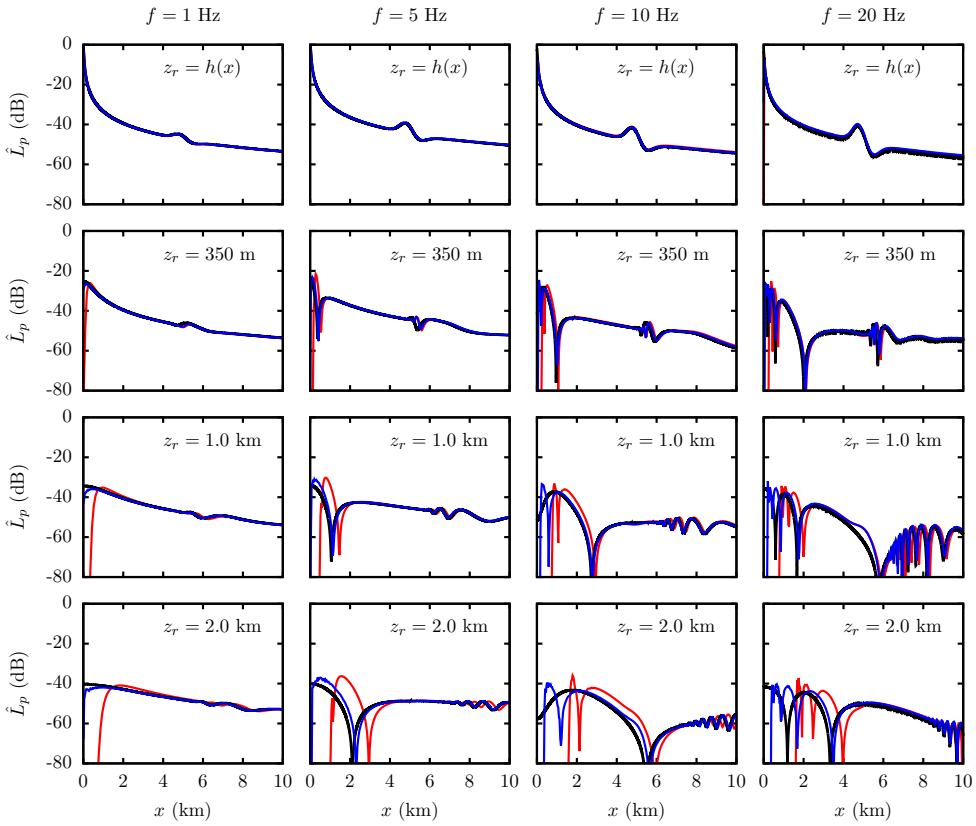

Figure 3.15: Validation of PE for a Gaussian hill of height $h_0 = 100\,\mathrm{m}$ (Case 1), homogeneous atmosphere ($c = c_0 = 343\,\mathrm{m \cdot s^{-1}}$), $f = [1, 5, 10, 20]$ Hz. Relative Sound Pressure Level (RSPL) $\hat{L}_p$ along distance at ground level (first row) and several altitudes $z_r = 350$ m (second row), 1.0 km (third row) and 2.0 km (fourth row), as computed by the narrow-angle BTPE (—), the wide-angle BTPE (—) and the FE solution (—).

enabling atmospheric coupling with terrain interaction. It has been shown that the PE agrees closely with normal modes solutions for an upward refracting atmosphere but is variably accurate for a downward refracting atmosphere. In presence of a three-dimensional problem, the 2D Beilis-Tappert PE can be used in an $N \times$ 2D approach, where the sound pressure level is estimated in different azimuthal planes (r, θ_i, z) for $i = 1, \ldots, N$, using the 2D method each time. This approach has a major limitation, which is the absence of azimuthal scattering between two adjacent planes. As a result, a complete modeling of the sound pressure level involves a full three-dimensional PE formulation with the inclusion of an irregular boundary.

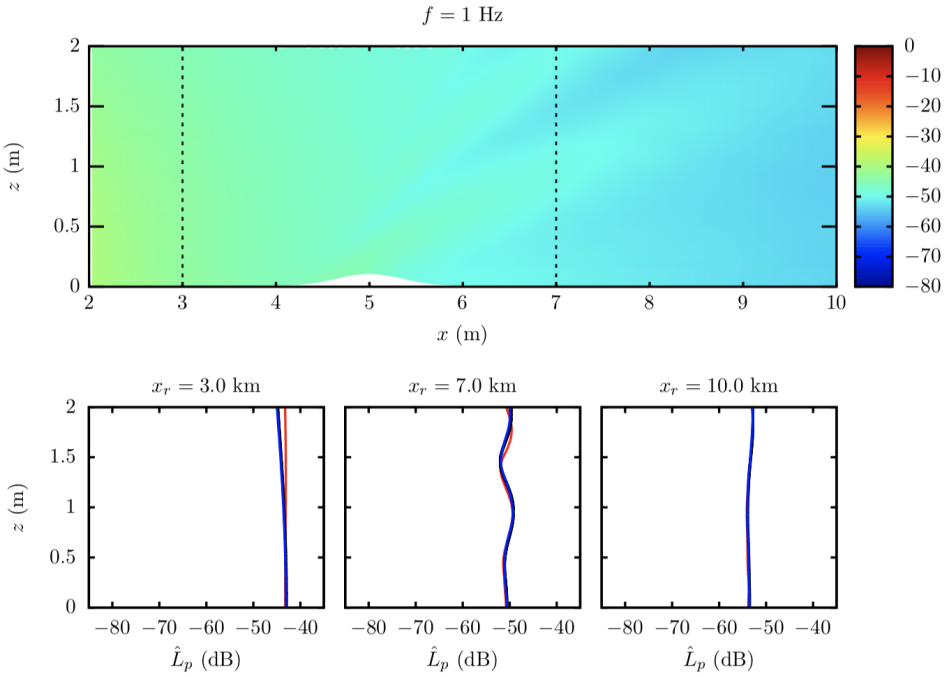

Figure 3.16: Validation of PE for a Gaussian hill of height $h_0 = 100\,\mathrm{m}$ (Case 1), homogeneous atmosphere ($c = c_0 = 343\,\mathrm{m \cdot s^{-1}}$), $f = 1$ Hz. Top row: RSPL $\hat{L}_p$ contour plot in the (x, z) plane, Bottom row: RSPL as a function of altitude at several ranges $x_r = 3.0\,\mathrm{km}$, $7.0\,\mathrm{km}$ and $10.0\,\mathrm{km}$, as computed by the narrow-angle BTPE (——), the wide-angle BTPE (——) and the FE solution (——).

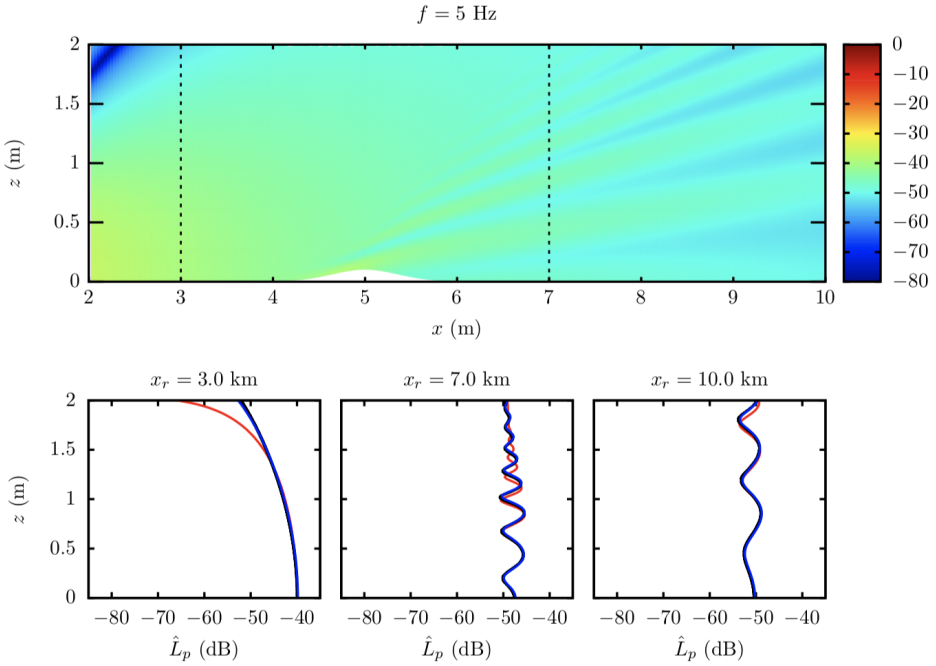

Figure 3.17: Validation of PE for a Gaussian hill of height $h_0 = 100\,\mathrm{m}$ (Case 1), homogeneous atmosphere ($c = c_0 = 343\,\mathrm{m \cdot s^{-1}}$), $f = 5$ Hz. Top row: RSPL $\hat{L}_p$ contour plot in the (x, z) plane, Bottom row: RSPL as a function of altitude at several ranges $x_r = 3.0\,\mathrm{km}$, $7.0\,\mathrm{km}$ and $10.0\,\mathrm{km}$, as computed by the narrow-angle BTPE (—), the wide-angle BTPE (—) and the FE solution (—).

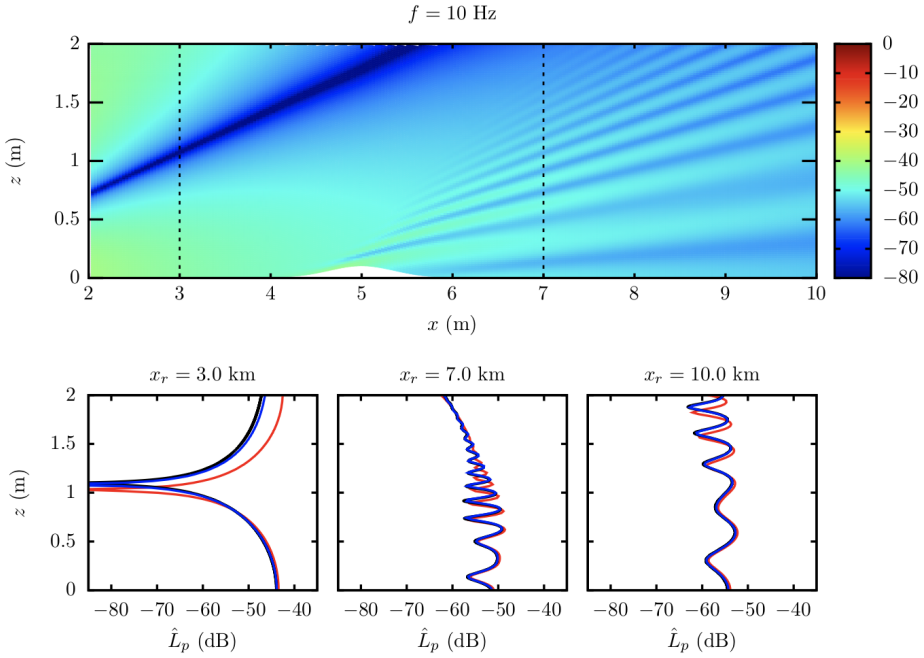

Figure 3.18: Validation of PE for a Gaussian hill of height $h_0 = 100\,\mathrm{m}$ (Case 1), homogeneous atmosphere ($c = c_0 = 343\,\mathrm{m}\cdot\mathrm{s}^{-1}$), $f = 10$ Hz. Top row: RSPL $\hat{L}_p$ contour plot in the (x, z) plane, Bottom row: RSPL as a function of altitude at several ranges $x_r = 3.0\,\mathrm{km}$, $7.0\,\mathrm{km}$ and $10.0\,\mathrm{km}$, as computed by the narrow-angle BTPE (—), the wide-angle BTPE (—) and the FE solution (—).

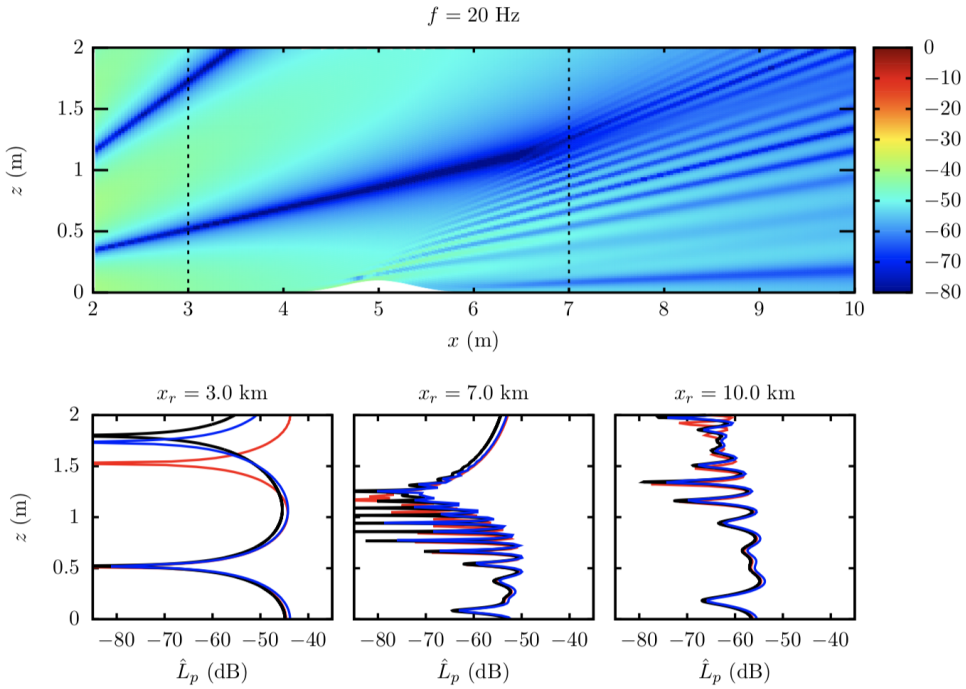

Figure 3.19: Validation of PE for a Gaussian hill of height $h_0 = 100\,\mathrm{m}$ (Case 1), homogeneous atmosphere ($c = c_0 = 343\,\mathrm{m \cdot s^{-1}}$), $f = 20$ Hz. Top row: RSPL $\hat{L}_p$ contour plot in the (x, z) plane, Bottom row: RSPL as a function of altitude at several ranges $x_r = 3.0\,\mathrm{km}$, $7.0\,\mathrm{km}$ and $10.0\,\mathrm{km}$, as computed by the narrow-angle BTPE (—), the wide-angle BTPE (—) and the FE solution (—).

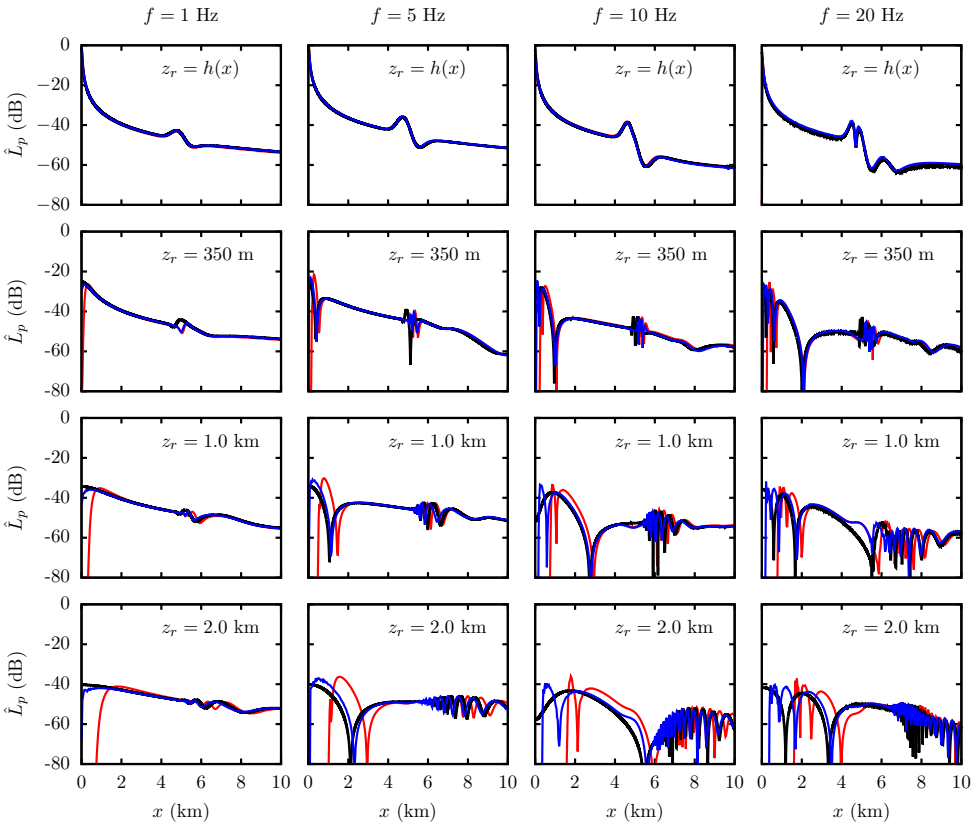

Figure 3.20: Validation of PE for a Gaussian hill of height $h_0 = 200\,\mathrm{m}$ (Case 2), homogeneous atmosphere ($c = c_0 = 343\,\mathrm{m}\cdot\mathrm{s}^{-1}$), $f = [1, 5, 10, 20]$ Hz. Relative Sound Pressure Level (RSPL) $\hat{L}_p$ along distance at ground level (first row) and several altitudes $z_r = 350$ m (second row), 1.0 km (third row) and 2.0 km (fourth row), as computed by the narrow-angle BTPE (—), the wide-angle BTPE (—) and the FE solution (—).

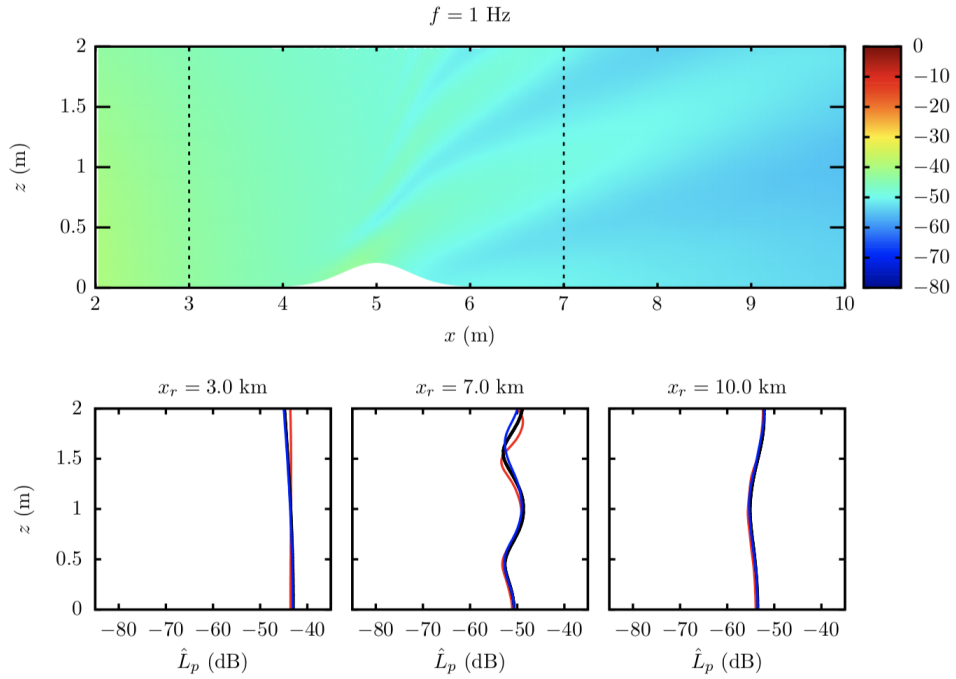

Figure 3.21: Validation of PE for a Gaussian hill of height $h_0 = 200\,\mathrm{m}$ (Case 1), homogeneous atmosphere ($c = c_0 = 343\,\mathrm{m}\cdot\mathrm{s}^{-1}$), $f = 1$ Hz. Top row: RSPL $\hat{L}_p$ contour plot in the (x, z) plane, Bottom row: RSPL as a function of altitude at several ranges $x_r = 3.0\,\mathrm{km}$, $7.0\,\mathrm{km}$ and $10.0\,\mathrm{km}$, as computed by the narrow-angle BTPE (—), the wide-angle BTPE (—) and the FE solution (—).

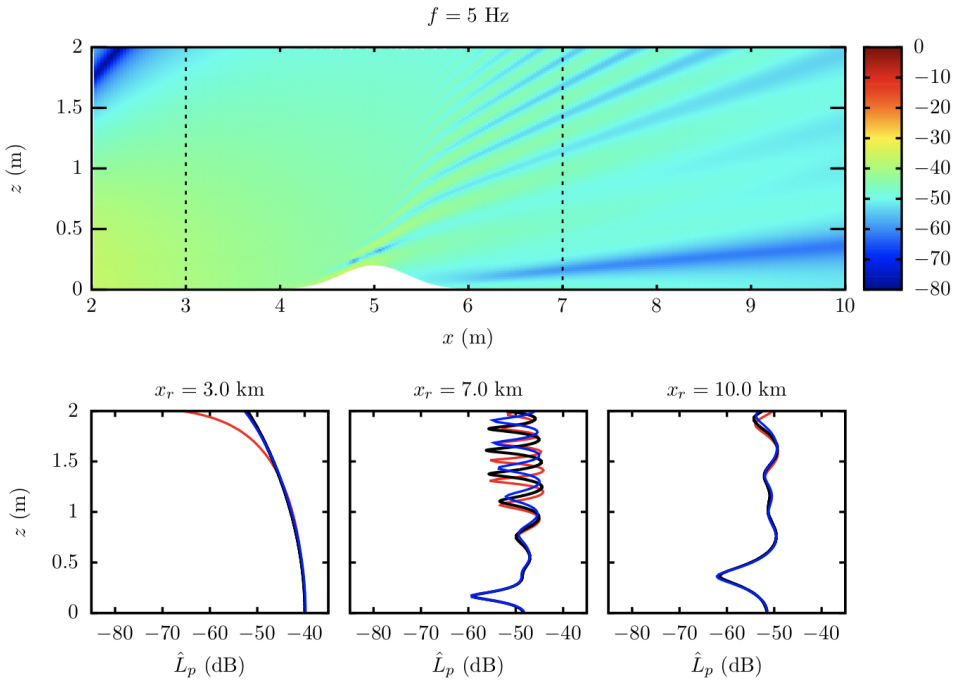

Figure 3.22: Validation of PE for a Gaussian hill of height $h_0 = 200\,\mathrm{m}$ (Case 1), homogeneous atmosphere ($c = c_0 = 343\,\mathrm{m}\cdot\mathrm{s}^{-1}$), $f = 5$ Hz. Top row: RSPL $\hat{L}_p$ contour plot in the (x, z) plane, Bottom row: RSPL as a function of altitude at several ranges $x_r = 3.0\,\mathrm{km}$, $7.0\,\mathrm{km}$ and $10.0\,\mathrm{km}$, as computed by the narrow-angle BTPE (—), the wide-angle BTPE (—) and the FE solution (—).

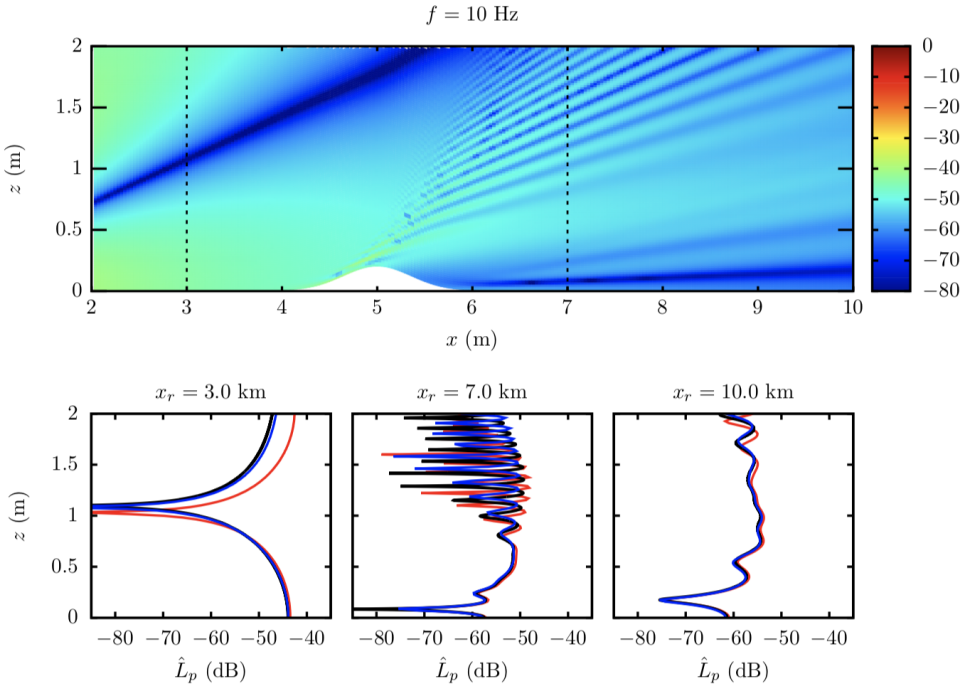

Figure 3.23: Validation of PE for a Gaussian hill of height $h_0 = 200\,\mathrm{m}$ (Case 1), homogeneous atmosphere ($c = c_0 = 343\,\mathrm{m}\cdot\mathrm{s}^{-1}$), $f = 10$ Hz. Top row: RSPL $\hat{L}_p$ contour plot in the (x, z) plane, Bottom row: RSPL as a function of altitude at several ranges $x_r = 3.0\,\mathrm{km}$, $7.0\,\mathrm{km}$ and $10.0\,\mathrm{km}$, as computed by the narrow-angle BTPE (—), the wide-angle BTPE (—) and the FE solution (—).

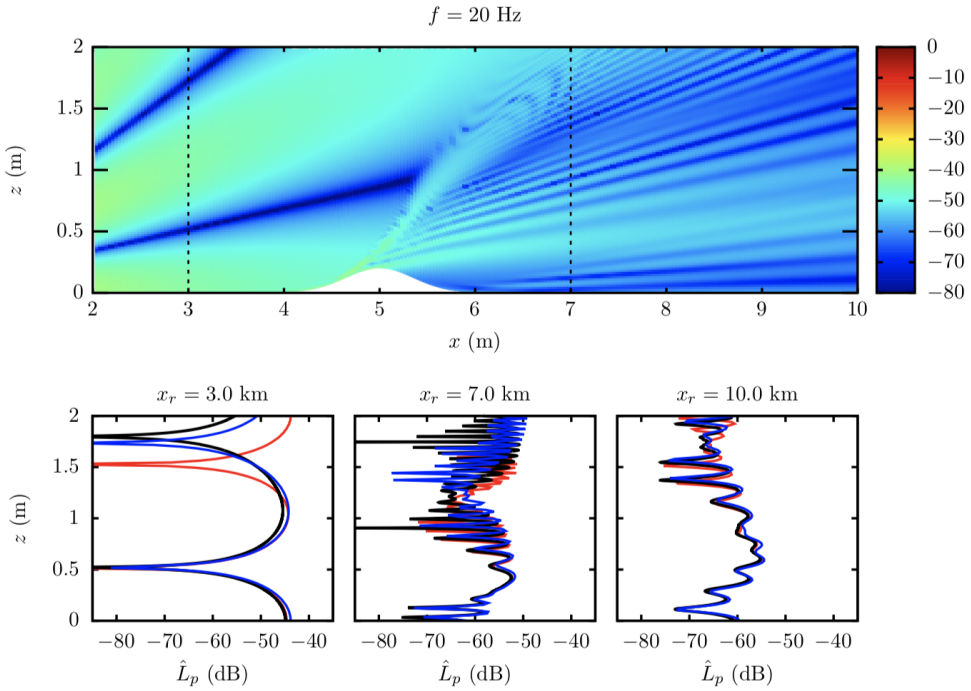

Figure 3.24: Validation of PE for a Gaussian hill of height $h_0 = 200\,\mathrm{m}$ (Case 1), homogeneous atmosphere ($c = c_0 = 343\,\mathrm{m \cdot s^{-1}}$), $f = 20$ Hz. Top row: RSPL $\hat{L}_p$ contour plot in the (x, z) plane, Bottom row: RSPL as a function of altitude at several ranges $x_r = 3.0\,\mathrm{km}$, $7.0\,\mathrm{km}$ and $10.0\,\mathrm{km}$, as computed by the narrow-angle BTPE (—), the wide-angle BTPE (—) and the FE solution (—).

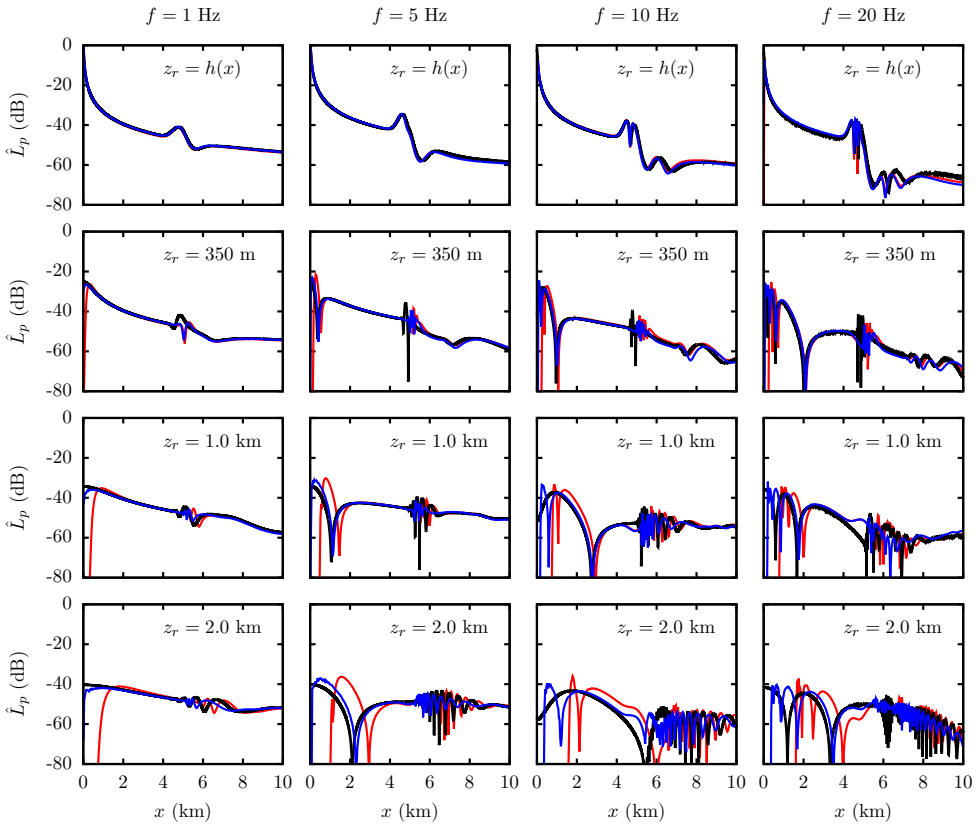

Figure 3.25: Validation of PE for a Gaussian hill of height $h_0 = 300\,\mathrm{m}$ (Case 3), homogeneous atmosphere ($c = c_0 = 343\,\mathrm{m} \cdot \mathrm{s}^{-1}$), $f = [1, 5, 10, 20]$ Hz. Relative Sound Pressure Level (RSPL) $\hat{L}_p$ along distance at ground level (first row) and several altitudes $z_r = 350$ m (second row), 1.0 km (third row) and 2.0 km (fourth row), as computed by the narrow-angle BTPE (—), the wide-angle BTPE (—) and the FE solution (—).

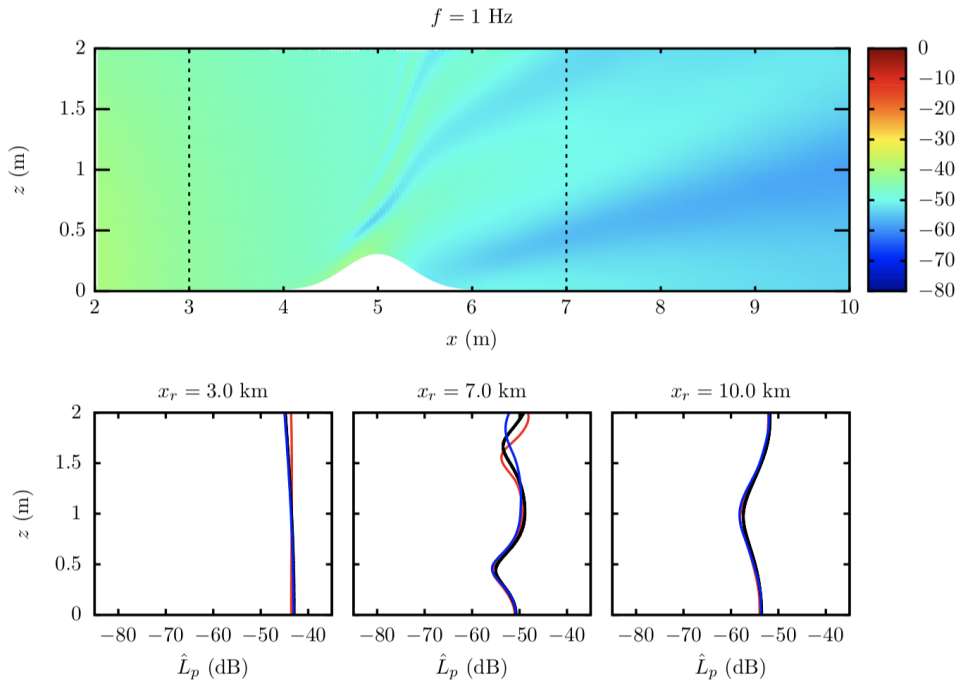

Figure 3.26: Validation of PE for a Gaussian hill of height $h_0 = 300\,\mathrm{m}$ (Case 1), homogeneous atmosphere ($c = c_0 = 343\,\mathrm{m \cdot s^{-1}}$), $f = 1$ Hz. Top row: RSPL $\hat{L}_p$ contour plot in the (x, z) plane, Bottom row: RSPL as a function of altitude at several ranges $x_r = 3.0\,\mathrm{km}$, $7.0\,\mathrm{km}$ and $10.0\,\mathrm{km}$, as computed by the narrow-angle BTPE (—), the wide-angle BTPE (—) and the FE solution (—).

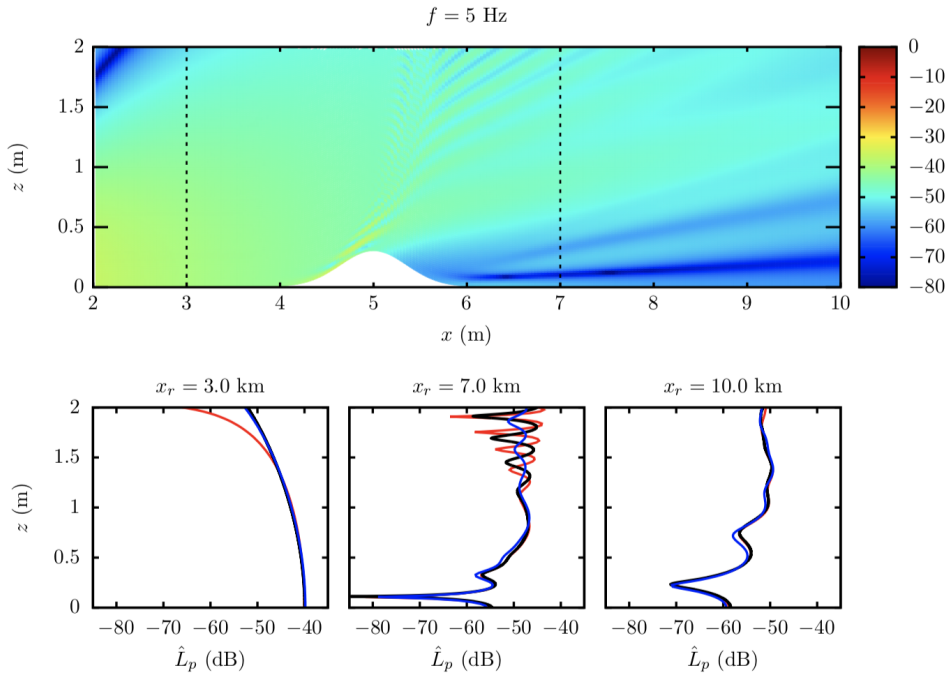

Figure 3.27: Validation of PE for a Gaussian hill of height $h_0 = 300\,\mathrm{m}$ (Case 1), homogeneous atmosphere ($c = c_0 = 343\,\mathrm{m} \cdot \mathrm{s}^{-1}$), $f = 5$ Hz. Top row: RSPL $\hat{L}_p$ contour plot in the (x, z) plane, Bottom row: RSPL as a function of altitude at several ranges $x_r = 3.0\,\mathrm{km}$, $7.0\,\mathrm{km}$ and $10.0\,\mathrm{km}$, as computed by the narrow-angle BTPE (—), the wide-angle BTPE (—) and the FE solution (—).

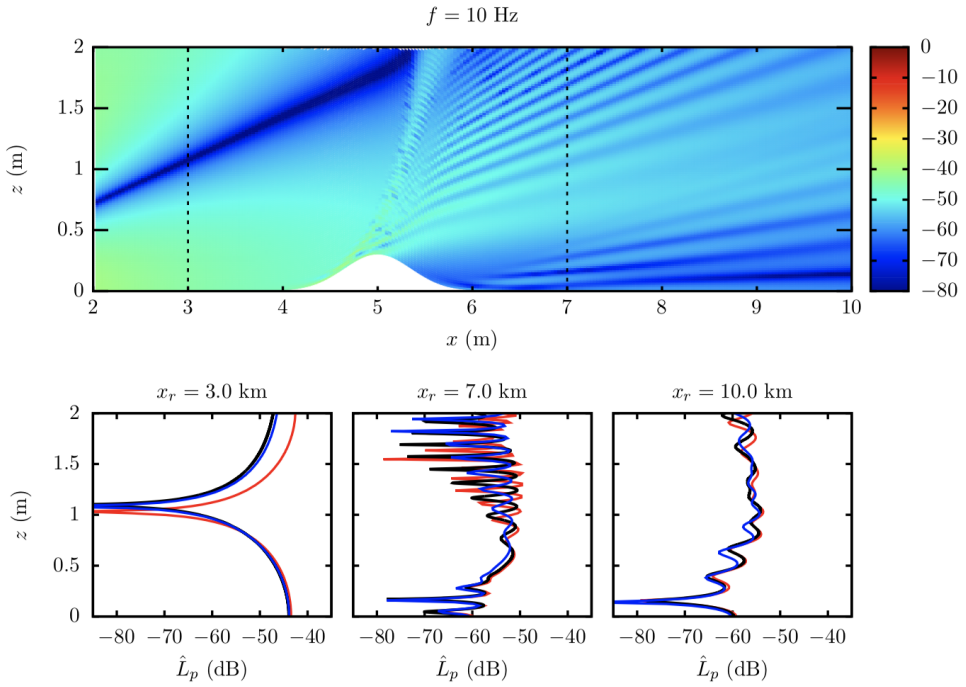

Figure 3.28: Validation of PE for a Gaussian hill of height $h_0 = 300\,\mathrm{m}$ (Case 1), homogeneous atmosphere ($c = c_0 = 343\,\mathrm{m \cdot s^{-1}}$), $f = 10$ Hz. Top row: RSPL $\hat{L}_p$ contour plot in the (x, z) plane, Bottom row: RSPL as a function of altitude at several ranges $x_r = 3.0\,\mathrm{km}$, $7.0\,\mathrm{km}$ and $10.0\,\mathrm{km}$, as computed by the narrow-angle BTPE (—), the wide-angle BTPE (—) and the FE solution (—).

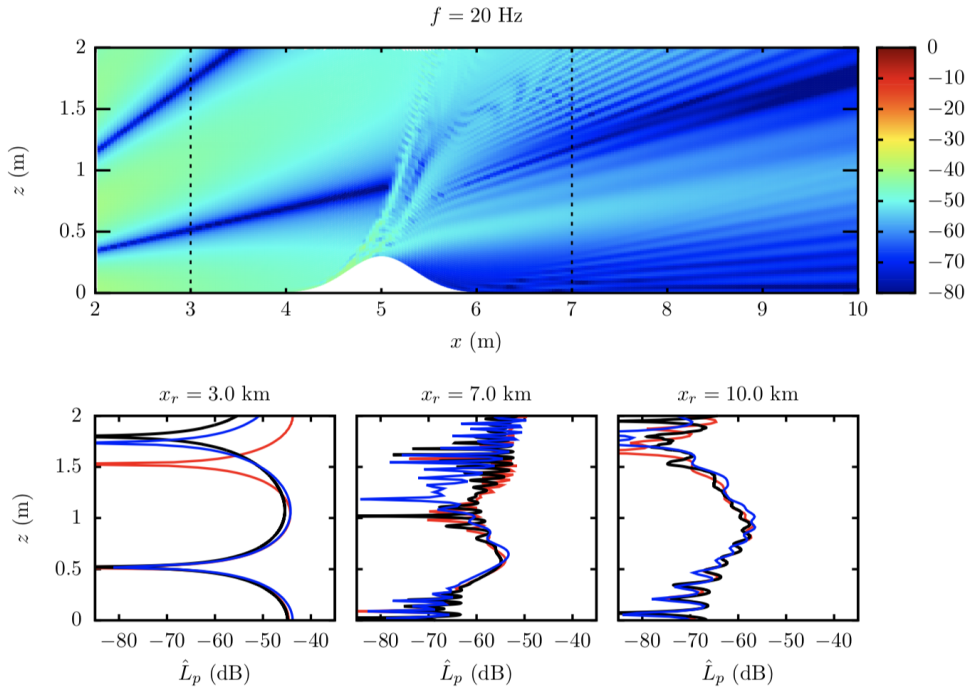

Figure 3.29: Validation of PE for a Gaussian hill of height $h_0 = 300\,\mathrm{m}$ (Case 1), homogeneous atmosphere ($c = c_0 = 343\,\mathrm{m \cdot s^{-1}}$), $f = 20$ Hz. Top row: RSPL $\hat{L}_p$ contour plot in the (x, z) plane, Bottom row: RSPL as a function of altitude at several ranges $x_r = 3.0\,\mathrm{km}$, $7.0\,\mathrm{km}$ and $10.0\,\mathrm{km}$, as computed by the narrow-angle BTPE (—), the wide-angle BTPE (—) and the FE solution (—).

Chapter 4

Development of a Three-Dimensional Parabolic Equation for propagation above irregular boundaries (3D-BTPE)

For a long time, three-dimensional PE modeling was not possible due to its great complexity, exceeding the amount of computational resources available. One of the first successful models implemented is known as FOR3D and was created by Lee et al. [116] for Underwater Acoustic modeling. The underlying numerical method relied on a wide-angle splitting of the exponential operator and an Alternate Direction Implicit (ADI) scheme to divide the problem into a set of two 2D problems along each transversal direction (i.e. in depth and width). Later, many efforts have been directed towards further improving the three-dimensional parabolic equation (3DPE), while considering more realistic waveguides [189, 194]. More recent models have taken advantage of high performance computing, enabling the use of higher-order splitting techniques. One of the most advanced 3DPE solver available is known

as the 3DWAPE (3D Wide-Angle PE), derived by Sturm [192]. It relies on a combination of the ADI scheme and the Split-Step Padé method, which was first developed in 2D by Collins [131], applied along each transversal direction separately.

The influence of three-dimensional irregular boundaries has been investigated thoroughly in Underwater Acoustics, with the objective of finding evidence of so-called "3D effects" [202]. The three-dimensional PE has been used to model such effects with success. In early 3DPE solvers, boundaries and interfaces were modeled using a stair-step approximation, such that it is locally flat at each grid point [116, 49]. As in the 2D cases, energy conservation issues arise from the stair-step approximation, so "parabolized" sloping boundary or interface conditions have been used to accurately treat transversal scattering [195]. In atmospheric acoustics, very few studies have been conducted to verify the existence of such effects in the presence of complex terrain.

A numerical investigation, relying on a novel method for three-dimensional propagation is proposed here. In Sec. 4.1, we generalize the Beilis-Tappert coordinate transform to derive a three-dimensional Cartesian space, which is a novel formulation of the 3DPE for propagation above irregular boundaries. Next, an iterative finite-differences solution is presented in Sec. 4.2 with a derivation of a three-dimensional source term. Finally, a validation of the new method against the 2DPE and a tridimensional COMSOL simulation is performed in Sec. 4.3. The method developed in this chapter will be used to carry out a parametric study of propagation above irregular boundaries in Chapter 5 and in a realistic environment in Chapter 6.

4.1 The parabolic equation in three dimensions

In this section, the theory of the three-dimensional parabolic equation (3DPE) will be presented and a three-dimensional model of the Beilis-Tappert coordinate transform, defined in Eq. (3.38), will be developed. The parabolic equation in three dimensions follows a similar theory as for an axisymmetric medium, with the only

difference being that the azimuthal term must be taken into account. A first step is to choose a tridimensional coordinate system, *i.e.* Cylindrical or Cartesian. Most 3D formulations to date have advocated the use of a cylindrical coordinate system, initially as a generalization of the azimuth-independent $N\times$ 2D PE method developed by Perkins and Baer [155]. This approach is relevant from a physical viewpoint, as it allows to constrain the region of interest within a small azimuthal aperture. However, the azimuthal step size $\Delta\theta$ becomes increasingly large away from the initial plane, so the number of steps in azimuth is constrained by the maximum propagation range. On the other hand, a Cartesian coordinate system can be more computationally expensive but allows the use of uniformly spaced grids, making finite-difference discretization and interpolation easier while preserving accuracy in the far-field. Hence, a Cartesian coordinate system will be used in the following sections.

4.1.1 Operator splitting

In this section, we will derive the PE in 3D and explore the phase error associated with the uncoupled splitting of the square-root operator. The PE is derived from the reduced Helmholtz equation in the Cartesian coordinates $\mathbf{x} = (x, y, z)$, which is written as

$$\left\{ \frac{\partial^2}{\partial x^2} + \Delta_\perp + k^2(z) \right\} p_c(\mathbf{x}) = 0, \tag{4.1}$$

where $\Delta_\perp = \partial^2/\partial y^2 + \partial^2/\partial z^2$ is the transversal Laplacian operator, $k(z) = \omega/c(z)$ is the wavenumber, $\omega = 2\pi f$ is the angular frequency and p_c is the complex pressure, earlier defined in Eq. (3.2) as the real part of the time-domain pressure amplitude. Factorizing the complex pressure amplitude p_c into a modulated form $p_c(\mathbf{x}) = \psi(\mathbf{x})e^{ik_0 x}$, and assuming that the derivatives along the propagating direction and transversal directions are commutative (i.e. their order can be switched), the envelope $\psi(\mathbf{x})$ satisfies the general 3DPE, which is given by

$$\left\{\frac{\partial}{\partial x} + ik_0(1-\mathcal{L})\right\}\psi(\mathbf{x}) = 0, \tag{4.2}$$

where $\mathcal{L} = \sqrt{1+\Delta_\perp/k_0^2} = \sqrt{1+\mathcal{Z}+\mathcal{Y}}$ is the three-dimensional square-root operator, with the differential operators $\mathcal{Z}$, $\mathcal{Y}$ given by

$$\mathcal{Z} = \frac{1}{k_0^2}\left(\rho\frac{\partial}{\partial z}\left(\frac{1}{\rho}\frac{\partial}{\partial z}\right) + k^2(z) - k_0^2\right), \tag{4.3a}$$

$$\mathcal{Y} = \frac{1}{k_0^2}\left(\frac{\partial^2}{\partial y^2}\right). \tag{4.3b}$$

If the Padé approximation is used on the operator $\mathcal{L}$, the marching scheme would lead to a large sparse system. To reach an efficient numerical solution, the operator $\mathcal{L}$ in the 3DPE, given by Eq. (4.2), must be expressed in a simpler form. Therefore, $\mathcal{L}$ is expanded into a sum of linear differential operators along different directions. A common approach consists of writing $\mathcal{L}$ into an uncoupled form (i.e. no $\mathcal{ZY}$ term), as

$$\mathcal{L} \simeq \sqrt{1+\mathcal{Z}} + \sqrt{1+\mathcal{Y}} - 1 + \mathcal{O}(\mathcal{ZY}), \tag{4.4}$$

and the square-root operators on the right hand side of Eq. (4.4) can be approximated using a Taylor (narrow-angle) or a Padé (wide-angle) expansion, as seen in Sec. 3.1.1. An extensive review of the several expansion methods used is available in Lee et al. [118] and Xu et al. [227]. One the most general cases to date is the 3D WAPE method developed by Sturm [192], who later proposed an expansion that includes a leading-order $\mathcal{ZY}$ cross-term [193]. The truncation of the cross-term in Eq. (4.4) implies that environmental parameters (topography and sound speed) vary gradually in both directions. Such an approximation is narrow-angle in nature, but greatly simplifies the numerical solution [192]. Using equation (4.4) to replace $\mathcal{L}_2$ in the general 3DPE, given by Eq. (4.2), leads to

$$\left\{\frac{\partial}{\partial x} + ik_0(2-\sqrt{1+\mathcal{Z}}-\sqrt{1+\mathcal{Y}})\right\}\psi(\mathbf{x}) = 0. \tag{4.5}$$

If the medium properties ρ and c varies slowly in the y direction, it is possible to

assume that the energy transferred between the transversal planes is negligible in comparison to the energy in the propagating in the altitude direction z, which can be translated into the condition $|\mathcal{Y}\Psi| \ll |\mathcal{Z}\Psi|$. This condition does not hold in presence of an irregular boundary, as it is likely to generate out-of plane propagation. The main advantage of the splitting introduced by Eq. (4.4) is that it reduces the three-dimensional square-root operator to an uncoupled sum of two-dimensional operators. As in the 2D case, the resulting three-dimensional parabolic equation derived in Eq. (4.5) is solved by approximating $\sqrt{1+\mathcal{Z}}$ and $\sqrt{1+\mathcal{Y}}$ using a Taylor (narrow-angle) or a rational Padé (wide-angle) expansion. After applying the Padé expansion to both square-root operators in Eq. (4.5), the 3D WAPE [192] is obtained,

$$\left\{\frac{\partial}{\partial x} - ik_0\left(\sum_{n=1}^{N}\frac{a_{n,N}\mathcal{Z}}{1+b_{n,N}\mathcal{Z}} + \sum_{j=1}^{M}\frac{a_{j,M}\mathcal{Y}}{1+b_{j,M}\mathcal{Y}}\right)\right\}\psi(\mathbf{x}) = 0, \tag{4.6}$$

where N and M are the orders associated with the Padé expansions in the altitude z and width y respectively. The Padé coefficients a_j, b_j are given by

$$a_{j,M} = \frac{2}{2M+1}\sin^2\left(\frac{j\pi}{2M+1}\right), \tag{4.7a}$$

$$b_{j,M} = \cos^2\left(\frac{j\pi}{2M+1}\right). \tag{4.7b}$$

It is possible to obtain the cylindrical version of the 3DPE given in Eq. (4.6) by replacing the variable x by r, and the $\mathcal{Y}$ by $1/(k_0 r)^2 \times \partial_\theta$, where θ is the azimuth.

4.1.2 Propagation angle and accuracy

Next, the accuracy of the three-dimensional wide-angle PE given by Eq. (4.6) is investigated and the error as a function of the propagation angle is estimated. Following Jensen et al. [100], it is possible to estimate this error by comparing the phase difference between the plane wave solution of Eq. (4.6) and the plane wave

solution of the full parabolic equation given by Eq. (4.2). Let ψ and ψ' be the respective plane wave solutions of Eq. (4.2) and Eq. (4.6), which can be defined by

$$\psi(\mathbf{x}) = \psi_0 e^{i\mathbf{k}\cdot\mathbf{x}}, \tag{4.8a}$$

$$\psi'(\mathbf{x}) = \psi_0 e^{i\mathbf{k}'\cdot\mathbf{x}}, \tag{4.8b}$$

where $\mathbf{k}$ and $\mathbf{k}'$ are the wave vectors associated with ψ and ψ' respectively, and $\mathbf{x}$ the receiver location. Denoting φ the elevation angle and θ the azimuth, the wave-vector $\mathbf{k}$ can be defined by

$$\mathbf{k} = \begin{bmatrix} k_x \\ k_y \\ k_z \end{bmatrix} = k_0 \times \begin{bmatrix} \cos\varphi\cos\theta \\ \cos\varphi\sin\theta \\ \sin\varphi \end{bmatrix}, \tag{4.9}$$

where $k_0 = \omega/c_0$. However, the form of $\mathbf{k}'$ is not known and must be derived in order to compute the phase error ϵ_p. Assuming $\mathbf{k}' = (k'_x, k_y, k_z)$, *i.e.* that the y and z-components of the approximate wave vector remain unchanged after the Padé expansion [177, 100], it is possible to express the unknown x-component k'_x using Eq. (4.6). Substituting the wave field ψ' given by Eq. (4.8b) in Eq. (4.6), the following dispersion relation can be established

$$\frac{k'_x}{k_0} = -\sum_{n=1}^{N} \frac{a_n k_z^2}{k_0^2 - b_n k_z} - \sum_{j=1}^{M} \frac{a_j k_y^2}{k_0^2 - b_j k_y^2}. \tag{4.10}$$

From Eqs. (4.8a) and (4.8b), and using the definition of $\mathbf{k}$ in Eq. (4.9), it follows that the phase error between ψ and ψ' can be expressed as $\epsilon_p = 2\pi n \epsilon_d$, where ϵ_d is the dispersion error, given by

$$\epsilon_d = \frac{|k'_x - k_x|}{k_0}, \tag{4.11}$$

and $n = x/\lambda_0$ is the number of wavelengths travelled in range. Unlike the phase error (ϵ_p) which depends on the range, the dispersion error ϵ_d characterizes the accuracy of the 3DPE as a function of the propagation angle. Inserting the expression

of k'_x derived in Eq. (4.10) into Eq. (4.11), the dispersion error becomes,

$$\boxed{\epsilon_d = \left| \cos^2\varphi \cos^2\theta + \sum_{n=1}^{N} \frac{a_n \sin^2\varphi}{1 - b_n \sin^2\varphi} + \sum_{j=1}^{M} \frac{a_j \cos^2\varphi \sin^2\theta}{1 - b_j \cos^2\varphi \sin^2\theta^2} \right|.} \tag{4.12}$$

The value of the dispersion error ϵ_d as a function of the azimuth and elevation angles for different orders of the paraxial approximation in Eq. (4.10) is given in Fig. 4.1. It is readily noticeable that the splitting in Eq. (4.4), which neglects the coupled term, induces a narrow-angle limitation in the $\varphi = \theta$ direction regardless of the order. The uncoupling of the operators $\mathcal{Z}$ and $\mathcal{Y}$ implies that the accuracy of the 3DPE in Eq. (4.5) in the directions y and z is solely dependent on the expansion order of $\sqrt{1+\mathcal{Y}}$ and $\sqrt{1+\mathcal{Y}}$ respectively. Therefore, the maximum elevation φ_p for $\theta = 0$ is the same as in the 2D case for the given order N. Similarly, the maximum azimuth θ_p for $\varphi = 0$ is governed by the expansion order M.

In the derivation performed above, it was assumed that the propagating modes $\mathbf{k}$ satisfies the dispersion relation of Eq. (4.2), which is defined by

$$\frac{k_x}{k_0} = \sqrt{1 - \frac{k_z^2}{k_0^2} - \frac{k_y^2}{k_0^2}}. \tag{4.13}$$

The x-component k_x of the wavenumber $\mathbf{k}$ becomes complex when $k_z^2 + k_y^2 > k_0^2$, which corresponds to evanescent modes. Since the Padé expansion given in Eq. (4.10) is real, the approximated component k'_x will fail to account for the imaginary part of the dispersion relation in Eq. (4.13). To improve the approximation, complex-valued Padé coefficients can be used [228, 137], they are obtained by a rotation of a_n, b_n given in Eq. (4.7b) in the complex plane. The new complex coefficients $\hat{a}_n$, $\hat{b}_n$ are given by

$$\hat{a}_{j,M} = \frac{a_{j,M} e^{-i\beta/2}}{(1 + b_{j,M}(e^{-i\beta} - 1))^2}, \tag{4.14a}$$

$$\hat{b}_{j,M} = \frac{b_{j,M} e^{-i\beta}}{1 + b_{j,M}(e^{-i\beta} - 1)}, \tag{4.14b}$$

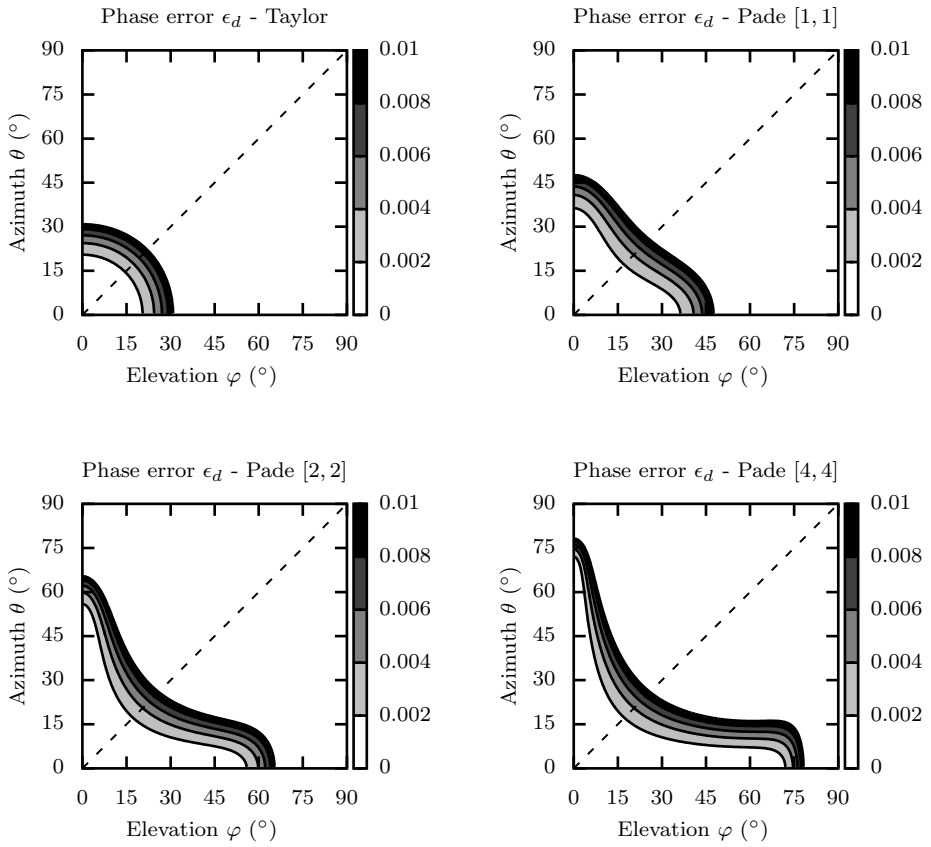

Figure 4.1: Angular mapping of the normalized dispersion error ϵ_d as a function of (φ, θ) for the Taylor, Padé $[1,1]$, Padé $[2,2]$ and Padé $[4,4]$ expansion of the rational square-root operator $\mathcal{L}$.

where β is the rotation angle. The complex Padé coefficients in Eq. (4.14b) are simply used in Eq. (4.10) instead of the original coefficients a_n, b_n. Doc et al. [67] have used complex Padé coefficients in conjunction with a coordinate transform for modeling propagation in a two-dimensional waveguide with varying cross-section, and determined that an optimal choice of β depends on the order of the Padé expansion. Extending this observation to three-dimensional propagation is straightforward if we use the operator splitting in Eq. (4.4) and apply the rotation in Eq. (4.14b) to each operator. Hence, following Doc et al. [67], an appropriate choice for β is 0.13 for $N, M = 1$, 0.55 for $N, M = 2$ and 1.0 for $N, M = 4$.

4.1.3 Tridimensional Beilis-Tappert map

In the following section, a Beilis-Tappert mapping will be applied to the three-dimensional PE derived in Eq. (4.5). The physical domain $\mathcal{P}$, described by the terrain-following coordinates (x, y, z), is transformed into a rectangular numerical domain $\mathcal{D}$, described by a set of new coordinates (ξ, ν, η). For a three-dimensional terrain surface defined by the $z = h(x, y)$, the three-dimensional equivalence of the Beilis-Tappert coordinate transformation given by Eq. (3.38) is simply

$$\mathcal{M} : \begin{cases} \xi = x, \\ \nu = y, \\ \eta = z - h(x, y), \end{cases} \tag{4.15}$$

where h is a real bivariate function of class $\mathcal{C}^2(\mathbb{R}^2)$. The transformation is symbolically defined as $\mathcal{M} : \mathbf{x} \longrightarrow \xi$, so we can write $\mathcal{M}(\mathcal{P}) = \mathcal{D}$. It is worth noting that the terrain profile h can be expressed in either coordinate systems. To proceed, the spatial derivatives in the physical coordinate system $\mathbf{x} = (x_i) = (x, y, z)$ are replaced using the chain rule,

$$\frac{\partial}{\partial x_i} = \sum_k \frac{\partial \xi_k}{\partial x_i} \frac{\partial}{\partial \xi_k}, \tag{4.16a}$$

$$\frac{\partial^2}{\partial x_i \partial x_j} = \sum_k \frac{\partial^2 \xi_k}{\partial x_i \partial x_j} \frac{\partial}{\partial \xi_k} + \sum_k \sum_n \frac{\partial \xi_k}{\partial x_i} \frac{\partial \xi_n}{\partial x_j} \frac{\partial^2}{\partial x_k \partial x_n}, \tag{4.16b}$$

where $\xi_1 = \xi$, $\xi_2 = \nu$ and $\xi_3 = \eta$. As in the 2D case, the Beilis-Tappert approach consists of applying the coordinate transformation, Eq. (4.15), to the parabolic equation defined in Eq. (4.2). This derivation can be equivalently carried out by applying Eq. (4.15) to the three-dimensional Helmholtz equation, given by Eq. (4.1), before making a paraxial approximation in the transformed coordinate system. First, the complex pressure p_c is written as,

$$p_c(\mathbf{x}) = A(X, \mathbf{x}_\perp) e^{ik_0 x}, \tag{4.17}$$

where A is the complex pressure envelope that depends on the slow variable $X = \epsilon x$, with $\epsilon \ll 1$, and $\mathbf{x}_\perp = (y, z)$. This formulation can be related to the perturbation theory, where ϵ is the perturbation parameter and will allow us to physically interpret the terms in the parabolic equation. After using Eq. (4.17) in Eq. (4.1) the second-order derivative in x is changed and the following equation is obtained

$$\left\{\epsilon^2 \frac{\partial^2}{\partial x^2} + 2ik_0\epsilon \frac{\partial}{\partial x} + \Delta_\perp + k^2(z) - k_0^2\right\} A = 0. \tag{4.18}$$

Then, the chain rules given by Eqs. (4.16) are used to express the spatial derivatives in Eq. (4.18) and obtain an equation for the complex pressure envelope A in the new coordinate system. After grouping the terms in terms of the perturbation factor ϵ, Eq. (4.18) becomes

$$\begin{aligned}\Bigg\{\epsilon^2 \Bigg(\frac{\partial^2}{\partial \xi^2} - 2\frac{\partial h}{\partial \xi}\frac{\partial^2}{\partial \xi \partial \eta} - \frac{\partial^2 h}{\partial \xi^2}\frac{\partial}{\partial \eta} + \left(\frac{\partial h}{\partial \eta}\right)^2 \frac{\partial^2}{\partial \eta^2} \Bigg) \\ + 2ik_0\epsilon \left(\frac{\partial}{\partial \xi} - \frac{\partial h}{\partial \xi}\frac{\partial}{\partial \eta} \right) + \Delta_\perp^* + k^2(z) - k_0^2 \Bigg\} A = 0,\end{aligned} \tag{4.19}$$

where $\Delta_\perp^*$ is the Laplacian expressed in the transformed coordinate system (ξ, ν, η). From inspecting Eq. (4.19), it appears that the coordinate transformation in Eq. (4.15) has introduced a number of additional terms. The narrow-angle approximation in 3D involves neglecting the terms factored by ϵ^2, which correspond to second-order fluctuations along the range x. Hence, the narrow-angle approximation retains first-order terms only, which is achieved by introducing the envelope ψ defined ad $A(X, \mathbf{x}_\perp) \equiv \psi(\mathbf{x}) + \mathcal{O}(\epsilon^2)$. As a result, Eq. (4.17) becomes

$$\left\{2ik_0 \left(\frac{\partial}{\partial \xi} - \frac{\partial h}{\partial \xi}\frac{\partial}{\partial \eta} \right) + \Delta_\perp^* + k^2(z) - k_0^2 \right\} \psi = 0, \tag{4.20}$$

where the transformed Laplacian $\Delta_\perp^*$ is given by

$$\Delta_\perp^* = \rho \frac{\partial}{\partial \eta}\left(\frac{1}{\rho}\frac{\partial}{\partial \eta}\right) + \left(\frac{\partial h}{\partial \nu}\right)^2 \frac{\partial^2}{\partial \eta^2} + \frac{\partial^2}{\partial \nu^2} - \frac{\partial^2 h}{\partial \nu^2}\frac{\partial}{\partial \eta} - 2\frac{\partial h}{\partial \nu}\frac{\partial^2 \psi}{\partial \eta \partial \nu}. \tag{4.21}$$

One of the difficulties arising from the three-dimensional extension of the Beilis-

Tappert map is that the transversal direction is not paraxial, i.e. the pressure field ψ varies quickly with ν. This has introduced three new low-order terms in the expression of $\Delta_\perp^*$ in Eq. (4.21), including a mixed derivative term $\partial^2/\partial\eta\partial\nu$, which will have great implications when deriving a numerical solution. While it is possible to derive numerical schemes that take into account mixed derivatives in parabolic equation [133], a first approach is to simplify the transversal operator in Eq. (4.21) by assuming that propagation along each transversal direction is uncoupled and we ignore the mixed derivative, i.e.

$$\left|\frac{\partial h}{\partial \nu}\frac{\partial^2 \psi}{\partial \eta \partial \nu}\right| \ll \left|2ik_0\frac{\partial \psi}{\partial \xi}\right|, \tag{4.22}$$

which holds as long as the transversal variation of the terrain is small. The assumption made in Eq. (4.22) does not hold for sharp transversal variations and high frequencies. Hence, an additional limitation on the validity of Eq. (4.20) have been introduced, in exchange of a more efficient numerical solution. In the new coordinate system (ξ, ν, η), the transformed differential operators $\mathcal{Z}^*$, $\mathcal{Y}^*$ are given by

$$\begin{aligned}\mathcal{Z}^* &= \mathcal{Z} + \frac{1}{k_0^2}\left(\left(\frac{\partial h}{\partial \nu}\right)^2\frac{\partial^2}{\partial \eta^2} - \left(\frac{\partial^2 h}{\partial \nu^2} + 2ik_0\frac{\partial h}{\partial \xi}\right)\frac{\partial}{\partial \eta}\right),\\ \mathcal{Y}^* &= \frac{1}{k_0^2}\frac{\partial^2}{\partial \nu^2},\end{aligned} \tag{4.23}$$

where $\mathcal{Z}$ and $\mathcal{Y}$ are given in Eq. (4.3). As a result, the first-order three-dimensional Beilis-Tappert PE given by Eq. (4.20) becomes

$$\boxed{\frac{\partial \psi}{\partial \xi} = \frac{ik_0}{2}(\mathcal{Z}^* + \mathcal{Y}^*)\psi.} \tag{4.24}$$

Similarly, Sturm [195] has developed a Finite-Element solution of the PE for the propagation of sound above an irregular rigid boundary using a similar transformation as the curvilinear Beilis-Tappert exposed here. Another approach that relies on a terrain-following curvilinear description of the atmospheric medium is the use of non-uniform grids, based on a Galerkin decomposition of the wave field [208]. In the present case, a simple finite difference discretization will be used for the derivatives

appearing in Eq. (4.24). An alternative derivation of Eq. (4.24) can be achieved by applying the Beilis-Tappert map in Eq. (4.15) to the generalized three-dimensional parabolic equation defined in Eq. (4.5), which leads to

$$\left\{\frac{\partial}{\partial\xi} - \frac{\partial h}{\partial\xi}\frac{\partial}{\partial\eta} + ik_0(2 - \sqrt{1+\mathcal{Z}^*} - \sqrt{1+\mathcal{Y}^*})\right\}\psi(\mathbf{x}) = 0, \tag{4.25}$$

where $\mathcal{Y}^*$ and $\mathcal{Z}^*$ are now simply given by

$$\mathcal{Z}^* = \mathcal{Z} + \frac{1}{k_0^2}\left(\left(\frac{\partial h}{\partial\nu}\right)^2\frac{\partial^2}{\partial\eta^2} - \frac{\partial^2 h}{\partial\nu^2}\frac{\partial}{\partial\eta}\right), \tag{4.26a}$$

$$\mathcal{Y}^* = \mathcal{Y}. \tag{4.26b}$$

After inspecting Eq. (4.25), it appears that applying the coordinate transformation to the parabolic equation instead of the Helmholtz equation has removed the elliptic term $\partial^2/\partial\xi\partial\eta$ present in Eq. (4.19). Neglecting elliptic terms, *i.e* that are second order in the propagation direction ξ, means that the pressure envelope ψ is slowly varying. This approach is consistent with the derivation of the two-dimensional Beilis-Tappert PE made by Parakkal et al. [152], as explained in Sec. 3.2.3. The Padé expansion can be used on both square-root operators in Eq. (4.25), leading to

$$\boxed{\left\{\frac{\partial}{\partial\xi} - \frac{\partial h}{\partial\xi}\frac{\partial}{\partial\eta} - ik_0\left(\sum_n^N \frac{a_{n,M}\mathcal{Z}^*}{1+b_{n,N}\mathcal{Z}^*} + \sum_l^M \frac{a_{j,M}\mathcal{Y}^*}{1+b_{j,M}\mathcal{Y}^*}\right)\right\}\psi(\mathbf{x}) = 0,} \tag{4.27}$$

where N and M are the Padé expansion orders in the directions z and y, respectively, and the Padé coefficients $a_{j,M}$, $b_{j,M}$ are given in Eq. (4.7b). Equation (4.27) is expressed in the transformed domain $\mathcal{M}(\mathcal{P}) = \mathcal{D}$, which is a three-dimensional rectangular waveguide of dimensions $\eta_{\max} = z_{\max} - h(x_s, y_s)$, $\nu_{\max} = y_{\max}$ and $\xi_{\max} = x_{\max}$, with a flattened bottom boundary located at $\eta = 0$. After coordinate transformation, the coefficients of Eq. (4.27) become locally dependent on the spatial derivatives of the terrain profile h.

4.1.4 Tridimensional impedance boundary conditions

In this section, the three-dimensional Impedance Boundary Condition (IBC) at the ground surface is derived in the transformed coordinate system (ξ, ν, η). The early 3DPE models made use of a simplified staircase approximation of the ground boundary [116, 118]. As a result, the associated boundary condition is flat everywhere and out-of-plane scattering is not accounted for properly. Rewriting the 3DPE in a shifted coordinate system where the bottom boundary is flat considerably simplifies the inclusion and specification of the boundary condition in the numerical scheme. As reported in Eq. (3.31c), the Impedance Boundary condition (IBC) governing the complex pressure p_c at the ground boundary is given by

$$\frac{\partial p_c}{\partial \mathbf{n}} = ik_0 Y_g p_c, \tag{4.28}$$

where $Y_g = 1/Z_g$ is the ground surface admittance and $\partial/\partial\mathbf{n} = \nabla \cdot \mathbf{n}$ is the directional derivative taken along the normal vector $\mathbf{n}$. At the ground boundary, defined by the two-dimensional surface $\partial\mathcal{P} : \{\mathcal{S}(x, y, z) = h(x, y) - z = 0\}$, the unit normal vector is given by

$$\mathbf{n} = \frac{\nabla\mathcal{S}}{||\nabla\mathcal{S}||} = \frac{1}{||\nabla\mathcal{S}||} \begin{bmatrix} \tan\theta_x \\ \tan\theta_y \\ -1 \end{bmatrix}, \tag{4.29}$$

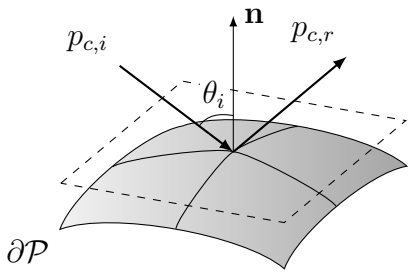

Figure 4.2: Three-dimensional reflection of an incident wave by a non-flat surface

where $\mathcal{S}$ is the equation of the ground surface, θ_x is the terrain slope along x and θ_y is the transversal terrain slope along y, i.e. $\tan\theta_x = \partial h/\partial x$ and $\tan\theta_y = \partial h/\partial y$. So, inserting Eq. (4.29) into Eq. (4.28) leads to

$$\tan\theta_x \left(\frac{\partial p_c}{\partial x}\right) + \tan\theta_y \left(\frac{\partial p_c}{\partial y}\right) - \left(\frac{\partial p_c}{\partial z}\right) = ik_0 Y_g ||\nabla\mathcal{S}|| p_c. \tag{4.30}$$

Next, the relation $p_c = e^{ik_0 x}\psi$ can be used, resulting in the following three-dimensional IBC for the complex pressure envelope ψ,

$$\tan\theta_x \left(\frac{\partial \psi}{\partial x}\right) + \tan\theta_y \left(\frac{\partial \psi}{\partial y}\right) - \left(\frac{\partial \psi}{\partial z}\right) = ik_0 \left(\frac{||\nabla\mathcal{S}||}{Z_g} - \tan\theta_x\right)\psi. \tag{4.31}$$

This equation cannot be used into the 3DPE in its current form and needs to be expressed in the curvilinear coordinate system. Equation (4.31) is first simplified by naming the coefficient of ψ on the right-hand side as $ik_0 Y_g'$. At the ground level, *i.e.* at $\eta = 0$, we have $k = k_0$ and the density is $\rho = \rho_0$ so the impedance boundary condition in the shifted coordinate system (ξ, ν, η) is

$$\tan\theta_x \left(\frac{\partial \psi}{\partial \xi}\right) + \tan\theta_y \left(\frac{\partial \psi}{\partial \nu}\right) - (\tan^2\theta_x + \tan^2\theta_y - 1)\left(\frac{\partial \psi}{\partial \eta}\right) = ik_0 Y_g' \psi, \tag{4.32}$$

which is valid at the interface $\eta = 0$. Equation (4.32) includes derivatives with respect to ξ and ν that were not present in the case of a flat boundary, which makes the boundary condition more difficult to implement in the numerical scheme. This is due to the non-orthogonality of the coordinate transform (the grid is not normal to the bottom boundary). In Parakkal et al. [153], the use of a polar conformal mapping allows for an equivalent impedance boundary condition which has a form $\partial\psi/\partial\eta = ik_0 Y_g + \chi/2$, where χ is the local curvature of the ground surface. Following Abrahamsson and Kreiss [4], the IBC given by Eq. (4.32) is "parabolized" in order to avoid numerical reflections that arise from the range derivative. Using the narrow-angle 3D BTPE defined in Eq. (4.24) to express the first-order derivative along ξ, the IBC in Eq. (4.32) becomes

$$I_2 \left(\frac{\partial^2 \psi}{\partial \eta^2}\right)_{\eta=0} + I_1 \left(\frac{\partial \psi}{\partial \eta}\right)_{\eta=0} + J_2 \left(\frac{\partial^2 \psi}{\partial \nu^2}\right)_{\eta=0} + J_1 \left(\frac{\partial \psi}{\partial \nu}\right)_{\eta=0} + I_0(\psi)_{\eta=0} = 0, \tag{4.33}$$

where the coefficients I_2, I_1, I_0, J_2 and J_1 are expressed as

$$I_2 = a_0' \frac{\partial h}{\partial \xi}\left(1 + \left(\frac{\partial h}{\partial \nu}\right)^2\right), \tag{4.34a}$$

$$I_1 = -\left(a_0' \frac{\partial h}{\partial \xi}\frac{\partial h^2}{\partial \nu^2} + \left(\frac{\partial h}{\partial \nu}\right)^2 - 1\right), \tag{4.34b}$$

$$I_0 = ik_0 Y_g', \tag{4.34c}$$

$$J_2 = a_0' \frac{\partial h}{\partial \xi}, \tag{4.34d}$$

$$J_1 = \frac{\partial h}{\partial \nu}, \tag{4.34e}$$

with $a_0' = i/2k_0$. If the boundary is assumed to be locally flat (staircase approximation), all these coefficients become null, with the exception of $I_1 = 1$ and I_0 remaining unchanged. Furthermore, $Y_g' = Y_g = 1/Z_g$ and we retrieve the flat boundary condition, as

$$\boxed{\left(\frac{\partial \psi}{\partial \eta}\right)_{\eta=0} = ik_0 Y_g(\psi)_{\eta=0}.} \tag{4.35}$$

The boundary condition given by Eq. (4.35) will be used to evaluate the pressure field ψ at $\eta = 0$ in the new coordinate system. Next, the reflection coefficient for a three-dimensional boundary is derived. Following the formulation developed by Salomons [177] in 2D, we derive a three-dimensional reflection coefficient for the boundary $\partial\mathcal{P}$. At a given interface point $\mathbf{x}_g = (x_g, y_g, h(x_g, y_g))$ on the ground boundary, the pressure and velocity continuity conditions $p_c(\mathbf{x}_g^+) = p_c(\mathbf{x}_g^-)$ and $\mathbf{v}_c(\mathbf{x}_g^+) = \mathbf{v}_c(\mathbf{x}_g^-)$ lead to the following condition at the boundary point $\mathbf{x}_g$,

$$\left(\frac{p_c}{\mathbf{v}_c \cdot \mathbf{n}}\right)_{\mathbf{x}_g^+} = \left(\frac{p_c}{\mathbf{v}_c \cdot \mathbf{n}}\right)_{\mathbf{x}_g^-}, \tag{4.36}$$

where $\mathbf{x}_g^-$ and $\mathbf{x}_g^+$ are the lower and upper vicinities of $\mathbf{x}_g$, $\mathbf{n}$ is the normal to the surface, defined by Eq. (4.29). The right-hand side is evaluated below the bottom

boundary, so it can be replaced by the ground characteristic impedance $Z_g\rho_0 c_0$. From fundamental linear acoustics equations, we can write $v_c = \nabla p_c / i\omega\rho_0$. Above the ground surface, the total pressure is the sum of incident and reflected waves, i.e. $p_c = p_{c,i} + p_{c,r}$, so the condition in Eq. (4.36) becomes

$$p_{c,i} + p_{c,r} = \frac{Z_g c_0}{i\omega}(\nabla p_{c,i} + \nabla p_{c,r}) \cdot \mathbf{n}. \tag{4.37}$$

If the incident wave is a plane wave defined by a wave-vector $\mathbf{k}_i$, the reflected wave direction is governed by the reflected wave-vector $\mathbf{k}_r = 2\mathbf{n}(\mathbf{k}_i \cdot \mathbf{n}) - \mathbf{k}_i$. Hence, the pressure gradients are defined as $\nabla p_{c,i} = i\mathbf{k}_i p_{c,i}$ and $\nabla p_{c,r} = i\mathbf{k}_r p_{c,r}$. Furthermore, the wave-vetcor norm $||\mathbf{k}_i|| = ||\mathbf{k}_r||$ is the wavenumber $k_0 = \omega/c_0$. We also notice that $\mathbf{k}_i \cdot \mathbf{n} = -\mathbf{k}_r \cdot \mathbf{n}$, so Eq. (4.37) becomes,

$$\left(1 + Z_g \frac{\mathbf{k} \cdot \mathbf{n}}{k_0}\right) p_{c,r} = -\left(1 - Z_g \frac{\mathbf{k} \cdot \mathbf{n}}{k_0}\right) p_{c,i}. \tag{4.38}$$

The amplitude of the reflected wave $p_{c,r}$ is factored by the 3D plane wave reflection coefficient R_p, i.e. $||p_{c,r}|| = R_p||p_{c,i}||$. The three-dimensional reflection coefficient R_p is evaluated by assuming that the incident and reflected pressure fields are plane waves in the vicinity of the ground surface, i.e.

$$p_{c,i}(\mathbf{x}_g) = p_{c,0} e^{i\mathbf{k_i}\cdot\mathbf{x}_g}, \tag{4.39a}$$

$$p_{c,r}(\mathbf{x}_g) = R_p p_{c,0} e^{i\mathbf{k_r}\cdot\mathbf{x}_g}, \tag{4.39b}$$

where $p_{c,0}$ is the complex pressure amplitude of the incident wave and the point $\mathbf{x}_g$ is a point at the ground boundary. Inserting the values of $p_{c,i}$ and $p_{c,r}$. given by Eq. (4.39a) and Eq. (4.39b), respectively, into the three-dimensional IBC, derived in Eq. (4.38), leads to

$$\left(1 + Z_g \frac{\mathbf{k}_i \cdot \mathbf{n}}{k_0}\right) R_p e^{i\mathbf{k}_r\cdot\mathbf{x}_g} = -\left(1 - Z_g \frac{\mathbf{k}_i \cdot \mathbf{n}}{k_0}\right) e^{i\mathbf{k}_i\cdot\mathbf{x}_g}. \tag{4.40}$$

Furthermore, we have $\mathbf{k}_r \cdot \mathbf{x}_g = \mathbf{k}_i \cdot \mathbf{n} - 2(\mathbf{k}_i \cdot \mathbf{n})(\mathbf{n} \cdot \mathbf{x}_g)$ from the definition of k_r given

earlier. This condition holds regardless of the choice of the origin of the coordinate system, so it is valid for any arbitrary value of the point $\mathbf{x}_g$. Therefore, the quantity $\mathbf{x}_g \cdot \mathbf{n}$ can be taken as 0, and the three-dimensional reflection coefficient R_p can be written as

$$\boxed{R_p = \frac{Z_g(\mathbf{k}_i \cdot \mathbf{n}) - k_0}{Z_g(\mathbf{k}_i \cdot \mathbf{n}) + k_0}.} \tag{4.41}$$

If the surface is flat, then we have $\mathbf{n} = (0, 0, 1)^T$ and $\mathbf{k}_i \cdot \mathbf{n} = k_0 \sin\varphi$, which reduces to the 2D plane wave reflection coefficient defined by Salomons [177], and is also provided in Eq. (2.50). The locally reacting assumption says that most of the reflection occurs normal to the surface, i.e. for $\mathbf{k}_i = k_0\mathbf{n}$, giving us a reflection coefficient $R_p = (Z_g - 1)/(Z_g + 1)$, which is exactly the same as the locally reacting reflection coefficient in 2D. Hence, the impedance boundary condition is handled similarly as in the 2D case without further treatment.

4.2 Iterative algorithms for 3D

Numerical solutions of tridimensional problems are significantly more challenging to derive and implement than for simpler 2D models. Indeed, the 3DPE has two normal components (ν and η) to the marching direction. Along the transversal direction ν, the field is discretized into N_y points $\nu_1, \cdots, \nu_{N_y}$, in such a way that the discretized 3D waveguide consists of a succession of planes $\mathbf{\Psi}^m = (\psi^m_{n,j})_{n,j}$, as shown in Fig. 4.3. Hence, the marching scheme can be derived for $\mathcal{V}^m = \mathrm{vec}(\mathbf{\Psi}^m)$ which is a vector of size $(N_y \times N_z)$ obtained by stacking columns of $\mathbf{\Psi}^m$, *i.e.*

$$\mathcal{V}^m = (\psi^m_{1,1}, \ldots, \psi^m_{N_z,1}, \ldots, \psi^m_{1,j}, \ldots, \psi^m_{N_z,j}, \ldots, \psi^m_{N_z,N_y})^T.$$

Therefore, a direct finite-difference solution require the inversion of a sparse system of a size $N_{3\mathrm{D}} = N_z \times N_y$, leading to prohibitive scales very rapidly. As an example, a small scale simulation for $f = 10$ Hz in a waveguide of section 10×10 km^2 and

a step $\delta = \lambda_0/10 = 34.3$ m gives $N_{3D} = 291^2 = 84681$. While parallel computing may now overcome this limitation, it is very system-dependent and greatly impacts implementation. Therefore, the 3DPE is usually solved using tailored iterative solutions that take advantage of the matrix structure and can be easily replicated. In this section, Fixed point and Alternate Direction Implicit (ADI) numerical solutions will be presented and applied to the three-dimensional Beilis-Tappert PE.

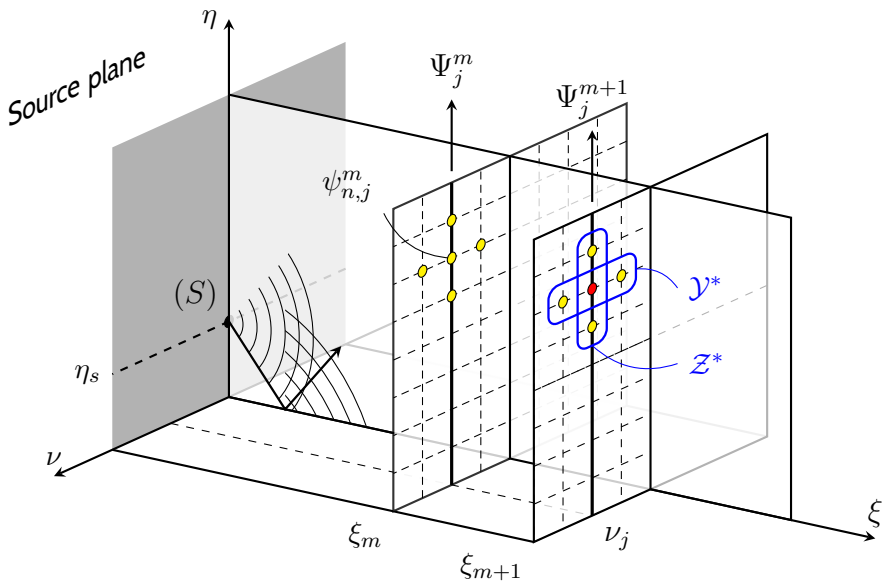

Figure 4.3: Discretization of a three dimensional Cartesian waveguide and the five-point Finite-Difference stencil (yellow dots).

In the following subsections, two implicit finite-difference schemes will be derived to solve the narrow-angle 3D BTPE, given by Eq. (4.24), and the wide-angle 3D BTPE, given by Eq. (4.27). Other numerical considerations, such as the initial and boundary conditions, which are common to both the narrow and wide-angle solutions, are also presented and discussed. The section is structured in the following way,

- In Sec. 4.2.1, the narrow-angle 3D BTPE derived in Eq. (4.24) is solved using

an iterative gradient scheme [232, 187], which seeks the solution at ξ_{m+1} by a recursive refinement of the solution at ξ_m. The advantage of this method is that it can generate an arbitrarily accurate solution, as long as the stability condition is met. This method enables to greatly limit memory requirements but may require longer computation times to converge.

- In Sec. 4.2.2, The wide-angle 3D BTPE derived in Eq. (4.27) is solved using a Split-Step Padé numerical scheme [192, 131], which is based on an Alternate Direction Implicit (ADI) formulation. In this approach, each transversal direction is treated independently. The main difference between the current approach and the original 3D Split-Step Padé is that it requires an additional step to integrate the term $\mathcal{W}^*$, which arises from the Beilis-Tappert transform in Eq. (4.15).

- In Sec. 4.2.3, the finite-difference matrices are assembled for first and second-order spatial derivatives in the transversal plane $\boldsymbol{\xi}_\perp = (\nu, \eta)$. The boundary conditions at the limit of the domain $\mathcal{D}$ are discretized and included in the appropriate locations of the finite-difference matrices. The domain is truncated by introducing an absorbing boundary layer around the propagation domain.

- In Sec. 4.2.4, a three-dimensional gaussian starting field is proposed, as an approximation of a spherical monopole source in free space.

4.2.1 Fixed-point method

The narrow-angle tridimensional Beilis-Tappert PE derived in Eq. (4.24) will be solved in a similar way as the one developed by Zelley [232], who proposed a marching scheme that relies on a fixed-point method. The idea behind the following derivation is to take advantage of the fixed-point method while, simplifying the boundary conditions thanks to the Beilis-Tappert coordinate transform given by Eq. (4.15). Integrating Eq. (4.24) between ξ and $\xi + \Delta\xi$, we obtain

$$\psi(\xi+\Delta\xi)=\exp\left\{\frac{ik_0}{2}\left(\mathcal{Z}^*+\mathcal{Y}^*\right)ds\right\}\psi(\xi), \tag{4.42}$$

which is valid for a small marching step $\Delta\xi$. Next, the Crank-Nicolson method is applied to Eq. (4.42), which leads to

$$\exp\left\{-\frac{ik_0\Delta\xi}{4}\left(\mathcal{Z}^*+\mathcal{Y}^*\right)\right\}\psi(\xi+\Delta\xi)=\exp\left\{\frac{ik_0\Delta\xi}{4}\left(\mathcal{Z}^*+\mathcal{Y}^*\right)\right\}\psi(\xi). \tag{4.43}$$

The exponential operators in Eq. (4.43) are then approximated using a first-order Taylor approximation, which yields the following the marching scheme

$$\left\{1+\mu_0^-\left(\mathcal{Z}^*+\mathcal{Y}^*\right)\right\}\psi(\xi+\Delta\xi)=\left\{1+\mu_0^+\left(\mathcal{Z}^*+\mathcal{Y}^*\right)\right\}\psi(\xi), \tag{4.44}$$

where $\mu_0^\pm=\pm ik_0\Delta\xi/4$. The operators $\mathcal{Z}^*$ and $\mathcal{Y}^*$ in Eq. (4.44) are expressed using the definitions given by Eq. (4.23). The fully discretized form of Eq. (4.44) is obtained by evaluating at a grid point (ν_j,η_n), leading to

$$\sum_{l=0}^{2}A_{l,j}^-\left(\frac{\partial^l\psi}{\partial\eta^l}\right)_{n,j}^{m+1}+B_{2,j}^-\left(\frac{\partial^2\psi}{\partial\nu^2}\right)_{n,j}^{m+1}=\sum_{l=0}^{2}A_{l,j}^+\left(\frac{\partial^l\psi}{\partial\eta^l}\right)_{n,j}^{m}+B_{2,j}^+\left(\frac{\partial^2\psi}{\partial\nu^2}\right)_{n,j}^{m}. \tag{4.45}$$

The spatially varying matrix $\mathbf{A}_0^\pm$ and the coefficients $A_2^\pm$, $A_1^\pm$, $B_2^\pm$ in Eq. (4.45) are defined by

$$A_{2,j}^\pm=\frac{\mu_0^\pm}{k_0^2}\left(\left(\frac{\partial h}{\partial\nu}\right)_{m,j}^2+1\right), \tag{4.46a}$$

$$A_{1,j}^\pm=-\frac{\mu_0^\pm}{k_0^2}\left(\frac{\partial^2 h}{\partial\nu^2}\right)_{m,j}+\frac{2i\mu_0^\pm}{k_0}\left(\frac{\partial h}{\partial\xi}\right)_{m,j}, \tag{4.46b}$$

$$\mathbf{A}_0^\pm=\mathbf{I}_{N_z}+\frac{\mu_0^\pm}{k_0^2}\mathbf{diag}_n\left(k_n^2-k_0^2\right), \tag{4.46c}$$

and

$$B_{2,j}^\pm=\frac{\mu_0^\pm}{k_0^2}. \tag{4.47}$$

Once written in a matrix form, the spatial derivatives can be replaced by finite-difference matrices and Eq. (4.45) can be written for the unknown $\mathbf{\Psi}^{m+1} = (\Psi_{n,j}^{m+1})$ of size $N_z \times N_y$. Inspecting Eqs. (4.46) and (4.47), one can infer that the coefficients of Eq. (4.45) depend on the transversal location j. As a result, we rather write a set of N_y equations, one for each column Ψ_j^{m+1} of the solution $\mathbf{\Psi}^{m+1}$, i.e.

$$\mathbf{M}_j^- \Psi_j^{m+1} + (\mathbf{\Psi}^{m+1}\mathbf{P}^-)_j = \mathbf{M}_j^+ \Psi_j^m + (\mathbf{\Psi}^m \mathbf{P}^+)_j, \qquad \forall j \in [1, N_y]. \tag{4.48}$$

which is a matrix equation of Sylvester-type (i.e. of the form $AX + XB = C$ for an unknown matrix X) [232, 187], where we have introduced the matrices

$$\mathbf{M}_j^{\pm} = A_{2,j}^{\pm}\mathbf{D}_{2,\eta} + A_{1,j}^{\pm}\mathbf{D}_{1,\eta} + \mathbf{A}_0^{\pm}, \tag{4.49a}$$

$$\mathbf{P}^{\pm} = B_2^{\pm}\mathbf{D}_{2,\nu}, \tag{4.49b}$$

in which $\mathbf{D}_{1,2}$ are the finite-difference matrices of the first and second-order, respectively. The form of the finite-difference matrices $\mathbf{D}_{1,2}$ will be specified in a separate section (Sec. 4.2.3), where we also address the concurrent issue of the discretization of the Impedance Boundary Conditions (IBC) at boundary points. The matrices $\mathbf{M}_j^{\pm}$ are of the size $N_z \times N_z$ and the matrix $\mathbf{P}^{\pm}$ has a size $N_y \times N_y$. An extensive review of available solutions for this type of matrix systems is provided by Simoncini [187]. Among the most popular methods for solving Sylvester equations with large N_y and N_z are the iterative gradient schemes, which aim at estimating the solution Ψ_j^{m+1} as the fixed point of Eq. (4.48). The algorithm we develop here is based on the one used by Zelley [232] which also falls into this category of iterative solutions. The algorithm to solve Eq. (4.48) can be divided into four successive steps:

▶ **Step 1.** Starting from the solution $\mathbf{\Psi}_m$ at step m, the right-hand-side of Eq. (4.48) is computed for every j and stored into a matrix $\mathbf{C}^m = (C_1^m, \ldots, C_{N_\nu}^m)$. The LAPACK routine ZGMBV [9] is used to perform the matrix product $\mathbf{\Psi}^m\mathbf{P}^+$. Therefore,

$$C_j^m = \mathbf{M}_j^+ \Psi_j^m + (\mathbf{\Psi}^m \mathbf{P}^+)_j. \tag{4.50}$$

▶ **Step 2.** Beginning with the initial guess $\mathbf{\Psi}^{(0)} = \mathbf{\Psi}^m$, the solution is successively refined and we name $\mathbf{\Psi}^{(i)}$ the intermediate solution after i iterations. Using Eq. (4.48), the solution at iteration i is computed by passing one term to the right-hand-side, which is then stored in the vector R_j^m,

$$R_j^m = C_j^m - (\mathbf{\Psi}^{(i-1)}\mathbf{P}^-)_j. \tag{4.51}$$

▶ **Step 3.** The system in Eq. (4.48) is solved using the LAPACK routine ZGBTRS [9], which uses Thomas algorithm for tridiagonal matrices [169]. The column vector $\Psi_j^{(i)}$ of size $N_\eta \times 1$ is computed as,

$$\Psi_j^{(i)} = (\mathbf{M}_j^-)^{-1} \cdot R_j^m. \tag{4.52}$$

▶ **Step 4.** The intermediate field $\mathbf{\Psi}^{(i)}$ is obtained by grouping all the columns Ψ_j^m computed in Step 2. This method assumes the existence of a fixed-point $\mathbf{\Psi}^{(\infty)}$ towards which the iterative scheme converges as $i \longrightarrow \infty$. In practice, an error threshold of $e = 10^{-4}$ is introduced and the intermediate solution $\mathbf{\Psi}^{(i)}$ is considered acceptable whenever the condition $||\mathbf{\Psi}^{(i)} - \mathbf{\Psi}^{(i-1)}|| < e$ is met, so we retain the last computed intermediate field, i.e. $\mathbf{\Psi}^{m+1} = \mathbf{\Psi}^{(i)}$.

The existence of the fixed-point at every step depends on the stability of the method. Zelley [232] has proven that it is unconditionally stable for propagation over a flat surface but numerical experiment suggest that stability is preserved with the Beilis-Tappert transform. The advantage of this method over the simpler Alternate Direction Implicit scheme used in the Split-Step Padé approximation is the improved accuracy, since it does not assume independence between the two transversal directions.

The algorithm presented above is implemented in Modern FORTRAN (2003/2008) using the LAPACK Mathematical Library [9] on a sequential workstation. Since all the matrices involved are tridiagonal, it is possible to use a special sparse format and avoid storage of a large quantity of zeros. Tridiagonal matrices are a special case of the Banded Matrix format available in LAPACK, so we have used

the corresponding routines ZGBMV (matrix-vector product), ZGBTRF (LU factorization) and ZGBTRS (LU solution by back-substitution). This implementation is versatile, as higher-order finite-differences can be used with the same routines, only increasing the number of upper and lower diagonals in the Band Matrix format descriptors.

4.2.2 Alternate Direction Implicit (ADI) method

Alternate Direction Implicit (ADI) methods are very common and efficient numerical solutions of parabolic systems and have been used extensively to solve the three-dimensional PE. It relies on the decomposition of the governing equation into two distinct equations along ν and η respectively, in a such a way that each step of the Crank-Nicolson marching scheme can be divided into two stages. Several types of ADI schemes exist, including schemes that take into account mixed derivatives [57, 24, 133]. As shown by Castor and Sturm [43], the ADI used in conjunction with the Padé expansion for each square-root operator in Eq. (4.5) leads to a stable iterative solution. In this section, we use the ADI scheme to propose a split-step solution of Eq. (4.27). In an incremental form, the solution at the $(m+1)$-th plane is related to to the solution at the m-th plane by

$$\boldsymbol{\Psi}^{m+1} = \exp\left(\Delta\xi \frac{\partial}{\partial \xi}\right) \boldsymbol{\Psi}^{m}. \tag{4.53}$$

Then, we use Eq. (4.27) to replace the parabolic derivative in ξ in Eq. (4.53), which leads to the following semi-discrete marching scheme

$$\boldsymbol{\Psi}^{m+1} = \exp\left\{\Delta\xi \frac{\partial h}{\partial \xi}\frac{\partial}{\partial \eta} + ik_0\Delta\xi\left(\sum_q^N \frac{a_q \mathcal{Z}^*}{1+b_q\mathcal{Z}^*} + \sum_l^M \frac{a_l \mathcal{Y}^*}{1+b_l\mathcal{Y}^*}\right)\right\}\boldsymbol{\Psi}^{m}, \tag{4.54}$$

resulting in a scheme that is closely related to the well-known Split-Step Padé method [131, 192], but in Cartesian coordinates. Hence, splitting Eq. (4.54) into three factors, we obtain the following recursive scheme in semi-discrete form

$$\boldsymbol{\Psi}_1^m = \left\{ \prod_{q=1}^{N} \exp\left(ik_0 \Delta\xi \frac{a_q \mathcal{Z}^*}{1 + b_q \mathcal{Z}^*} \right) \right\} \boldsymbol{\Psi}^m, \tag{4.55a}$$

$$\boldsymbol{\Psi}_2^m = \left\{ \prod_{l=1}^{M} \exp\left(ik_0 \Delta\xi \frac{a_l \mathcal{Y}^*}{1 + b_l \mathcal{Y}^*} \right) \right\} \boldsymbol{\Psi}^m, \tag{4.55b}$$

$$\boldsymbol{\Psi}^{m+1} = \exp\left\{ \Delta\xi \mathcal{W}^* \right\} \boldsymbol{\Psi}_2^m, \tag{4.55c}$$

where $\mathcal{W}^* = (\partial h/\partial\xi) \cdot (\partial/\partial\eta)$ is an operator and $\boldsymbol{\Psi}_1^m$, $\boldsymbol{\Psi}_2^m$ are intermediate solution fields. Equations (4.55a), (4.55b) and (4.55c) can be written recursively, resulting in a set of $N + M + 1$ linear systems to solve. Again, the Crank-Nicolson scheme [191] is used to approximate each exponential operator in Eqs. (4.55a), (4.55b) and (4.55c), leading to

$$\left\{ 1 + \mu_q^- \mathcal{Z}^* \right\} \mathbf{U}_{q+1}^m = \left\{ 1 + \mu_q^+ \mathcal{Z}^* \right\} \mathbf{U}_q^m, \qquad q = 1, \ldots, N, \tag{4.56a}$$

$$\left\{ 1 + \lambda_l^- \mathcal{Y}^* \right\} \mathbf{V}_{l+1}^m = \left\{ 1 + \lambda_l^+ \mathcal{Y}^* \right\} \mathbf{V}_l^m, \qquad l = 1, \ldots, M, \tag{4.56b}$$

$$\left\{ 1 + \chi_0^- \mathcal{W}^* \right\} \boldsymbol{\Psi}^{m+1} = \left\{ 1 + \chi_0^+ \mathcal{W}^* \right\} \boldsymbol{\Psi}_2^m. \tag{4.56c}$$

where $\mu_q^\pm = b_q \pm ik_0 \Delta\xi a_q/2$, $\lambda_l^\pm = b_l \pm ik_0 \Delta\xi a_l/2$ and $\chi_0^\pm = \pm\Delta\xi/2$ are coefficients. The complex pressure fields $\mathbf{U}_q^m$ in Eq. (4.56a) and $\mathbf{V}_l^m$ in Eq. (4.56b) are matrices of size $N_z \times N_y$, which verify $\mathbf{U}_0^m = \boldsymbol{\Psi}^m$, $\mathbf{U}_N^m = \mathbf{V}_0^m = \boldsymbol{\Psi}_1^m$ and $\mathbf{V}_M^m = \boldsymbol{\Psi}_2^m$. As in Sec. 4.2.1, the operators $\mathcal{Z}^*$, $\mathcal{Y}^*$ and $\mathcal{W}^*$ are fully discretized using finite-differences and Eqs. (4.56a) to (4.56c) become, in matrix form and column-wise,

$$\mathbf{M}_{q,j}^- V_{q+1,j}^m = \mathbf{M}_{q,j}^+ V_{q,j}^m, \qquad q = 1, \ldots, N, \tag{4.57a}$$

$$U_{l+1}^m \mathbf{P}_{l,n}^- = U_l^m \mathbf{P}_{l,n}^+, \qquad l = 1, \ldots, M, \tag{4.57b}$$

$$\mathbf{Q}_j^- \Psi_j^{m+1} = \mathbf{Q}_j^+ U_{M,j}^m, \tag{4.57c}$$

where the vector $V_{q,j}^m$ is the j-th column of $\mathbf{V}_q^m$, and $U_{l,n}^m$ is the n-th row of $\mathbf{U}_l^m$. The

matrices $\mathbf{M}^{\pm}_{q,j}$, $\mathbf{P}_l, j^{\pm}$ and $\mathbf{Q}_j$ introduced above are defined as

$$\mathbf{M}^{\pm}_{q,j}=A^{\pm}_{2,q,j}\mathbf{D}_{2,\eta}+A^{\pm}_{1,q,j}\mathbf{D}_{1,\eta}+\mathbf{A}^{\pm}_{0,q}, \tag{4.58a}$$

$$\mathbf{P}^{\pm}_{l,n} =B^{\pm}_{2,l,n}\mathbf{D}_{2,\eta}, \tag{4.58b}$$

$$\mathbf{Q}^{\pm}_{j} =C^{\pm}_{1,j}\mathbf{D}_{1,z}+C^{\pm}_{0,j}\mathbf{I}, \tag{4.58c}$$

where the spatially-varying coefficients $A^{\pm}_{2,q,j}$, $A^{\pm}_{1,q,j}$ and $\mathbf{A}^{\pm}_{0,q,j}$ in Eq. (4.58a) are, for $q=1,\ldots,N$ and $j=1,\ldots N_y$, defined as

$$A^{\pm}_{2,q,j} = \frac{\mu^{\pm}_q}{k_0^2}\left(\left(\frac{\partial h}{\partial \nu}\right)^2_{m,j}+1\right), \tag{4.59a}$$

$$A^{\pm}_{1,q,j} = -\frac{\mu^{\pm}_q}{k_0^2}\left(\frac{\partial^2 h}{\partial \nu^2}\right)_{m,j}, \tag{4.59b}$$

$$\mathbf{A}^{\pm}_{0,q} = \mathbf{I}_{N_z}+\frac{\mu^{\pm}_q}{k_0^2}\mathbf{diag}_n\left(k_n^2-k_0^2\right), \tag{4.59c}$$

the coefficients $B_{2,l,n}$ in Eq. (4.58b) are, for $l=1,\ldots,M$ and $j=1,\ldots N_y$, defined as

$$B^{\pm}_{2,l,n} = \frac{\lambda^{\pm}_l}{k_0^2}, \tag{4.60}$$

and the coefficients $C^{\pm}_{1,j}$ and $C^{\pm}_{0,j}$ are given by

$$C^{\pm}_{1,j}=\frac{\chi^{\pm}_0}{k_0^2}\left(\frac{\partial h}{\partial \xi}\right)_{m,j}, \tag{4.61a}$$

$$C^{\pm}_{0,j}=1 \tag{4.61b}$$

From the previous equations it appears that the ADI method requires the inversion of tridiagonal matrices of size $N_z\times N_z$ and $N_y\times N_y$ only, which is an order of magnitude lower than the direct method. The total number of matrix inversions required to

advance one step in range is $N+M+1$, with each inversion involving N_y right-hand sides. The solution at step $(m+1)$ is simply obtained by solving Eq. (4.56a), Eq. (4.56b) and Eq. (4.56c) successively, which is similar to the Split-Step Padé method developed by Collins [131] and later implemented for three-dimensional propagation by Surm. The ADI approach is more computationally advantageous than the fixed point method since its stability is unconditional. Splitting the problem into two uncoupled directions is equivalent to solving two simultaneous parabolic equations of lower dimensions, .

4.2.3 Finite-difference matrices and operator discretization

As discussed in Sec. 4.2.1 and Sec. 4.2.2, the numerical scheme requires the discretization of spatial derivatives using finite-differences in order to obtain a linear system of equations. In this section, we present elements of finite-difference calculus to reach a definition of the systems matrices $\mathbf{M}^{\pm}$, $\mathbf{P}^{\pm}$ and $\mathbf{Q}^{\pm}$ defined in Sec. 4.2.1 and 4.2.2. In order to do so, it is necessary to discretize first-order and second-order spatial derivatives of the wave field ψ at a given grid point ξ_m, ν_j, η_n, where $m = 1, \ldots, N_x$, $j = 1, \ldots, N_y$ and $n = 1, \ldots, N_z$. Using second-order finite-difference approximations [81], the first and second-order spatial derivatives with respect to the altitude η are given by

$$\left(\frac{\partial^2\psi}{\partial\eta^2}\right)^m_{n,j} = \frac{\psi^m_{n+1,j} - 2\psi^m_{n,j} + \psi^m_{n-1,j}}{\Delta\eta^2}, \tag{4.62a}$$

$$\left(\frac{\partial\psi}{\partial\eta}\right)^m_{n,j} = \frac{\psi^m_{n+1,j} - \psi^m_{n-1,j}}{2\Delta\eta}, \tag{4.62b}$$

where $\Delta\eta = \eta_{n+1} - \eta_n$ is the uniform grid spacing. The first-order and second-order derivatives in the transversal direction ν can be simply obtained by replacing η by ν in Eqs. (4.62).

IBC discretization

It appears that at the limit points $n = 1$ (bottom boundary), $n = N_z$ (top boundary), $j = 1$ (left boundary) and $j = N_y$ (right boundary), the finite-difference formulas in Eqs. (4.62) will contain discrete values of ψ that are outside the numerical domain, as shown in Fig. 4.4. There is, therefore, the need for a definition of virtual points to enable the numerical scheme. The virtual points associated with each boundary are

$$\begin{aligned}
&\text{Bottom boundary} && \mathcal{D}_g : && \psi^m_{0,j}, && \forall j \in [1, N_y] \\
&\text{Top boundary} && \mathcal{D}_t : && \psi^m_{N_z+1,j}, && \forall j \in [1, N_y] \\
&\text{Left boundary} && \mathcal{D}_1 : && \psi^m_{n,0}, && \forall n \in [1, N_z] \\
&\text{Right boundary} && \mathcal{D}_2 : && \psi^m_{n,N_y+1}, && \forall n \in [1, N_z]
\end{aligned}$$

This leads to a total number of $N_{\text{bnd}} = 2(N_z + N_y)$ unknown virtual points, which must be expressed using boundary conditions. At the bottom of the domain (i.e. at $\eta = 0$), the boundary condition is given by Eq. (4.36) for a ground of impedance Z_g. The top and side boundaries ($\eta = \eta_{\max}$ and $\nu = y_{\min}, y_{\max}$) are truncations of the propagation domain, and are governed by an impedance $Z_0 = 1$ since the interface is made of air. We begin by dealing with the bottom boundary condition at $\eta = 0$ by inserting Eq. (4.62b) in the discretized flat Impedance Boundary Condition (IBC) defined in Eq. (4.35), leading to

$$\frac{-\psi^m_{2,j} + 4\psi^m_{1,j} - 3\psi^m_{0,j}}{2\Delta\eta} = \frac{ik_0}{Z_g}\psi^m_{0,j}, \qquad \forall j = [1, N_y]. \tag{4.63}$$

The top boundary condition at $\eta = \eta_{\max}$ is similarly defined by

$$\frac{-\psi^m_{N_z-1,j} + 4\psi^m_{N_z,j} - 3\psi^m_{N_z+1,j}}{2\Delta\eta} = \frac{ik_0}{Z_0}\psi^m_{N_z,j}, \qquad \forall j = [1, N_y]. \tag{4.64}$$

The side boundary conditions will contain the same coefficients as Eq. (4.64). A schematic of the numerical domain and finite-difference stencils at the domain

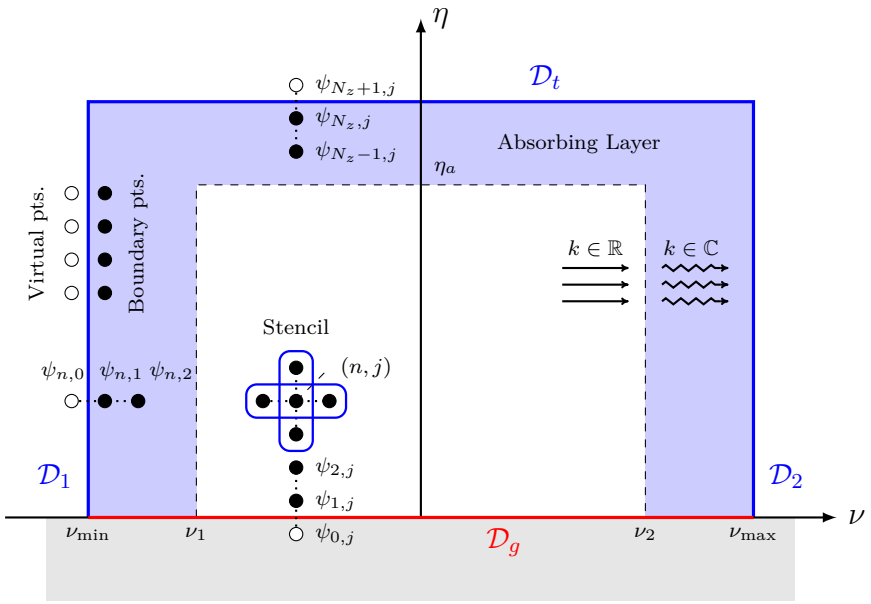

Figure 4.4: Transversal slice of the rectangular numerical domain $\mathcal{D}$ with side, top and bottom impedance boundary conditions. The light red domain represents the physical Absorbing Boundary Layer where the wavenumber is complex.

boundaries are presented in Fig. 4.4. Rearranging the coefficients of Eqs. (4.63) and (4.64) allows us to obtain a value for the virtual points, which will then be inserted into the finite-difference matrices. Thus, the virtual points $\psi^m_{0,j}$, $\psi^m_{N_z+1,j}$, $\psi^m_{n,0}$ and ψ^m_{n,N_y+1} are given by

$$\psi^m_{0,j} = \alpha^g_1 \psi^m_{1,j} + \alpha^g_2 \psi^m_{2,j}, \qquad \forall j \in [1, N_y] \tag{4.65a}$$

$$\psi^m_{N_z+1,j} = \alpha^t_1 \psi^m_{N_z,j} + \alpha^t_2 \psi^m_{N_z-1,j}, \qquad \forall j \in [1, N_y] \tag{4.65b}$$

$$\psi^m_{n,0} = \alpha^t_1 \psi^m_{n,1} + \alpha^t_2 \psi^m_{n,2}, \qquad \forall n \in [1, N_z] \tag{4.65c}$$

$$\psi^m_{n,N_y+1} = \alpha^t_1 \psi^m_{n,N_y} + \alpha^t_2 \psi^m_{n,N_y-1}, \qquad \forall n \in [1, N_z] \tag{4.65d}$$

where the constant coefficients α^t_1, α^t_2, α^g_1 and α^g_2 are given by

$$\alpha_1^t = \frac{4}{3 + 2ik_0\Delta\eta}, \tag{4.66a}$$

$$\alpha_2^t = \frac{-1}{3 + 2ik_0\Delta\eta}, \tag{4.66b}$$

$$\alpha_1^g = \frac{4Z_g}{3Z_g - 2ik_0\Delta\eta}, \tag{4.66c}$$

$$\alpha_2^g = \frac{-Z_g}{3Z_g - 2ik_0\Delta\eta}. \tag{4.66d}$$

The ground impedance Z_g in Eqs. (4.66a) to (4.66d), can stem from different analytical or empirical poro-acoustic models, as specified in Sec. 2.2.4. If the ground impedance is spatially variable, *i.e.* $Z_g = Z_{m,n}$ at the grid point (ξ_m, η_n), then the α coefficients are changed accordingly.

FD matrix assembly

The finite-difference equations, provided in Eqs. (4.65a) and (4.65d), can also be expressed in a matrix format by building the matrix of spatial derivatives in the plane $\xi = \xi_m$, evaluated at the $N_z \times N_y$ transversal grid points (ν_j, η_n). This matrix, symbolically written as $\boldsymbol{\delta}_\eta^l \boldsymbol{\Psi}^m$ for the l-th order spatial derivative with respect to η (or $\boldsymbol{\delta}_\nu^l \boldsymbol{\Psi}^m$ with respect to ν) is determined as a product between a finite-difference matrix $\mathbf{D}_{l,\eta}$ (or $\mathbf{D}_{l,\nu}$) and the wave field $\boldsymbol{\Psi}^m$ at the step ξ_m. Therefore, Eqs. (4.62) are, under matrix format, equivalent to

$$\boldsymbol{\delta}_\eta^l \boldsymbol{\Psi}^m = \left(\frac{\partial^l \psi}{\partial \eta^l}\right)^m = \mathbf{D}_{l,\eta} \boldsymbol{\Psi}^m, \tag{4.67a}$$

$$\boldsymbol{\delta}_\nu^l \boldsymbol{\Psi}^m = \left(\frac{\partial^l \psi}{\partial \nu^l}\right)^m = \boldsymbol{\Psi}^m \mathbf{D}_{l,\nu}. \tag{4.67b}$$

The derivatives in η (or ν) involve a left (or right) matrix product of size N_z (or N_y). The first-order and second-order derivatives are obtained for $l = 1$ and $l = 2$

in Eq. (4.67a). The elements of the corresponding matrices $\mathbf{D}_{2,\eta}$ (and $\mathbf{D}_{1,\eta}$) are deduced from Eq. (4.62a) (and Eq. (4.62a)), so we have

$$\mathbf{D}_{1,z}=\frac{1}{2\Delta\eta}\times\left.\begin{bmatrix} -\alpha_1^g & 1-\alpha_2^g & & & \\ -1 & 0 & +1 & & \\ & \ddots & \ddots & \ddots & \\ & & -1 & 0 & +1 \\ & & & \alpha_2^t-1 & \alpha_1^t \end{bmatrix}\right\} N_z, \tag{4.68a}$$

$$\mathbf{D}_{2,z}=\frac{1}{\Delta\eta^2}\times\left.\begin{bmatrix} \alpha_1^g-2 & \alpha_2^g+1 & & & \\ +1 & -2 & +1 & & \\ & \ddots & \ddots & \ddots & \\ & & +1 & -2 & +1 \\ & & & \alpha_2^t+1 & \alpha_1^t-2 \end{bmatrix}\right\} N_z. \tag{4.68b}$$

where the first ($n=1$) and last ($n=N_z$) row of Eqs. (4.68) are expressed using the bottom and top boundary conditions defined in Eq. (4.63) and Eq. (4.64) respectively. Similarly, the finite-difference matrices $\mathbf{D}_{2,\nu}$ and $\mathbf{D}_{1,\nu}$ associated with the first-order and second-order derivatives in ν are given by

$$\mathbf{D}_{1,\nu}=\frac{1}{2\Delta\nu}\times\left.\begin{bmatrix} -\alpha_1^t & 1-\alpha_2^t & & & \\ -1 & 0 & +1 & & \\ & \ddots & \ddots & \ddots & \\ & & -1 & 0 & +1 \\ & & & \alpha_2^t-1 & \alpha_1^t \end{bmatrix}\right\} N_y, \tag{4.69a}$$

$$\mathbf{D}_{2,\nu}=\frac{1}{\Delta\nu^2}\times\left.\begin{bmatrix} \alpha_1^t-2 & \alpha_2^t+1 & & & \\ +1 & -2 & +1 & & \\ & \ddots & \ddots & \ddots & \\ & & +1 & -2 & +1 \\ & & & \alpha_2^t+1 & \alpha_1^t-2 \end{bmatrix}\right\} N_y. \tag{4.69b}$$

The number of lower and upper diagonals in the finite-difference matrices in Eqs.

(4.68) and Eqs. (4.69) is a function of the finite-difference approximations of the differential operators. In the present case, we are using a cross-shaped 5-point stencil, as shown in Fig. 4.4, which leads to tridiagonal matrices in both η and ν. The Beilis-Tappert transform given in Eq. (4.15) has greatly simplified the handling of boundary conditions, overcoming the need for an interpolation to get an expression at virtual points. An alternative implementation of the boundary conditions consists in using "ghost" values that satisfy Eqs. (4.63) and (4.64) for the virtual points outside of the numerical domain [114].

Domain truncation

Finally, the numerical domain $\mathcal{D}$, shown in Fig 4.4, is truncated in order to limit reflections from the boundary limits. Following Salomons [177], waves can be artificially damped by introducing atmospheric absorption. This is achieved by making the use of a complex wavenumber $\tilde{k} = k + i\kappa$ in an absorbing layer that is placed far from the receiver location. The absorbing layer is placed inside the numerical domain $\mathcal{D}$ just before the outer boundaries, above the altitude η_a and transversally beyond ν_1 and ν_2, as shown in Fig. 4.4. The general expression of the wavenumber k in the three-dimensional parabolic equation given in Eq. (4.2) can be synthesized as $\tilde{k}(\eta,\nu) = k(\eta) + i\kappa_{\text{side}}(\eta) + i\kappa_{\text{top}}(\nu)$ where the function κ_{side} and κ_{top} are the side and top absorbing functions. Here, the following profiles are used

$$\kappa_{\text{side}}(\nu) = \kappa_0 \times \begin{cases} \left(\dfrac{\nu-\nu_2}{\nu_{\max}-\nu_2}\right)^2 & , \quad \nu \geq \nu_2, \\ \left(\dfrac{\nu-\nu_1}{\nu_1-\nu_{\min}}\right)^2 & , \quad \nu \leq \nu_1, \\ 0 & , \quad \nu_1 \geq \nu \leq \nu_2, \end{cases} \tag{4.70}$$

for the side absorbing layer, where ν_1, ν_2, $\nu_{\min}$ and $\nu_{\max}$ are the side absorbing layer limits, as shown in Fig. 4.4, and

$$\kappa_{\text{top}}(\eta) = \kappa_0 \times \begin{cases} \left(\dfrac{\eta - \eta_a}{\eta_{\max} - \eta_a}\right)^2 & , \quad \eta \geq \eta_a, \\ 0 & , \quad \eta \leq \eta_a, \end{cases} \tag{4.71}$$

for the top absorbing layer, where η_a and $\eta_{\max}$ are the top absorbing layer limits, as shown in Fig. 4.4. In Eqs. (4.70) and Eq. (4.71), κ_0 is an absorbing coefficient. Numerical considerations for physical absorbing layers are similar to the ones made earlier for Perfectly Matched Layers, with a trade-off between size of the layer and the magnitude of reflections. For a large enough value of the layer thickness, we can ensure that spurious refections from the layer boundary are negligible. The refractive term $\mathbf{A}^{\pm}_{0,j}$ in Eqs. (4.46c) and (4.59c) is identical in both approaches. Inserting Eqs. (4.70) and (4.71) into the imaginary part of k in the operator $\mathcal{Z}$, given by Eq. (4.2), leads to

$$\mathbf{A}^{\pm}_{0,j} = \mathbf{I}_{N_z} + \frac{\mu_0^{\pm}}{k_0^2}\mathbf{diag}_n\left(\tilde{k}^2_{n,j} - k_0^2\right) \tag{4.72}$$

where $\tilde{k}$ is the complex wavenumber in the absorbing region, defined by

$$\tilde{k}_{n,j} = \tilde{k}(\eta_n, \nu_j) = k(\eta_n) + i(\kappa_{\text{side}}(\nu_j) + \kappa_{\text{top}}(\eta_n)), \qquad \forall j \in [1, N_y], \quad , \forall n \in [1, N_z], \tag{4.73}$$

where κ_{side} and κ_{top} are given in Eq. (4.70) and Eq. (4.71), respectively, and $\mathbf{I}_{N_z}$ is the identity matrix of size N_z. The matrices $\mathbf{A}^{\pm}_0$ now include transversal dependency in the side absorbing regions and must be updated for every column computation. The value of the absorption coefficient κ_0 is frequency-dependent and must be kept as small as possible so as to limit reflection from the absorbing layer interfaces. Therefore, we rather increase the size of the absorbing layer in both η and ν directions, ensuring a layer with a depth of at least $50\lambda_0$. The real advantage of the physical absorber over the PML is that it involves a change of the wavenumber k rather than the second-order derivatives. The solver introduced in Sec. 4.2.1 is not unconditionally stable, therefore it is safer to use a physical absorber defined in Eq. (4.73) as only the diagonal terms of the matrices $\mathbf{M}^{\pm}$ are modified.

4.2.4 Source and spectral properties

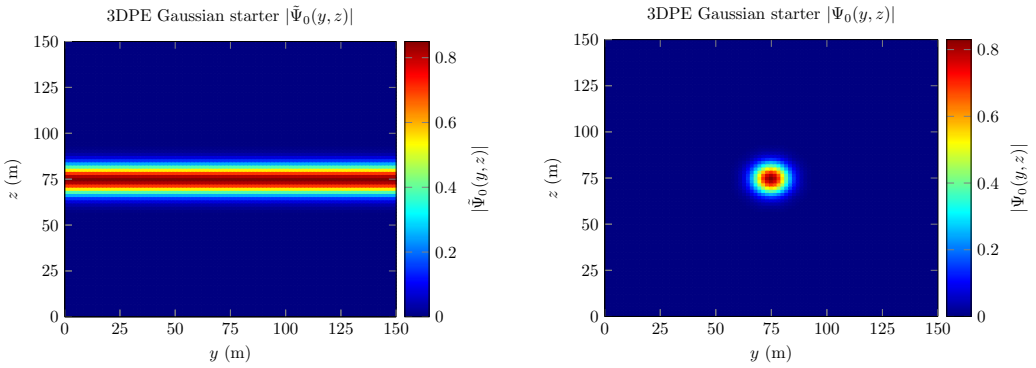

Figure 4.5: Close-up of the 3DPE starting fields for a frequency $f = 10$ Hz. Univariate Gaussian source $\tilde{\Psi}_0$ (left) and multivariate Gaussian source Ψ_0 (right) in the transversal starting plane $x = x_s$.

In the previous chapter, a Gaussian source was derived for the 2D parabolic equation method by matching the asymptotic expansion of the analytical solution of the parabolic equation in free field with the Helmholtz solution. It is possible to extend this result to three-dimensional propagation without having to perform the whole analysis again. Assuming the source to be transversally invariant, the three-dimensional PE in free-field reduces to the two-dimensional PE in any plane corresponding to a constant y. Since the solution in all these planes is the same, the transversally invariant starting field can be expressed by $\tilde{\Psi}_0(y,z) = \psi_0(z)$, and is shown in Fig. 4.5. For a source located at (y_z, z_s) in the initial plane $x = 0$, the corresponding three-dimensional starting field is written as

$$\Psi_0(y - y_s, z - z_s) = A\psi_0(z - z_s)\psi_0(y - y_s), \tag{4.74}$$

where A is a constant to be determined and ψ_0 is the two-dimensional starting field of the y-invariant problem. For the 3D initial condition to be consistent with the analytical solution, the amplitude of the starting field must be equal to $|\Psi_0(0,0)| = k_0$ which is done by using $A = 1/k_0$, so the starting field is simply

$$\Psi_0(y-y_s, z-z_s) = k_0 \exp\left(-\frac{k_0^2}{2}(y-y_s)^2\right) \exp\left(-\frac{k_0^2}{2}(z-z_s)^2\right). \tag{4.75}$$

This source function is plotted in Fig. 4.5 for $x_s = 75\,\text{m}$, $y_s = 75\,\text{m}$ and $f = 10\,\text{Hz}$. The initial value of the envelope ψ, given in Eq. (4.75), is derived by generalizing the 2D derivation made in Jensen et al.[100]. Considering the two-dimensional Fourier transform $\hat{\psi}$ of the envelope ψ, defined as,

$$\hat{\psi}(x, k_y, k_z) = \frac{1}{4\pi^2} \iint_{\mathbb{R}^2} \psi(x, y, z) e^{-i\mathbf{k}\cdot\mathbf{x}} \mathrm{d}y\mathrm{d}z, \tag{4.76}$$

where $\mathbf{k} = (k_y, k_z)^T$ and $\mathbf{x} = (y, z)^T$. In free-field, the narrow-angle three-dimensional PE is,

$$\left\{\frac{\partial}{\partial x} - \frac{i}{2k_0}\left(\frac{\partial^2}{\partial y^2} + \frac{\partial^2}{\partial z^2}\right)\right\}\psi = 0. \tag{4.77}$$

Applying the two-dimensional Fourier transform to Eq. (4.77) leads to,

$$\left\{\frac{\partial}{\partial x} + \frac{i(k_z^2 + k_y^2)}{2k_0}\right\}\hat{\psi} = 0, \tag{4.78}$$

and the solution of the first-order problem given by Eq. (4.78) can be written as

$$\hat{\psi}(x, k_y, k_z) = \hat{\psi}(0, k_y, k_z) \exp\left(\frac{-i(k_z^2 + k_y^2)x}{2k_0}\right), \tag{4.79}$$

where $\hat{\psi}(0, k_y, k_z)$ is the value of the transformed field $\hat{\psi}$ at $x = 0$. Applying the two-dimensional Fourier transform to the Gaussian starter in Eq. (4.74), the following expression for $\hat{\psi}(0, k_y, k_z)$ is obtained

$$\hat{\psi}(0, k_y, k_z) = \frac{A}{4\pi^2}\left(\int_{\mathbb{R}} e^{-(z-z_s)^2/w_z^2} e^{-ik_z z}\mathrm{d}z\right) \times \left(\int_{\mathbb{R}} e^{-(y-y_s)^2/w_y^2} e^{-ik_y y}\mathrm{d}y\right). \tag{4.80}$$

The integrals in Eq. (4.80) can then be simplified by introducing the change of variables $z' = z - z_s$ and $y' = y - y_s$, which leads to,

$$\hat{\psi}(0,k_y,k_z) = \frac{A}{4\pi^2} e^{-ik_z z_s} e^{-ik_y y_s} \times \left(\int_{\mathbb{R}} e^{-z'^2/w_z^2} e^{-ik_z z'} \mathrm{d}z' \right) \times \left(\int_{\mathbb{R}} e^{-y'^2/w_y^2} e^{-ik_y y'} \mathrm{d}y' \right). \tag{4.81}$$

Similarly to Jensen et al. [100], the two integrals in Eq. (4.81) are calculated using the identity

$$\int_{\mathbb{R}} e^{-at^2} e^{\pm ibt} \mathrm{d}t = \sqrt{\frac{\pi}{a}} e^{-b^2/4a}, \tag{4.82}$$

where $a > 0$ and b are real coefficients. Substituting Eq. (4.82) into Eq. (4.81) leads to,

$$\hat{\psi}(x,k_y,k_z) = \frac{A w_z w_y}{4\pi} \times \exp\left(-ik_z z_s - \left(\frac{ix}{2k_0} + \frac{w_z^2}{4} \right) k_z^2 \right) \times \exp\left(-ik_y y_s - \left(\frac{ix}{2k_0} + \frac{w_y^2}{4} \right) k_y^2 \right). \tag{4.83}$$

The initial condition on the envelope ψ is obtained by performing an inverse Fourier transform of Eq. (4.83). Again, the identity given in Eq. (4.82) is used to evaluate the integrals. Introducing the new variables $x_1 = 2x/k_0 w_z^2$ and $x_2 = 2x/k_0 w_y^2$, the free-field solution ψ is given by,

$$\psi(x,y,z) = \frac{A}{\sqrt{(1+ix_1)(1+ix_2)}} \times \exp\left(\frac{-(z-z_s)^2}{w_z^2(1+ix_1)} \right) \times \exp\left(\frac{-(y-y_s)^2}{w_y^2(1+ix_2)} \right) \tag{4.84}$$

Next, the coefficients A, w_y and w_z in Eq. (4.74) are deduced by matching the acoustic energy of the free-field solution with the energy of a normalized monopole source. In cartesian coordinates, the acoustic energy density is given by $|p|^2 = \psi\bar{\psi}$, where $\bar{\psi}$ is the conjugate of the complex pressure envelope ψ. In the far-field, $x_1, x_2 \longrightarrow +\infty$, so the acoustic energy becomes

$$|p(x,y,z)|^2 = \frac{A^2 k_0^2 w_z^2 w_y^2}{4x^2} \times \left(1 - \frac{k_0^2 w_y^2}{2x^2}(y-y_s)^2 - \frac{k_0^2 w_z^2}{2x^2}(z-z_s)^2 \right) \tag{4.85}$$

In free-field, the monopole source solution is given by,

$$p_H(x,z) = S_0 \frac{e^{ik_0 R}}{4\pi R}, \tag{4.86}$$

where $R = |\mathbf{x} - \mathbf{x}_s|$. In the far-field, the region of validity of the PE is characterized by $x \gg y, z$, since the propagation angle is small. Therefore, $R \approx x$ and the acoustic energy associated with the monopole source has the following asymptotic behavior with x,

$$|p_H(x,z)|^2 \sim \left(\frac{S_0}{4\pi R}\right)^2. \tag{4.87}$$

The coefficients w_z, w_y and A are identified by comparing Eq. (4.87) with Eq. (4.85),

$$w_y = \sqrt{2}/k_0, \tag{4.88a}$$
$$w_z = \sqrt{2}/k_0, \tag{4.88b}$$
$$A = S_0 k_0/4\pi, \tag{4.88c}$$

which leads to the expression given in Eq. (4.75) for $S_0 = 4\pi$. Following Jensen [100], it is possible to generalize this function and obtain a Gaussian beam-style starter by introducing angle of propagation with respect to the horizontal φ_t, also called beam tilt. In three dimensions, the azimuthal angle of the beam is defined by θ_t. Furthermore, the width of a Gaussian source is governed by the amplitude of the coefficient in the exponential, which is equal to $k_0^2/2$, meaning that beam width is larger at lower frequencies. The beam width can be controlled by introducing the aperture angle of the source b_w. The resulting source is then given by

$$\Psi_0(y - y_s, z - z_s) = k_0 \tan b_w \exp\left(-\frac{k_0^2 b_w^2}{2}(y - y_s)^2\right) \exp\left(ik_0(y - y_s)\tan\theta_t\right) \times \\ \exp\left(-\frac{k_0^2 b_w^2}{2}(z - z_s)^2\right) \exp\left(ik_0(z - z_s)\tan\varphi_t\right). \tag{4.89}$$

In the context of propagation above a complex impedance plane, the total pressure field can be expressed as the sum of a direct and reflected wave. The source term is therefore adapted to $\Psi_0 \leftarrow \Psi_0(y - y_s, z - z_s) + Q(\varphi)\Psi_0(y - y_s, z - z_s)$ where $Q(\varphi)$

is the angle-dependent spherical reflection coefficient. This configuration is geometrically equivalent to having a set of two equidistant sources in free-field, which are symmetrical with respect to the plane. In a homogeneous three-dimensional space, the analytical pressure field from a monopole source is then given by

$$p_c(\mathbf{x}) = S_0 \left(\frac{e^{ik_0 R_i}}{R_i} + Q(\varphi) \frac{e^{ik_0 R_r}}{R_r} \right), \tag{4.90}$$

where $R_i = \sqrt{x^2 + (y - y_s)^2 + (z - z_s)^2}$ and $R_r = \sqrt{x^2 + (y - y_s)^2 + (z + z_s)^2}$ are the direct and reflected ray lengths. Assuming that we are far enough from the source to enforce $r \gg z_s$, we can expand these quantities as $R_i = \sqrt{x^2 + (y - y_s)^2} - z_s \sin\varphi$ and $R_i = \sqrt{x^2 + (y - y_s)^2} + z_s \sin\varphi$ where φ is the elevation angle. Denoting $r = \sqrt{x^2 + (y - y_s)^2}$, the total field can be written as,

$$p_c(\mathbf{x}) = S_0 \frac{e^{ik_0 r}}{r} \left(e^{-ik_0 z_s \sin\varphi} + Q(\varphi) e^{ik_0 z_s \sin\varphi} \right). \tag{4.91}$$

For a perfectly reflecting surface, $Q = 1$, so the total pressure field amplitude can be written as

$$|p_c(\mathbf{x})| = \frac{2S_0}{r} |\cos(k_0 z_s \sin\varphi)|, \tag{4.92}$$

which is essentially the amplitude difference due to phase difference. Destructive interference happens when pressure becomes null upon two opposite phase waves, i.e. $|p_c| = 0$. This leads to the following condition, also known as the Lloyd's mirror pattern [100],

$$\sin\varphi_n = \frac{\pi}{k_0 z_s} \left(n + \frac{1}{2} \right) \qquad , \qquad n \in \mathbb{N}. \tag{4.93}$$

This equation indexes the far-field location of destructive interference lines. It is worth noting that in a three-dimensional space, the interference pattern is independent in azimuth. The maximum number of these lines van be estimated by verifying the condition $\sin\varphi < 1$, leading to $N_d \approx 2z_s/\lambda_0 - 1/2$. From this formula, we can foresee that if the source is so close enough to the ground that $z_s < \lambda_0/4$, no

destructive interference line is possible. As an example, for a source that is 25 m height and a frequency of 10 Hz (the wavelength is $\lambda_0 = 34.3\,\mathrm{m}$, we have $N_d = 1$. If the ground is not rigid, then the pressure energy formula is given by

$$|p_c(\mathbf{x})|^2 = \frac{S_0^2}{r^2}\left(1 + |Q|^2 + 2|Q|\cos\left(2k_0 z_s \sin\varphi + \arg Q\right)\right). \tag{4.94}$$

The zeros of the Lloyd's mirror equation for a non rigid boundary is not straightforward. Determining the interference angles requires to find the zeros of a non-linear functional equation and numerical methods can be used to achieve this, like the iterative Newton-Raphson scheme.

4.2.5 Interpolation of realistic topographic data

As mentioned in Chapter 1, modeling realistic environmental parameters is one of the main difficulties faced when applying numerical methods to infrasound problems. Topographic data is usually extracted from geological databases like the SRTM, typically under DEM (digital elevation modeling) format among others. Software like GMT (Generic Mapping Tool) allow us to convert this raw data to XYZ form, so we get regularly spaced surface points $\mathcal{G} = (x_k^*, y_l^*, h_{k,l}^*)$ where x_k^* and y_l^* are the coordinates calculated from an origin (x_0^*, y_0^*). The point spacing is equal to the SRTM data resolution δ_r, which is either 90 m or 30 m. This data cannot be used in its raw form and must be processed before being incorporated into the numerical scheme as a physical boundary. Specifically five operations must be performed to transform this data into a compatible form.

Starting from the location of the source $\mathbf{X}_s^* = (x_s^*, y_s^*)$ and the receiver (x_r^*, y_r^*) in terms of raw data, which may not fall on a raw grid point, we begin by computing the the direction of propagation $\theta^* = \arctan_2(x_r^* - x_s^*, y_r^* - y_s^*)$. Then, we generate a cartesian numerical grid $(x_0, \cdots, x_{N_x}) \times (y_0, \cdots, y_{N_y})$ of size $x_{\max} - x_{\min}$ along the propagation direction and $y_{\max} - y_{\min}$ transversally. In this new grid, $(x_s, y_s) = (0, 0)$ is the source location. It is now possible to relate each numerical grid point to its raw position defined by $\mathbf{X}_{m,j}^* = (X_m^*, Y_j^*)$ using a grid rotation

defined by $\mathbf{X}^*_{m,j} = \mathbf{X}^*_s + \mathbf{R}\mathbf{x}_{m,j}$. Then, we perform a linear interpolation of the terrain data at the grid points $\mathbf{X}^*_{m,j}$ in order to get the value of the terrain elevation $h_{i,j} = h^*(X^*_m, Y^*_j) = h(x_m, y_j)$. At this stage, the raw value of the terrain elevation is known on the entire numerical grid. In order to smooth the profile, we introduce an average window filter defined by

$$\hat{h}(x,y) = \frac{1}{w^2} \iint_{S_w(x,y)} h(x',y')dx'dy', \tag{4.95}$$

where $S_w(x,y) = [x - w/2, x + w/2] \times [y - w/2, y + w/2]$ is a square domain of size w centered around the evaluation point (x,y). The last step has been added for the reasons exposed in Waagan [210]. Indeed, for a propagation problem with a wavelength λ, any geometrical asperity of dimensions $\delta \ll \lambda$ is considered as noise and can be ignored, up to a certain limit. The same procedure can be followed for the $N\times$2D PE, where the data is interpolated along several azimuthal paths indexed by their respective direction θ^*_i. In order to limit reflections from the transversal numerical boundaries, the domain should be made as large as possible around the region of interest.

Realistic topographic features fall within three main categories of interest for infrasound propagation. The earth curvature is accounted for through a modified index of refraction n in the PE and irregular terrain obstacles, such as small scale mountain ranges and long range waveguide variations are handled by a transformation of the numerical grid. Both features can be superposed in any PE formulation without further development. The last category of topographic features are noise barriers, which include all highly irregular obstacles, such as urban canyons or cliffs. Mathematically, a topographic feature is considered to be a noise barrier if the descriptor $h(x,y)$ of its profile is not of class $\mathcal{C}_0$, in which case it is impossible to use a coordinate transform and the interface will have to be treated explicitly. Furthermore, topographic variations inducing a slope higher than the PE limit on a single wavelength must be either ignored [210], or handled by a hybrid terrain method, where sharp obstacles are incorporated "naturally" through an appropriate discontinuity condition. Such a method would be significantly difficult to implement in 3D, and the challenges posed by the pre-processing of the topographic data into a hybrid

smooth profile/sound barrier features would far outweigh the benefits of using a PE method.

4.3 Validation of the method

Research has shown that the validation of three-dimensional PE codes is a difficult task not only due to the scarcity of experimental data available, but more fundamentally because of the lack of universally defined criteria to qualify 3D topographic effects. So far, most successful models typically work for a limited scope of problems and were developed to achieve a specific objective in the estimation of the pressure field. Furthermore, discrepancies between numerical results and measurements may be beyond control (e.g. uncertainty in atmospheric parameters) or include inherent errors. In consequence, a state of the art validation would require to match numerical results with measurements obtained in a controlled environment, where all input parameters are fixed. In absence of these experimental benchmarks, the method developed above can be validated in three different ways: (i) by computing the numerical solution of a problem for which the analytical solution is known, (ii) by comparing against other numerical methods (inter-model comparison) or (iii) by validating a transversally invariant problem against 2D benchmarks. In this section, the 3D BTPE will be validated against a linear acoustics frequency-domain BEM solution obtained with COMSOL Multiphysics. The propagation domain for validation is depicted in Fig. 4.6.

4.3.1 Propagation over a flat surface in a homogeneous media

First, a validation of the 3DPE is achieved by investigating the propagation of sound above a rigid plane in three dimensional space. The analytical solution has been given previously in Eq. (4.90), and for the case of a rigid boundary, the spherical reflection coefficient is $Q = 1$. We also assume that the source is normalized, so

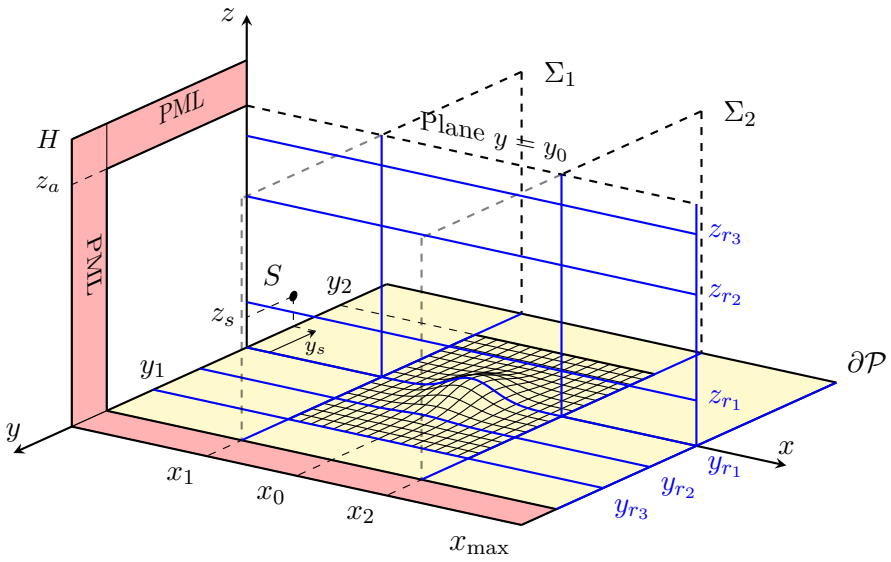

Figure 4.6: Schematic of the three-dimensional propagation domain used in the validation of the 3D BTPE and in the parametric study of terrain interaction with infrasound. The sample terrain is located between x_1 and x_2 in range and y_1 and y_2 transversally. The blue lines correspond to the receiver locations and the planes Σ_1 and Σ_2 are the cross-sections of the waveguide before and after the obstacle respectively. The figure shows the case of a positive gaussian hill profile.

$S_0 = 1\,\text{Pa}$. The propagation space is a rectangular waveguide of size $10 \times 4 \times 3\,\text{km}^3$ described by cartesian coordinates (x, y, z). Frequencies considered are $f = 1$ Hz, 5 Hz, 10 Hz and 20 Hz and the source is located at $z_s = 25\,\text{m}$, $y_s = 0\,\text{m}$. The Relative Sound Pressure Level (RSPL) is given in Fig. 4.7, which show that the 3DPE solution is asymptotically identical to the analytical solution. In the near-field, the discrepancies between the PE and the analytical solution is due to the paraxial approximation. Numerical simulations show that the solver developed in Sec. 4.2.1 is stable, and the number of iterations before convergence increases for a smaller step size $\Delta\xi$. For $f = 10$ Hz and a step size $\lambda/10$, the solver takes $N_i = 9$ iterations per numerical step to reach the tolerance $e = 10^{-4}$. In particular, the system is well-posed for all complex values of the the ground impedance Z_g.

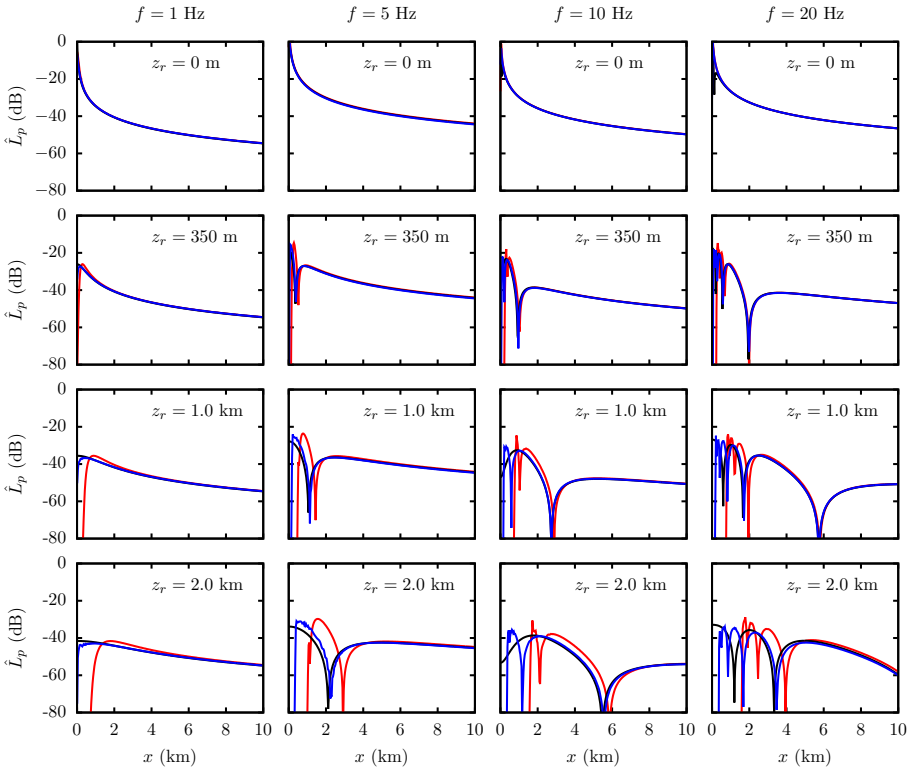

Figure 4.7: Validation of the 3DPE for a flat rigid surface, homogeneous atmosphere ($c = c_0 = 343\,\mathrm{m}\cdot\mathrm{s}^{-1}$), $f = [1, 5, 10, 20]$ Hz. Relative Sound Pressure Level (RSPL) $\hat{L}_p$ along distance at ground level (first row) and several altitudes $z_r = 350$ m (second row), 1.0 km (third row) and 2.0 km (fourth row), as computed by the narrow-angle 3DPE (—), the wide-angle 3DPE (—) and the analytical solution (—).

4.3.2 Propagation over a gaussian hill in a homogeneous atmosphere

In this section, the 3D BTPE is validated for propagation above a generic irregular boundary. The atmosphere is assumed to be homogeneous, with a constant sound speed of $c_0 = 343$ m/s. In order to validate the method developed above, a Boundary Element solution, implemented in COMSOL Multiphysics [2], is used as a benchmark. A 2D BTPE solution is also computed in the middle plane $y = 0$. The propagation domain is a rectangular waveguide of size $10 \times 4 \times 3$ km^3, delimited

by $0 < x < 10$ km, $-2 < y < 2$ km and $0 < z < 3$ km. The bottom boundary is a Gaussian hill, centered at $x_0 = 5$ km and $y_0 = 0$ km. The profile function is given by

$$h(x, y) = h_0 \exp\left(-\frac{(x - x_0)^2}{2s_x^2}\right) \exp\left(-\frac{(y - y_0)^2}{2s_y^2}\right), \tag{4.96}$$

where $h_0 = 200$ m and $s_x = s_y = 500$ m. The maximum sloping angle of the hill is 19.6°, which is close to the theoretical limit of the narrow-angle BTPE [152]. The quantity of interest in the following simulations is the sound pressure level (SPL), defined in Eq. (2.63). The reference pressure p_{ref} is taken one numerical step away from the source in the x direction. The source is located at $\mathbf{x}_s = (0, 0, 25)$ m and has a strength $S_0 = 1$ Pa. Two frequencies are considered: $f = 1$ Hz and $f = 5$ Hz. At $f = 1$ Hz, the total domain range is 29λ and the terrain height is equal to 0.58λ. At $f = 5$ Hz, the total range extends to 145λ and the terrain height is 2.91λ. The artificial absorbing layer, defined in Eq. (4.73), is placed at the top of the domain, in the region $2 < z < 3$ km, and, on each side of the propagation domain, in the regions $-2 < y < -1$ km and $1 < y < 2$ km.

The COMSOL model is created with the boundary element method (BEM) physics interface in the Acoustics Module. Using the BEM interface presents a number of advantages over the traditional Finite Element Methods (FEM), as only the scattering objects (i.e., the Gaussian hill) need to be discretized with surface elements. The solution in the rest of the domain is calculated using the Kirchhoff-Helmholtz boundary integral

$$\psi(\mathbf{x}) = \psi_i(\mathbf{x}) + \iint_{\mathcal{S}} \frac{\partial G}{\partial \mathbf{n}}(\mathbf{x}, \mathbf{x}')\psi(\mathbf{x}')d\mathbf{x}', \tag{4.97}$$

where G is the three-dimensional Green function, ψ_i is the incident field and $\mathcal{S}$ is the scattering surface. The BEM typically reduces the size of the problem since no volumetric mesh is needed. The mesh quality is controlled through the maximum element size, which is defined as $\lambda/8$, where λ is the wavelength. For $f = 1$ Hz, the number of degrees of freedom (DOFs) can be reduced to $N_d \sim 14 \cdot 10^3$ DOFs with the BEM and appropriate use of symmetry, instead of $\sim 4 \cdot 10^6$ DOFs with a standard FEM. In the simulations presented here, a GMRES iterative solver is used, with a Sparse Approximate Inverse (SAI) preconditioning. The residual error

for convergence is set to $e = 10^{-3}$ and the rest of the parameters are left at their default values.

The results from the 3D BTPE for the Gaussian hill are compared against the BEM solution and the 2D BTPE. The Sound Pressure Level (SPL), defined in Eq. (2.63), is plotted in Figs. 4.8 to 4.10 for $f = 1$ Hz, and Figs. 4.11 to 4.13 for $f = 5$ Hz.

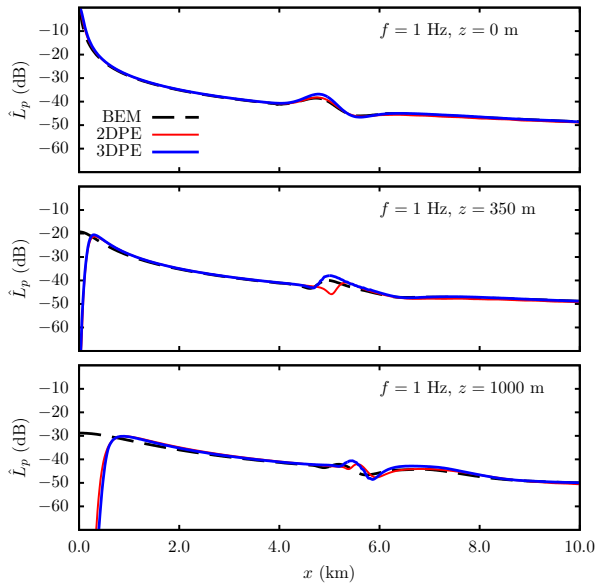

Figure 4.8: Variation of the SPL with range in the middle plane and for $f = 1$ Hz, taken along the ground surface (first row), the line $z = 350$ m (second row) and $z = 1$ km (third row).

Figure 4.8 shows the SPL variation, for $f = 1$ Hz, along x in the middle plane $y = 0$ and at several altitudes. The presence of the obstacle causes an increase in SPL upstream of the hill ($x < 5.0$ km) and a shadow zone downstream of the hill ($x > 5.0$ km). Contour plots of the SPL at the ground surface and in the middle plane are given in Fig. 4.9, where it appears that the reflected wave leads to destructive interferences at higher altitudes. The last row of Fig. 4.9 shows the altitude variation of the SPL at different ranges, and proves that the 3D BTPE correctly estimates the location and intensity of the pressure lobes. The transversal

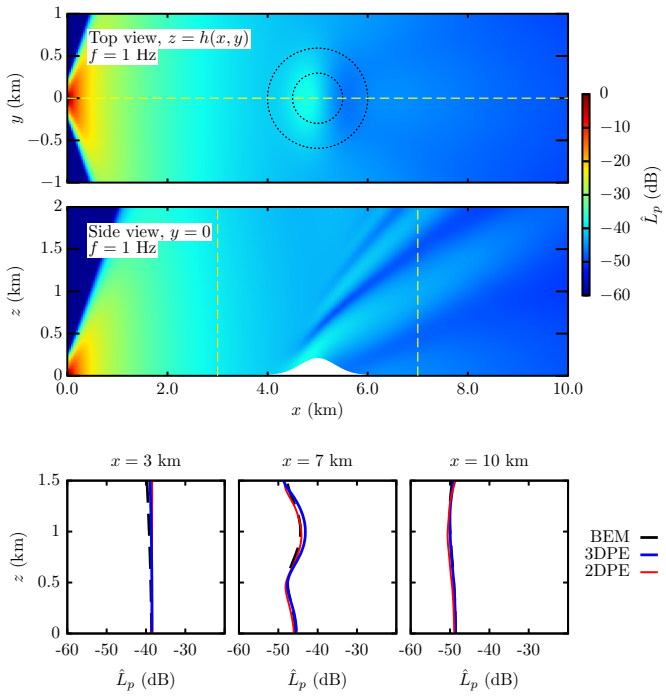

Figure 4.9: 3D BTPE solution of the propagation above the Gaussian hill at $f = 1$ Hz. The first row shows the SPL at the ground surface. The second row shows the SPL in the middle plane $y = 0$. The third row shows the SPL along the lines $x = 3$, 7 and 10 km in the middle plane.

variation of the SPL at $x = 7.0$ km, *i.e.* just downstream of the hill, is shown in Fig. 4.10. Results show that the 3D BTPE matches the BEM closely.

At $f = 5$ Hz, the ratio between the terrain height and the wavelength h_0/λ is larger than 1, which leads to a greater interaction between the obstacle and the incident wave. The SPL variation along x is shown in Fig. 4.11. The important discrepancy between the 3D BTPE and the BEM at short ranges is due to the paraxial approximation. In the far-field, the 3D BTPE agrees with the BEM very well, with a difference of ± 1 dB. Figure 4.12 shows the contour plot of the SPL at the ground surface and in the middle plane, as well as the variation of the SPL with altitude at different ranges. The contour plot in the middle plane shows a large number of interferences at higher altitude and a strong pressure decrease in the shadow zone. The 3D BTPE performs very well and captures three-dimensional

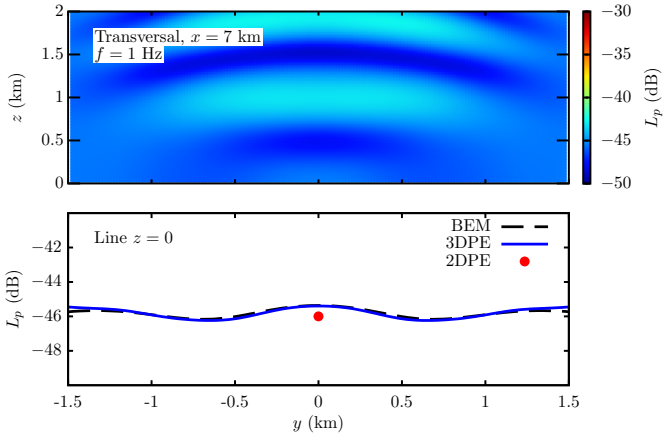

Figure 4.10: Transversal variation of the SPL at $x = 7$ km and $f = 1$ Hz. The first row shows the contour plot of the 3D BTPE solution in the plane $x = 7$ km. The second row shows the SPL along the transversal line $z = 0$ at $x = 7$ km.

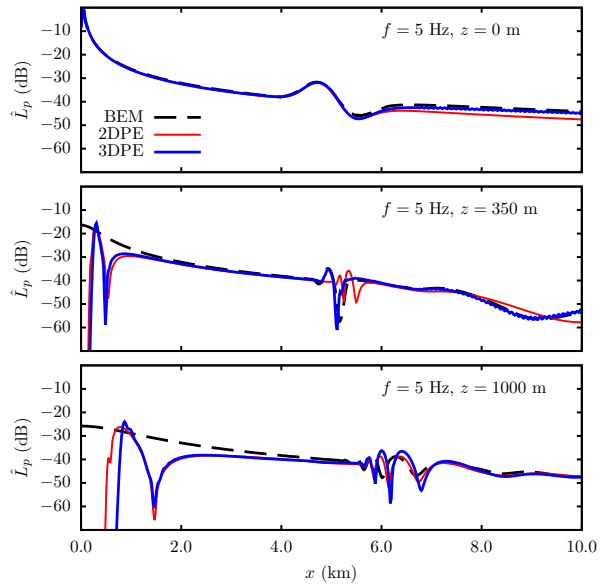

Figure 4.11: Variation of the SPL with range in the middle plane and for $f = 5$ Hz, taken along the ground surface (first row), the line $z = 350$ m (second row) and $z = 1$ km (third row).

effects correctly. This is specifically visible in the last two plots of Fig. 4.12 (for $x = 7$ km and $x = 10$ km), where the 2D BTPE fails to properly account for the

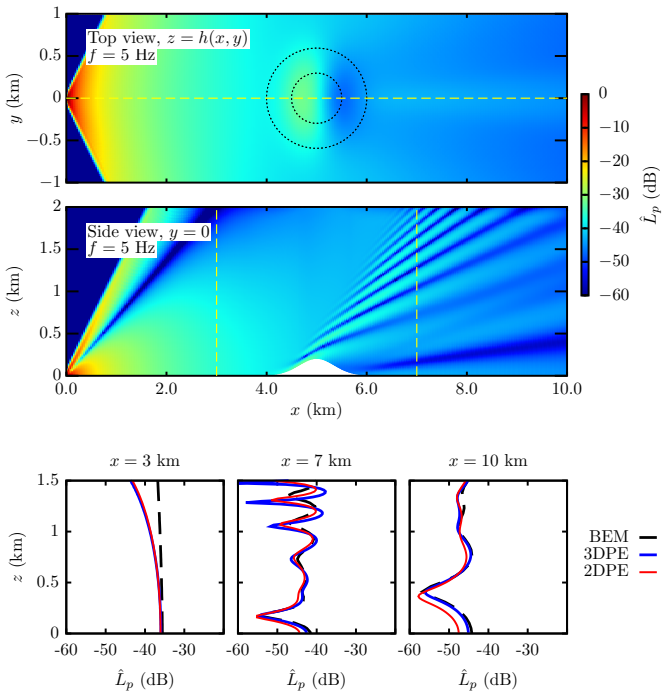

Figure 4.12: 3D BTPE solution of the propagation above the Gaussian hill at $f = 5$ Hz. The first row shows the SPL at the ground surface. The second row shows the SPL in the middle plane $y = 0$. The third row shows the comparison of the SPL along the lines $x = 3$, 7 and 10 km in the middle plane.

pressure increase in the shadow zone, by a margin of -4 dB. This pressure increase is explained by the presence of out-of-plane scattering due to the transversal variation of the hill. The transversal variation of the SPL at $x = 7.0$ km is shown in Fig. 4.13. Again, the 3D BTPE performs well and matches the BEM within a margin of 1 dB.

Overall, results show a good agreement between the 3D BTPE and the BEM method, with a discrepancy that is smaller than 1 dB for both frequencies. The important discrepancies in the near-field are due to the paraxial approximation, constraining the validity of the PE solution to small propagation angles. The comparisons with the 2D solution highlight the presence of three-dimensional effects at $f = 5$ Hz, which cause a difference of ~ 2 dB downstream of the obstacle, as shown in Fig.

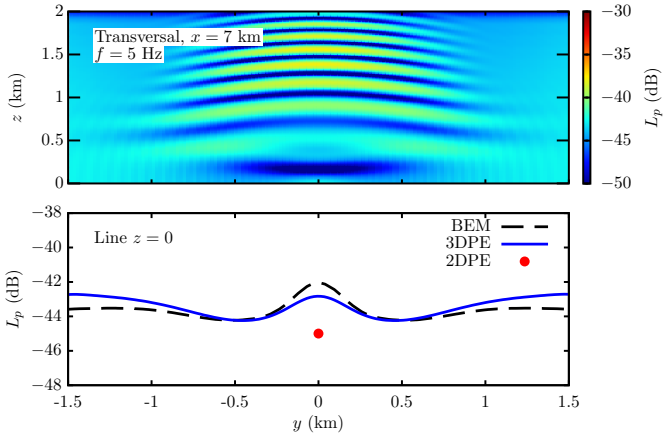

Figure 4.13: Transversal variation of the SPL at $x = 7$ km and $f = 5$ Hz. The first row shows the contour plot of the 3D BTPE solution in the plane $x = 7$ km. The second row shows the SPL along the transversal line $z = 0$ at $x = 7$ km.

4.13.

4.3.3 Propagation over two gaussian hills in a homogeneous atmosphere

In this section, we study the propagation of infrasound over a complex ridge, composed of two symmetrical Gaussian hill. This test case is similar to the problem exposed earlier by Silva et al. [186], who developed a parabolic equation method for irregular terrain scattering using a coordinate transform similar to the Beilis-Tappert map in Eq. (4.15). Instead of using an iterative scheme, Silva et al. [186] used a direct sparse solver at every marching step. This work was an extension of the modeling of transversal scattering from urban canyons done by Awadallah et al. [20]. The bottom boundary is described by the sum of the two hills, so the total profile function is given by $h = h^+ + h^-$ where we have defined $h^\pm$ as Gaussian hills, i.e.

$$h^\pm = h_0 \exp\left(-\frac{(x - x_0)^2}{2s_x^2}\right) \exp\left(-\frac{(y \pm y_0)^2}{2s_y^2}\right), \tag{4.98}$$

where we fix $s_x = s_y = 250\,\mathrm{m}$ and $h_0 = 300\,\mathrm{m}$. The two hills are located at a range $x_0 = 5.0\,\mathrm{km}$ and at a transversal distance $\pm y_0 = 500\,\mathrm{m}$, in such a way that the boundary in the middle plane $y = 0$. The source is located at $(x_s, y_s, z_s) = (0\,\mathrm{m}, 0\,\mathrm{m}, 25\,\mathrm{m})$ as in the previous section and we consider the frequency $f = 10\,\mathrm{Hz}$ only. Because the bottom boundary is flat in the middle plane ($h(x, 0) \approx 0$), any two-dimensional propagation model would fail to account for the part of the wave field that is scattered by the two hills. The Relative Sound Pressure Level (RSPL) obtained from the three-dimensional Beilis-Tappert parabolic equation is given in Fig. 4.14, which show interferences in the middle plane $y = 0$ at $x > 6.0\,\mathrm{km}$. This induces a small fluctuation of $\sim 3\,\mathrm{dB}$ around the analytical solution, computed using the monopole pressure field in Eq. (4.90). The top plot in Fig. 4.14 provides a strong argument in favor of the existence of non-negligible three-dimensional topographic effects even without atmospheric refraction or transversal winds.

4.4 Conclusions

The Beilis-Tappert coordinate transform has been naturally extended to three dimensions and the corresponding Impedance Boundary Condition (IBC) has been derived. This allows a simpler incorporation of the IBC into the finite-difference matrices but includes a limitation on the maximum slope of the terrain profile which is a function of the expansion order of the square-root operator. Unlike the two-dimensional case, it has not been possible to derive an appropriate phase shift in three-dimensions, so the first-order derivative in altitude must be included, leading to an additional matrix assembly at every step. This constitutes a major difference with the original formulation of the Beilis-Tappert PE [26, 152], where the phase shift allowed the derivation of simplified equivalent impedance boundary condition. The solution is derived using two different approaches: (i) an iterative gradient scheme which seeks the solution as the fixed point at every marching step, (ii) an Alternate Direction Implicit (ADI) scheme combined with a Split-Step Padé decomposition of the square-root operators which solves every transversal direction separately. In the present thesis, only the former has been implemented, however, the Split-Step Padé

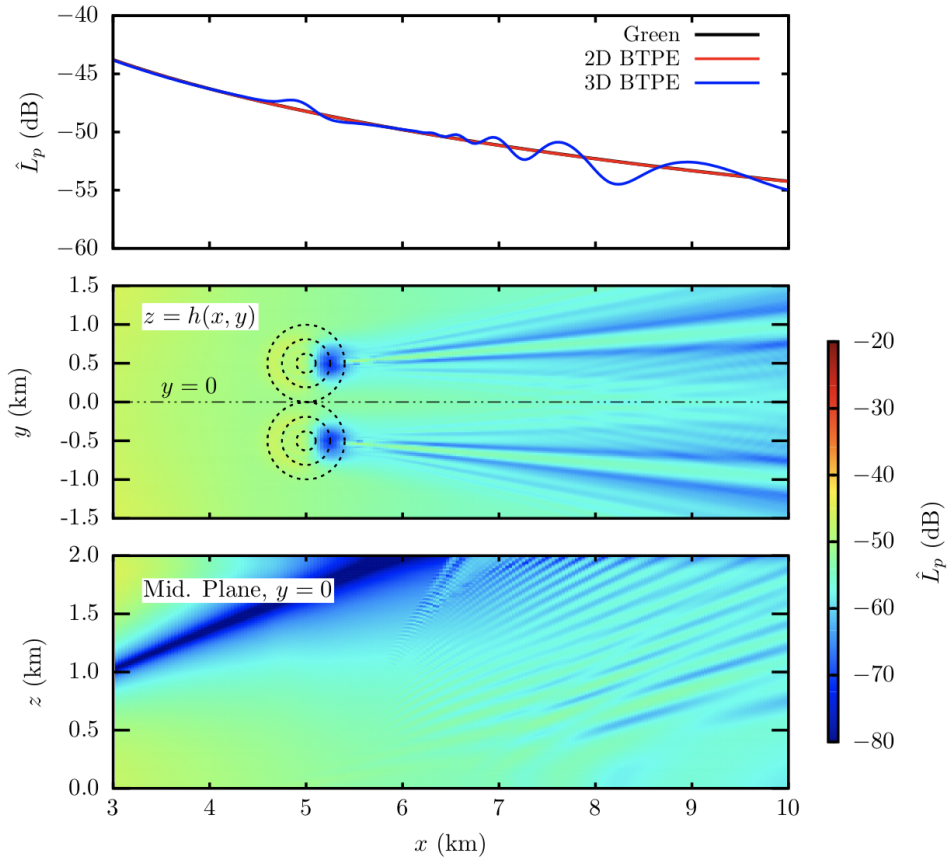

Figure 4.14: Propagation over two adjacent Gaussian hills located at $y_0 = \pm 500\,\mathrm{m}$ and $x_0 = 5.0\,\mathrm{km}$. The source is located at $x_s = 0\,\mathrm{m}$, $y_s = 0\,\mathrm{m}$ and at an altitude $z_s = 25\,\mathrm{m}$. The frequency is $f = 10\,\mathrm{Hz}$. Top: RSPL at the ground level in the middle plane as computed by the 2D BTPE, 3D BTPE and Analytical solution. Middle: RSPL contour plot along the bottom boundary $\partial\mathcal{P}$. Bottom: RSPL contour slice in the middle plane $y = 0$.

solution provides an optimization for a wide-angle solution. The method developed has been successfully validated against a stationary frequency-domain FE model built in COMSOL Multiphysics. The existence of tree-dimensional effects has been further justified by considering propagation over two adjacent hills, highlighting the importance of transversal scattering from out-of-plane obstacles.

Chapter 5

Parametric study of the interaction of sound with irregular boundaries

In this Chapter, a numerical investigation of sound propagation over parametrized irregular boundaries is carried out. The purpose of this study is two-fold, (i) to verify the existence of three-dimensional effects, i.e. variations in the pressure field that failed to be captured by 2D models, and (ii) establish a relation between boundary parameters and the radiation field past the obstacle, where the receiver is located. As mentioned in Sec. 2.2, interaction of sound with the ground can be interpreted as both reflection (first-order) and diffraction (second-order) effects, which can lead to a very complex scattering field. To quantify these effects, the three-dimensional BTPE will be compared against the two-dimensional narrow-angle and wide-angle BTPE in a number of different scenarios. In the first section, we consider propagation in a homogeneous and stationary atmosphere, so as to isolate three-dimensional topographic effects, both with regards to transversal scattering and diffraction in the shadow zone. Then, we add an effective sound speed profile in order to estimate the effect of coupling between atmospheric and topographic parameters in the case of propagation in the surface boundary layer.

5.1 Definition of test cases

In the present study, we constrain ourselves to smooth boundaries defined by a Gaussian surface. We recall that the physical three-dimensional domain is named $\mathcal{P}$ and the bottom boundary $\partial\mathcal{P}$. The propagation domain is divided into three regions: the near-field region ($x < x_1$), the terrain region ($x_1 < x < x_2$) and the radiation region ($x > x_2$). The terrain obstacle is delimited by the abscissas x_1 and x_2 and transversal locations y_1 and y_2, so that the total obstacle length in x is given by $L = x_2 - x_1$ and the obstacle width by $W = y_2 - y_1$. As a result, the terrain is located in a rectangular region $\Omega_t = [x_1, x_2] \times [y_1, y_2]$ of size $W \times L$ centered at the location (x_0, y_0). The bottom surface $\partial\mathcal{P}$ is flat everywhere else, so the extended boundary function is defined by

$$h(x,y) = \begin{cases} h_0 \exp\left(\dfrac{-(x-x_0)^2}{2s_x^2}\right) \exp\left(\dfrac{-(y-y_0)^2}{2s_y^2}\right) & , \quad \forall (x,y) \in \Omega_t \\ 0 & , \quad \forall (x,y) \in \partial\mathcal{P} \setminus \Omega_t \end{cases} \tag{5.1}$$

where s_x and s_y are the Gaussian surface variances along x and y respectively, which must be defined to ensure continuity of the profile function defined in Eq. (5.1). In the present case, we choose $s_x = L/4$ and $s_y = W/4$, so that the terrain height h is almost zero at the limits $y = y_1, y_2$ and $x = x_1, x_2$ of the terrain region Ω_t. The values of L and W will be fixed and the terrain will be parametrized by the maximum height h_0, so that the terrain region Ω_t remains unchanged throughout the study. The domain $\mathcal{P}$ size is 10.0 km in range, 6.0 km in width and 3.0 km in height. We take set $x_1 = 4.0\,\text{km}$, $x_2 = 6.0\,\text{km}$ and $y_1 = -1.0\,\text{km}$, $y_2 = 1.0\,\text{km}$ so that $L = W = 2.0\,\text{km}$ and we make the terrain height vary discretely between $h_0 = 0\,\text{m}$ for a flat surface to the limiting case $h_0 = 300\,\text{m}$. The maximum terrain sloping angle $\bar{\theta}_x$ along x is given by

$$\bar{\theta}_x = \arctan\left(\frac{4h_0}{L\sqrt{e}}\right), \tag{5.2}$$

and similarly for the maximum sloping angle $\bar{\theta}_y$ along y, by replacing L by W in

Eq. (5.2). For the maximum height $h_0 = 300\,\mathrm{m}$, the maximum sloping angle in both directions is about 20°, which is within the domain of validity of the three-dimensional first order BTPE defined in Eq. (4.24). The source is centered in the middle plane $y_s = 0\,\mathrm{m}$ and located at an altitude $z_s = 25\,\mathrm{m}$ above the bottom boundary. Frequencies emitted vary between $f = 0.1\,\mathrm{Hz}$ and $f = 10\,\mathrm{Hz}$ so as to cover a large range of propagation scales, which we characterize by the non-dimensional height, or "obstacle scale" defined as h_0/λ where λ is the wavelength. The non-dimensional height in function of frequency and terrain height is given in Table 5.1.

Terrain height h_0 (m)	0 m	100 m	200 m	300 m
Max. sloping angle $\bar{\theta}_x$,$\bar{\theta}_y$ (°)	0.0	7.0	14.0	20.0
Frequency (Hz)	Obstacle scale h_0/λ			
0.5	0.0	0.14	0.29	0.44
1.0	0.0	0.29	0.58	0.87
5.0	0.0	1.46	2.91	4.37
10.0	0.0	2.91	5.83	8.74

Table 5.1: Maximum sloping angle $\bar{\theta}_x$ and obstacle scales h_0/λ for the different terrain heights and source frequencies.

The numerical step size is fixed as one tenth of the wavelength of the highest frequency, so that the grid remains unchanged between simulations. Hence, we have $\Delta\xi = c_0/100 \approx 3.4\,\mathrm{m}$, which generates a grid of size $N_\xi \times N_\nu \times N_\eta$ of size $2915 \times 1752 \times 876$. This implies that the system is solved for a total of 1.53 MDOF per marching step. This step size ensures that enough points are considered to get an accurate description of the range and transversal variation of the terrain, however, the large size of the numerical domain poses a limitation on the frequency range, making simulations for 20 Hz very costly in memory and computation time, so we stay within the limit of 10 Hz in the present study. The PML thickness H_a and D_a in directions z and y is taken as a fifth of the waveguide, so $H_a = 2z_{\max}/5$ and $D_a = (y_{\max} - y_{\min})/5$. The pressure reference is taken at $x_{\mathrm{ref}} = 1.0\,\mathrm{km}$ and $z_{\mathrm{ref}} = z_s = 25\,\mathrm{m}$.

5.2 Three-dimensional irregular boundary in homogeneous media

In this section, we study propagation over the Gaussian hill defined in Eq. (5.1) in a homogeneous atmosphere defined by a constant sound speed $c_0 = 343\,\mathrm{m}\cdot\mathrm{s}^{-1}$. The near-field domain ($x < x_1$) is not affected by terrain scattering, so the field up to $x = x_1$ can be estimated by the analytical solution for propagation over a flat impedance surface given in Eq. (2.25). After interacting with the terrain, located between x_1 and x_2, part of the wave is reflected in the higher part of the waveguide while another part is diffracted in the shadow zone. We begin by giving a physical description of the scattered field before determining the relation between the obstacle scale h_0/λ and the sound pressure level in the shadow zone. Finally, we give a more accurate representation of three-dimensional effects by comparing the 3DPE simulations against 2DPE.

5.2.1 Heuristic description of the scattered field

We begin by plotting the Relative Sound Pressure Level (RSPL) in the planes $xz-$planes $\mathcal{C}_0$, $\mathcal{C}_{1/2}$ and $\mathcal{C}_1$ defined by $y = y_0 = 0\,\mathrm{m}$, $y = y_{1/2} = 500\,\mathrm{m}$ and $y = y_1 = 1.0\,\mathrm{km}$, for the four frequencies given in Table 5.1. The results are given in Figs. 5.1b to 5.12b, where we see that transversal reflection in the higher waveguide is substantial. In particular, the RSPL in the plane $\mathcal{C}_1$, located at the edge of the terrain region Ω_t, is presented in Figs. 5.3b, 5.6b, 5.9b and 5.12b. We see that in this plane, the boundary is flat but contains interferences between the direct and reflected fields, which indicates a clear transversal scattering, even for small terrain slopes. For $f = 0.5\,\mathrm{Hz}$ and $f = 1.0\,\mathrm{Hz}$, the terrain height has very little influence on the RSPL in the shadow zone. However, for higher frequencies, the number of destructive interferences in the shadow zones increases with terrain height. We also notice that the RSPL in the plane $\mathcal{C}_1$, e.g. Fig. 5.9b, show a great similarity in interference locations but a difference in amplitude as a function of height.

Next, we examine the RSPL at different yz-planes, namely $\partial\mathcal{P}$ (bottom surface), Π_1 ($z = 350\,\mathrm{m}$) and Π_2 ($z = 1.0\,\mathrm{km}$). The RSPL at the bottom boundary is given in Figs. 5.13b, 5.16b, 5.19b and 5.22b for $f = 0.5\,\mathrm{Hz}$, $f = 1\,\mathrm{Hz}$, $f = 5\,\mathrm{Hz}$ and $f = 10\,\mathrm{Hz}$ respectively. We observe the formation of a beam in the shadow zone, for $h_0 \geq 200\,\mathrm{m}$ and $f \geq 1\,\mathrm{Hz}$, which stems from diffraction by waves grazing the obstacle. For $f = 5\,\mathrm{Hz}$, transversal interferences appear, and we see the formation of a loss cone at $f = 10\,\mathrm{Hz}$ in the far-field region. In the plane Π_1, which is located just above the terrain peak, we see a clear distinction between the two wave structures that scatter from the terrain. In Fig. 5.20b, the destructive interference located at $x \approx 5.0\,\mathrm{km}$ represents reflections on the exposed face of the obstacle, while the pressure lobe at $x \approx 8.0\,\mathrm{km}$ is the diffracted field. These effects are enhanced at $f = 10\,\mathrm{Hz}$, e.g. at in Fig. 5.23b, but do not appear clearly at $f = 1\,\mathrm{Hz}$. Hence, from examining the obstacle scales for different frequencies given in Table 5.1, we see that destructive interferences begin to appear as soon as $h_0/\lambda \sim 1$, which is a well-known result of diffraction theory. For the cases where $h_0/\lambda < 1$, we are in the case of low-frequency Rayleigh scattering, which is mainly defined by first-order reflections. When $h_0/\lambda > 1$, we are in high-frequency scattering, and the shadow zone displays a dipole (second-order) field, as seen in Sec. 2.2.

In order to convince ourselves of the influence of h_0/λ on the scattered field structure, we plot the RSPL at the yz-plane Σ located at $x = 7.0\,\mathrm{km}$, just after the terrain region Ω_t. The RSPL for $f = 0.5\,\mathrm{Hz}$ and $f = 1\,\mathrm{Hz}$ are given in Figs. 5.26b and 5.26b respectively, which show that at low frequency, the terrain acts like a secondary monopole source. However, at $f = 5\,\mathrm{Hz}$ (Fig. 5.27b) and $f = 10\,\mathrm{Hz}$ (Fig. 5.28b), we see second-order diffractive effects in the shadow zone and a high pressure beam radiating in the upper section of waveguide, which happen for $h_0/\lambda > 1$. Hence, we have another justification of the following argument: for $h_0/\lambda < 1$, second-order diffractive effects are negligible and the scatterer is mostly a monopole source; for $h_0/\lambda > 1$, the second-order diffractive effects are important in the shadow zone and the scatterer includes dipole sources.

Next, we explore the differences between 2D BTPE and 3D BTPE in the computation of the scattered field in the middle plane $\mathcal{C}_0$. While the 2DPE assumes an axisymmetric medium, the three-dimensional model at the basis of Eq. (4.24)

accounts for transversal variation of the propagation medium, so the plane $\mathcal{C}_0$ can receive signals from scatterers located off-axis. Hence, the discrepancies between the 2D and 3D PE sound pressure level provide a quantification of three-dimensional scattering as a function of the terrain height h_0. The Relative Sound Pressure Level (RSPL) for $f = 1\,\text{Hz}$, $f = 5\,\text{Hz}$ and $f = 10\,\text{Hz}$ are given in Figs. 5.29 to 5.32, where the 2DPE results are taken from Sec. 3.4. In Fig. 5.29, we show the RSPL at the cut line $z = 350\,\text{m}$ in the middle plane $\mathcal{C}_0$. The 3D BTPE and 2D BTPE exhibit a very similar behavior for $h_0 = 100\,\text{m}$ ($\sim 7^\circ$ slope) and $f = 1\,\text{Hz}$ and $f = 5\,\text{Hz}$, while the 3D BTPE shows an increase in pressure of about 3 dB appears past the obstacle at $f = 10\,\text{Hz}$. At $h_0 = 300\,\text{m}$ we notice a shift in the interference pattern in the middle plane, which is probably due to transversal scattering from the sides of the hill. At $x = 10.0\,\text{km}$ the transmission loss (difference of sound pressure level) between the 3DPE and analytical (flat) solution is significant at $h_0 = 200\,\text{m}$ and $h_0 = 300\,\text{m}$, as expected. Another discrepancy is observable for $f = 1\,\text{Hz}$ at $x = 5.0\,\text{km}$, where the 3D BTPE solution maximum is higher ($+5\,\text{dB}$ at $h_0 = 300\,\text{m}$) and shifted to the left.

The Relative Sound Pressure Level (RSPL) at altitude $z = 1.0\,\text{km}$ is plotted in Fig. 5.30, where we see a much better agreement between the 2D BTPE and the 3D BTPE, within a margin of $\pm 2\,\text{dB}$. At the altitude $z = 2.0\,\text{km}$, the discrepancies become larger but the location of the interferences are very similar in both 2D and 3D. The RSPL at altitude $z = 2.0\,\text{km}$ is presented in Fig. 5.31, where we see an important discrepancy at $f = 10\,\text{Hz}$ and $h_0 = 100\,\text{m}$. The 3D BTPE sound pressure level in the region $x > 6.0\,\text{km}$ is about 10 dB greater than the 2D BTPE sound pressure. The exact cause is not clear, as at high altitudes the PE decreases in accuracy and some mismatches in SPL may also be caused by spurious reflections from the Perfectly Matched Layer (PML). Finally, we present the sound pressure level variation with altitude in Fig. 5.32, which highlights similarities in the interferences locations between 2D BTPE and 3D BTPE. The interferences located at $z > 1.0\,\text{km}$ represent reflection from the exposed face of the terrain while the important sound pressure level loss below $z < 500\,\text{m}$ accounts for the shadow zone, as sound is blocked by the obstacle.

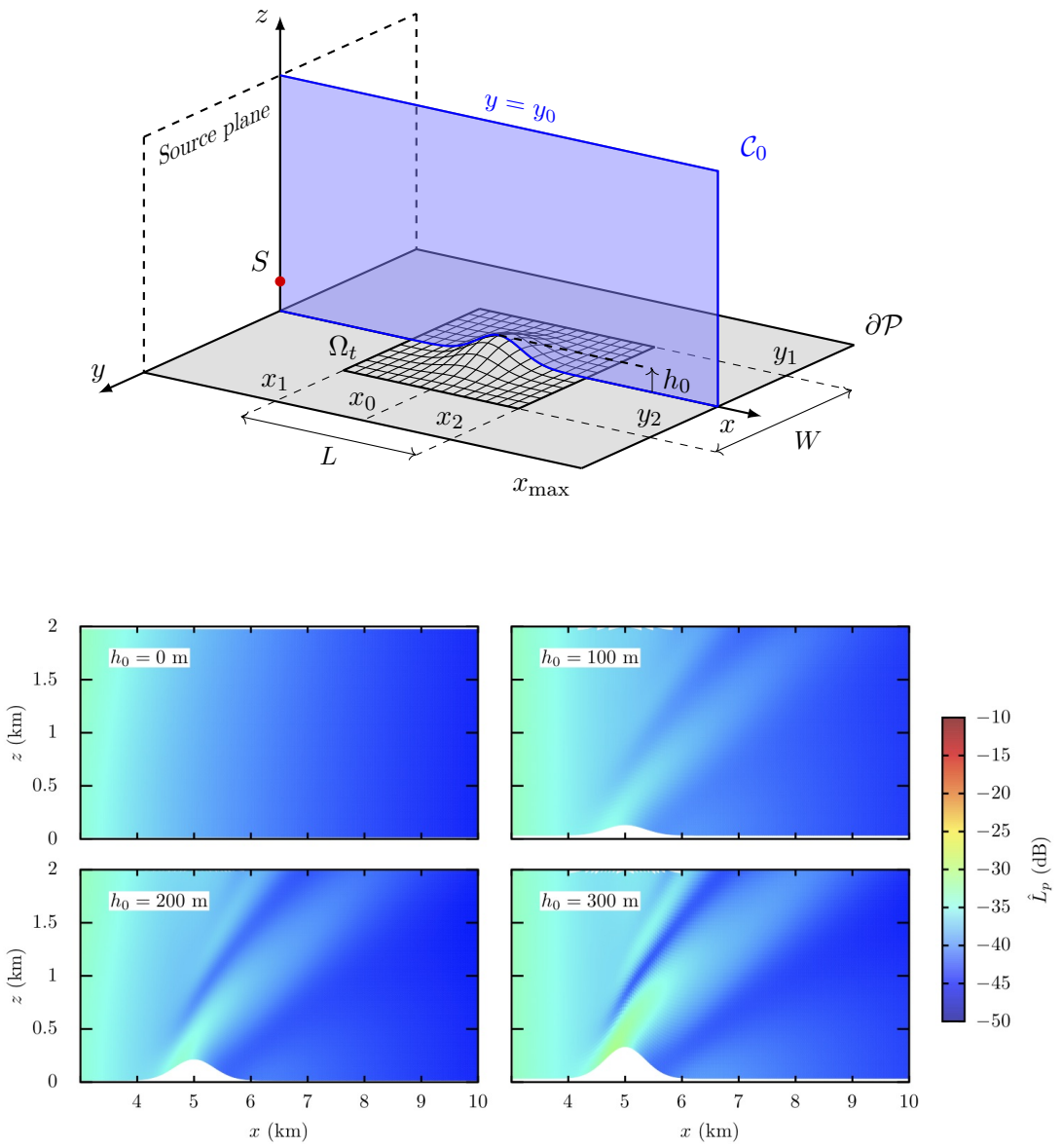

Figure 5.1: 3D BTPE simulation in a homogeneous atmosphere ($c_0 = 343\,\mathrm{m}\cdot\mathrm{s}^{-1}$), $f = 0.5\,\mathrm{Hz}$ and source located at $x_s = 0$, $y_s = 0$ and $z_s = 25\,\mathrm{m}$. Contour plot of the Relative Sound Pressure Level (RSPL) $\hat{L}_p$ in the plane $\mathcal{C}_0$ defined by $y = 0$ m, for a Gaussian Hill located at $(x_0, y_0) = (5, 0)$ (km), a width $s_x = s_y = 500$ and a terrain height of $h_0 = 0$ (flat), 100, 200 and 300 m.

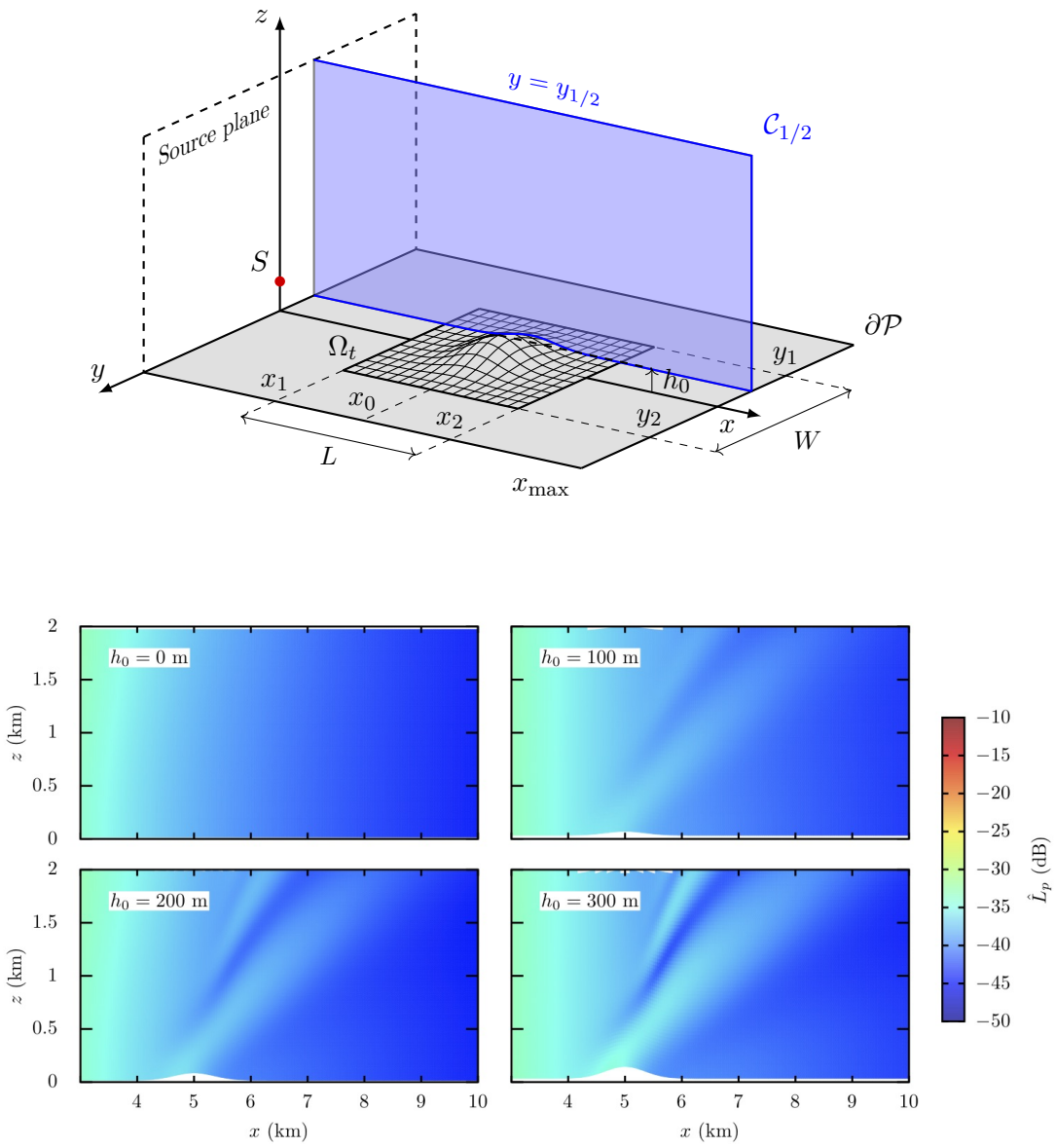

Figure 5.2: 3D BTPE simulation in a homogeneous atmosphere ($c_0 = 343\,\mathrm{m}\cdot\mathrm{s}^{-1}$), $f = 0.5\,\mathrm{Hz}$ and source located at $x_s = 0$, $y_s = 0$ and $z_s = 25\,\mathrm{m}$. Contour plot of the Relative Sound Pressure Level (RSPL) $\hat{L}_p$ in the plane $\mathcal{C}_{1/2}$ defined by $y = 500$ m, for a Gaussian Hill located at $(x_0, y_0) = (5, 0)$ (km), a width $s_x = s_y = 500$ and a terrain height of $h_0 = 0$ (flat), 100, 200 and 300 m.

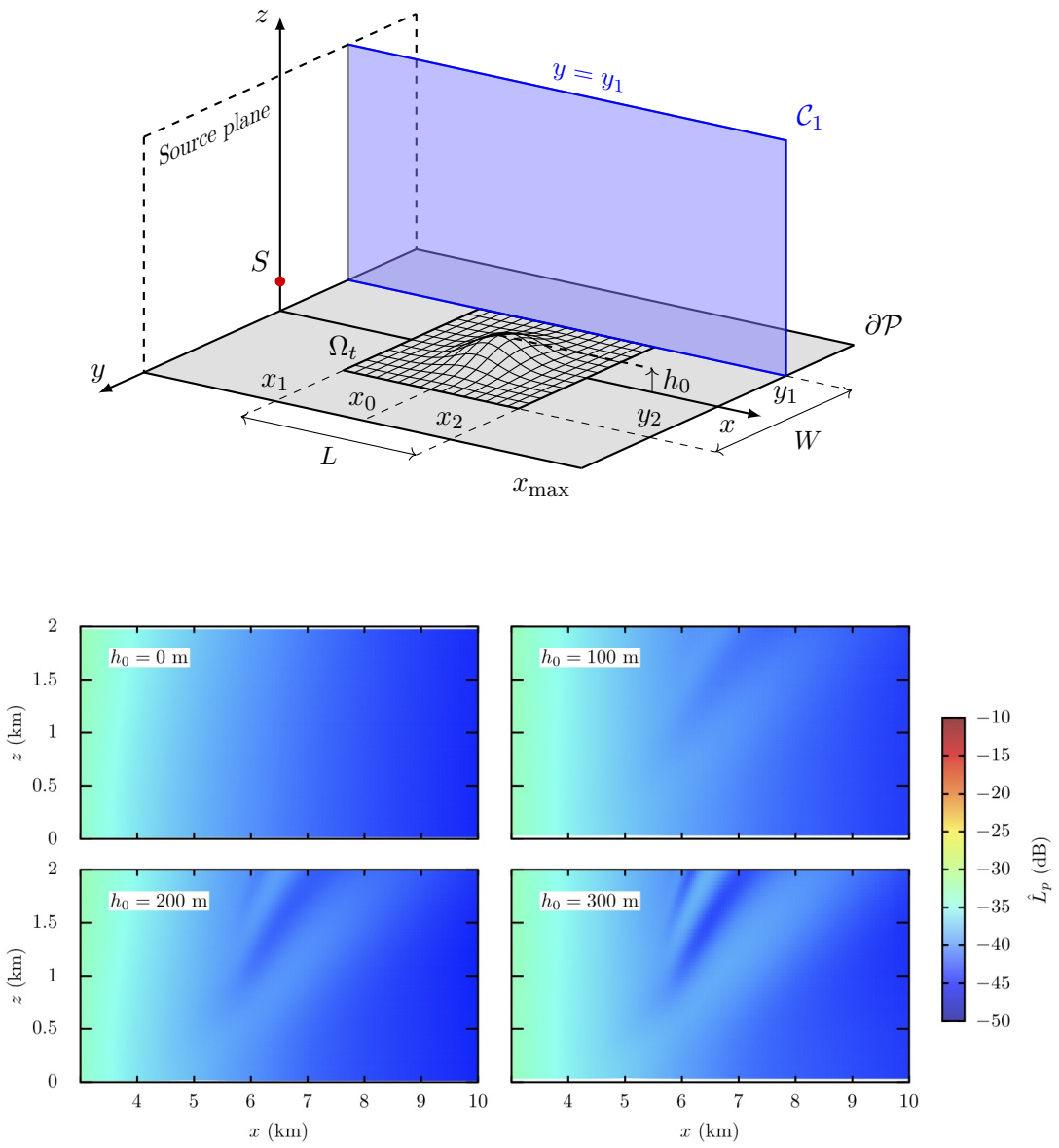

Figure 5.3: 3D BTPE simulation in a homogeneous atmosphere ($c_0 = 343\,\mathrm{m}\cdot\mathrm{s}^{-1}$), $f = 0.5\,\mathrm{Hz}$ and source located at $x_s = 0$, $y_s = 0$ and $z_s = 25\,\mathrm{m}$. Contour plot of the Relative Sound Pressure Level (RSPL) $\hat{L}_p$ in the plane $\mathcal{C}_1$ defined by $y = 1000$ m, for a Gaussian Hill located at $(x_0, y_0) = (5, 0)$ (km), a width $s_x = s_y = 500$ and a terrain height of $h_0 = 0$ (flat), 100, 200 and 300 m.

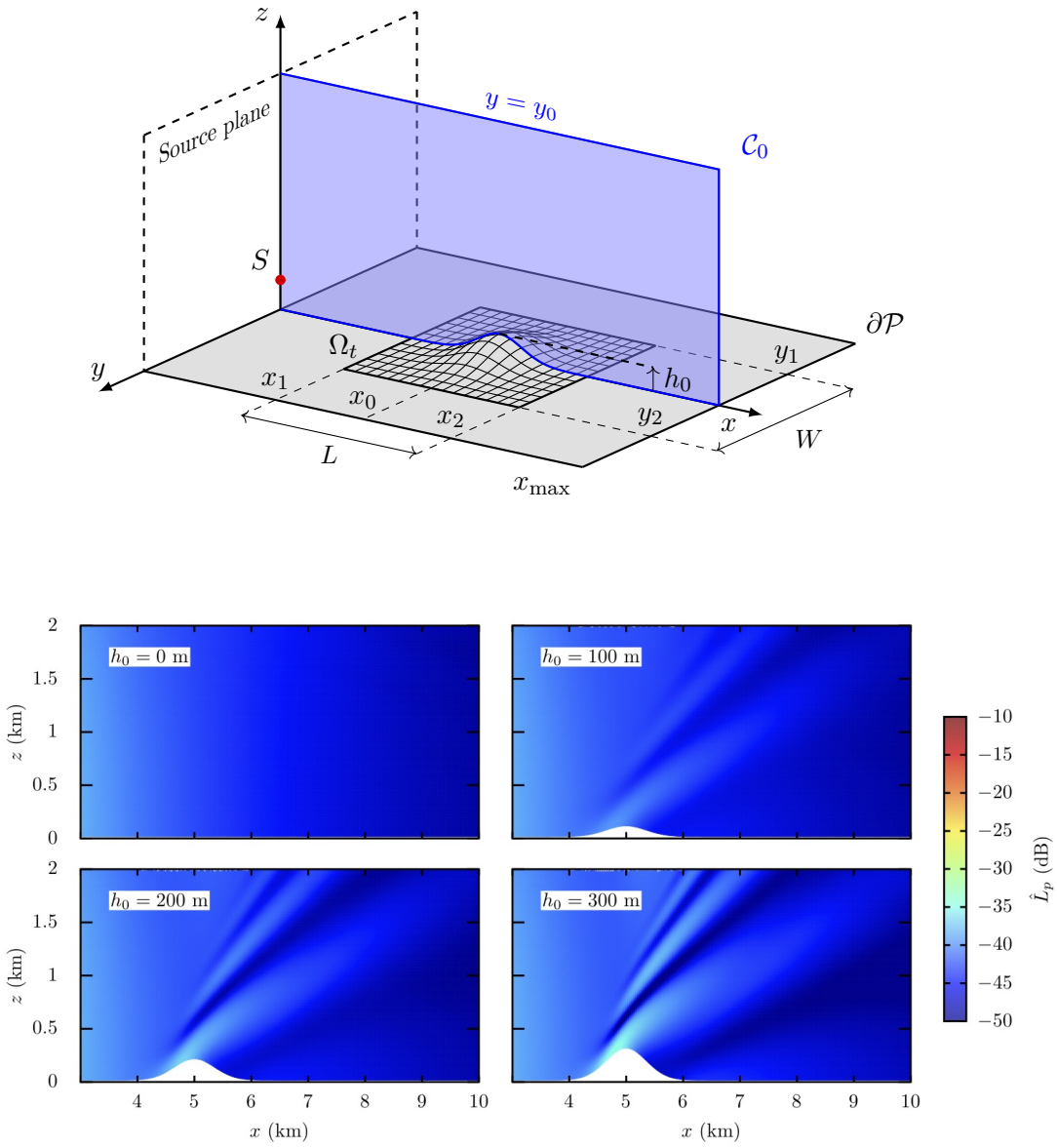

Figure 5.4: 3D BTPE simulation in a homogeneous atmosphere ($c_0 = 343\,\mathrm{m}\cdot\mathrm{s}^{-1}$), $f = 1\,\mathrm{Hz}$ and source located at $x_s = 0$, $y_s = 0$ and $z_s = 25\,\mathrm{m}$. Contour plot of the Relative Sound Pressure Level (RSPL) $\hat{L}_p$ in the plane $\mathcal{C}_0$ defined by $y = 0$ m, for a Gaussian Hill located at $(x_0, y_0) = (5, 0)$ (km), a width $s_x = s_y = 500$ and a terrain height of $h_0 = 0$ (flat), 100, 200 and 300 m.

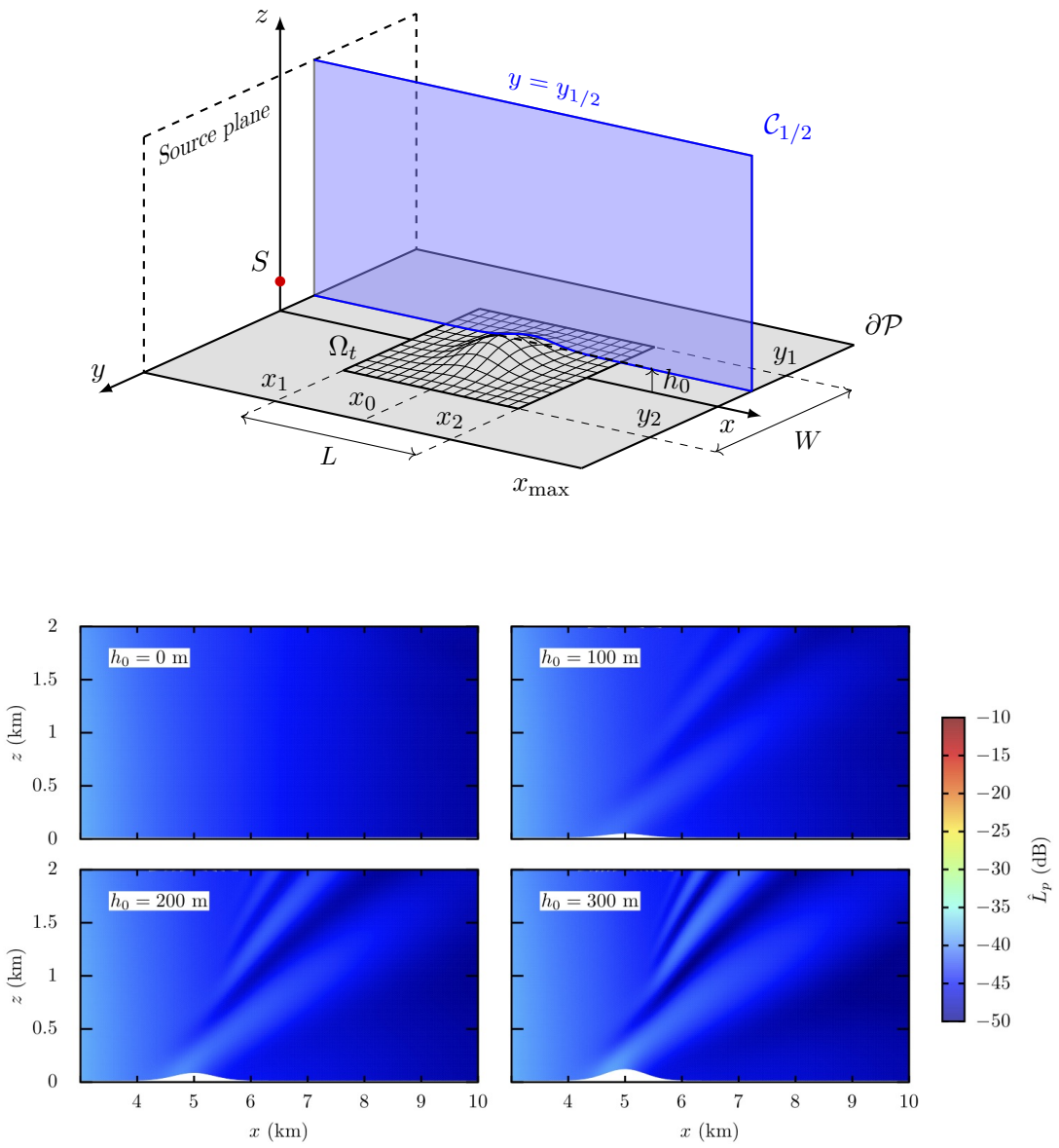

Figure 5.5: 3D BTPE simulation in a homogeneous atmosphere ($c_0 = 343\,\mathrm{m}\cdot\mathrm{s}^{-1}$), $f = 1\,\mathrm{Hz}$ and source located at $x_s = 0$, $y_s = 0$ and $z_s = 25\,\mathrm{m}$. Contour plot of the Relative Sound Pressure Level (RSPL) $\hat{L}_p$ in the plane $\mathcal{C}_{1/2}$ defined by $y = 500$ m, for a Gaussian Hill located at $(x_0, y_0) = (5, 0)$ (km), a width $s_x = s_y = 500$ and a terrain height of $h_0 = 0$ (flat), 100, 200 and 300 m.

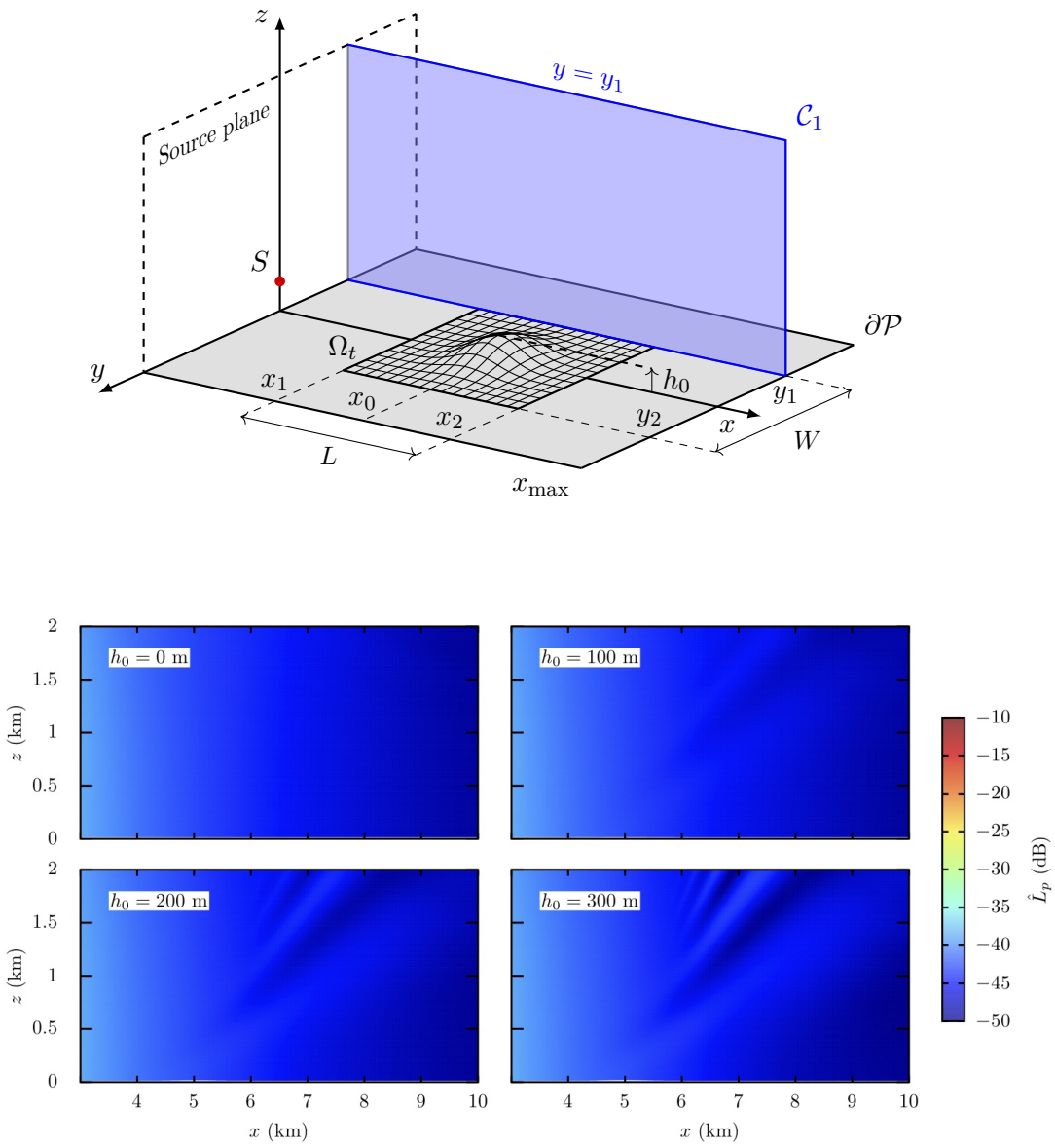

Figure 5.6: 3D BTPE simulation in a homogeneous atmosphere ($c_0 = 343\,\mathrm{m}\cdot\mathrm{s}^{-1}$), $f = 1\,\mathrm{Hz}$ and source located at $x_s = 0$, $y_s = 0$ and $z_s = 25\,\mathrm{m}$. Contour plot of the Relative Sound Pressure Level (RSPL) $\hat{L}_p$ in the plane $\mathcal{C}_1$ defined by $y = 1000$ m, for a Gaussian Hill located at $(x_0, y_0) = (5, 0)$ (km), a width $s_x = s_y = 500$ and a terrain height of $h_0 = 0$ (flat), 100, 200 and 300 m.

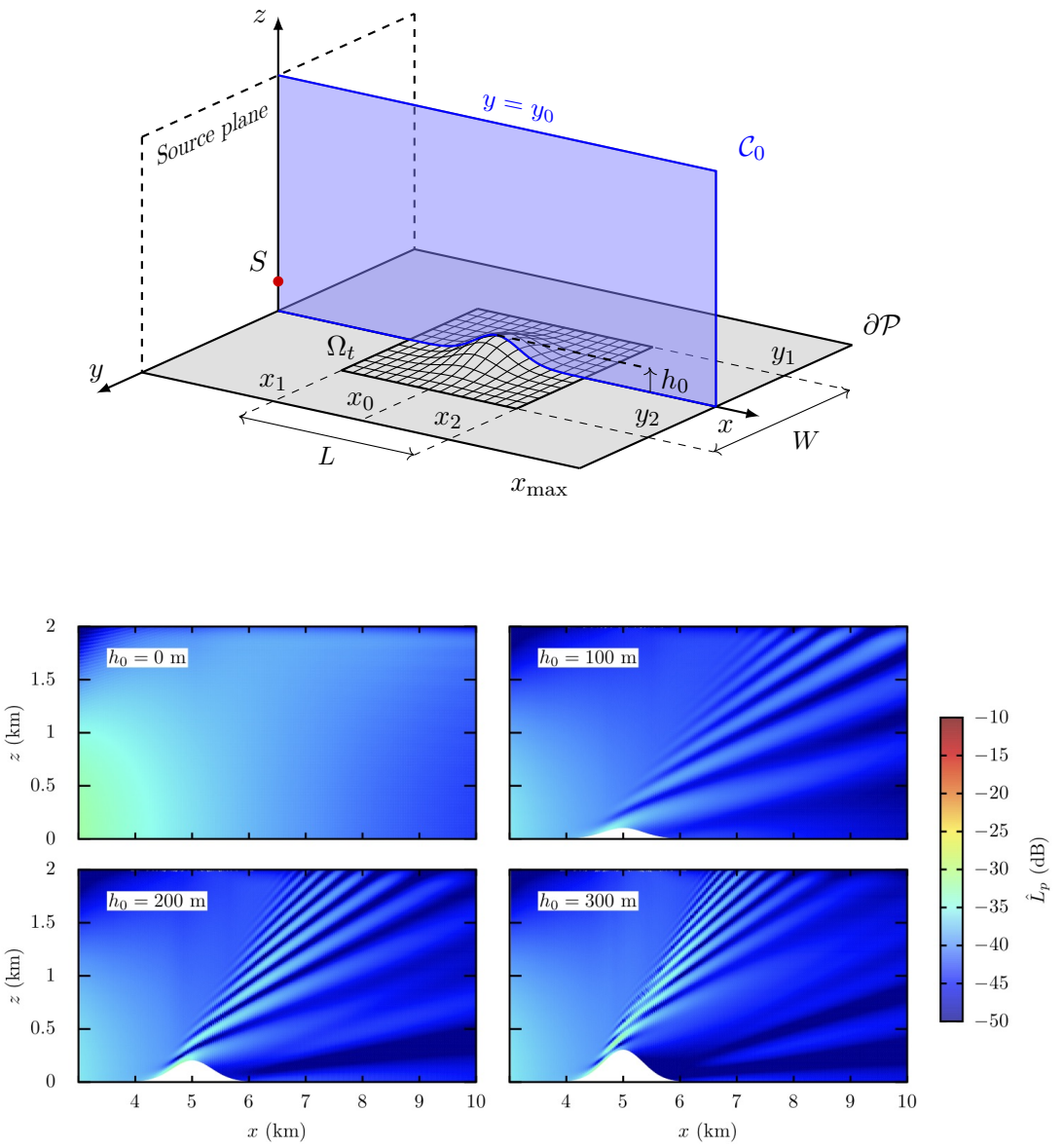

Figure 5.7: 3D BTPE simulation in a homogeneous atmosphere ($c_0 = 343\,\mathrm{m}\cdot\mathrm{s}^{-1}$), $f = 5\,\mathrm{Hz}$ and source located at $x_s = 0$, $y_s = 0$ and $z_s = 25\,\mathrm{m}$. Contour plot of the Relative Sound Pressure Level (RSPL) $\hat{L}_p$ in the plane $\mathcal{C}_0$ defined by $y = 0$ m, for a Gaussian Hill located at $(x_0, y_0) = (5, 0)$ (km), a width $s_x = s_y = 500$ and a terrain height of $h_0 = 0$ (flat), 100, 200 and 300 m.

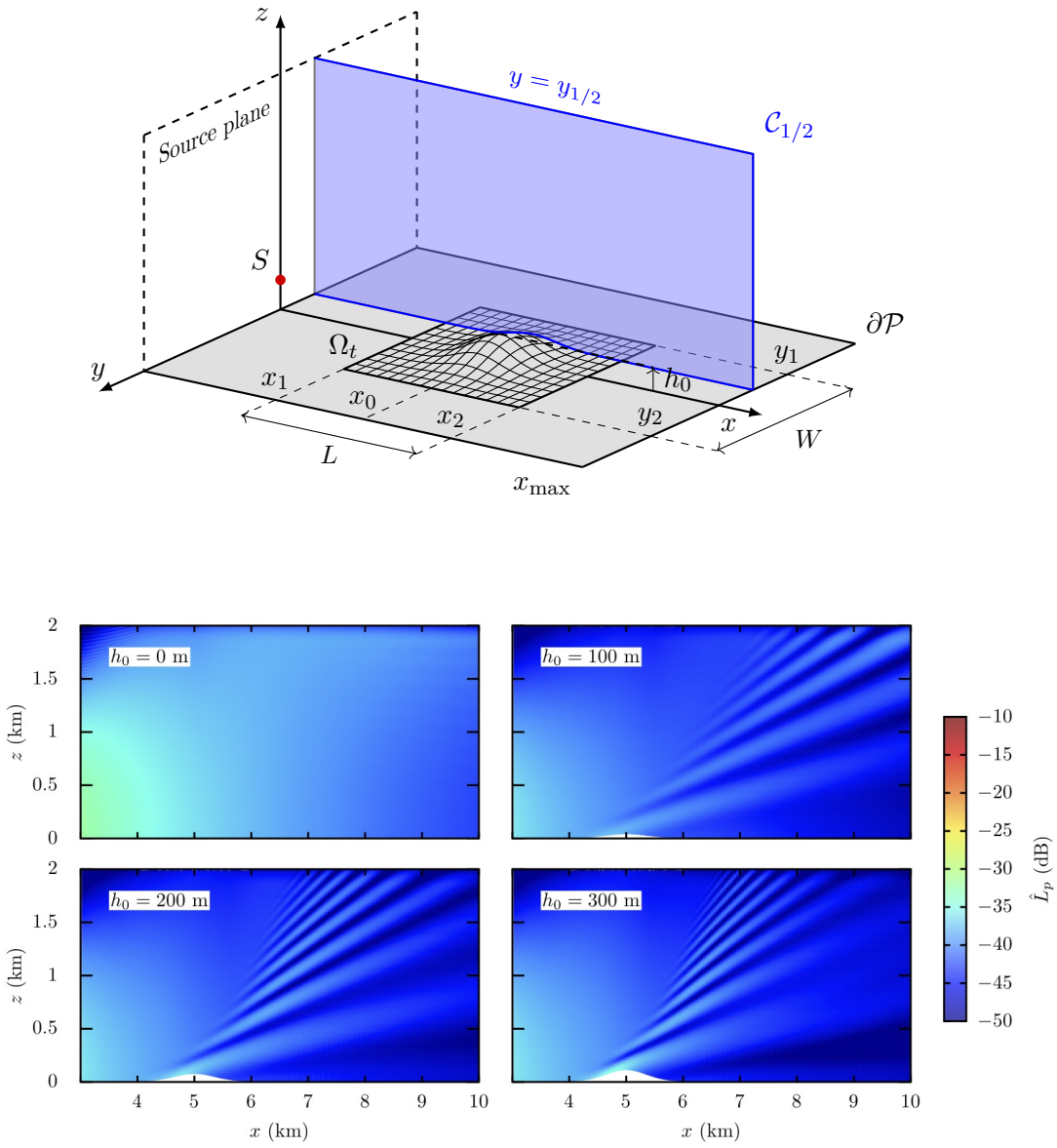

Figure 5.8: 3D BTPE simulation in a homogeneous atmosphere ($c_0 = 343\,\mathrm{m}\cdot\mathrm{s}^{-1}$), $f = 5\,\mathrm{Hz}$ and source located at $x_s = 0$, $y_s = 0$ and $z_s = 25\,\mathrm{m}$. Contour plot of the Relative Sound Pressure Level (RSPL) $\hat{L}_p$ in the plane $\mathcal{C}_{1/2}$ defined by $y = 500$ m, for a Gaussian Hill located at $(x_0, y_0) = (5, 0)$ (km), a width $s_x = s_y = 500$ and a terrain height of $h_0 = 0$ (flat), 100, 200 and 300 m.

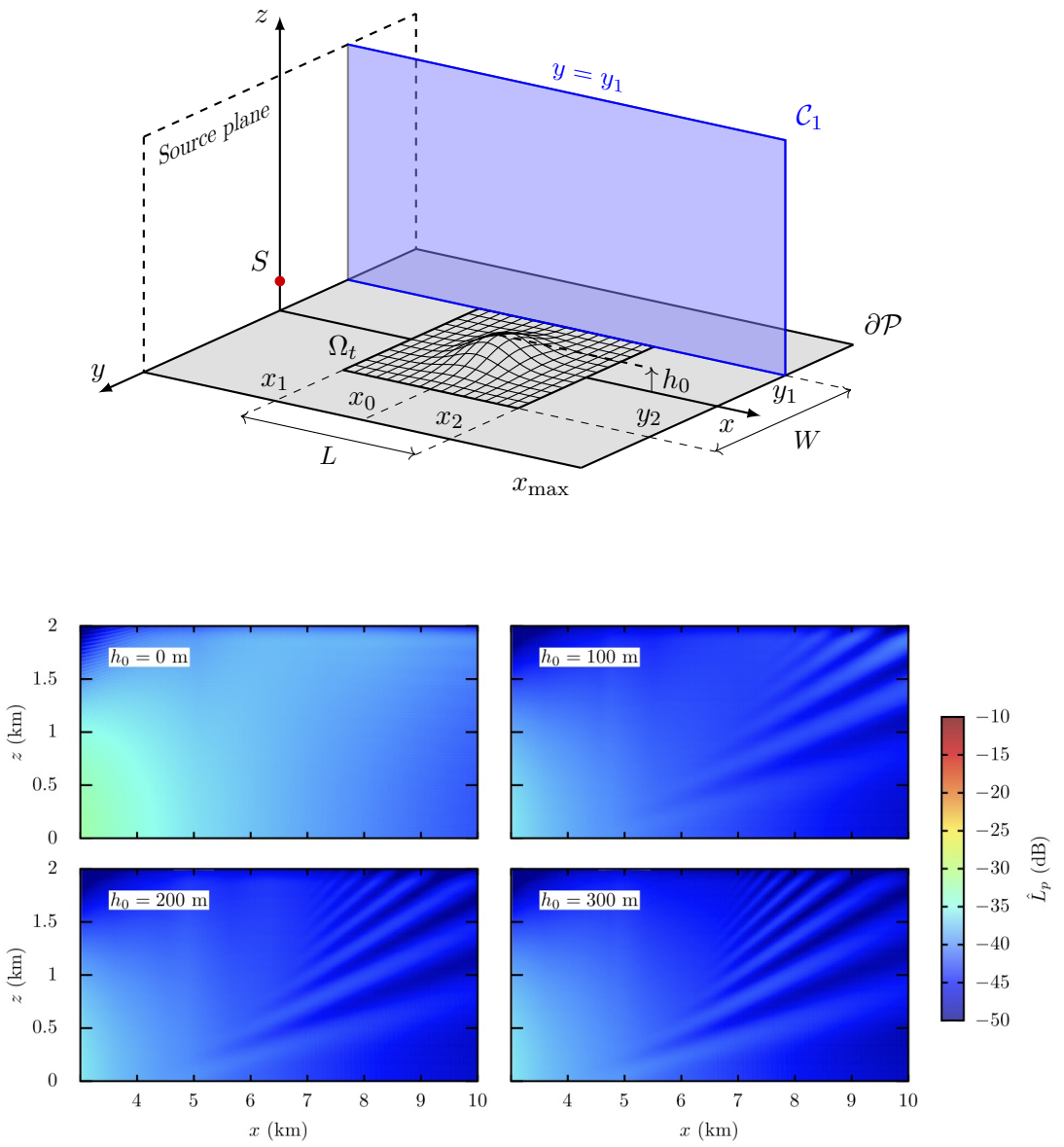

Figure 5.9: 3D BTPE simulation in a homogeneous atmosphere ($c_0 = 343\,\mathrm{m}\cdot\mathrm{s}^{-1}$), $f = 5\,\mathrm{Hz}$ and source located at $x_s = 0$, $y_s = 0$ and $z_s = 25\,\mathrm{m}$. Contour plot of the Relative Sound Pressure Level (RSPL) $\hat{L}_p$ in the plane $\mathcal{C}_1$ defined by $y = 1000$ m, for a Gaussian Hill located at $(x_0, y_0) = (5, 0)$ (km), a width $s_x = s_y = 500$ and a terrain height of $h_0 = 0$ (flat), 100, 200 and 300 m.

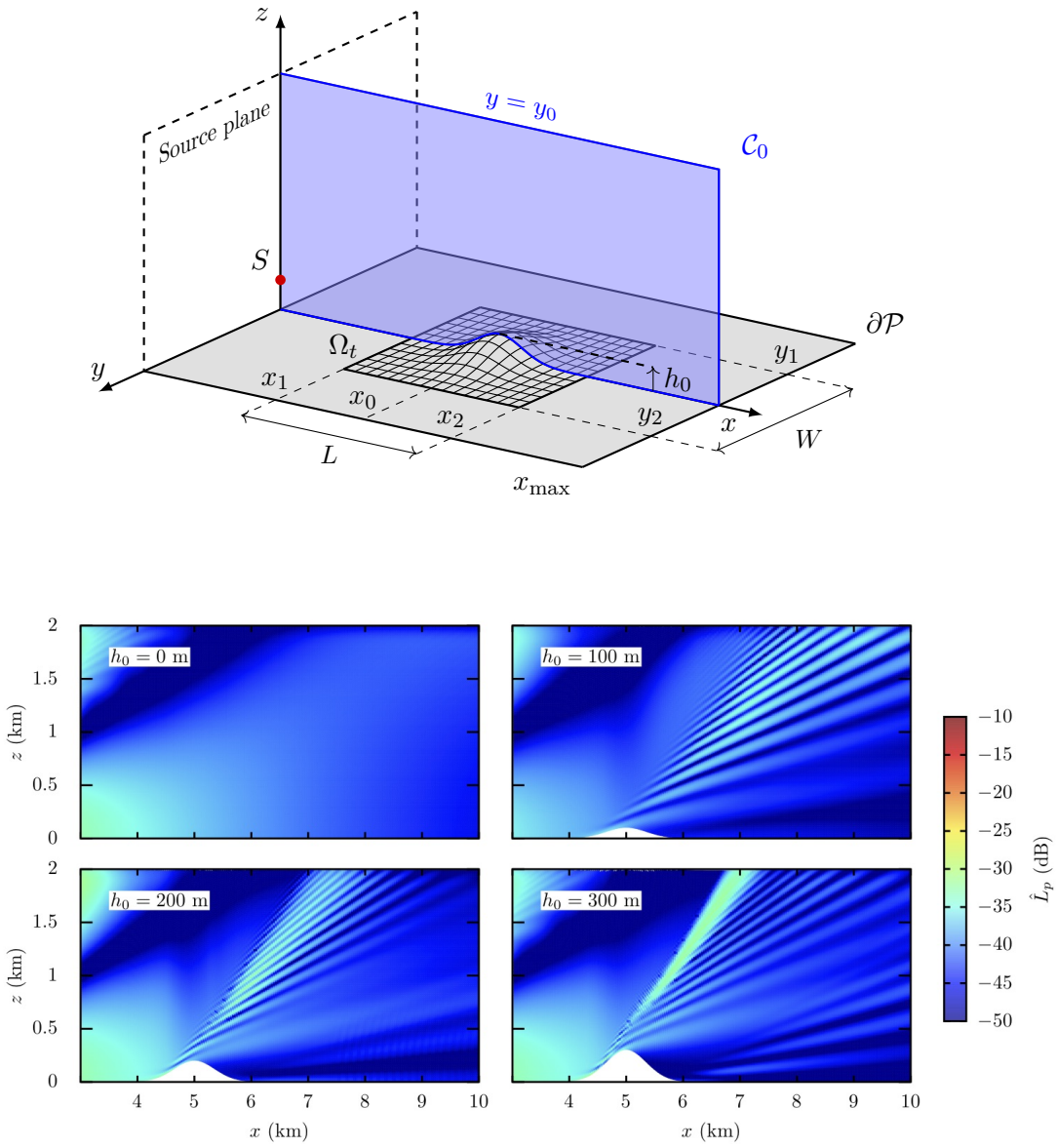

Figure 5.10: 3D BTPE simulation in a homogeneous atmosphere ($c_0 = 343\,\mathrm{m}\cdot\mathrm{s}^{-1}$), $f = 10\,\mathrm{Hz}$ and source located at $x_s = 0$, $y_s = 0$ and $z_s = 25\,\mathrm{m}$. Contour plot of the Relative Sound Pressure Level (RSPL) $\hat{L}_p$ in the plane $\mathcal{C}_0$ defined by $y = 0$ m, for a Gaussian Hill located at $(x_0, y_0) = (5, 0)$ (km), a width $s_x = s_y = 500$ and a terrain height of $h_0 = 0$ (flat), 100, 200 and 300 m.

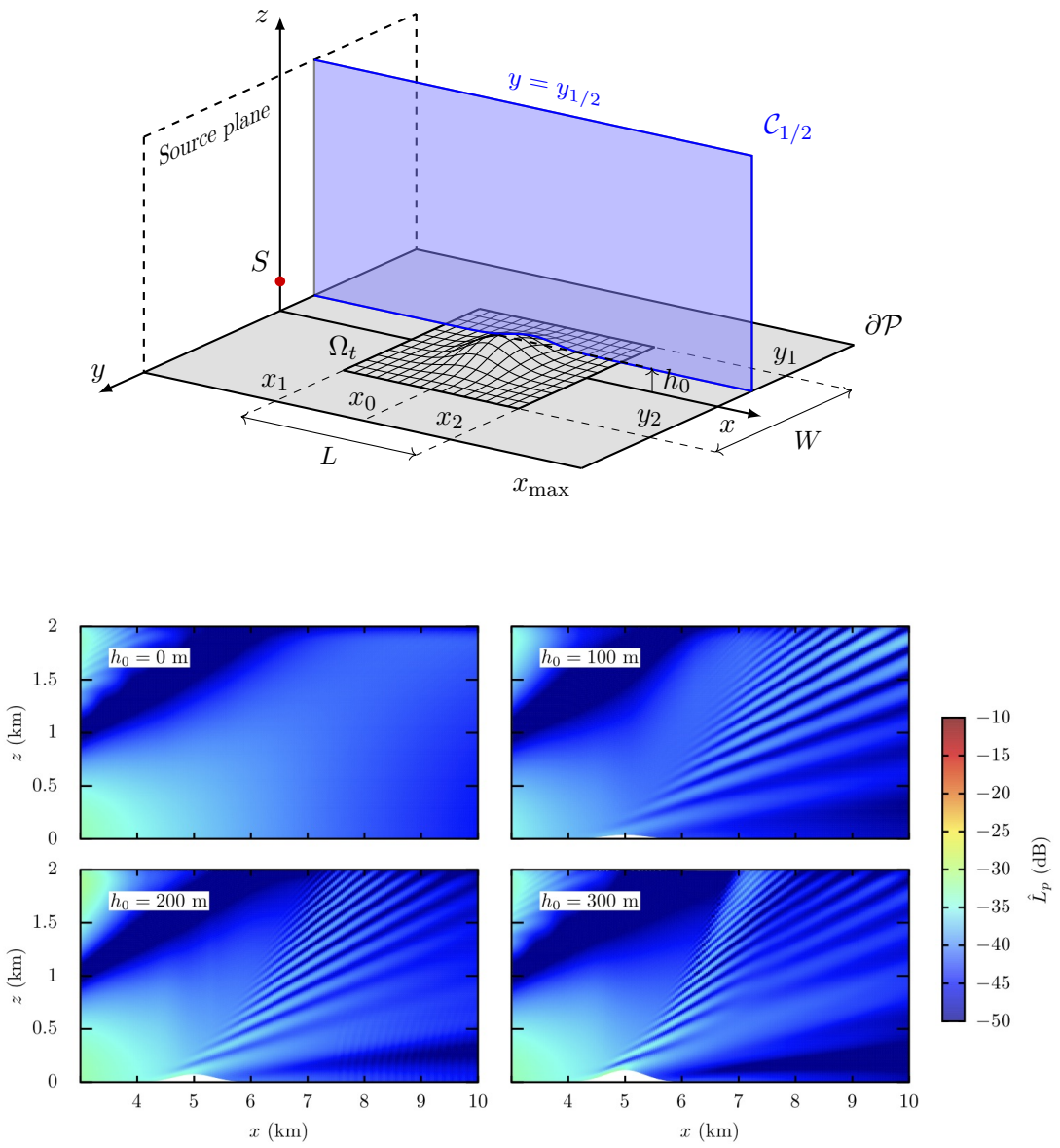

Figure 5.11: 3D BTPE simulation in a homogeneous atmosphere ($c_0 = 343\,\mathrm{m}\cdot\mathrm{s}^{-1}$), $f = 10\,\mathrm{Hz}$ and source located at $x_s = 0$, $y_s = 0$ and $z_s = 25\,\mathrm{m}$. Contour plot of the Relative Sound Pressure Level (RSPL) $\hat{L}_p$ in the plane $\mathcal{C}_{1/2}$ defined by $y = 500$ m, for a Gaussian Hill located at $(x_0, y_0) = (5, 0)$ (km), a width $s_x = s_y = 500$ and a terrain height of $h_0 = 0$ (flat), 100, 200 and 300 m.

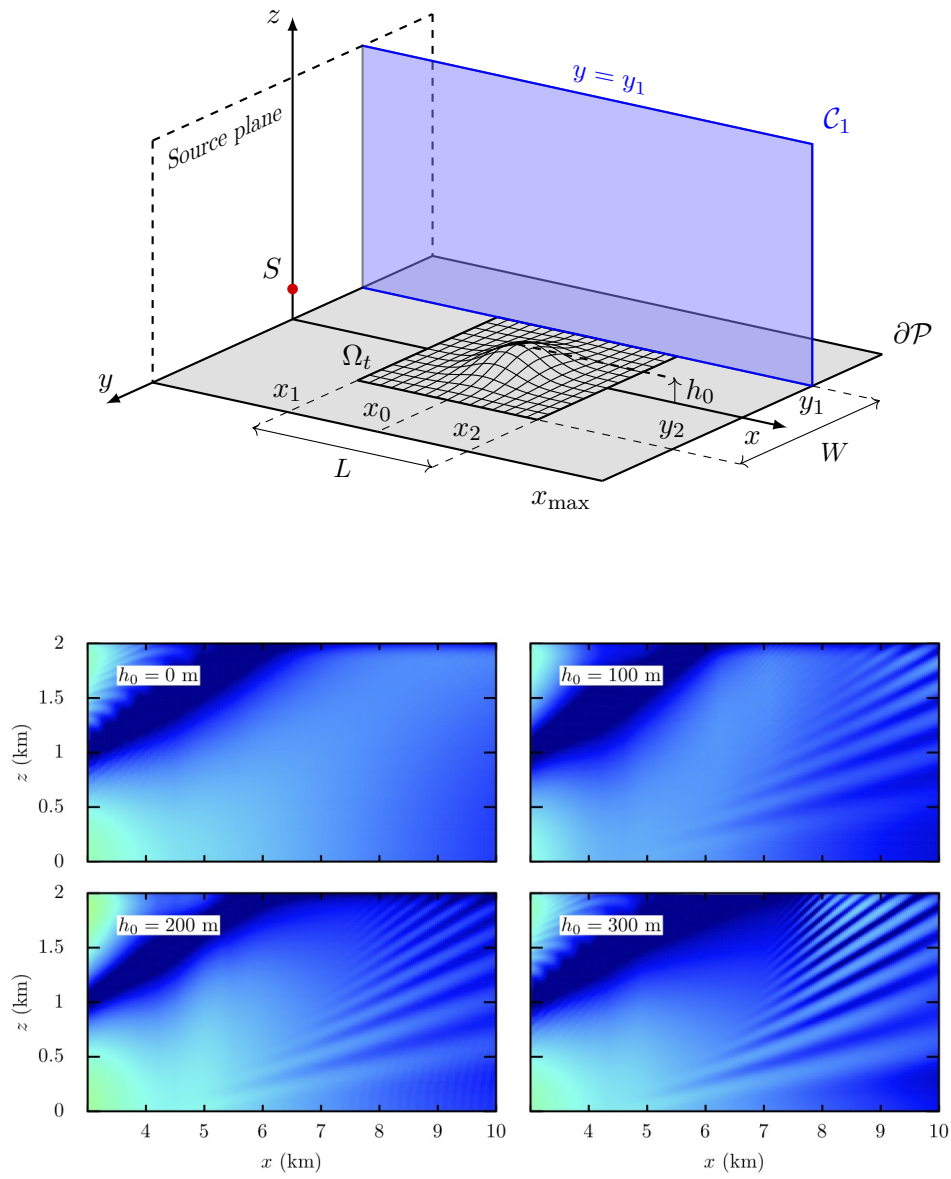

Figure 5.12: 3D BTPE simulation in a homogeneous atmosphere ($c_0 = 343\,\mathrm{m}\cdot\mathrm{s}^{-1}$), $f = 10\,\mathrm{Hz}$ and source located at $x_s = 0$, $y_s = 0$ and $z_s = 25\,\mathrm{m}$. Contour plot of the Relative Sound Pressure Level (RSPL) $\hat{L}_p$ in the plane $\mathcal{C}_1$ defined by $y = 1000$ m, for a Gaussian Hill located at $(x_0, y_0) = (5, 0)$ (km), a width $s_x = s_y = 500$ and a terrain height of $h_0 = 0$ (flat), 100, 200 and 300 m.

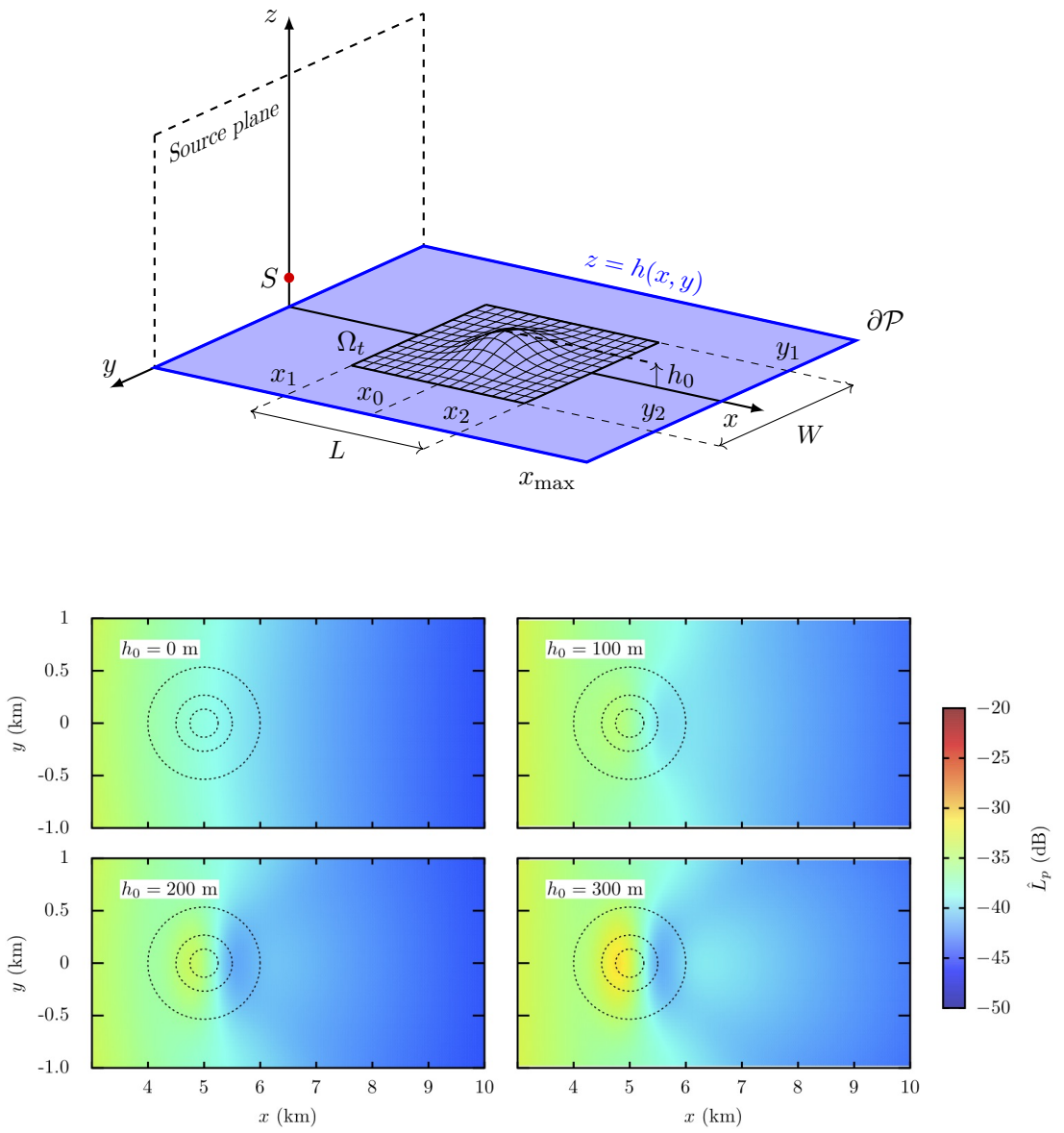

Figure 5.13: 3D BTPE simulation in a homogeneous atmosphere ($c_0 = 343\,\mathrm{m}\cdot\mathrm{s}^{-1}$), $f = 0.5\,\mathrm{Hz}$ and source located at $x_s = 0$, $y_s = 0$ and $z_s = 25\,\mathrm{m}$. Contour plot of the Relative Sound Pressure Level (RSPL) $\hat{L}_p$ accross the bottom boundary $\partial\mathcal{P}$ defined by $z = h(x, y)$, for a Gaussian Hill located at $(x_0, y_0) = (5, 0)$ (km), a width $s_x = s_y = 500$ and a terrain height of $h_0 = 0$ (flat), 100, 200 and 300 m.

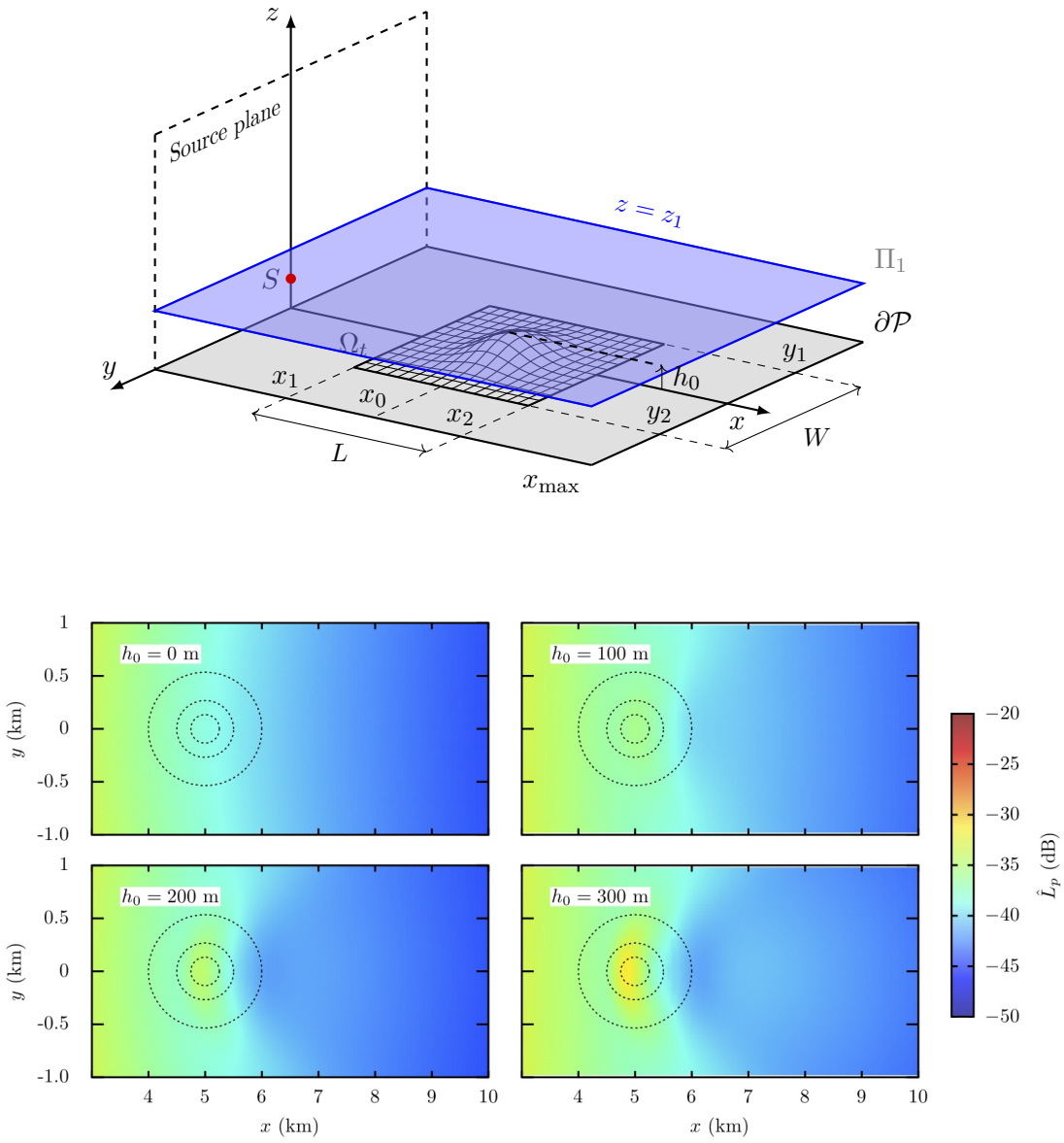

Figure 5.14: 3D BTPE simulation in a homogeneous atmosphere ($c_0 = 343\,\mathrm{m}\cdot\mathrm{s}^{-1}$), $f = 0.5\,\mathrm{Hz}$ and source located at $x_s = 0$, $y_s = 0$ and $z_s = 25\,\mathrm{m}$. Contour plot of the Relative Sound Pressure Level (RSPL) $\hat{L}_p$ in the plane Π_1 defined by $z = 350$ m, for a Gaussian Hill located at $(x_0, y_0) = (5, 0)$ (km), a width $s_x = s_y = 500$ and a terrain height of $h_0 = 0$ (flat), 100, 200 and 300 m.

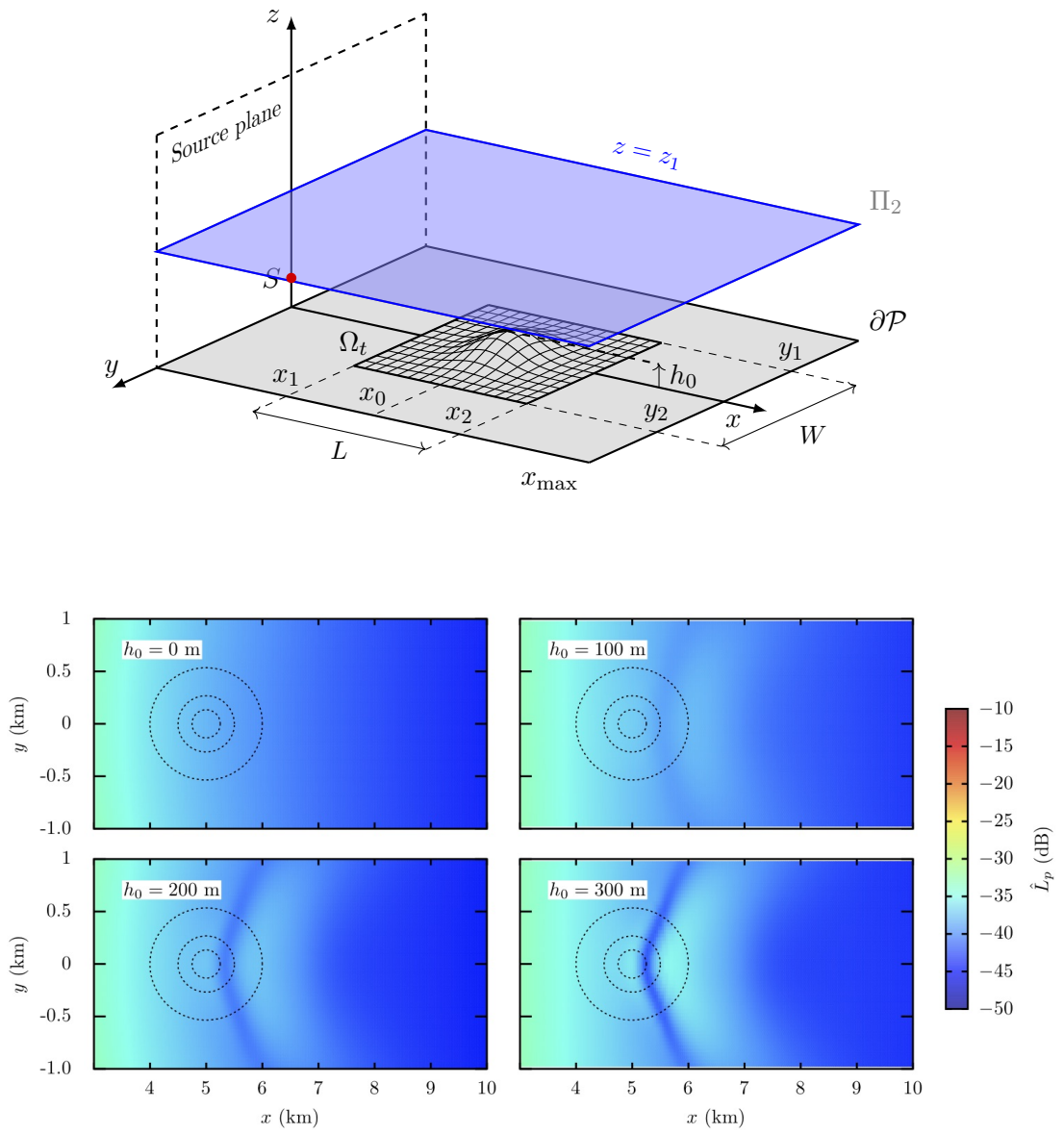

Figure 5.15: 3D BTPE simulation in a homogeneous atmosphere ($c_0 = 343\,\mathrm{m}\cdot\mathrm{s}^{-1}$), $f = 0.5\,\mathrm{Hz}$ and source located at $x_s = 0$, $y_s = 0$ and $z_s = 25\,\mathrm{m}$. Contour plot of the Relative Sound Pressure Level (RSPL) $\hat{L}_p$ in the plane Π_2 defined by $z = 1000$ m, for a Gaussian Hill located at $(x_0, y_0) = (5, 0)$ (km), a width $s_x = s_y = 500$ and a terrain height of $h_0 = 0$ (flat), 100, 200 and 300 m.

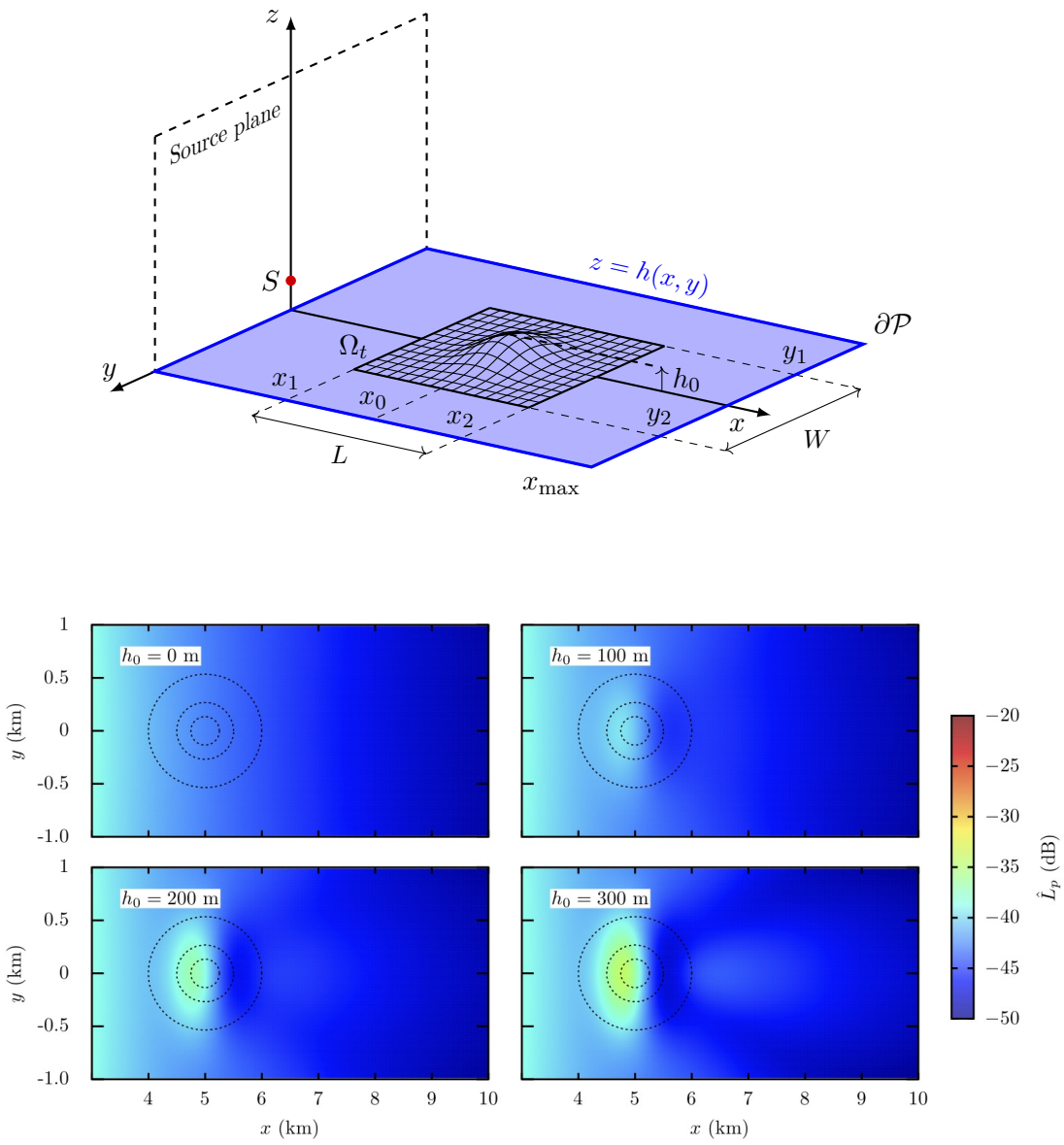

Figure 5.16: 3D BTPE simulation in a homogeneous atmosphere ($c_0 = 343\,\mathrm{m}\cdot\mathrm{s}^{-1}$), $f = 1\,\mathrm{Hz}$ and source located at $x_s = 0$, $y_s = 0$ and $z_s = 25\,\mathrm{m}$. Contour plot of the Relative Sound Pressure Level (RSPL) $\hat{L}_p$ accross the bottom boundary $\partial\mathcal{P}$ defined by $z = h(x, y)$, for a Gaussian Hill located at $(x_0, y_0) = (5, 0)$ (km), a width $s_x = s_y = 500$ and a terrain height of $h_0 = 0$ (flat), 100, 200 and 300 m.

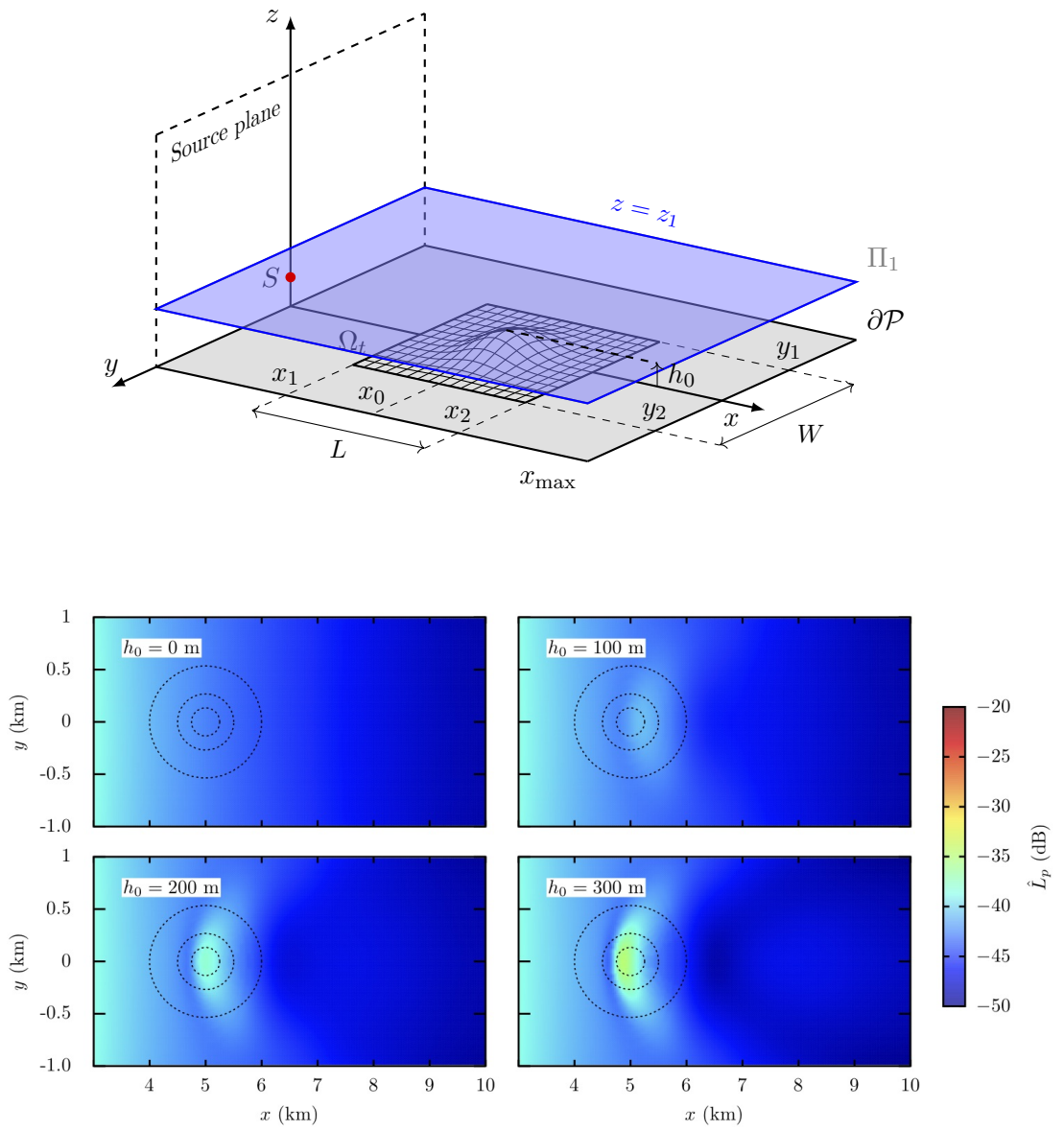

Figure 5.17: 3D BTPE simulation in a homogeneous atmosphere ($c_0 = 343\,\mathrm{m}\cdot\mathrm{s}^{-1}$), $f = 1\,\mathrm{Hz}$ and source located at $x_s = 0$, $y_s = 0$ and $z_s = 25\,\mathrm{m}$. Contour plot of the Relative Sound Pressure Level (RSPL) $\hat{L}_p$ in the plane Π_1 defined by $z = 350$ m, for a Gaussian Hill located at $(x_0, y_0) = (5, 0)$ (km), a width $s_x = s_y = 500$ and a terrain height of $h_0 = 0$ (flat), 100, 200 and 300 m.

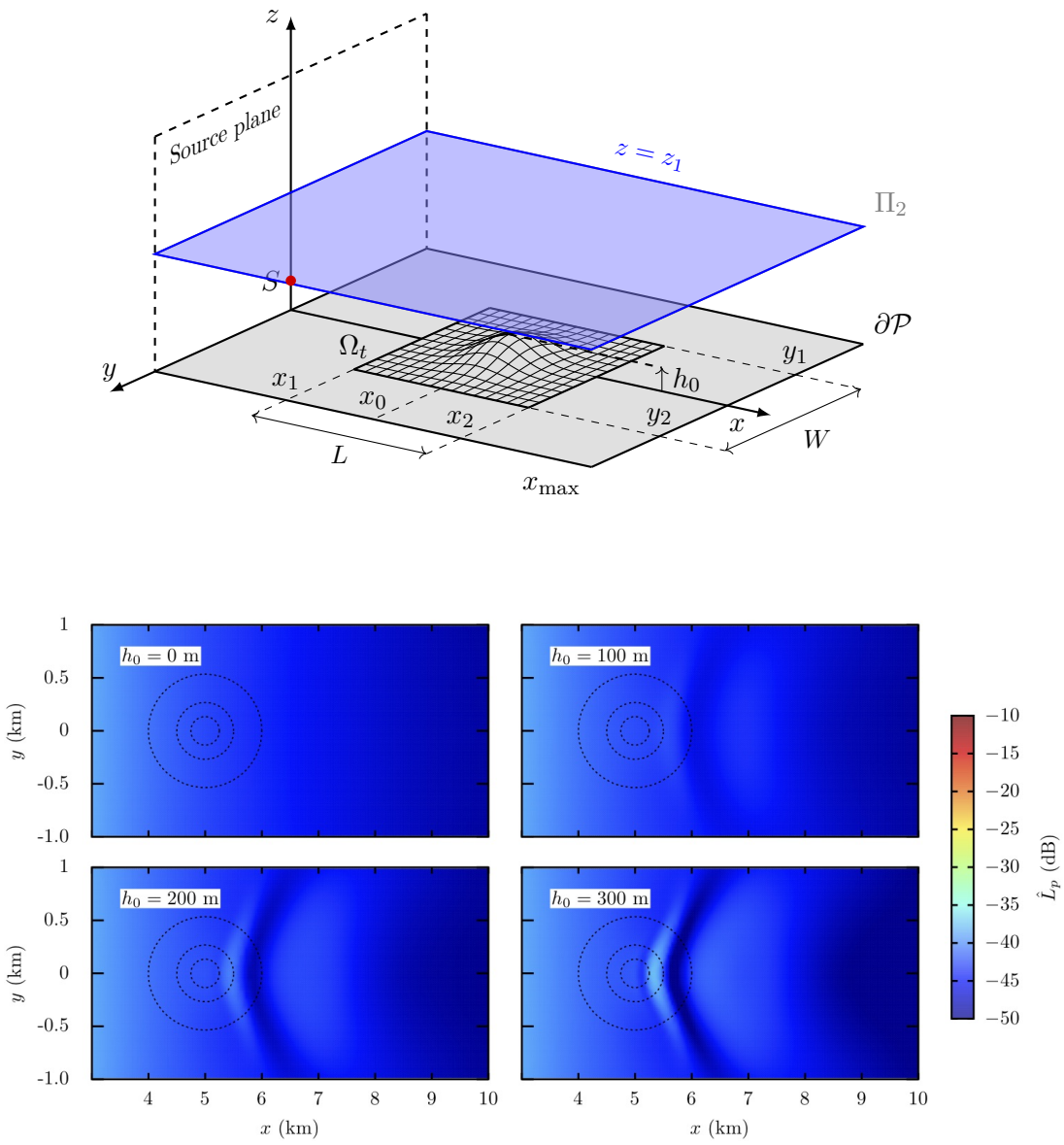

Figure 5.18: 3D BTPE simulation in a homogeneous atmosphere ($c_0 = 343\,\mathrm{m}\cdot\mathrm{s}^{-1}$), $f = 1\,\mathrm{Hz}$ and source located at $x_s = 0$, $y_s = 0$ and $z_s = 25\,\mathrm{m}$. Contour plot of the Relative Sound Pressure Level (RSPL) $\hat{L}_p$ in the plane Π_2 defined by $z = 1000$ m, for a Gaussian Hill located at $(x_0, y_0) = (5, 0)$ (km), a width $s_x = s_y = 500$ and a terrain height of $h_0 = 0$ (flat), 100, 200 and 300 m.

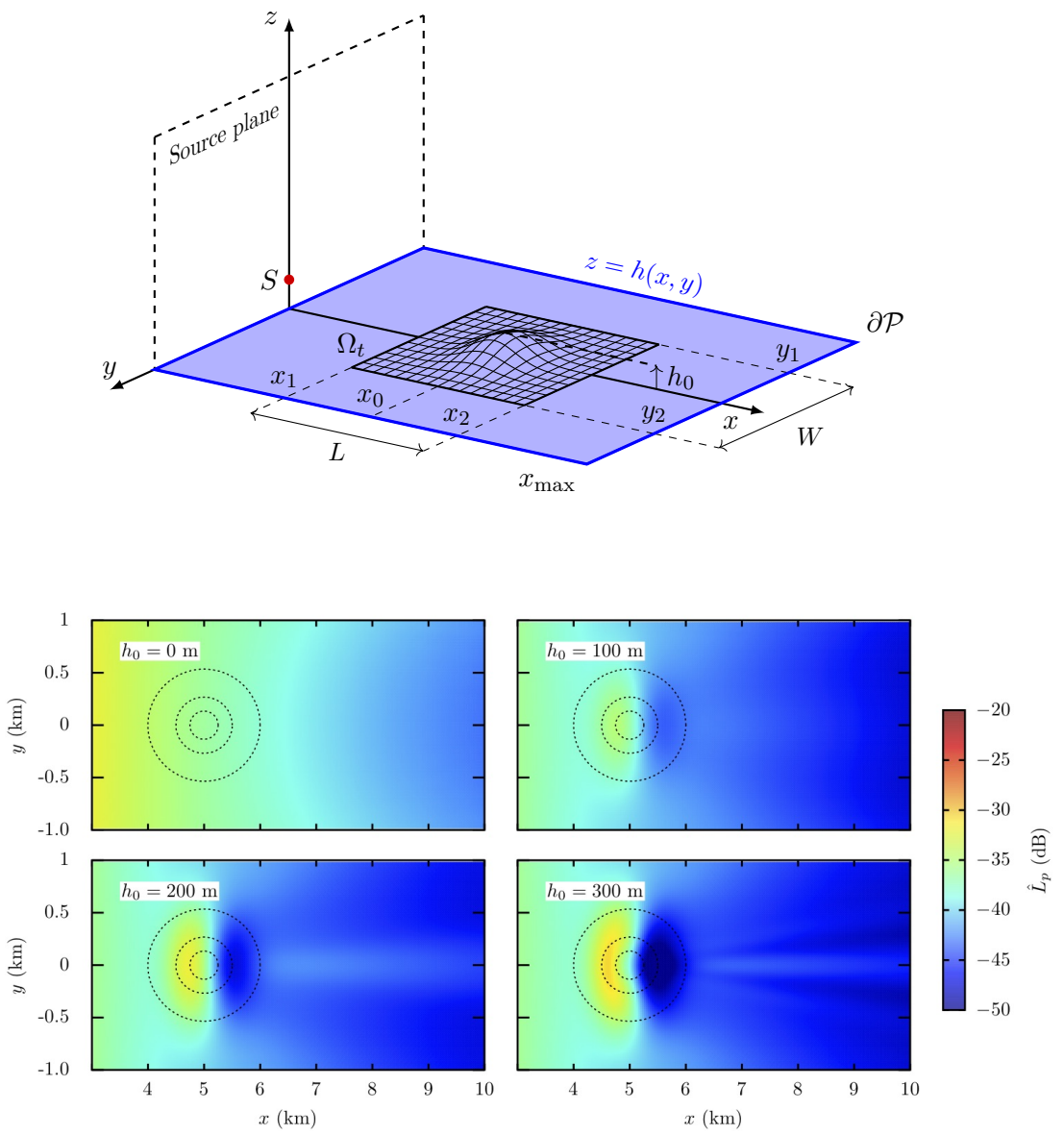

Figure 5.19: 3D BTPE simulation in a homogeneous atmosphere ($c_0 = 343\,\mathrm{m}\cdot\mathrm{s}^{-1}$), $f = 5\,\mathrm{Hz}$ and source located at $x_s = 0$, $y_s = 0$ and $z_s = 25\,\mathrm{m}$. Contour plot of the Relative Sound Pressure Level (RSPL) $\hat{L}_p$ accross the bottom boundary $\partial\mathcal{P}$ defined by $z = h(x, y)$, for a Gaussian Hill located at $(x_0, y_0) = (5, 0)$ (km), a width $s_x = s_y = 500$ and a terrain height of $h_0 = 0$ (flat), 100, 200 and 300 m.

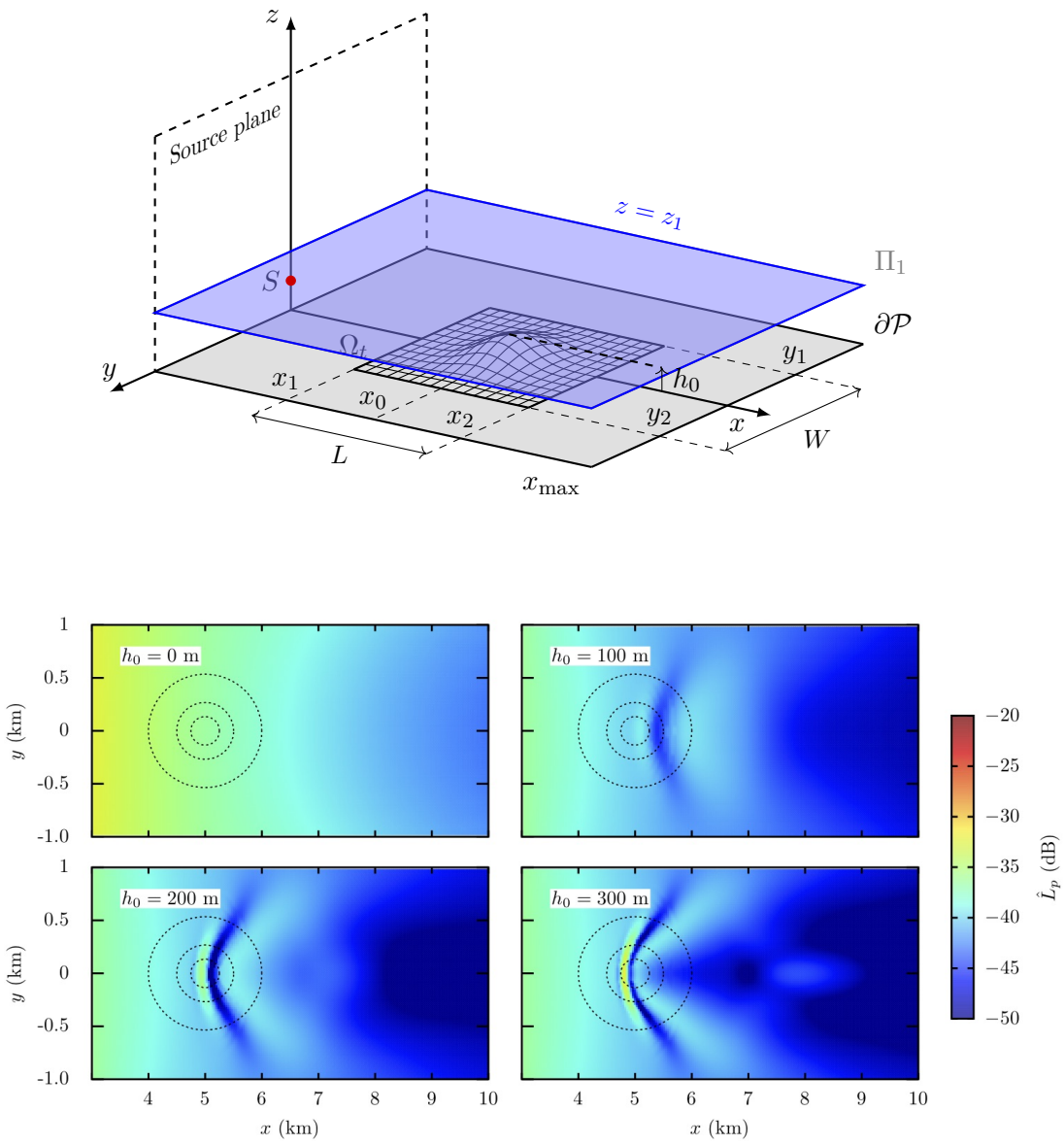

Figure 5.20: 3D BTPE simulation in a homogeneous atmosphere ($c_0 = 343\,\mathrm{m}\cdot\mathrm{s}^{-1}$), $f = 5\,\mathrm{Hz}$ and source located at $x_s = 0$, $y_s = 0$ and $z_s = 25\,\mathrm{m}$. Contour plot of the Relative Sound Pressure Level (RSPL) $\hat{L}_p$ in the plane Π_1 defined by $z = 350$ m, for a Gaussian Hill located at $(x_0, y_0) = (5, 0)$ (km), a width $s_x = s_y = 500$ and a terrain height of $h_0 = 0$ (flat), 100, 200 and 300 m.

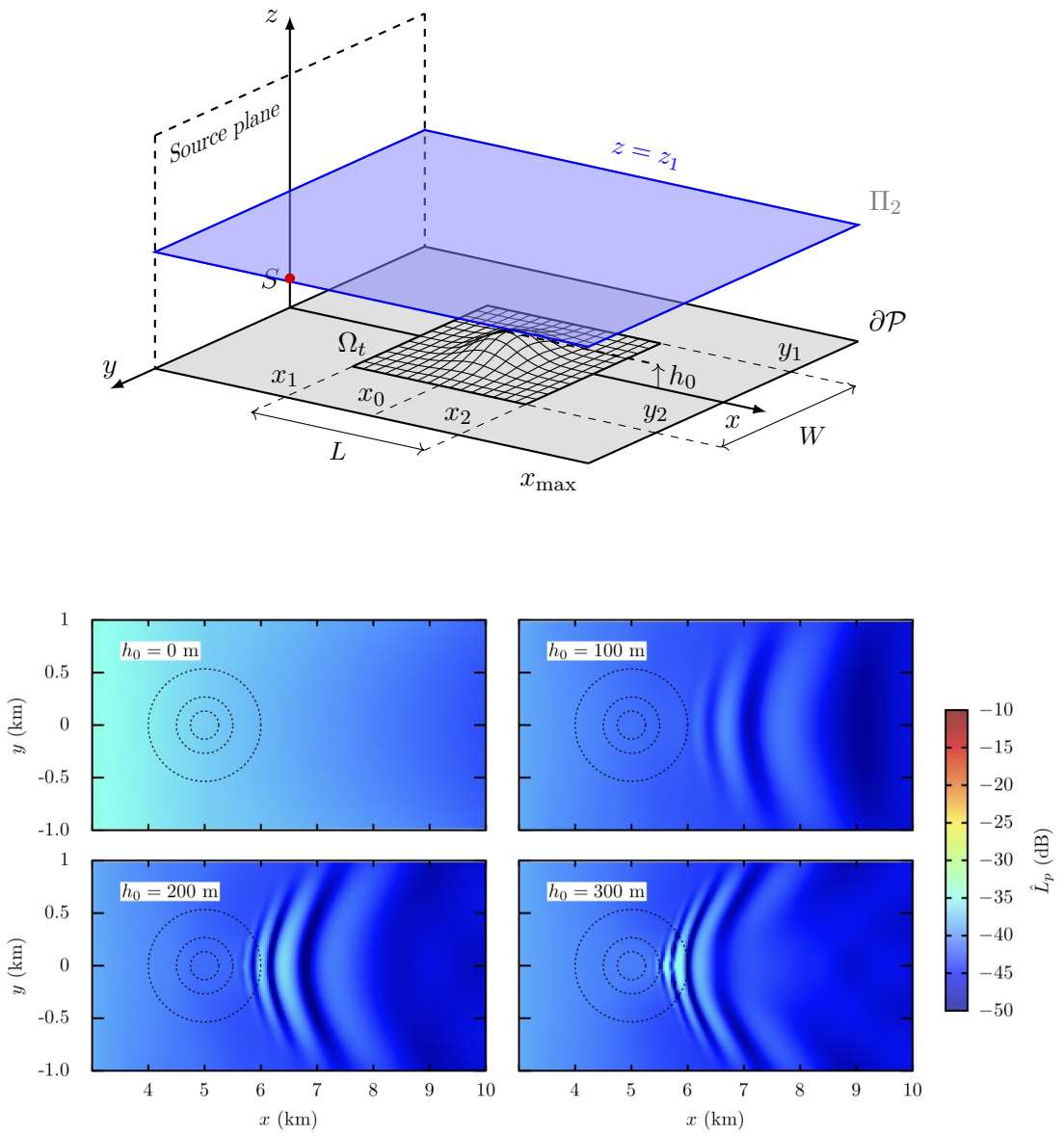

Figure 5.21: 3D BTPE simulation in a homogeneous atmosphere ($c_0 = 343\,\mathrm{m}\cdot\mathrm{s}^{-1}$), $f = 5$ Hz and source located at $x_s = 0$, $y_s = 0$ and $z_s = 25$ m. Contour plot of the Relative Sound Pressure Level (RSPL) $\hat{L}_p$ in the plane Π_2 defined by $z = 1000$ m, for a Gaussian Hill located at $(x_0, y_0) = (5, 0)$ (km), a width $s_x = s_y = 500$ and a terrain height of $h_0 = 0$ (flat), 100, 200 and 300 m.

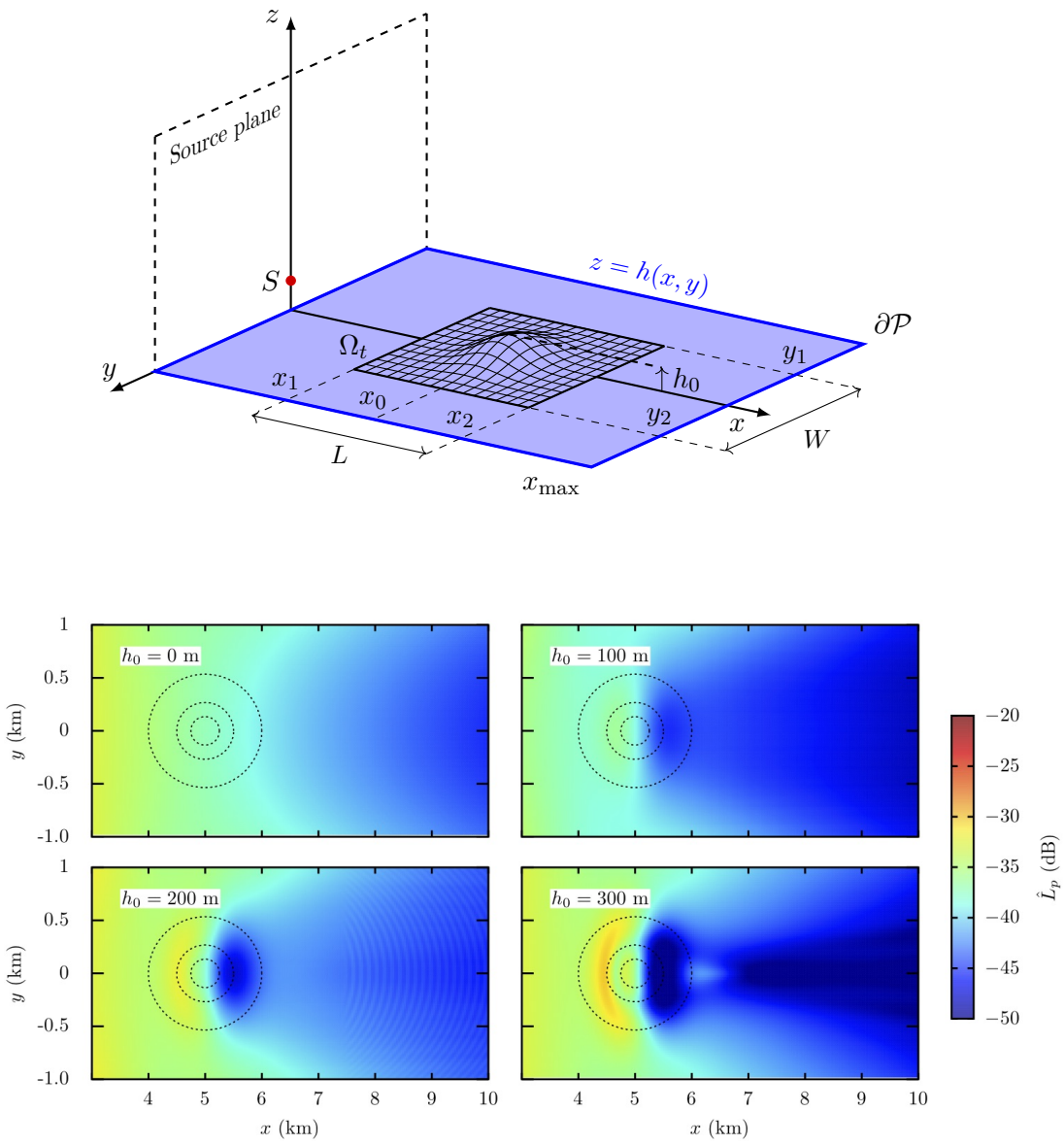

Figure 5.22: 3D BTPE simulation in a homogeneous atmosphere ($c_0 = 343\,\mathrm{m}\cdot\mathrm{s}^{-1}$), $f = 10\,\mathrm{Hz}$ and source located at $x_s = 0$, $y_s = 0$ and $z_s = 25\,\mathrm{m}$. Contour plot of the Relative Sound Pressure Level (RSPL) $\hat{L}_p$ accross the bottom boundary $\partial\mathcal{P}$ defined by $z = h(x, y)$, for a Gaussian Hill located at $(x_0, y_0) = (5, 0)$ (km), a width $s_x = s_y = 500$ and a terrain height of $h_0 = 0$ (flat), 100, 200 and 300 m.

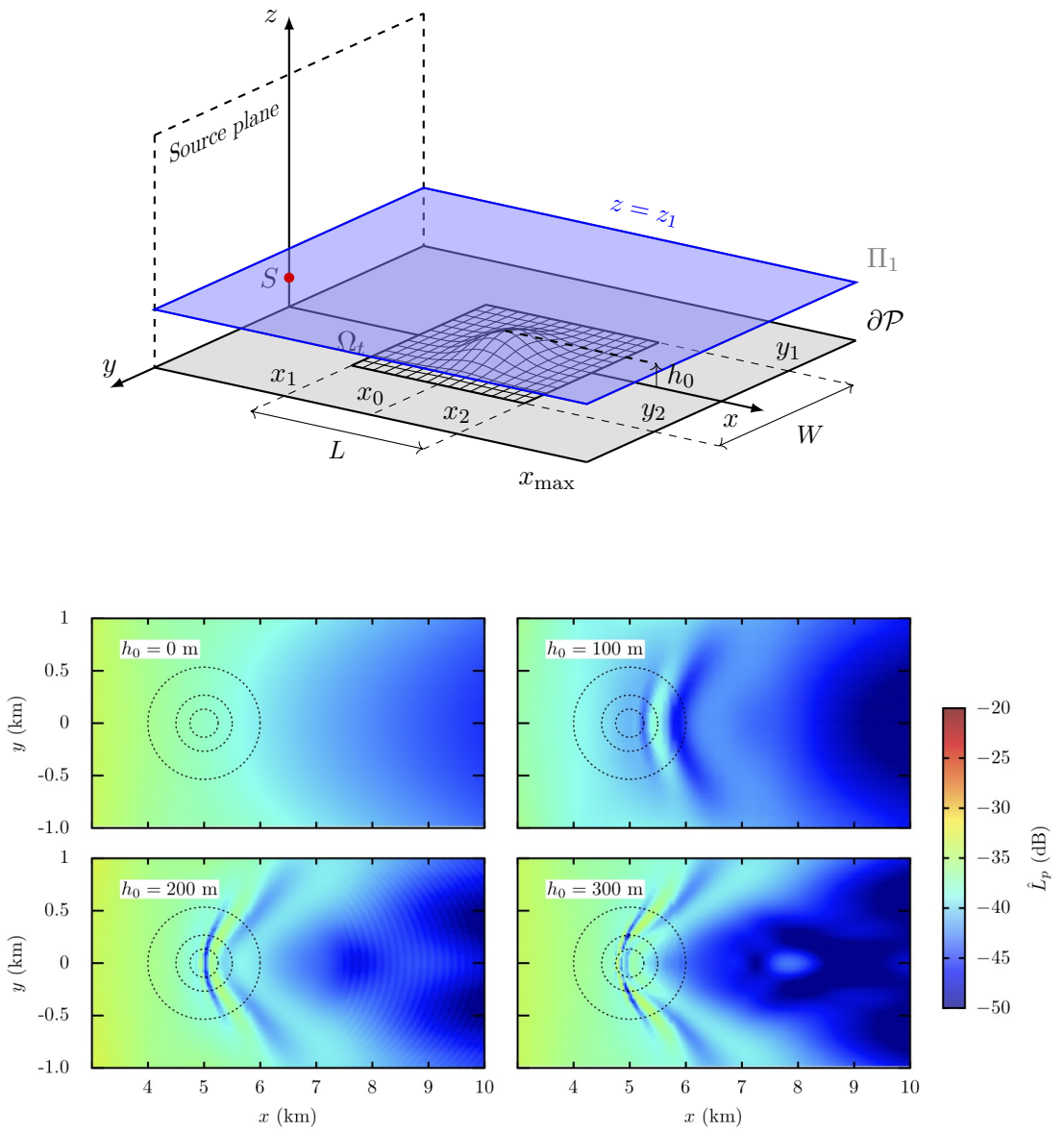

Figure 5.23: 3D BTPE simulation in a homogeneous atmosphere ($c_0 = 343\,\mathrm{m}\cdot\mathrm{s}^{-1}$), $f = 10\,\mathrm{Hz}$ and source located at $x_s = 0$, $y_s = 0$ and $z_s = 25\,\mathrm{m}$. Contour plot of the Relative Sound Pressure Level (RSPL) $\hat{L}_p$ in the plane Π_1 defined by $z = 350$ m, for a Gaussian Hill located at $(x_0, y_0) = (5, 0)$ (km), a width $s_x = s_y = 500$ and a terrain height of $h_0 = 0$ (flat), 100, 200 and 300 m.

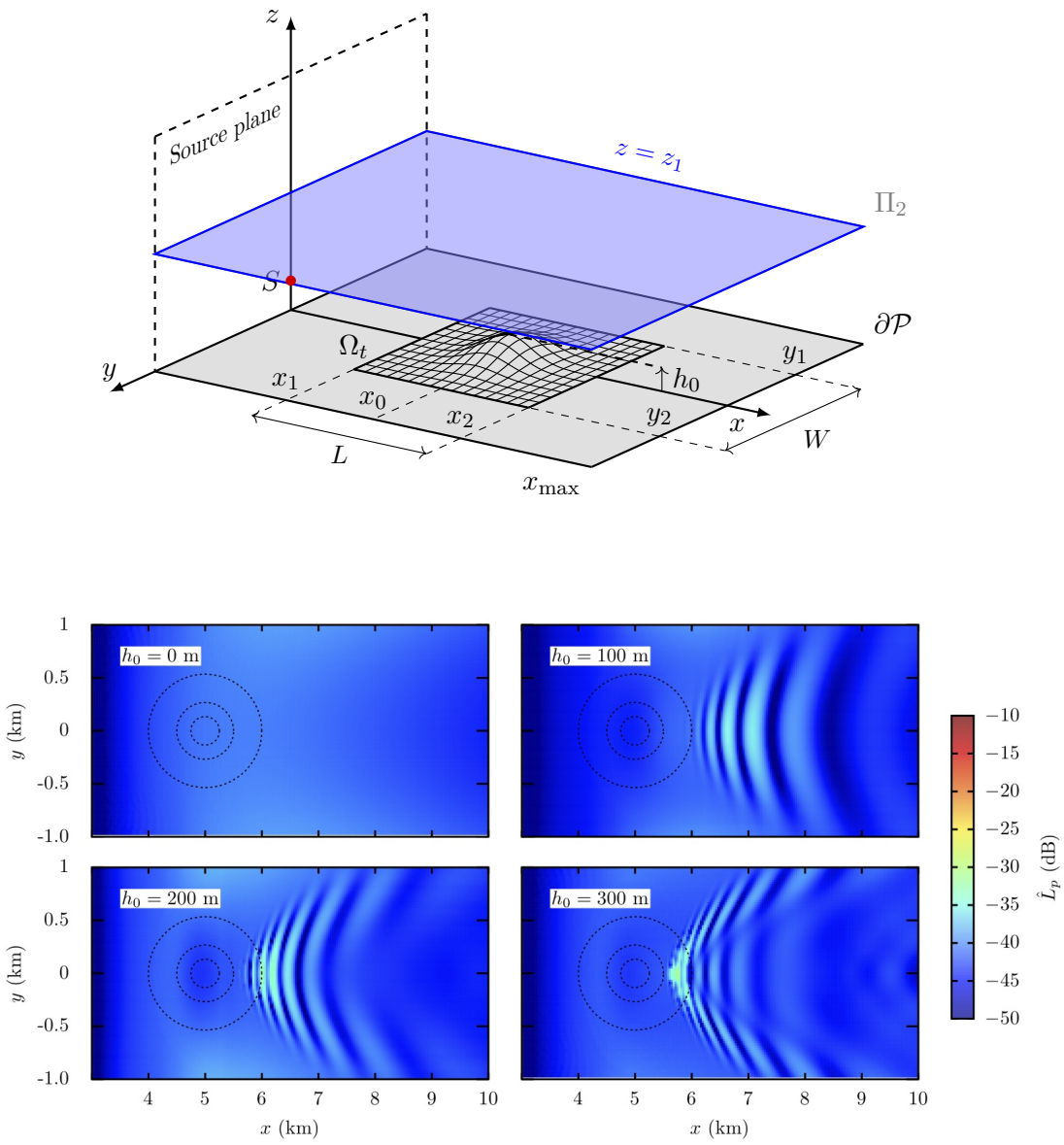

Figure 5.24: 3D BTPE simulation in a homogeneous atmosphere ($c_0 = 343\,\mathrm{m}\cdot\mathrm{s}^{-1}$), $f = 10\,\mathrm{Hz}$ and source located at $x_s = 0$, $y_s = 0$ and $z_s = 25\,\mathrm{m}$. Contour plot of the Relative Sound Pressure Level (RSPL) $\hat{L}_p$ in the plane Π_2 defined by $z = 1000$ m, for a Gaussian Hill located at $(x_0, y_0) = (5, 0)$ (km), a width $s_x = s_y = 500$ and a terrain height of $h_0 = 0$ (flat), 100, 200 and 300 m.

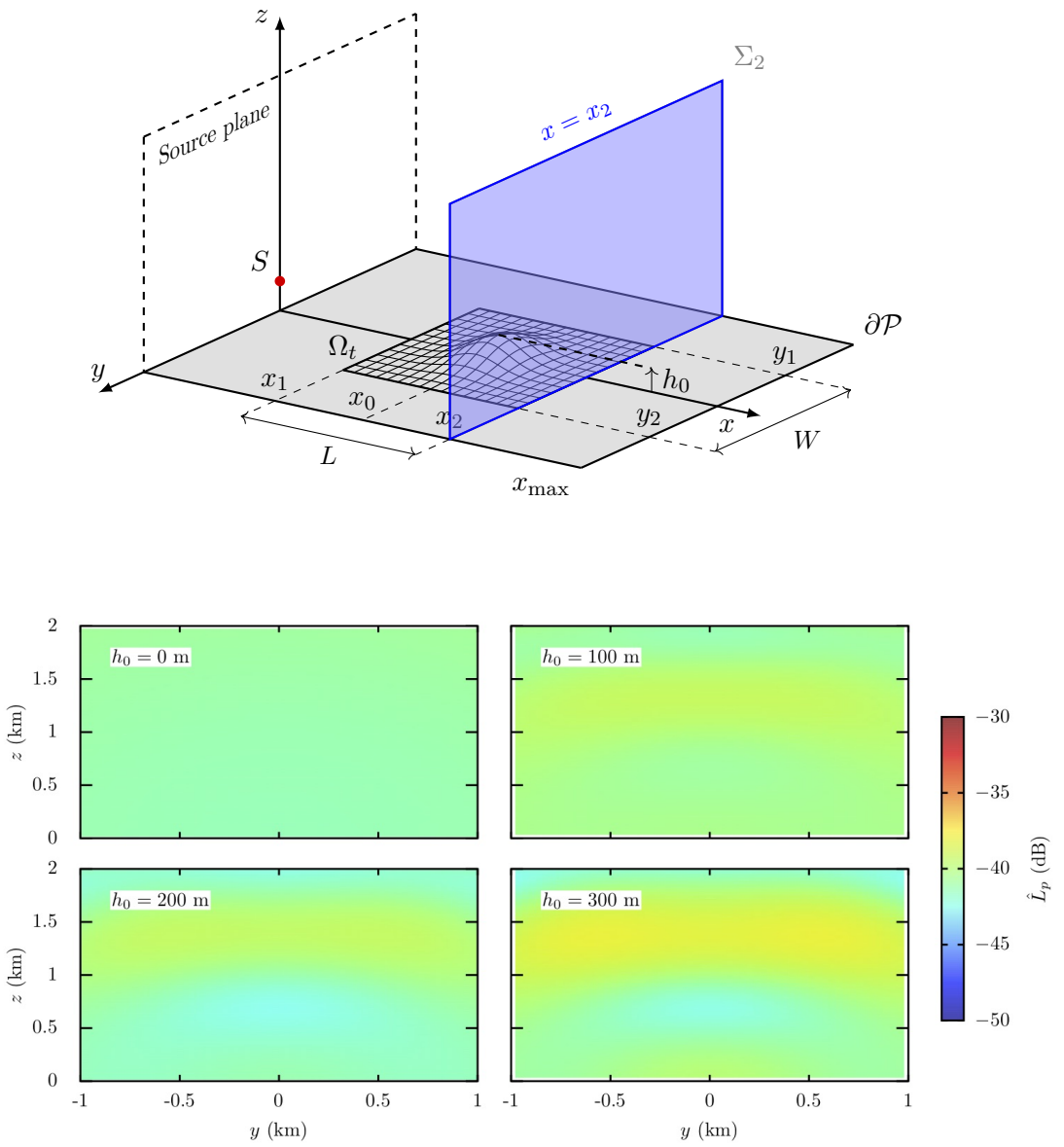

Figure 5.25: 3D BTPE simulation in a homogeneous atmosphere ($c_0 = 343\,\mathrm{m}\cdot\mathrm{s}^{-1}$), $f = 0.5\,\mathrm{Hz}$ and source located at $x_s = 0$, $y_s = 0$ and $z_s = 25\,\mathrm{m}$. Contour plot of the Relative Sound Pressure Level (RSPL) $\hat{L}_p$ in the plane Σ_2 defined by $z = 1000$ m, for a Gaussian Hill located at $(x_0, y_0) = (5, 0)$ (km), a width $s_x = s_y = 500$ and a terrain height of $h_0 = 0$ (flat), 100, 200 and 300 m.

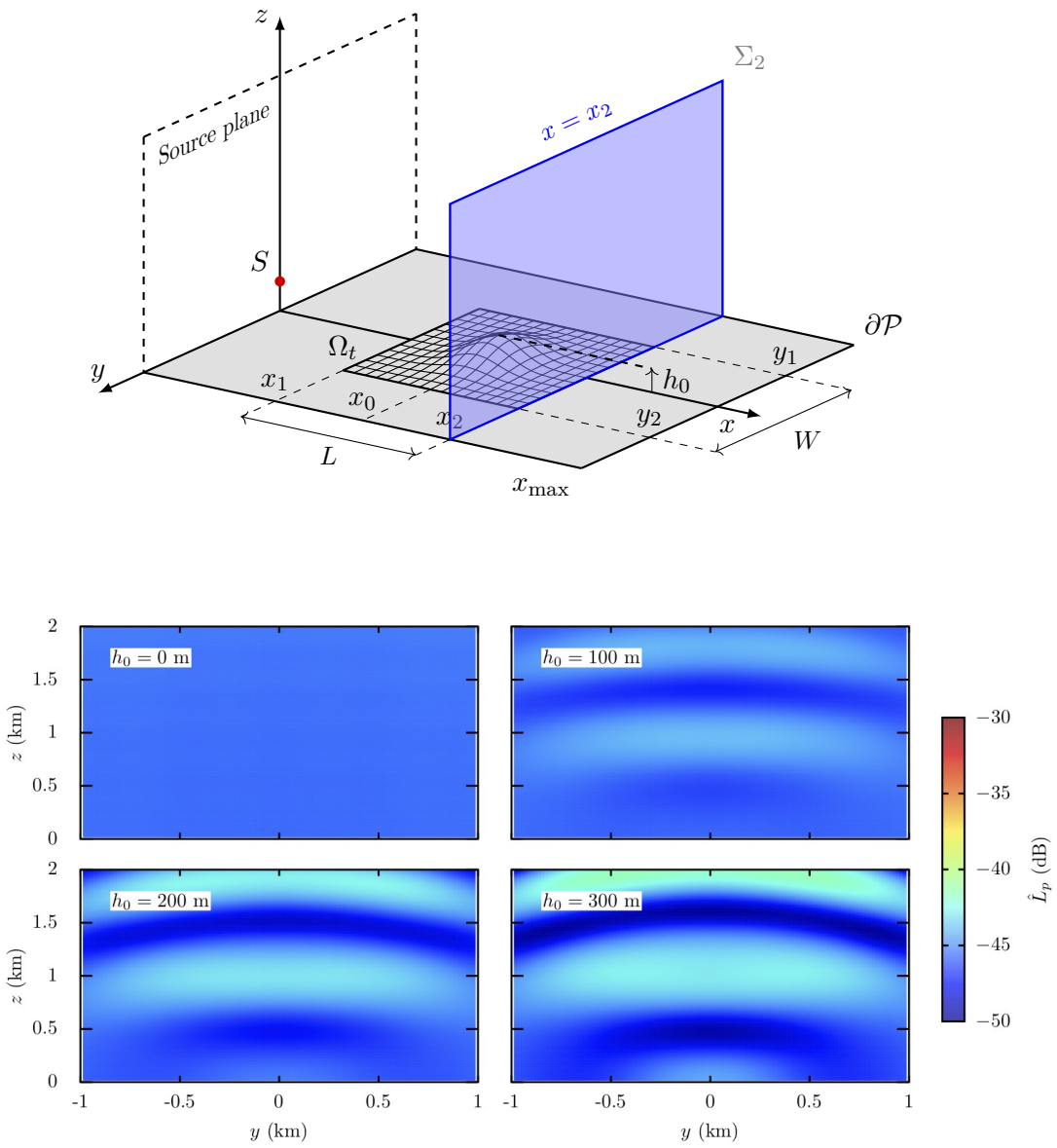

Figure 5.26: 3D BTPE simulation in a homogeneous atmosphere ($c_0 = 343\,\mathrm{m}\cdot\mathrm{s}^{-1}$), $f = 1\,\mathrm{Hz}$ and source located at $x_s = 0$, $y_s = 0$ and $z_s = 25\,\mathrm{m}$. Contour plot of the Relative Sound Pressure Level (RSPL) $\hat{L}_p$ in the plane Σ_2 defined by $z = 1000$ m, for a Gaussian Hill located at $(x_0, y_0) = (5, 0)$ (km), a width $s_x = s_y = 500$ and a terrain height of $h_0 = 0$ (flat), 100, 200 and 300 m.

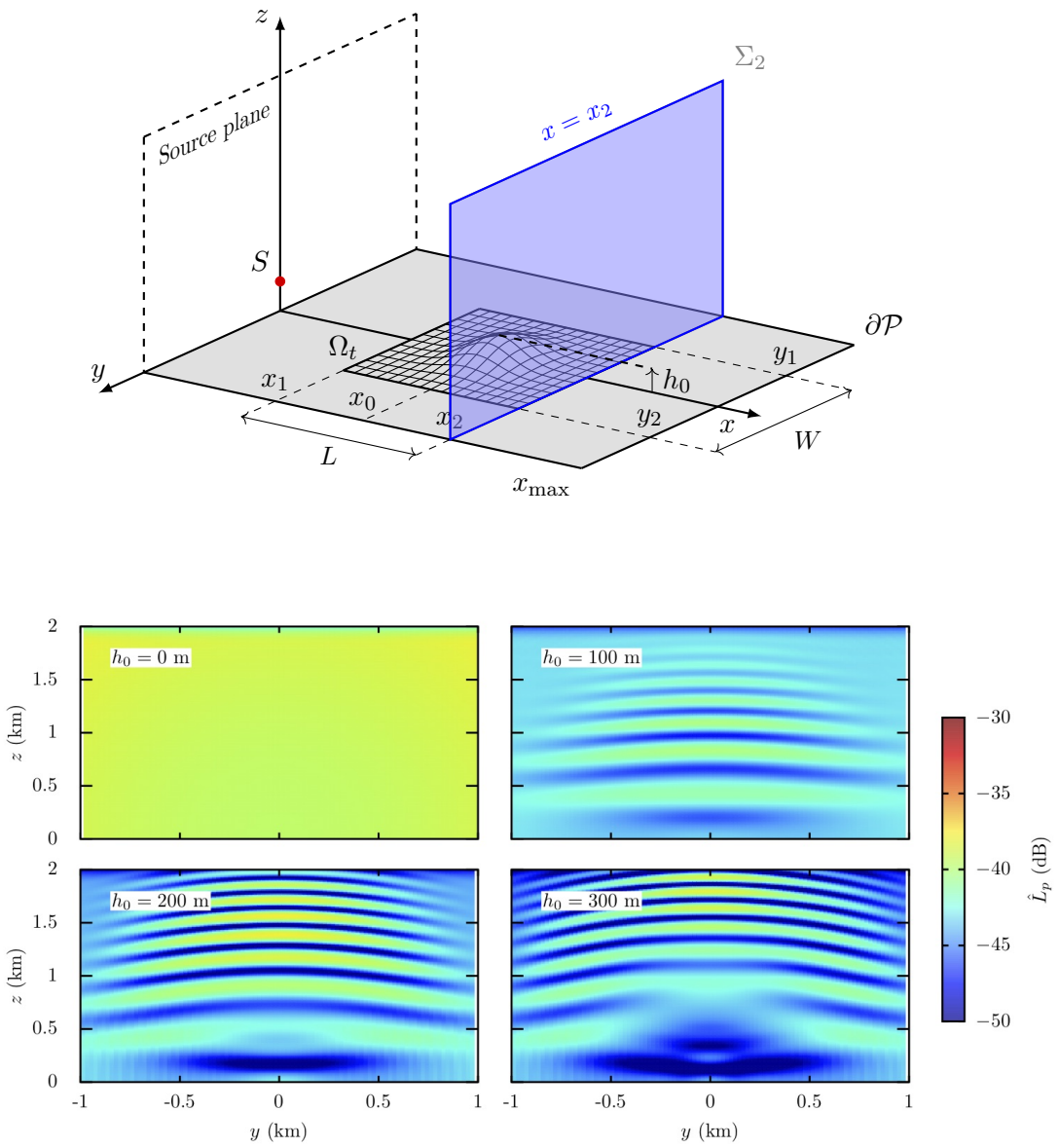

Figure 5.27: 3D BTPE simulation in a homogeneous atmosphere ($c_0 = 343\,\mathrm{m}\cdot\mathrm{s}^{-1}$), $f = 5\,\mathrm{Hz}$ and source located at $x_s = 0$, $y_s = 0$ and $z_s = 25\,\mathrm{m}$. Contour plot of the Relative Sound Pressure Level (RSPL) $\hat{L}_p$ in the plane Σ_2 defined by $z = 1000$ m, for a Gaussian Hill located at $(x_0, y_0) = (5, 0)$ (km), a width $s_x = s_y = 500$ and a terrain height of $h_0 = 0$ (flat), 100, 200 and 300 m.

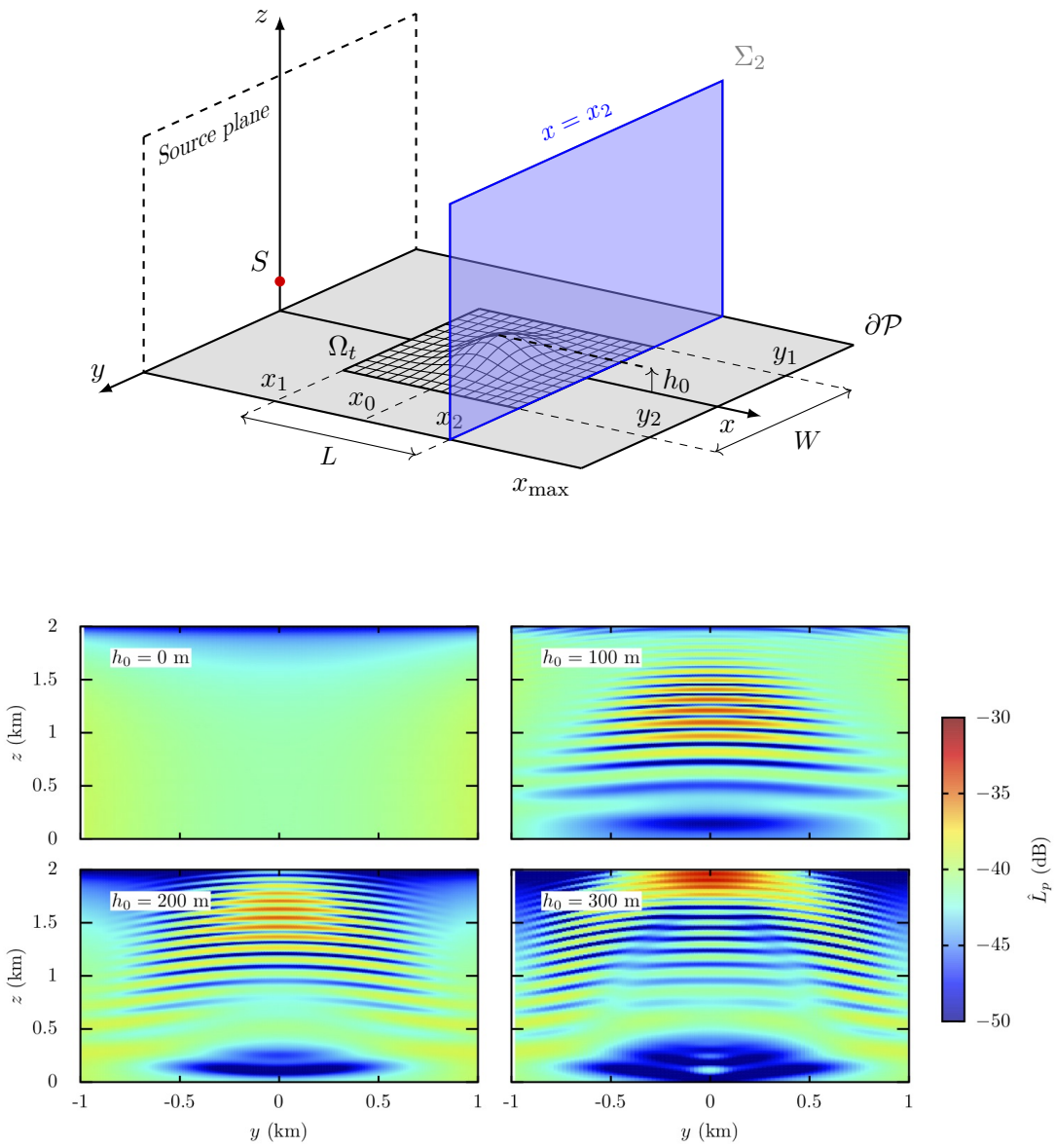

Figure 5.28: 3D BTPE simulation in a homogeneous atmosphere ($c_0 = 343\,\mathrm{m}\cdot\mathrm{s}^{-1}$), $f = 10\,\mathrm{Hz}$ and source located at $x_s = 0$, $y_s = 0$ and $z_s = 25\,\mathrm{m}$. Contour plot of the Relative Sound Pressure Level (RSPL) $\hat{L}_p$ in the plane Σ_2 defined by $z = 1000$ m, for a Gaussian Hill located at $(x_0, y_0) = (5, 0)$ (km), a width $s_x = s_y = 500$ and a terrain height of $h_0 = 0$ (flat), 100, 200 and 300 m.

5.2.2 Comparison between 2D and 3D PE

In this section, the 3D BTPE and the 2D BTPE are compared for the Relative Sound Pressure Level (RSPL) in the middle plane $\mathcal{C}_0$. The purpose is to estimate the importance of three-dimensional effects in the shadow zone, *i.e.* downstream of the Gaussian hill and below the line of sight. The parameters of the simulations described here have been presented in Sec. 5.1. The analytical solution for the complex pressure above a flat impedance surface, given in Eq. (2.25), is used as a baseline for the results shown below. The difference between the baseline and the PE simulations account for the absolute contributions of the Gaussian hill to the scattered field, while the discrepancies between the 2DPE and 3DPE shall reflect the importance of transversal scattering in the middle plane.

First, Fig. 5.29 shows the RSPL computed by the 3D BTPE and 2D BTPE (narrow-angle and wide-angle), taken along $z = 350\,\text{m}$, in the middle plane $\mathcal{C}_0$ ($y = 0$). The location of the irregular boundary, centered at $x_0 = 5\,\text{km}$ is shown. Upstream of the Gaussian hill, for $x < 5\,\text{km}$, the 2D BTPE and 3D BTPE pressure fields are identical to the baseline, since no ground effects occur. At the upstream vicinity of the hill, the 2D BTPE and 3D BTPE show a pressure fluctuation of $\sim 5\,\text{dB}$, as a result of interference between the direct wave from the source and the reflected wave from the exposed surface of the obstacle. Downstream of the Gaussian hill, important discrepancies appear between the 2D BTPE and the 3D BTPE, especially for $h_0 = 300\,\text{m}$. First, a mismatch in the interference pattern location is visible, *e.g.* at $f = 10\,\text{Hz}$ and $h_0 = 200\,\text{m}$, where the destructive interference is estimated about $300\,\text{m}$ more upstream than the 2D BTPE. Moreover, the fluctuation in RSPL is larger in the three-dimensional case, and tends to increase with the obstacle height. For $h_0 = 200\,\text{m}$, three-dimensional effects account for $\pm 5\,\text{dB}$ of the scattered field, but differences of $\pm 10\,\text{dB}$ can be seen for $300\,\text{m}$ (*e.g.* at $x = 8\,\text{km}$ for $f = 5\,\text{Hz}$).

A similar plot is presented in Fig. 5.30, for $z = 1.0\,\text{km}$, from which very interesting observations can be made. The discrepancy between the 2D BTPE and 3D BTPE are very small, which shows that three-dimensional scattering is mitigated at higher altitude. This observation is well demonstrated for $h_0 = 100\,\text{m}$ and $f = 5\,\text{Hz}$, but

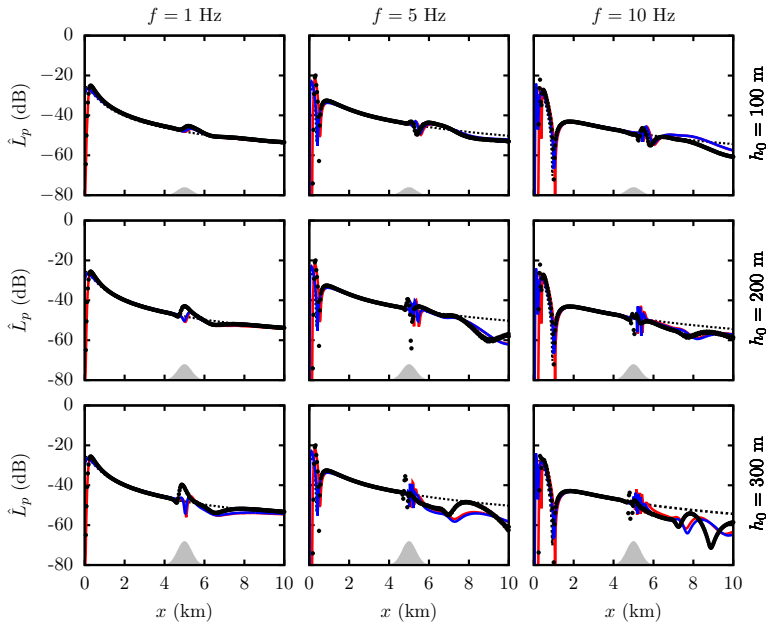

Figure 5.29: Propagation above a Gaussian hill located at $\mathbf{x}_0 = (5.0, 0)$ km, with a standard deviation $s_x = s_y = 1000$ m. Comparison of the Relative Sound Pressure Level (RSPL) along $z = 350\,\text{m}$ in the middle plane $\mathcal{C}_0$, as computed by the narrow-angle 2D BTPE, wide-angle 2D BTPE and the 3D BTPE. The height is $h_0 = 100\,\text{m}$ (top), $h_0 = 200\,\text{m}$ (center) and $h_0 = 300\,\text{m}$ (bottom). The source is located at $\mathbf{x}_s = (0, 0, 25)$ m and radiates a wave of frequency $f = 1\,\text{Hz}$ (left), $f = 5\,\text{Hz}$ (middle) and $f = 10\,\text{Hz}$ (right).RSPL computed by the narrow-angle 2D BTPE (——), the wide-angle 2D BTPE (——), the 3D BTPE (•) and for a flat boundary (·····).

is still consistent at for a larger obstacle height, *e.g.* $h_0 = 200\,\text{m}$. Furthermore, comparison with the (flat) baseline show that the computed SPL differs only by localized fluctuations, downstream of the Gaussian hill, while following the same behavior. The pressure localized fluctuations occur around $x = 6\,\text{km}$ in all cases and range from $\pm 5\,\text{dB}$ for $f = 1\,\text{Hz}$, while reaching values of up to $\pm 10\,\text{dB}$ at higher frequencies. A similar discussion can be applied to the results presented in Fig. 5.31, which shows the RSPL at $z = 2.0\,\text{km}$, with an additional precaution regarding the limited accuracy of the 2D BTPE and 3D BTPE at higher altitudes. For the sake of completeness, it is pointed that the 3D BTPE shows a numerical artifact for $h_0 = 300\,\text{m}$ and $f = 10\,\text{Hz}$, causing a sharp increase in SPL at $x \approx 7.0\,\text{km}$. This can be explained by the parameters considered for this particular simulation,

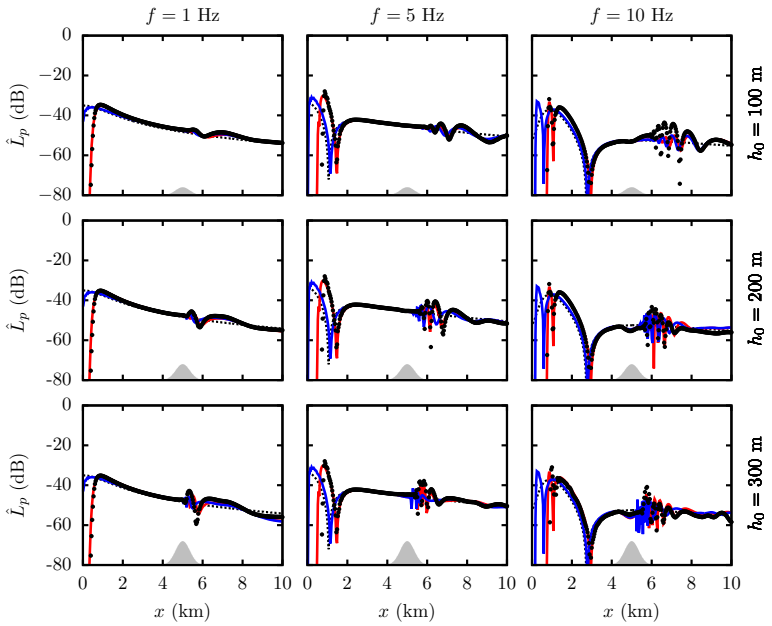

Figure 5.30: Propagation above a Gaussian hill located at $\mathbf{x}_0 = (5.0, 0)$ km, with a standard deviation $s_x = s_y = 1000$ m. Comparison of the Relative Sound Pressure Level (RSPL) along $z = 1.0$ km in the middle plane $\mathcal{C}_0$, as computed by the narrow-angle 2D BTPE, wide-angle 2D BTPE and 3D BTPE. The height is $h_0 = 100$ m (top), $h_0 = 200$ m (center) and $h_0 = 300$ m (bottom). The source is located at $\mathbf{x}_s = (0, 0, 25)$ m and radiates a wave of frequency $f = 1$ Hz (left), $f = 5$ Hz (middle) and $f = 10$ Hz (right). RSPL computed by the narrow-angle 2D BTPE (——), the wide-angle 2D BTPE (——), the 3D BTPE (•) and for a flat boundary (·····).

since the narrow-angle approximation made in the derivation of Eq. (4.24) allows high accuracy for sloping angles smaller than 15°, whereas the $h_0 = 300$ m case corresponds to a slope of 20°, according to Table 5.1.

Another characterization of the three-dimensional scattering can be achieved by examining the Relative Sound Pressure Level (RSPL) along altitude, downstream of the Gaussian hill. In this respect, Fig. 5.32 shows the RSPL computed by the 2D BTPE and 3D BTPE, taken along $x = 7.0$ km in the middle plane $\mathcal{C}_0$. Based on the results shown, important discrepancies are visible for $h_0 = 300$ m in the shadow zone, *i.e.* for $z < h_0$. At $f = 5$ Hz, the contribution from transversal scattering results in an increase of ~ 8 dB at the ground level ($z = 0$ m). At $f = 10$ Hz, a

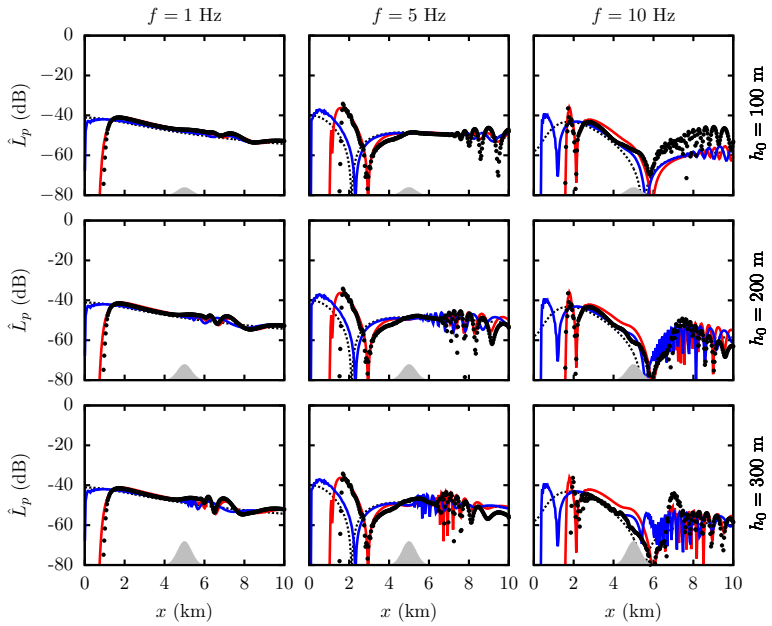

Figure 5.31: Propagation above a Gaussian hill located at $\mathbf{x}_0 = (5.0, 0)$ km, with a standard deviation $s_x = s_y = 1000$ m. Comparison of the Relative Sound Pressure Level (RSPL) along $z = 2.0$ km in the middle plane $\mathcal{C}_0$, as computed by the narrow-angle 2D BTPE, wide-angle 2D BTPE and 3D BTPE. The height is $h_0 = 100$ m (top), $h_0 = 200$ m (center) and $h_0 = 300$ m (bottom). The source is located at $\mathbf{x}_s = (0, 0, 25)$ m and radiates a wave of frequency $f = 1$ Hz (left), $f = 5$ Hz (middle) and $f = 10$ Hz (right). RSPL computed by the narrow-angle 2D BTPE (——), the wide-angle 2D BTPE (——), the 3D BTPE (•) and for a flat boundary (·····).

similar behavior is noticeable in the shadow zone, with an increase of ~ 5 dB at an altitude $z \approx 150$ m above the ground. These effects are mitigated for lower values of h_0 and f. After further inspection, another observation can be made regarding the numerical procedure. The scattered field downstream of the hill contain two distinct structures, in accordance with the discussion given in Sec. 3.4.4. In the shadow zone, *i.e.* for $z < h_0$, the interference locations are similar for the 2D BTPE and the 3D BTPE, which can be explained by the fact that the pressure field in this region is largely within the domain of validity of the narrow-angle approximation. However, at higher altitude ($z > 1.0$ km), the wide-angle 2DPE shows a shift in the interference pattern, suggesting that the order of expansion used in Eq. (3.13) and Eq. (4.27), rather than the ground effects, is the key parameter in the estimation

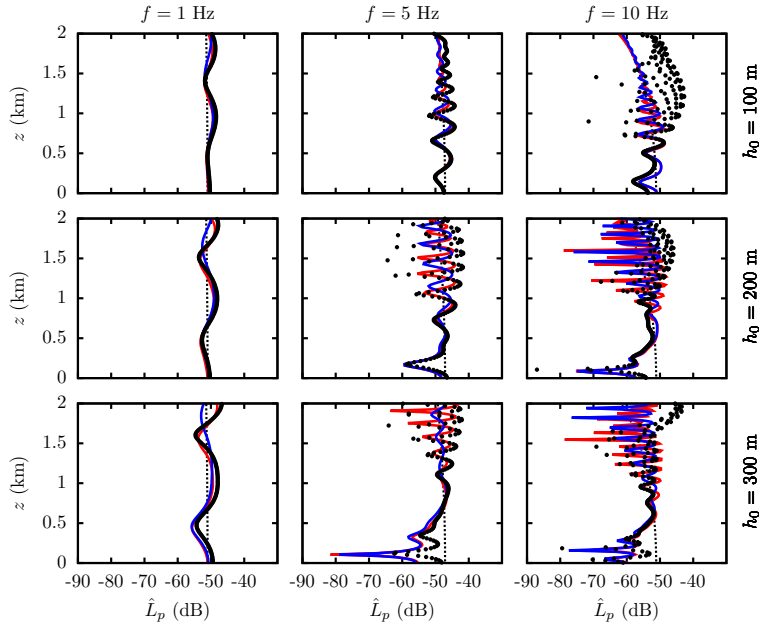

Figure 5.32: Propagation above a Gaussian hill located at $\mathbf{x}_0 = (5.0, 0)$ km, with a standard deviation $s_x = s_y = 1000$ m. Comparison of the Relative Sound Pressure Level (RSPL) along $x = 7.0$ km in the middle plane $\mathcal{C}_0$, as computed by the narrow-angle 2D BTPE, wide-angle 2D BTPE and 3D BTPE. The height is $h_0 = 100$ m (top), $h_0 = 200$ m (center) and $h_0 = 300$ m (bottom). The source is located at $\mathbf{x}_s = (0, 0, 25)$ m and radiates a wave of frequency $f = 1$ Hz (left), $f = 5$ Hz (middle) and $f = 10$ Hz (right). RSPL computed by the narrow-angle 2D BTPE (——), the wide-angle 2D BTPE (——), the 3D BTPE (•) and for a flat boundary (·····).

of the SPL at higher altitude.

5.3 Three-dimensional irregular boundary in a refractive media

In this section, a set of simulations of infrasound in a refractive atmosphere and above an irregular surface are carried out. The purpose is to explore the ability of the three-dimensional Beilis-Tappert Parabolic Equation (3D BTPE), defined in Eq. (4.24), to account for ground effects on infrasound arrivals. As seen in Gossard

and Hooke [90], infrasound can be trapped into several atmospheric waveguides and significant ground interaction can occur over large distances in the troposphere ($z < 20\,\mathrm{km}$)[134, 13]. In the current approach the boundary layer simply follows the terrain profile; effects due to the generation of mountain induced gravity waves [77] are predicted to be small and are therefore neglected. Since we are studying infrasound propagation at low altitudes, the atmospheric medium is assumed to be isothermal, i.e. at a constant temperature T_0, and the effective sound speed is simply given by the sum of the adiabatic sound speed $c_0 = \sqrt{\gamma R T_0}$ and the background fluid motion in the direction of propagation $v_0(z) \approx \mathbf{v}_0(z) \cdot \mathbf{e}_x$. Here we consider several possible profiles for v_0, namely the standard linear, jet and logarithmic profiles, given by

$$\text{Linear:} \qquad v_0(z) = a\left(\frac{z}{\delta}\right), \tag{5.3a}$$

$$\text{Jet:} \qquad v_0(z) = a\exp\left(-\frac{(z-z_0)^2}{2\delta^2}\right), \tag{5.3b}$$

$$\text{Logarithmic:} \qquad v_0(z) = a\log\left(1+\frac{z}{\delta}\right), \tag{5.3c}$$

where a is the wind speed amplitude, δ is the boundary layer thickness and z_0 is the wind jet altitude. For the simulations presented here, we use $a = 0.1\,\mathrm{m}\cdot\mathrm{s}^{-1}$ and $\delta = 1\,\mathrm{m}$ in Eq. (5.3a), $a = 100\,\mathrm{m}\cdot\mathrm{s}^{-1}$, $z_0 = 1000\,\mathrm{m}$ and $\delta = 50\,\mathrm{m}$ in Eq. (5.3b), $a = 20\,\mathrm{m}$ and $\delta = 10\,\mathrm{m}$ in (5.3c). The choice of a $100\,\mathrm{m}\cdot\mathrm{s}^{-1}$ wind jet is here justified by the values used in Attenborough et al. [17], who considered linear profiles with a slope of $\pm 0.1\,\mathrm{s}^{-1}$ in altitude. The effective sound speed profile in each case is calculated as $c_{\text{eff}}(z) = c_0 + v_0(z)$, where the adiabatic sound speed is fixed at $c_0 = 343\,\mathrm{m}\cdot\mathrm{s}^{-1}$. The effective sound speed profiles given in Eqs. (5.3a), (5.3a) and (5.3a) are plotted in Fig 5.33.

The regime of the flow over the gaussian hill can be characterized by the Froude number Fr, given by

$$Fr = \frac{v_0}{NL}, \tag{5.4}$$

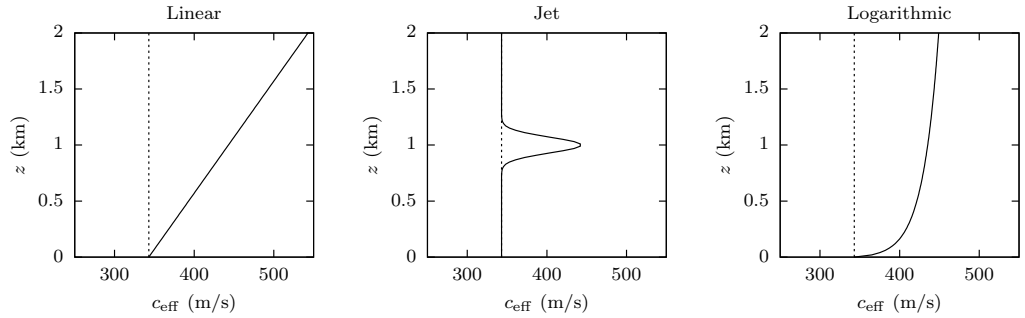

Figure 5.33: Effective sound speed profile for a linear (left), logarithmic (middle) and (jet) wind speed. The dashed line shows the constant speed $c_0 = 343\,\mathrm{m}\cdot\mathrm{s}^{-1}$.

where v_0 is the wind velocity, N is the Brunt-Väisälä frequency of the atmosphere, given by $N = 0.012\,\mathrm{s}^{-1}$, and L is the length of the terrain obstacle. The Froude number is the ratio between the flow wavelength and the obstacle length. If $Fr > 1$ then the flow will be strong enough to cross the terrain, while $Fr < 1$ represent the subcritical case where the flow is obstructed, leading to non-linear effects. The linear profile in Eq. (5.3a) has a constant gradient, so the associate drays are circular and refraction is smooth. The wind jet in Eq. (5.3b) on the other hand, creates a sharp disturbance in the effective sound speed profile, which creates a strong refraction at high frequencies. Finally, the logarithmic profile in Eq. (5.3c) corresponds to a typical tropospheric boundary layer profile, where the waves close to the ground are strongly refracted. In the results presented here, the frequency is fixed at $f = 10\,\mathrm{Hz}$ and the Gaussian hill, defined by Eq. (5.1), will vary in height only. The three cases considered are, as before, $h_0 = 100\,\mathrm{m}$, $h_0 = 200\,\mathrm{m}$ and $h_0 = 300\,\mathrm{m}$. For each value of h_0, the three effective sound speed profiles, given by Eqs. (5.3a), (5.3b) and (5.3c), are taken into account, resulting in a total of 9 simulations.

For the linear effective sound speed profile, given by Eq. (5.3a), the Relative Sound Pressure Level (RSPL) in the middle plane $\mathcal{C}_0$ is plotted in Fig. 5.34 and the RSPL along the ground surface $\partial\mathcal{P}$ is plotted in Fig. 5.35. The results in Fig. 5.34, show the presence of a creeping wave layer along the ground surface. Upstream of the obstacle, *i.e.* for $x < x_1$, the creeping wave layer thickness is constant and can be estimated using Eq. (2.45a). The radius of curvature of the rays is calculated as $R_0 = \delta c_0/a$, where $a = 0.1\,\mathrm{m}\cdot\mathrm{s}^{-1}$, $\delta = 1\,\mathrm{m}$ and $c_0 = 343\,\mathrm{m}\cdot\mathrm{s}^{-1}$, resulting in a

creeping wave layer thickness $l_c \approx 37\,\mathrm{m}$. The presence of the Gaussian hill between $x_1 = 6.0\,\mathrm{km}$ and $x_2 = 6.0\,\mathrm{km}$ breaks the continuity of the creeping wave layer, and part of the creeping wave is reflected at higher altitude before being refracted back to the ground level. The reflection angle is higher as the value of h_0 increases, leading to a larger shadow zone downstream of the Gaussian hill. For $h_0 = 300\,\mathrm{m}$, an increase of the SPL is observed downstream of the hill, for $x > 7.0\,\mathrm{km}$, which can be attributed to the refraction of the field scattered by the hill. Additionally, the results presented in Fig. 5.35 suggest that the height h_0 has a significant effect on the transversal location of the destructive interferences at ground level.

Next, the c_{eff} profile given by Eq. (5.3b) is considered. The results are presented in Fig. 5.36, which provides the RSPL in the middle plane $\mathcal{C}_0$, and Fig. 5.36, which provides the RSPL along the ground surface $\partial\mathcal{P}$. According to Fig. 5.33, the wind jet is located at $z = 1.0\,\mathrm{km}$. The large amplitude of the jet, *i.e.* $v_0 = 100\,\mathrm{m}\cdot\mathrm{s}^{-1}$, leads to a strong ducting of the wave in the lower part of the atmosphere. After inspecting Fig. 5.36, it appears that the wave is partially trapped in a waveguide located below $z = 1.0\,\mathrm{km}$, resulting in significant interaction with the ground surface. Upstream of the obstacle, at $x = 4\,\mathrm{km}$, a refracted beam with a $-45\,\mathrm{dB}$ amplitude interacts with the ground at the vicinity of the Gaussian hill. Additionally, smaller refracted beams travel horizontally and interact with the obstacle at a grazing angle. After interacting with the Gaussian hill, the wave is reflected back to the jet stream, located at the altitude $z = 1.0\,\mathrm{km}$. For $h_0 = 100\,\mathrm{m}$, the reflected wave follows a curved trajectory, with a turning point located around $x = 6\,\mathrm{km}$ and $z = 1.0\,\mathrm{km}$. As the height increases, a larger part of the grazing beams are reflected to higher altitudes and exit the lower waveguide. For $h_0 = 300\,\mathrm{m}$, most of the wave is reflected beyond $z = 1.0\,\mathrm{km}$, and a larger shadow zone appear downstream of the Gaussian hill. Another observation is made for the RSPL at $x > 8.0\,\mathrm{km}$, which contains more refracted beams at $h_0 = 100\,\mathrm{m}$.

Finally, the case of the logarithmic profile, given by Eq. (5.3b), is plotted in Figs. 5.38 and 5.39. As in the linear case, plotted in Fig. 5.34, the logarithmic profile generates a creeping wave along the ground surface, resulting in an increase of the Relative Sound Pressure Level (RSPL) to a value of $\sim -40\,\mathrm{dB}$ within a small layer. The form of the scattered field can be understood by examining the properties of

the logarithmic profile, defined in Eq. (5.3b). The effective sound speed gradient is very high at low altitude, *i.e.* for $z < 200\,\text{m}$, but reaches smaller values in the higher parts of the domain. It follows that only the waves that are close to the ground are strongly refracted. For $h_0 = 300\,\text{m}$, a shadow zone is noticeable downstream of the Gaussian hill, which is also visible by inspecting the RSPL at the ground level, plotted in Fig. 5.39. Furthermore, Fig. 5.39 suggests that for $h_0 = 100\,\text{m}$ and $h_0 = 200\,\text{m}$, the effects of the logarithmic sound speed profile play a more important part than the topographic parameters. For $h_0 = 300\,\text{m}$, however, topographic effects become significant and generate destructive interferences of $-50\,\text{dB}$ in the far-field region.

5.4 Conclusions

In this chapter, the three-dimensional Beilis-Tappert parabolic equation (3D BTPE), derived in Eq. (4.24), was used to perform a parametric study of infrasonic propagation above a Gaussian surface, in a homogeneous and a refracting atmosphere. The two variable parameters used are the frequency f of the acoustic source, which was fixed at a location $\mathbf{x}_s$, and the Gaussian hill height h_0. Three-dimensional effects were significant in the shadow zone, with increases of up to $10\,\text{dB}$ for $h_0 = 300\,\text{m}$, due to out-of-plane scattering that is not captured by the two-dimensional parabolic equation (2DPE). Results further suggest that the absolute influence of ground effects, in comparison to the flat surface model, is significant only in the higher end of the infrasonic spectrum, *i.e.* for $f \geq 5\,\text{Hz}$, and $h_0 = 300\,\text{m}$. As a result, it was postulated that the key parameter for the existence of three-dimensional effects is the value of the *obstacle ratio*, defined as h_0/λ, which is equivalent to the Rayleigh scattering criteria in theoretical acoustics [157]. Indeed, the cases in which significant diffractive effects were identified correspond to a value $h_0/\lambda > 1$. Finally, the coupling between atmospheric refraction and ground effects was studied, for a linear, jet and logarithmic effective sound speed profiles. It was shown that the terrain height h_0 plays a crucial role in the downstream interference pattern. Atmospheric refraction creates new infrasonic arrivals, which were identified as wave

beams scattered by the Gaussian hill.

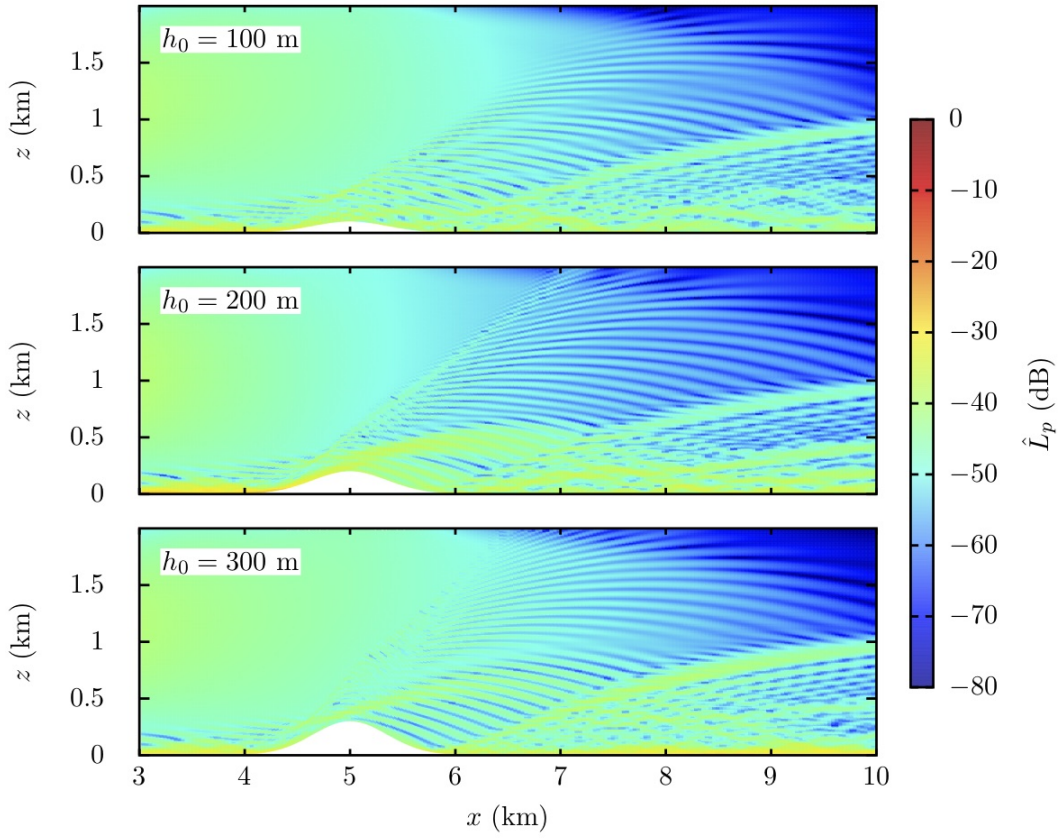

Figure 5.34: 3DPE simulation in a refractive atmosphere with a linear wind speed profile for a gradient $u_0 = +0.1\,\mathrm{m}\cdot\mathrm{s}^{-1}$, $f = 10\,\mathrm{Hz}$ and source located at $x_s = 0$, $y_s = 0$ and $z_s = 25\,\mathrm{m}$. Contour plot of the Relative Sound Pressure Level (RSPL) $\hat{L}_p$ in the middle plane $\mathcal{P}_{y,0}$ defined by $z = h(x, y)$, for a Gaussian Hill located at $(x_0, y_0) = (5, 0)$ (km), a width $s_x = s_y = 500$ and a terrain height of $h_0 = 0$ (flat), 100, 200 and 300 m.

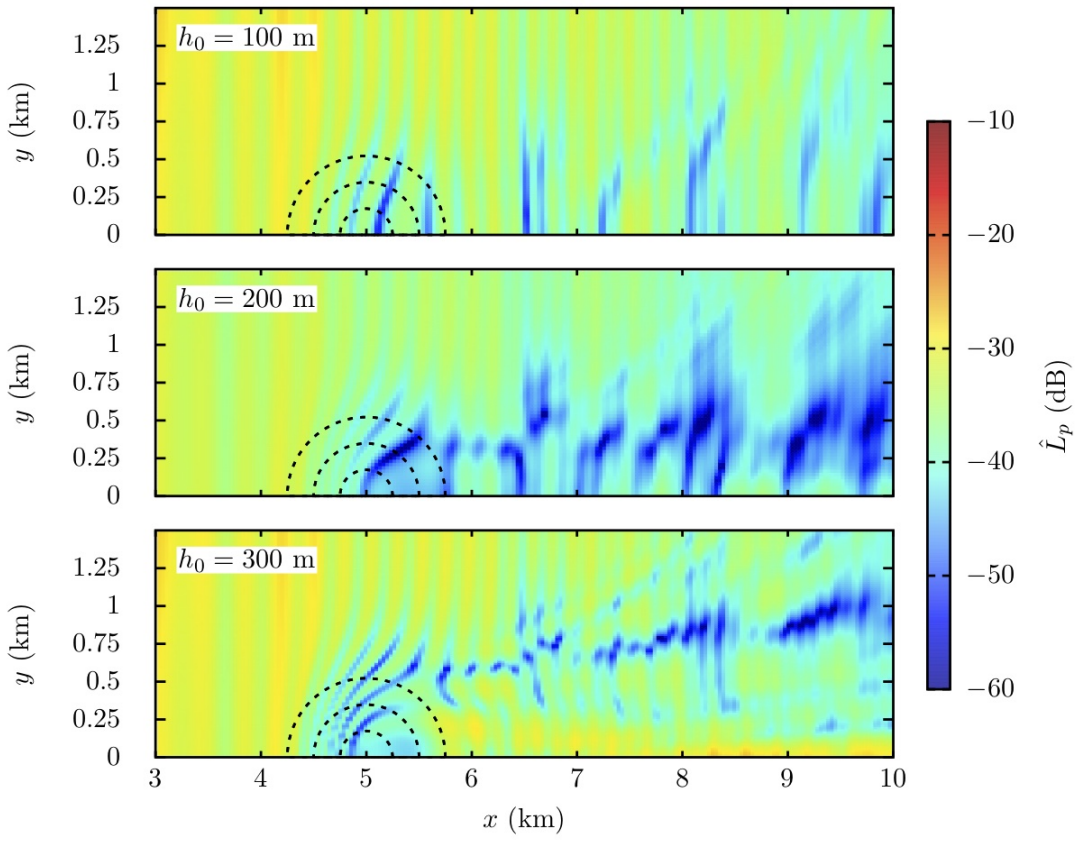

Figure 5.35: 3DPE simulation in a refractive atmosphere with a linear wind speed profile for a gradient $u_0 = +0.1\,\mathrm{m}\cdot\mathrm{s}^{-1}$, $f = 10\,\mathrm{Hz}$ and source located at $x_s = 0$, $y_s = 0$ and $z_s = 25\,\mathrm{m}$. Contour plot of the Relative Sound Pressure Level (RSPL) $\hat{L}_p$ accross the bottom boundary $\partial\mathcal{P}$ defined by $z = h(x, y)$, for a Gaussian Hill located at $(x_0, y_0) = (5, 0)$ (km), a width $s_x = s_y = 500$ and a terrain height of $h_0 = 0$ (flat), 100, 200 and 300 m.

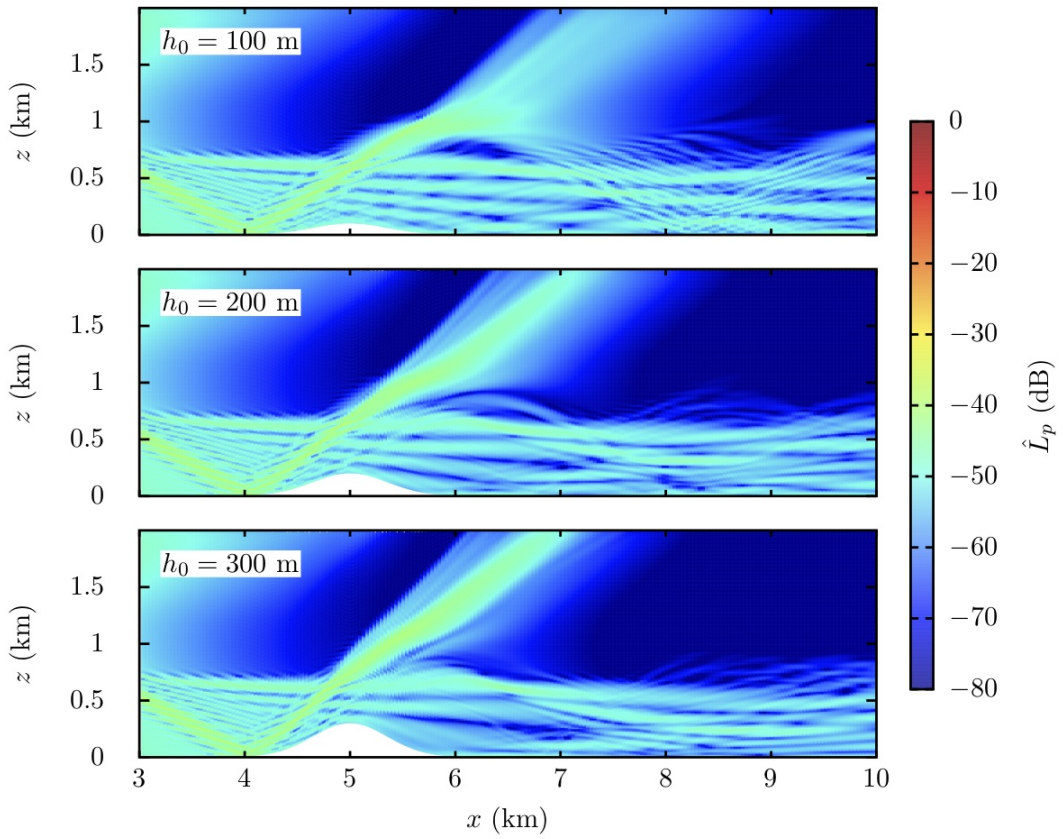

Figure 5.36: 3DPE simulation in a refractive atmosphere with a jet wind speed profile located at $z_0 = 1.0\,\text{km}$, with a layer thickness $d = 100\,\text{m}$ and amplitude $u_0 = +100\,\text{m} \cdot \text{s}^{-1}$, $f = 10\,\text{Hz}$ and source located at $x_s = 0$, $y_s = 0$ and $z_s = 25\,\text{m}$. Contour plot of the Relative Sound Pressure Level (RSPL) $\hat{L}_p$ accross the bottom boundary $\partial\mathcal{P}$ defined by $z = h(x, y)$, for a Gaussian Hill located at $(x_0, y_0) = (5, 0)$ (km), a width $s_x = s_y = 500$ and a terrain height of $h_0 = 0$ (flat), 100, 200 and 300 m.

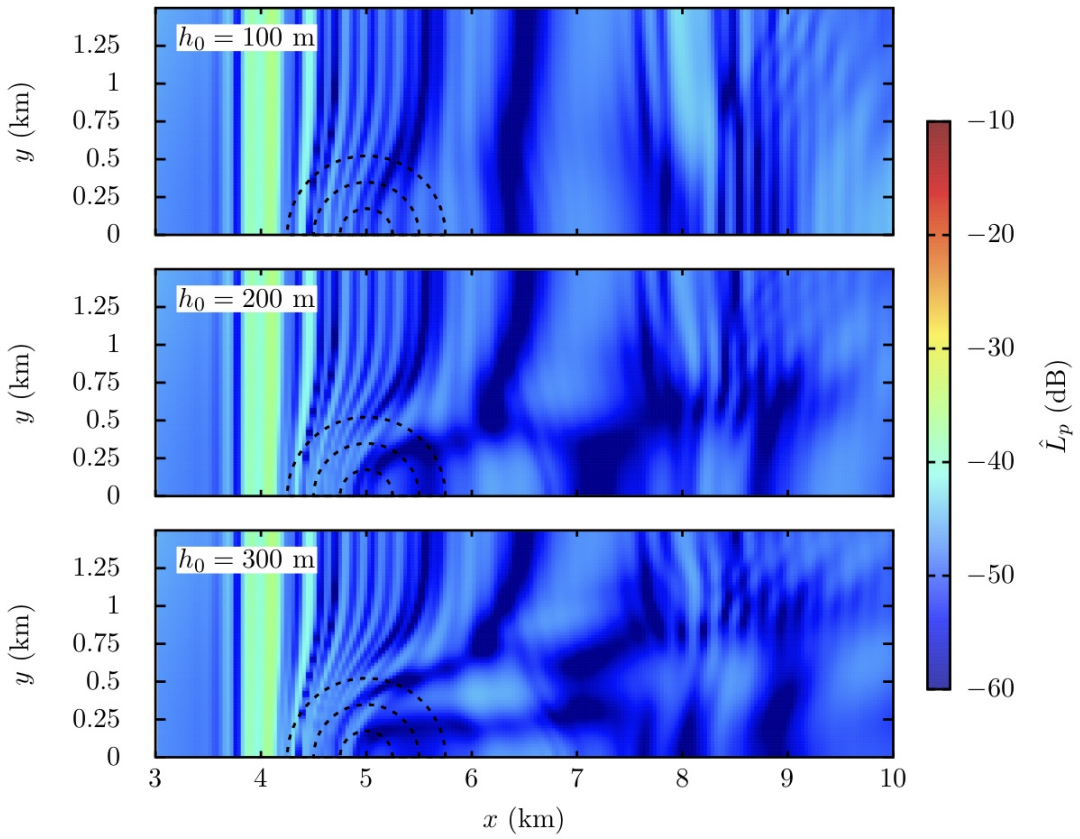

Figure 5.37: 3DPE simulation in a refractive atmosphere with a jet wind speed profile located at $z_0 = 1.0\,\text{km}$, with a layer thickness $d = 100\,\text{m}$ and amplitude $u_0 = +100\,\text{m} \cdot \text{s}^{-1}$, $f = 10\,\text{Hz}$ and source located at $x_s = 0$, $y_s = 0$ and $z_s = 25\,\text{m}$. Contour plot of the Relative Sound Pressure Level (RSPL) $\hat{L}_p$ accross the bottom boundary $\partial\mathcal{P}$ defined by $z = h(x, y)$, for a Gaussian Hill located at $(x_0, y_0) = (5, 0)$ (km), a width $s_x = s_y = 500$ and a terrain height of $h_0 = 0$ (flat), 100, 200 and 300 m.

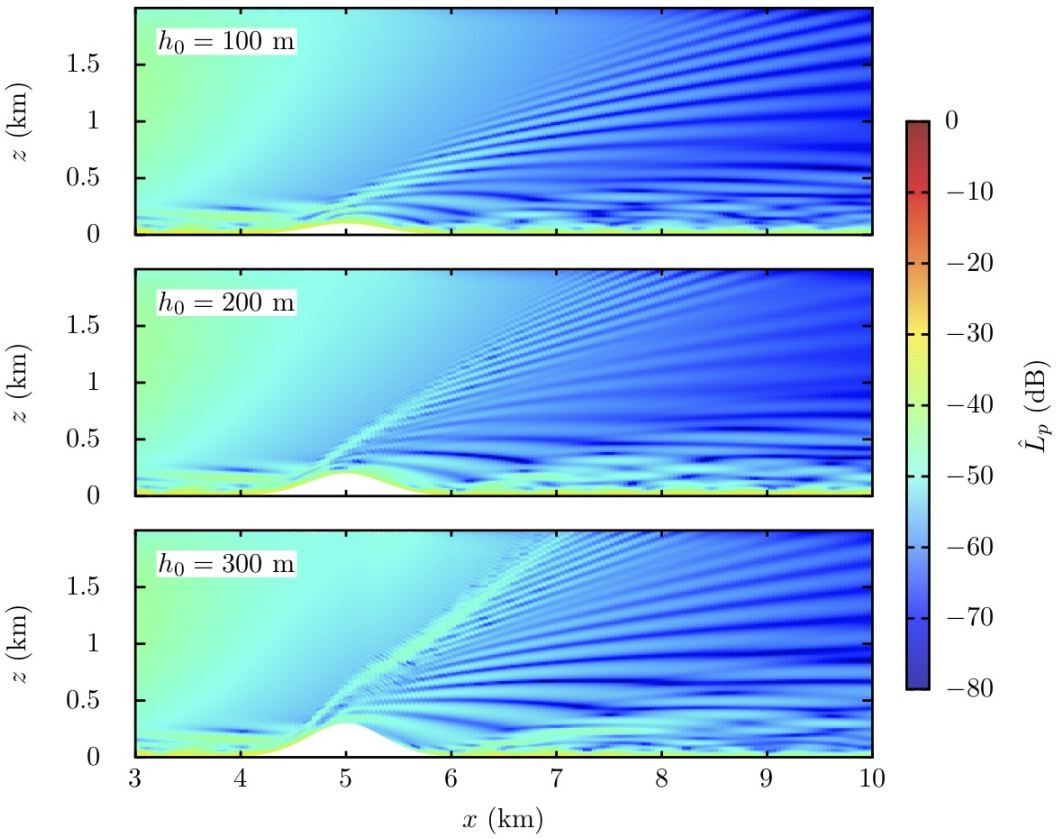

Figure 5.38: 3DPE simulation in a refractive atmosphere with a jet wind speed profile located at $z_0 = 1.0\,\text{km}$, with a layer thickness $d = 100\,\text{m}$ and amplitude $u_0 = +100\,\text{m} \cdot \text{s}^{-1}$, $f = 10\,\text{Hz}$ and source located at $x_s = 0$, $y_s = 0$ and $z_s = 25\,\text{m}$. Contour plot of the Relative Sound Pressure Level (RSPL) $\hat{L}_p$ accross the bottom boundary $\partial\mathcal{P}$ defined by $z = h(x, y)$, for a Gaussian Hill located at $(x_0, y_0) = (5, 0)$ (km), a width $s_x = s_y = 500$ and a terrain height of $h_0 = 0$ (flat), 100, 200 and 300 m.

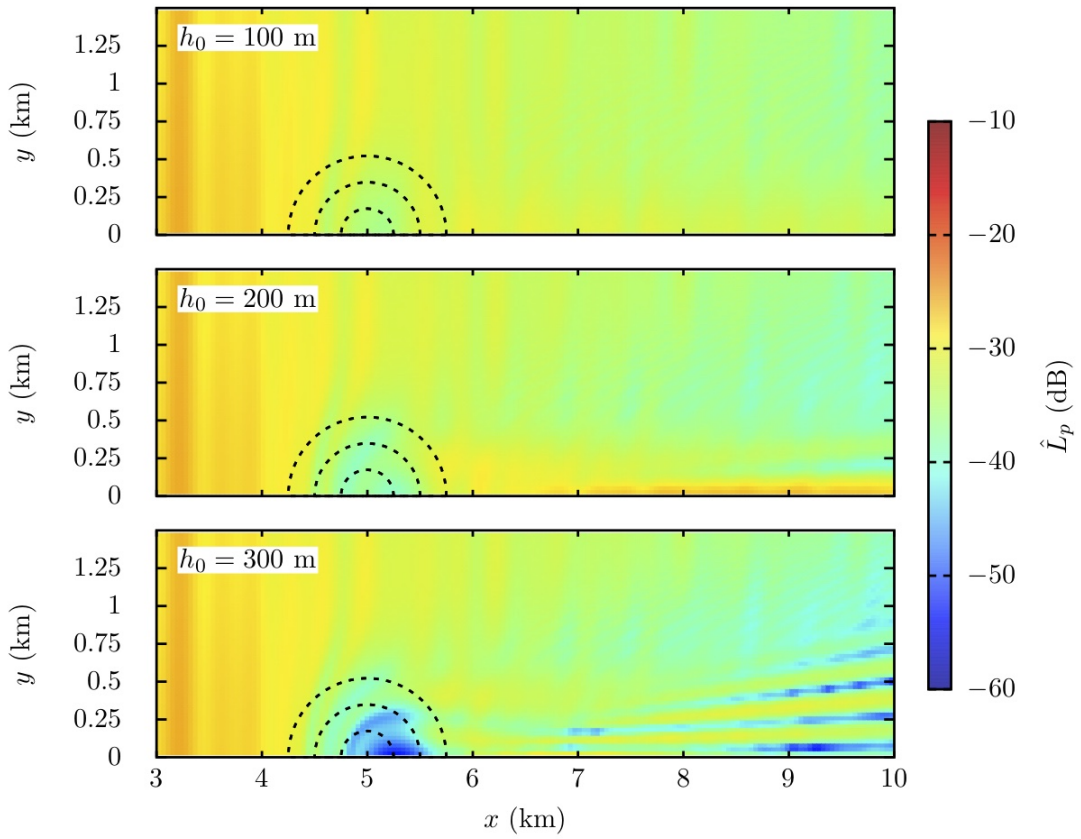

Figure 5.39: 3DPE simulation in a refractive atmosphere with a jet wind speed profile located at $z_0 = 1.0\,\text{km}$, with a layer thickness $d = 100\,\text{m}$ and amplitude $u_0 = +100\,\text{m} \cdot \text{s}^{-1}$, $f = 10\,\text{Hz}$ and source located at $x_s = 0$, $y_s = 0$ and $z_s = 25\,\text{m}$. Contour plot of the Relative Sound Pressure Level (RSPL) $\hat{L}_p$ accross the bottom boundary $\partial\mathcal{P}$ defined by $z = h(x, y)$, for a Gaussian Hill located at $(x_0, y_0) = (5, 0)$ (km), a width $s_x = s_y = 500$ and a terrain height of $h_0 = 0$ (flat), 100, 200 and 300 m.

Chapter 6

Infrasound propagation in a complex realistic environment

In this Chapter, the three-dimensional parabolic equation method developed in Chap. 4 is applied to a realistic scenario of sound propagation in a complex environment. The identification of three-dimensional topographic effects in realistic infrasound propagation is not straightforward, since a large number of environmental factors enter into account. A proper physical characterization of realistic three-dimensional effects can be only achieved if two conditions are met. Firstly, we need an experimental dataset that isolates topography as the only parameters between several recordings while neglecting atmospheric parameters. This assumption is not representative of reality, where even weak wind conditions play a major role on long-range propagation. Secondly, the problem must be within the domain of validity of the numerical method used. The problem that will be investigated will focus on sound propagation from a wind farm located on the Ascension Island, in the southern Atlantic ocean. This problem is of interest as it provides the opportunity to analyze topographic effects on infrasound and compare 2D and 3D numerical predictions with measurements. We start by presenting the topographic data in Sec. 6.1, then we proceed to expose the methodology used in this study in Sec. 6.2, which is based on the calculation of amplitude ratios between receiver locations. In Sec. 6.3, we discuss the miscellaneous details regarding grid generation

for realistic terrains and present the simulation results. Conclusions and remarks regarding possible improvements are exposed in Sec. 6.4.

6.1 Ascension Island dataset

The purpose of the study is to predict the Sound Pressure Level (SPL) from a Wind Farm located on the Ascension Island, which is the likely source of several signals recorded at the IS50 array. IS50 is a 2770m aperture, eight element microbarometer array located on Ascension Island. It is one of sixty planned microbarometer arrays within the International Monitoring System (IMS). Four of the elements are attached to low-frequency (70m aperture) wind noise reduction systems, while four are attached to high-frequency (18m) systems (Walker and Hedlin [211]). For the present study we focus only on pressure amplitudes recorded at the four low-frequency elements, named L_1, L_2, L_3 and L_4, due to their geographical separation. The exact locations of the micro-barographs L_n and the Wind Farm turbines W are shown in and listed in Table 6.1.

Element	Latitude ϕ_n (°)	Longitude λ_n (°)	Elevation (m)	Distance to W (m)
W	-7.96129	-14.38680	158	0.0
L_1	-7.93774	-14.37517	189	2890.0
L_2	-7.93190	-14.38204	147	3240.0
L_3	-7.92500	-14.35721	218	4580.0
L_4	-7.95113	-14.37409	192	1830.0

Table 6.1: Geographical data of the windfarm W and low-frequency microbarographs L_1, L_2, L_3 and L_4.

Data provided by AWE Blacknest has shown that there is a disagreement between recorded signals and expected SPL values based on a simple analysis for a flat terrain, suggesting that the presence of topography has an effect on sound propagation between the Windfarm (W) and receivers L_n. Moreover, similarities between sig-

nals recorded in October 2006 and October 2010 allows to assume that the windfarm under consideration rotate at a constant speed and that they constitute the only source of noise. The specifications of the source have been derived from the technical specifications of the wind turbines present on Ascension Island. It has been determined that four harmonics arise from the rotation of the blades at a constant speed, with a fundamental frequency $f_0 = 1.90\,\text{Hz}$ and three overtones $f_1 = 2f_0 = 3.79\,\text{Hz}$, $f_2 = 3f_0 = 5.69\,\text{Hz}$ and $f_3 = 4f_0 = 7.59\,\text{Hz}$. No further analysis on the sound generation mechanisms is taken into account in this study.

The geographical data provided in Table 6.1 is not in an appropriate format, so it is converted to a cartesian form first. We introduced the raw coordinate system $\mathbf{X}^* = (x^*, y^*)$ as defined in Sec. 4.2.5, and we name $\mathbf{X}_n^*$ the raw position of the microbarograph L_n. The topographic profile of the Ascension Island in raw coordinates (x^*, y^*) is plotted in Fig. 6.1, with the location of the windfarm W, centered at $(0, 0)$, and micrbarographs L_n. From the geographical data given in Table 6.1, we can derive the raw positions (x_n^*, y_n^*) of the receivers L_n by first determining the azimuthal angles θ_n^* between the windfarm W, located at the origin, and each one of the receivers L_n. These are calculated by

$$\theta_n^* \simeq \tan\left(\frac{\lambda_n - \lambda_W}{\phi_n - \phi_W}\right), \tag{6.1}$$

where ϕ_W and λ_w are the latitude and longitude of the windfarm, respectively. Then, using the distances R_n between the windfarm and each receiver L_n, given in Table 6.1, we get the raw position of each receiver,

$$x_n^* = R_n \sin(\theta_n^*), \tag{6.2a}$$
$$y_n^* = R_n \cos(\theta_n^*). \tag{6.2b}$$

These positions are all given in Table 6.2. These positions will be used to determine the receiver positions in the numerical domain, which will be interpolated from the raw topographic input of the Ascension Island.

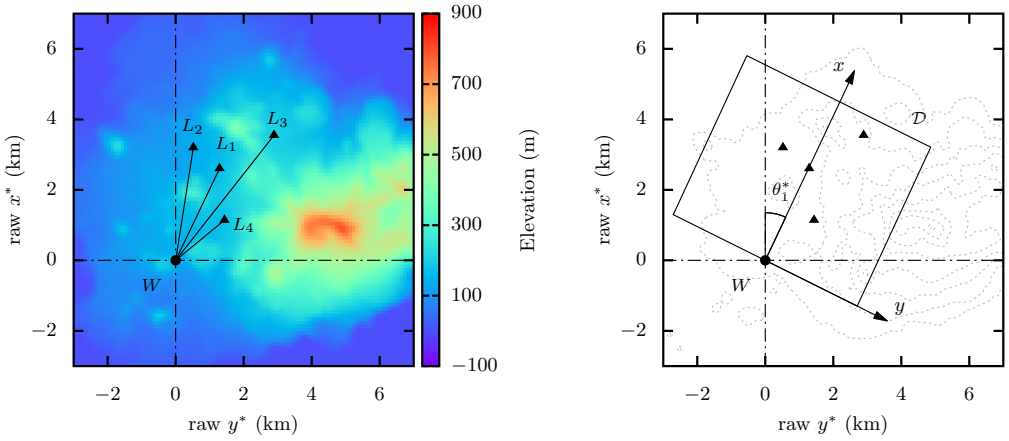

Figure 6.1: Left: Ascension Island input topographic data with microbarographs and windfarm locations. Right: (x, y) numerical domain $\mathcal{D}$ for the 3DPE modeling in the paraxial direction defined by the raw azimuthal angle θ_1^*.

Raw coordinates	W	L_1	L_2	L_3	L_4
x_n^* (m)	0.0	1289.0	518.0	2892.0	1433.0
y_n^* (m)	0.0	2606.0	3198.0	3550.0	1137.0
θ_n^* (°)	-	25.61	9.21	39.17	51.56

Table 6.2: Raw positions (x^*, y^*) of the windfarm W and microbarographs L_1, L_2, L_3 and L_4.

6.2 Methodology

Due to the lack of knowledge of the sound source, the approach advocated here consisted in determining amplitude ratios respectively to one of the microbarographs, in this case L_1. This allows us to implicitly account for three-dimensionality, since the element L_1 is centered and the path $W - L_1$ between the source location W and L_1 is almost flat. The difference of Sound Pressure Level between L_1 and L_n provides a measure of the scattering from topography. Hence, we define the dimensionless amplitude ratios A_n relative to L_1 as

$$A_n(\omega) = \left| \frac{p_c(\omega, \mathbf{X}_n^*)}{p_c(\omega, \mathbf{X}_1^*)} \right|, \tag{6.3}$$

where p_c is the complex pressure amplitude and $\omega = 2\pi f$ the angular frequency. Since we are considering discrete harmonics, we write $\omega_m = 2\pi f_m$ for the m-th harmonic and $A_n^m = A_n(\omega_m)$ the corresponding amplitude ratio for the harmonic f_m. The difference of sound pressure level (SPL) between L_1 and other receivers can be accounted for by the Relative Sound Pressure Level (RSPL) with respect to L_1, which we define as

$$\mathcal{T}_n^m = 20 \log A_n^m, \tag{6.4}$$

for the frequency f_m and microbarograph L_n. We use the letter $\mathcal{T}$ for the RSPL instead of $\hat{L}_p$ to avoid confusion with the microbarometer identifier L introduced above. Then, we provide the values of A_n^m in Eq. (6.3) based on both measurements from the IS50 and the analytical pressure p_c obtained when topographic variations are neglected. In absence of topographic variation, the complex pressure p_c is given by the three-dimensional Green function with ground reflections, as defined in Eq. (4.90). However, the difference of elevation between the source and the microbarographs is negligible, so the amplitude ratio for a flat topography is simply the ratio of the distance R_1 to the distances R_n . We name this quantity $A_{n,\text{flat}}^m$ and define it as

$$A_{n,\text{flat}}^m = \frac{R_1}{R_n}, \tag{6.5}$$

which is a frequency-independent quantity. On the other hand, experimental data extracted from IS50 recordings and provided by AWE Blacknest give a mean and standard deviation for the measured amplitude ratio, which we name $A_{n,\text{exp}}^m$. Amplitudes were extracted from the IMS data, under the assumption that the wind turbine waves are near-sinusoidal signals that exhibit insignificant frequency variations across the time series. This last assumption was checked: the spectral peaks do not fluctuate significantly with time, consistently with the assumption of fixed rotor speed. Pressure amplitudes were identified from amplitude spectral coefficients, which are equal to the root-mean-square amplitude of a sinusoidal signal within the data in units of Pa [94]. Estimates of the amplitude spectral coefficients were made for non-overlapping twenty minute sections of data using a modified periodogram approach. The twenty minute (24000 sample) section is windowed using a 4096

sample Hanning window. Consecutive windows are overlapped by 50%, and each segment is padded with zeros to provide a smooth spectral estimate for the peak-finding algorithm. The results indicate that the frequency of each harmonic peak is stable, but the absolute amplitude changes significantly. However, these temporal changes are highly correlated across all four microbarographs indicating a common source that is most likely to be meteorological in origin. The mean and standard deviation for the distribution of amplitude ratios $A^m_{n,\text{exp}}$ between elements are reported in Table 6.3. The difference between measured and flat amplitude ratios show that sound propagation from the windfarm cannot be accounted for by assuming a flat topography. On the other hand, the variation in the discrepancy between $A^m_{n,\text{exp}}$ and $A^m_{n,\text{flat}}$ across the different receivers and the small value of the standard deviation of $A^m_{n,\text{exp}}$ show that there must be a constant parameter behind this discrepancy, which is believed to be topographic effects rather than atmospheric variability.

Microbarograph	Frequency (Hz)	Flat ratio $A^m_{n,\text{flat}}$	Measured ratio $A^m_{n,\text{exp}}$
L_2/L_1	1.89	0.89	0.79 ± 0.09
	3.79		0.95 ± 0.14
	5.69		0.95 ± 0.15
	3.79		0.77 ± 0.15
L_3/L_1	1.89	0.63	-
	3.79		0.37 ± 0.05
	5.69		0.39 ± 0.07
	7.59		-
L_4/L_1	1.89	1.58	1.48 ± 0.14
	3.79		1.18 ± 0.15
	5.69		1.24 ± 0.15
	7.59		0.59 ± 0.12

Table 6.3: Flat and measured amplitude ratios with respect to L_1 for all four harmonics. The mark "-" indicates missing data.

6.3 Parabolic Equation modeling

In this section, an attempt to explain the influence of topography will be made by undertaking a 2D and 3D parabolic equation simulation of sound propagation from the windfarm W to all the four receivers L_n. The methods that will be used are the narrow angle and wide angle 2D BTPE, defined in Eq. (3.52) and Eq. (3.59) respectively, and the first-order uncoupled 3D BTPE introduced in Eq. (4.24). First, details about the numerical grid and interpolation of topographic data will be presented, as well as a list of all the parameters. Then, the results of the simulations will be presented and discussed. In particular, we want to compare the amplitude ratio A_n^m computed by the PE against data provided in Table 6.3.

6.3.1 Grid and input parameters

In this subsection, we expose the methodology used to carry out the 2D and 3D parabolic equation modeling of sound propagation from the wind-farm W. The first issue to address is the exact location of the source, since the location of the wind-farm W in Table 6.1 is calculated as the barycentre of all the wind turbines. While the 2D BTPE will be run along each radial line W-L_n between the source and each receiver L_n separately, the 3D model requires a greater amount of preprocessing. In 2D, each radial line W-L_n is defined by $\theta^* = \theta_n^*$ in the raw coordinate system, where θ_n^* is the raw azimuthal angle aiming at the microbarograph L_n. Hence, the radial line W-L_n is defined by the points $(r\sin(\theta_n^*), r\cos(\theta_n^*))$ where $r \in [1, R_n]$ is the range variable between W and L_n. The 2D topographic profiles $h_n(r) = h$ along each cut line W-L_n are given in Fig. 6.2 and will be used as the input in the 2D PE simulations. A total of 4×4 simulations, i.e. one for each frequency f_m and W-L_n line combination.

For the 3D simulations, we begin from the topographic profile in raw coordinates (x^*, y^*) and follow the procedure in Sec. 4.2.5 to generate a numerical grid, described by the coordinate system (x, y), where the paraxial direction coincide with the axis

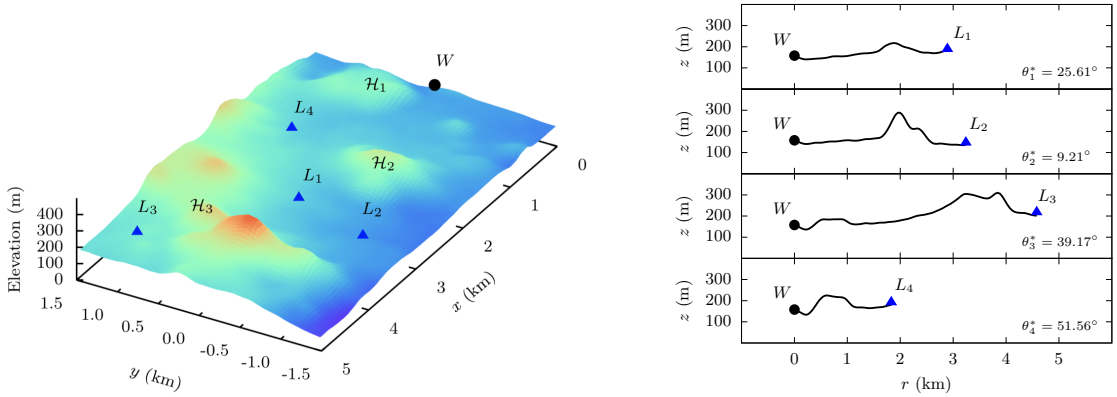

Figure 6.2: Left: Digital Elevation of the terrain in the numerical domain $\mathcal{D}$, orientated in the $W - L_1$ direction defined by $\theta_1^* = 25.61°$. The hills $\boldsymbol{\mathcal{H}}_1$, $\boldsymbol{\mathcal{H}}_2$, $\boldsymbol{\mathcal{H}}_3$ are the three terrain obstacles. Right: Topographic profiles along the tracks $W - L_k$ for the two-dimensional PE modeling.

between the wind-farm W and each micro-barograph L_n. Hence, we need to generate four different numerical grids to perform the 3D simulations, which are defined by the angles $\theta_1^* = 25.61°$ (for L_1), $\theta_2^* = 9.21°$ (for L_2), $\theta_3^* = 39.17°$ (for L_3) and $\theta_4^* = 51.56°$ (for L_4). The numerical waveguide spans from $y_{\min} = -3000\,\text{m}$ to $y_{\max} = 3000\,\text{m}$ transversally and has a total range of $x_{\max} = 5000\,\text{m}$, with $x_{\min} = 0\,\text{m}$. The maximum height of the numerical domain is fixed at $z_{\max} = 5000\,\text{m}$. The numerical domain generated for θ_1^* is represented in Fig. 6.1 and the digital elevation of the bottom topography is given in Fig 6.2. We have identified and named several hills and terrain obstacles in the computational domain that are likely to block or scatter sound propagating from the source. The small irregular hill located at ~ 300 m to the North East of the source is called $\boldsymbol{\mathcal{H}}_1$, it peaks at around 230 m and stands along the path to L_4. Another larger hill $\boldsymbol{\mathcal{H}}_2$ is located further away to the North at about 2 km from the source and stands in the direct paths to both L_1 and L_2. Finally, a larger ridge $\boldsymbol{\mathcal{H}}_3$ located about 4 km to the north is an important sound barrier that stands just before L_3.

In order to ensure a constant level of accuracy between the several frequencies, the numerical step δ is defined as one tenth of the wavelength of the highest harmonic $f_3 = 7.59\,\text{Hz}$, so we have $\delta = 4.51\,\text{m}$. A total of 4 simulations will be done for each frequency. The source height is assumed to be located at an altitude $z_s = 25\,\text{m}$ with

a normalized strength $S_0 = 1\,\text{Pa}$. The absolute pressure values at L_n are taken at ground level and the reference pressure is taken as $p_{\text{ref}} = 1\,\text{Pa}$. The atmosphere is assumed to be homogeneous with $c_0 = 343\,\text{m}$ and the ground to be rigid, so the ground impedance Z_g is infinite. In order to ensure no spurious reflections arise from the boundaries of the domain, the Absorbing Boundary Layer (ABL) has to be made large enough. Numerical simulations show that a layer of thickness of $H_a = (2/5) \times z_{\max}$ below the upper limit and a thickness $D_a = (1/5) \times (y_{\max} - y_{\min})$ on each side of the numerical domain is acceptable.

6.3.2 Results and discussions

The Relative Sound Pressure Levels (RSPL) and pressure amplitudes at the four micro-barographs L_k as computed by the 2DPE and 3DPE, are listed in Table 6.4. The associated amplitude ratios are computed using Eq. (6.3) and plotted in Fig. 6.3, where we see a good agreement between the three-dimensional PE and experimental data in specific cases only. The 2D and 3D amplitude ratios are very close at L_3 and L_4, the discrepancy between the two seems to be smaller than the discrepancy with measured amplitude ratios $A^m_{n,\text{exp}}$. It also appears that the 3D amplitude ratios are consistently higher than the 2D case, which can be explained by three-dimensional scattering from out-of-plane terrain obstacles. The 3D model, however, reasonably improves the amplitude ratios for the micro-barograph L_2 at frequencies $f = 3.79\,\text{Hz}$ and $f = 5.69\,\text{Hz}$. The amplitude ratios computed for L_3 and L_4 are lower than the flat amplitude ratio $A^m_{n,\text{flat}}$ and decrease when frequency increases. For L_2, we see a clear difference between the 2D and 3D models: unlike in 2D, the 3D amplitude ratio increase with frequency.

The most significant three-dimensional effects appear to be along the path $W - L_2$, where the 3D parabolic equation simulations give a better match of the experimental amplitude ratios for $f < 7.59\,\text{Hz}$, suggesting the existence of diffractive effects from the hill $\boldsymbol{\mathcal{H}}_2$ at higher frequencies. This observation is in line with previous findings established in Sec. 5.2.1, where we have shown that 3D diffractive effects occur in the middle plane leading to less attenuation past the obstacle (cf. Figs.

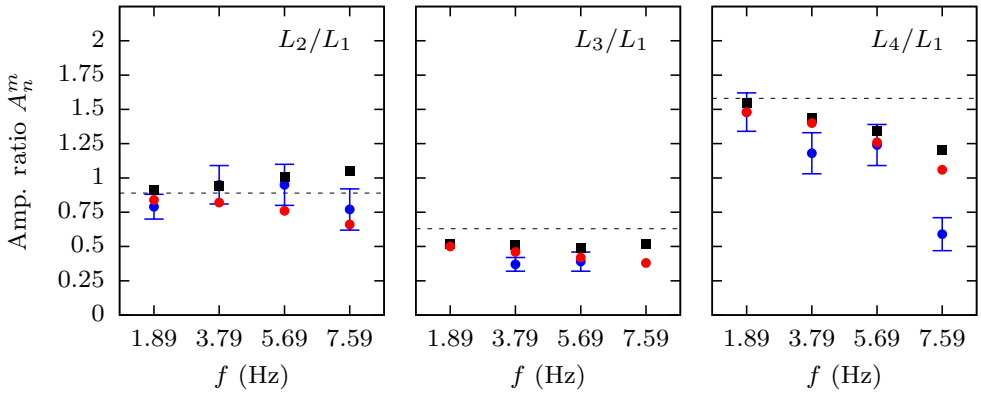

Figure 6.3: Numerical amplitude ratios A_n^m for $n = 2$ (left), $n = 3$ (middle) and $n = 4$ (right), as computed by the 3D BTPE (■), the 2D BTPE (●) and experimental amplitude ratios $A_{n,\text{exp}}^m$ from the IS50 microbaraographs (●). The dashed lines represent the flat amplitude ratios $A_{n,\text{flat}}^m$.

5.19b and 5.22b). As expected, the 2DPE shows an underestimated RSPL as the hill $\boldsymbol{\mathcal{H}}_2$ blocks the path between the source W and the micro-barometer array L_2. Topography seems to play a lesser role along the paths $W - L_3$ and $W - L_4$. The mismatch between the measured and computed amplitude ratios for the frequency 7.59 Hz at the array L_4 could be explained by the Wind Noise Reduction Systems on low-frequency micro-barometers, which would induce a stronger filtering of higher infrasonic frequencies.

Moreover, slices of the RSPL in the numerical domain $\mathcal{D}$ (cf. Fig 6.2) are plotted in Fig. 6.4. We can see that the hill $\boldsymbol{\mathcal{H}}_1$ in the near-field creates substantial diffuse reflection. The hill $\boldsymbol{\mathcal{H}}_2$ creates a first shadow zone between $x = 2.0\,\text{km}$ and $x = 4.0\,\text{km}$. The ridge $\boldsymbol{\mathcal{H}}_3$ acts a sound barrier and creates a shadow zone that is very visible at $f = 7.59\,\text{Hz}$, with a difference of RSPL of about $-20\,\text{dB}$ after the obstacle. In the present model, mismatch with experimental data can be explained by a number of factors. While the exact location of the wind farm is known, there is an uncertainty regarding the exact sound source location among the distributed set of possible sources. In order to account for this uncertainty, we could consider several source locations around the point W. Furthermore, numerical errors stem from the interpolation of the topographic profile, inducing noise in the computed derivatives at every grid point. The heights are extracted from the raw elevation data using

a linear interpolation and a uniform smoothing filter defined by Eq. (4.95). An alternative approach, like gaussian filtering, may lead to better results.

Physical parameters that influence propagation include the impedance of the ground surface and the upward refracting conditions. While surface impedance will have a great impact on propagation at higher frequencies, it is unclear how using a realistic ground model instead of a rigid boundary condition could account for the persistent discrepancy between 2D and 3D PE. On the other hand, upward refraction from tropospheric winds are anisotropic and will enhance propagation in a given direction, which would decrease propagation along one path $W - L_k$ more than the others. This could explain the strong amplitude ratio loss at L_4. This is even more critical considering that the stations L_k are all within a large azimuthal aperture of about $\theta_2^* - \theta_4^* \approx 42.2°$. Another more elaborate consideration on the proposed modeling is to evaluate the sound source more accurately. In the present case, the wind farm is modeled using the Gaussian source given in Eq. (4.75), which is an approximation of a monopole source. Orientation of the wind turbines and interaction between the sound sources generated by the two turbines of the wind farm W may affect the directivity of sound field [142]. A better PE starting field can be derived by matching the typical directivity field $D(\theta, \varphi)$ of the wind farm with the directivity of a modified Gaussian starting field. Notably, Vecherin et al. [205] have used the Equivalent Source Method (ESM) to successfully incorporate a directional source into both narrow-angle and wide-angle 2DPE schemes.

6.4 Conclusions

In this Chapter, we have applied the 3DPE to a realistic problem of infrasound propagation above an irregular boundary. First, we have shown that topography plays a role in the estimation of amplitude ratios across all micro-barometer arrays. Three-dimensional effects are substantial for frequencies on the higher end of the infrasound spectrum ($f = 5.79\,\mathrm{Hz}$), leading to higher amplitude ratios compared to the 2DPE simulations. The proposed modeling has shown the existence of three

Microbarograph	Frequency (Hz)	3D BTPE		2D BTPE	
		Abs. Pres. (mPa)	SPL (dB)	Abs. Pres. (mPa)	SPL (dB)
L_1	1.89	0.644	−69.8	0.752	−68.5
	3.79	0.721	−68.9	0.849	−67.4
	5.69	0.701	−69.1	0.874	−67.1
	7.59	0.658	−69.7	0.874	−67.1
L_2	1.89	0.601	−70.4	0.638	−69.9
	3.79	0.679	−69.4	0.703	−69.9
	5.69	0.708	−69.0	0.667	−69.5
	7.59	0.692	−69.2	0.581	−70.7
L_3	1.89	0.345	−75.3	0.378	−74.5
	3.79	0.365	−74.7	0.393	−74.1
	5.69	0.351	−75.1	0.373	−74.6
	7.59	0.344	−75.3	0.338	−75.4
L_4	1.89	1.016	−64.7	1.115	−65.0
	3.79	1.018	−64.6	1.189	−64.5
	5.69	0.985	−65.3	1.100	−65.2
	7.59	0.852	−66.4	0.923	−66.7

Table 6.4: 2D and 3D PE simulation results. Acoustic absolute pressure (mPa) and Sound Pressure Level (dB) at the different micro-barogrameter arrays L_n for the four harmonics f_m. The source amplitude is $S_0 = 1\,\text{Pa}$.

dimensional effects but results highlight that more parameters could be taken into account for a better match of measured amplitude ratios. Furthermore, tackling the uncertainty surrounding the source definition require a more thorough characterization of the radiation pattern from the aerodynamic sound, generated by the rotating blades. Yet, the most plausible explanation for discrepancies is the coupling between atmospheric and topographic features, which may significantly enhance propagation in one specific direction [124]. As we are interested in propagation over a few kilometers, we would need to incorporate the effective sound speed c_{eff} in the atmospheric boundary layer, up to 5 km of altitude. In the current situation, no information

Microbarograph	Frequency (Hz)	3D ratio A_n^m	2D ratio A_n^m
L_2/L_1	1.89	0.93	0.85
	3.79	0.94	0.83
	5.69	1.01	0.76
	7.59	1.05	0.66
L_3/L_1	1.89	0.54	0.50
	3.79	0.51	0.46
	5.69	0.50	0.43
	7.59	0.52	0.38
L_4/L_1	1.89	1.57	1.48
	3.79	1.40	1.40
	5.69	1.39	1.26
	7.59	1.29	1.06

Table 6.5: Amplitude ratios A_n^m at L_2, L_3 and L_4 relatively to L_1 calculated from the 2D and 3D PE simulations.

on the wind turbines was available, outside of technical specifications and IMS data recordings. It has been pointed out that a better characterization of the source directivity could improve on the proposed modeling, which assumed the source generated by rotating blades to be monopole.

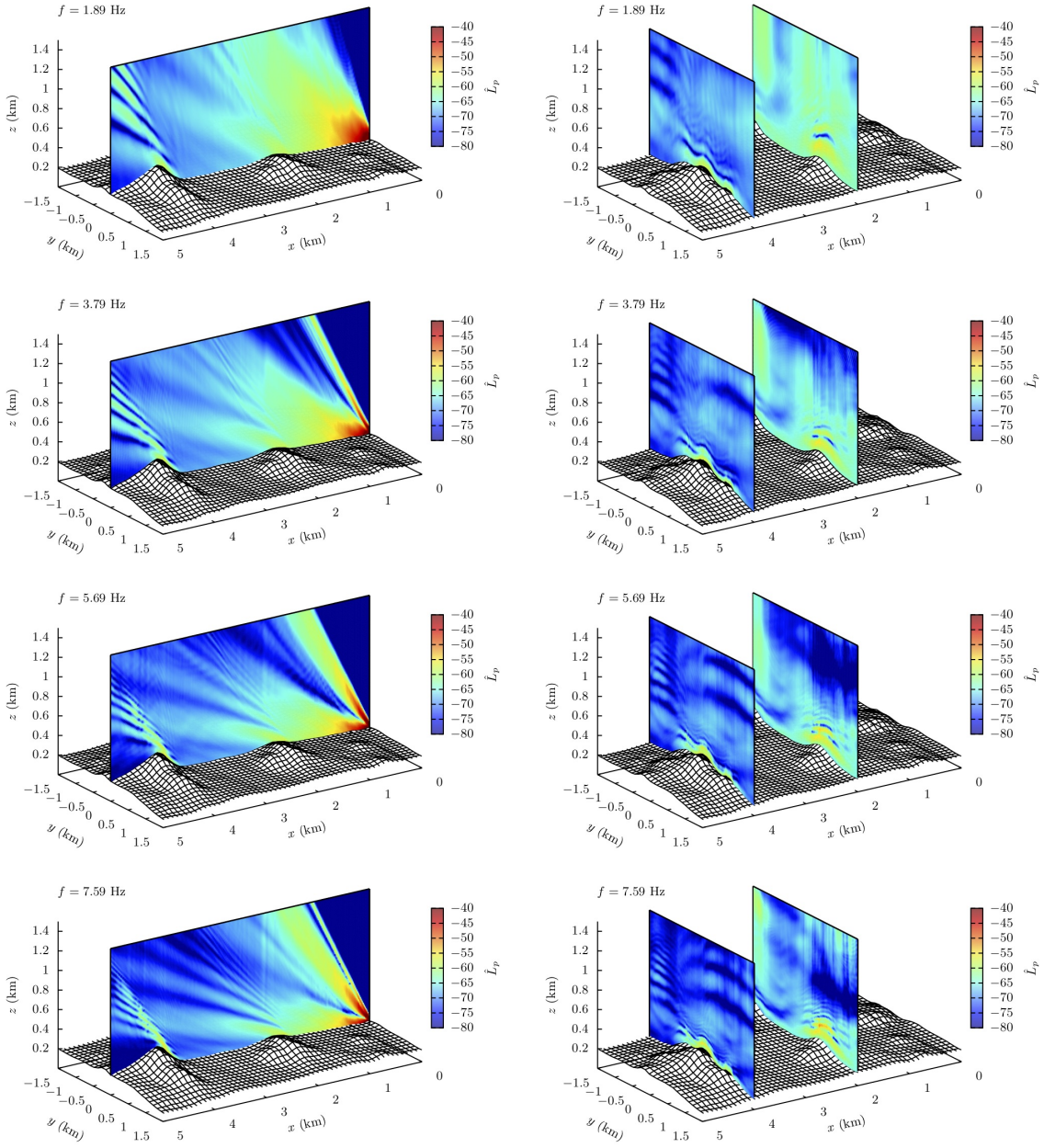

Figure 6.4: 3DPE Simulation results for the four harmonics f_m. Left: Relative Sound Pressure Level (RSPL) slice along $y = 0\,\text{km}$. Right: Relative Sound Pressure Level (RSPL) slices along $x = 2.0\,\text{km}$ and $x = 4.0\,\text{km}$. The basemap is the relief of the topography for the $W - L_1$ simulation.

Chapter 7

Conclusions and Further work

In this thesis, a novel three-dimensional Parabolic Equation (PE) method has been developed for propagation in a refractive atmosphere and over irregular boundaries. The mathematical derivations presented are related to existing two-dimensional methods, specifically the Beilis-Tappert coordinate transform and subsequent models. The numerical solution is computed through an iterative scheme that seeks the solution at every range as the fixed point of a Sylvester matrix equation. The method has been implemented in a code that was validated against a COMSOL Multiphysics Finite-Element Model for propagation over a smooth gaussian boundary. The assumption a small slope boundary is consistent with the narrow-angle limitation, which allows for grazing propagation ($\varphi_p < 20°$) only, and allows us to neglect the cross-derivative term. This assumption is central to the development of an efficient numerical scheme instead of a sparse system and provides a satisfying model for smooth boundaries. Indeed, if the problem was to be handled through a three-dimensional sparse system, the size of the problem at the frequencies of interest (e.g. $f = 10\,\mathrm{Hz}$ on a $3\,\mathrm{km} \times 3\,\mathrm{km}$ waveguides) would lead to prohibitively large computation times, requiring the use of parallel strategies. This observation has been made by previous authors in the computational acoustics community who addressed three-dimensional propagation. It has been used here as an additional justification for our model.

The existence of three-dimensional effects has been highlighted through a parametric study, which shows that substantial diffractive effects occur as soon as the ratio of the obstacle size (height in this case) to the wavelength, named *obstacle ratio*, is equal or larger than 1. This leads to an increase in Sound Pressure Level anywhere between 2 dB and $\sim$ 5 dB in the shadow zone. When irregular boundaries are coupled with atmospheric refraction, interaction in the atmospheric boundary layer becomes critically important and transversal scattering (i.e. normal to the paraxial direction) causes three-dimensional effects even for reasonably small terrain obstacles. However, these effects are mitigated at lower frequencies ($f < 1$ Hz) and show that topographic effects are substantial only on the higher end of the infrasound spectrum (i.e. $f > 1$ Hz). Beyond the numerical method, this study is the first extensive investigation of three-dimensional topographic effects in the atmospheric acoustics/infrasound community and provide some answers to recent concerns in infrasound modeling. The method has also been applied to a realistic propagation case of wind turbine noise, where numerical PE computations in both 2D and 3D have been compared against data obtained from the International Monitoring System (IMS). Results show a close agreement of numerical results with measurements but marginal three-dimensional effects. From these observations, we deduced that isolated topographic effect are not sufficient to account for amplitude loss in a realistic scenario.

The numerical method developed has been implemented in a FORTRAN software package called InfraTopo, and delivered to AWE Blacknest. This code has many potential applications in the modeling of infrasonic waves in realistic environments, one of which is the analysis of regional infrasound close to IMS micro-barometers, where topography has been proven to influence recorded signals. This sort of applications is of importance in the deployment of new infrasound arrays. Furthermore, the method developed is versatile and close enough to the existing theory to allow for use in different disciplines involving long-range wave propagation, such as electromagnetic propagation (optical waves, radar, VHF/UHF) or underwater acoustics.

While the method developed in this thesis constitutes an original contribution to the current understanding of infrasonic wave propagation, the physical assumptions

made lead to a number of limitations. For a given frequency, only a subset of all physical effects will be relevant, and it has been established that topography will have an influence on medium-range infrasound but not at very low frequencies ($f \leq 0.1$ Hz). Assuming that the final aim is to include all possible environmental parameters into a single 3D PE formulation, a few improvements must be brought to the proposed model to reach this objective. In this respect, there are (at least) four possible directions to extend the work carried out in this thesis:

- **Wide-angle formulation**. A straightforward improvement is the use of a higher-order formulation of the PE, in order to increase the maximum angle of propagation. As a first step in this direction, the theory for a wide-angle formulation was presented in Sec. 4.2.2 and takes advantage of the Split-Step Padé solution for the 3D PE [192]. Furthermore, the mixed derivative that arise from the coordinate transform can be included by considering a more elaborate ADI scheme and generalize the Split-Step Padé solution to irregular waveguides. In this case, the cross-term is handled explicitly so that the system can be solved with tridiagonal matrices and avoid the computation of a large sparse system.

- **Numerical accuracy**. Beyond the use of a higher-order paraxial approximation, other minor numerical improvements are possible. For example, by considering a curvilinear grid rather than the original Beilis-Tappert transform [207, 105, 93], which can be readily solved with the iterative fixed-point scheme presented in this thesis. Another important extension of the method can be achieved by solving the backscattered wave (in 2D, q_c^- in Eq. (3.8b)), as done by Zhu and Bjørnø (2000) [233] in cylindrical coordinates. This is relevant in situations where sound barriers, such as canyons and ridges, create substantial reflections at short ranges.

- **Atmospheric model**. The accuracy of the method can be improved by taking more atmospheric parameters into account - such as turbulence, transversal wind or absorption. The inclusion of turbulence into the existing model can be carried out following the existing literature on the subject [32, 222, 147]. Typically, the study of turbulence on acoustic propagation involves the com-

putation of the statistical moments of the complex pressure $p_c(\mathbf{x})$ over a set of realizations for the random adiabatic sound speed $\tilde{c}(\mathbf{x})$ and wind velocity $\tilde{\mathbf{v}}(\mathbf{x})$.

- **Experimental benchmark**. A better validation of the 3D PE and other numerical methods in atmospheric acoustics can be achieved by comparison with scaled laboratory experiments. Such experiments are aimed at producing datasets with controlled parameters, whereas recorded signals from real infrasound events are subject to uncertainty. The main challenge of a scaled experiment is the specification of the acoustic source. Existing studies on the matter have generally used a spark-gap generator, which consists in two narrowly spaced electrodes submitted to a high-voltage differential ($V > 2$ kV) [21, 230]. The overpressure from the electric spark, which lasts about 40 microseconds, is a non-linear N-wave with a very high amplitude ($P > 1$kPa). Many difficulties are associated with the characterization of such sources, as the peak amplitude and duration is highly dependent on the gap diameter [231].

Bibliography

[1] *NIST Digital Library of Mathematical Functions*. http://dlmf.nist.gov/, Release 1.0.24 of 2019-09-15. F. W. J. Olver, A. B. Olde Daalhuis, D. W. Lozier, B. I. Schneider, R. F. Boisvert, C. W. Clark, B. R. Miller, B. V. Saunders, H. S. Cohl, and M. A. McClain, eds.

[2] *COMSOL Multiphysics® v. 5.4.* COMSOL AB, Stockholm, Sweden, www.comsol.com.

[3] A. Abawi, W. Kuperman, and M. Collins. The coupled mode parabolic equation. *J. Acoust. Soc. Am.*, 102(1):233–238, 1997.

[4] L. Abrahamsson and H-O. Kreiss. Boundary conditions for the parabolic equation in a range-dependent duct. *J. Acoust. Soc. Am.*, 87(6):2438–2441, 1990.

[5] M. Abramowitz, I. Stegun, and et al. *Handbook of mathematical functions*. Dover New York, 1972.

[6] B. Alcoverro and A. Le Pichon. Design and optimization of a noise reduction system for infrasonic measurements using elements with low acoustic impedance. *J. Acoust. Soc. Am.*, 117(4):1717–1727, 2005.

[7] M. Almquist, I. Karasalo, and K. Mattsson. Atmospheric sound propagation over large-scale irregular terrain. *Journal of Scientific Computing*, 61(2):369–

397, Nov 2014.

[8] C. Amante and B. Eakins. Etopo1 1 arc-minute global relief model: Procedures, data sources and analysis. *NOAA Technical Memorandum NESDIS NGDC-24*, 2009.

[9] E. Anderson, Z. Bai, C. Bischof, L.S. Blackford, J. Demmel, J. Dongarra, J. Du Croz, A. Greenbaum, S. Hammarling, A. McKenney, and D. Sorensen. *LAPACK Users' Guide (Third Ed.)*. Society for Industrial and Applied Mathematics, 1999.

[10] S. Arrowsmith, J. Johnson, D. Drob, and M. Hedlin. The seismoacoustic wavefield: a new paradigm in studying geophysical phenomena. *Reviews of Geophysics*, 48(4), 2010.

[11] Stephen J. Arrowsmith, Douglas P. Drob, Michael A. H. Hedlin, and Wayne Edwards. A joint seismic and acoustic study of the washington state bolide: Observations and modeling. *Journal of Geophysical Research: Atmospheres*, 112(D9), 2007.

[12] J. Arvelo and A. Rosenberg. Three-dimensional effects on sound propagation and matched-field processor performance. *J. Comp. Acoustics*, 9(1):17–39, 2001.

[13] J. Assink, G. Averbuch, P. Smets, and L. Evers. On the infrasound detected from the 2013 and 2016 dprk's underground nuclear tests. *Geophys. Res. Lett.*, 43(7):3526–3533, 2016.

[14] J. Assink, R. Waxler, and D. Velea. A wide-angle high mach number modal expansion for infrasound propagation. *J. Acoust. Soc. Am.*, 141(3):1781–1792, 2017.

[15] K. Attenborough. Acoustical impedance models for outdoor ground surfaces. *J. Sound Vibration*, 99(4):521 – 544, 1985.

[16] K. Attenborough. Sound propagation close to the ground. *Annual Review of Fluid Mechanics*, 34(1):51–82, 2002.

[17] K. Attenborough, S. Taherzadeh, H. E. Bass, X. Di, R. Raspet, G. R. Becker, A. Güdesen, A. Chrestman, G. A. Daigle, A. L'Espérance, Y. Gabillet, K. E. Gilbert, Y. L. Li, M. J. White, P. Naz, J. M. Noble, and H. A. J. M. van Hoof. Benchmark cases for outdoor sound propagation models. *J. Acoust. Soc. Am.*, 97(1):173–191, 1995.

[18] K. Attenborough and T. Waters-Fuller. Effective impedance of rough porous ground surfaces. *J. Acoust. Soc. Am.*, 108(3):949–956, 2000.

[19] Keith Attenborough, Imran Bashir, and Shahram Taherzadeh. Outdoor ground impedance models. *The Journal of the Acoustical Society of America*, 129(5):2806–2819, 2011.

[20] R. Awadallah. Effects of lateral terrain variations on tropospheric radar propagation. *IEEE Transactions on Antennas and Propagation*, 53(1 II):420–434, 2005.

[21] Christophe Ayrault, Philippe Béquin, and Sophie Baudin. Characteristics of a spark discharge as an adjustable acoustic source for scale model measurements. In Société Française d'Acoustique, editor, *Acoustics 2012*, Nantes, France, 2012.

[22] A. Bamberger, B. Engquist, L. Halpern, and P. Joly. Higher order paraxial wave equation approximations in heterogeneous media. *SIAM Journal on Applied Mathematics*, 48(1):129–154, 1988.

[23] H. Bass, C. Hetzer, and R. Raspet. On the speed of sound in the atmosphere as a function of altitude and frequency. *Journal of Geophysical Research: Atmospheres*, 112(D15), 2007.

[24] R. Beam and R. Warming. Alternating direction implicit methods for

parabolic equations with a mixed derivative. *SIAM J. Sci. Stat. Comput.*, 1(1):131–159, March 1980.

[25] A. Bedard and T. Georges. Atmospheric infrasound. *Physics Today*, 53:32–37, 03 2000.

[26] A. Beilis and F. D. Tappert. Coupled mode analysis of multiple rough surface scattering. *J. Acoust. Soc. Am.*, 66:811, 1979.

[27] J-P. Berenger. A perfectly matched layer for the absorption of electromagnetic waves. 114(2):185 – 200, 1994.

[28] M. Berengier. Outdoor sound propagation: A short review on analytical and numerical approaches. *Acta Acustica united with Acustica*, 89(6):980–991, 2003.

[29] A. Berry and G. A. Daigle. Controlled experiments of the diffraction of sound by a curved surface. *J. Acoust. Soc. Am.*, 83(6):2047–2058, 1988.

[30] M. Bertin, C. Millet, and D. Bouche. A low-order reduced model for the long range propagation of infrasounds in the atmosphere. *J. Acoust. Soc. Am.*, 136(1):37–52, 2014.

[31] E. Blanc. Observations in the upper atmosphere of infrasonic waves from natural or artificial sources - A summary. *Annales Geophysicae*, 3:673–687, December 1985.

[32] P. Blanc-Benon, L. Dallois, and D. Juvé. Long range sound propagation in a turbulent atmosphere within the parabolic approximation. *Acta Acustica united with Acustica*, 87:659–669, 11 2001.

[33] P. Blom. Modeling infrasonic propagation through a spherical atmospheric layer—analysis of the stratospheric pair. *J. Acoust. Soc. Am.*, 145(4):2198–2208, 2019.

[34] P. Blom, F. K. Dannemann, and O. E. Marcillo. Bayesian characterization of explosive sources using infrasonic signals. *Geophys. J. Int.*, 215(1):240–251, 2018.

[35] P. Blom and R. Waxler. Impulse propagation in the nocturnal boundary layer: Analysis of the geometric component. *J. Acoust. Soc. Am.*, 131(5):3680–3690, 2012.

[36] C. Bogey and C. Bailly. Three-dimensional non-reflective boundary conditions for acoustic simulations: Far-field formulation and validation test cases. *Acta Acust. Acust.*, 88:463, 2002.

[37] P. Boulanger, K. Attenborough, S. Taherzadeh, T. Waters-Fuller, and K. M. Li. Ground effect over hard rough surfaces. *The Journal of the Acoustical Society of America*, 104(3):1474–1482, 1998.

[38] L. Brekhovskikh and O. Godin. *Acoustics of Layered Media II: Point Sources and Bounded Beams*. Springer Series on Wave Phenomena. Springer Berlin Heidelberg, 1999.

[39] Leonid M. Brekhovskikh and Oleg A. Godin. *Monochromatic Plane-Wave Reflection from Continuously Layered Media*, pages 41–86. Springer Berlin Heidelberg, Berlin, Heidelberg, 1990.

[40] G. Brooke, D. Thomson, and P. Wort. A sloping boundary condition for efficient pe calculations in range-dependent media. *J. Comp. Acoustics*, 04(01):11–27, 1996.

[41] G. H. Brooke, D. J. Thomson, and G. R. Ebbeson. Pecan: A canadian parabolic equation model for underwater sound propagation. *Journal of Computational Acoustics*, 09(01):69–100, 2001.

[42] Y. Cansi and A. Le Pichon. *Infrasound Event Detection Using the Progressive Multi-Channel Correlation Algorithm*, pages 1425–1435. Springer New York,

2008.

[43] K. Castor and F. Sturm. Investigation of 3d acoustical effects using a multiprocessing parabolic equation based algorithm. *J. Comp. Acoustics*, 16(02):137–162, 2008.

[44] R. Cheng, P. Morris, and K. Brentner. A three dimensional parabolic equation method for sound propagation in moving inhomogeneous media. *J. Acoust. Soc. Am.*, 126(4):1700–1710, 2009.

[45] Y. Choo, H. Song, and W. Seong. Time-domain helmholtz-kirchhoff integral for surface scattering in a refractive medium. *J. Acoust. Soc. Am.*, 141(3):EL267–EL273, 2017.

[46] D. Christie and P. Campus. The ims infrasound network: Design and establishment of infrasound stations. *Infrasound Monitoring for Atmospheric Studies*, pages 29–75, 2010.

[47] J. F. Claerbout. *Fundamentals of geophysical data processing.* McGraw-Hill Inc., New York, March 1976.

[48] M. Collins and S. Chin-Bing. A three-dimensional parabolic equation model that includes the effects of rough boundaries. *J. Acoust. Soc. Am.*, 87(3):1104–1109, 1990.

[49] M. Collins and R. Evans. A two-way parabolic equation for acoustic backscattering in the ocean. *J. Acoust. Soc. Am.*, 91(3):1357–1368, 1992.

[50] M. Collins and E. Westwood. A higher-order energy-conserving parabolic equation for range-dependent ocean depth, sound speed, and density. *J. Acoust. Soc. Am.*, 89(3):1068–1075, 1991.

[51] M. D. Collins. A higher-order parabolic equation for wave propagation in an ocean overlying an elastic bottom. *J. Acoust. Soc. Am.*, 86(4):1459–1464,

1989.

[52] M. D. Collins and W. L. Siegmann. Treatment of variable topography with the seismoacoustic parabolic equation. *IEEE Journal of Oceanic Engineering*, 42(2):488–493, 2017.

[53] Michael D. Collins. The rotated parabolic equation and sloping ocean bottoms. *The Journal of the Acoustical Society of America*, 87(3):1035–1037, 1990.

[54] Michael D. Collins. A single-scattering correction for the seismo-acoustic parabolic equation. *J. Acoust. Soc. Am.*, 131(4):2638–2642, 2012.

[55] Michael D. Collins and William L. Siegmann. Treatment of a sloping fluid-solid interface and sediment layering with the seismo-acoustic parabolic equation. *J. Acoust. Soc. Am.*, 137(1):492–497, 2015.

[56] B. Cotté. Coupling of an aeroacoustic model and a parabolic equation code for long range wind turbine noise propagation. *J. Sound Vibration*, 422:343 – 357, 2018.

[57] I. Craig and A. Sneyd. An alternating-direction implicit scheme for parabolic equations with mixed derivatives. *Computers and Mathematics with Applications*, 16(4):341 – 350, 1988.

[58] D. Crighton, A. Dowling, J. Ffowcs-Williams, M. Heckl, F. Leppington, and J. Bartram. *Modern Methods in Analytical Acoustics Lecture Notes*. Springer-Verlag London, 1992.

[59] L. Dallois, P. Blanc-Benon, and D. Juvé. A wide-angle parabolic equation for acoustic waves in inhomogeneous media: applications to atmospheric sound propagation. *J. Comp. Acoustics*, 9(2):477–494, 2001.

[60] C. de Groot-Hedlin. Finite-difference time-domain synthesis of infrasound propagation through an absorbing atmosphere. *J. Acoust. Soc. Am.*,

124(3):1430–1441, 2008.

[61] C. de Groot-Hedlin. Long-range propagation of nonlinear infrasound waves through an absorbing atmosphere. *J. Acoust. Soc. Am.*, 139(4):1565–1577, 2016.

[62] C. de Groot-Hedlin. Infrasound propagation in tropospheric ducts and acoustic shadow zones. *J. Acoust. Soc. Am.*, 142(4):1816–1827, 2017.

[63] M.E. Delany and E.N. Bazley. Acoustical properties of fibrous absorbent materials. *Applied Acoustics*, 3(2):105–116, 1970.

[64] J. DeSanto. Exact boundary integral equations for scattering of scalar waves from perfectly reflecting infinite rough surfaces. *Wave Motion*, 45(7):918 – 926, 2008.

[65] J. DeSanto and P. Martin. On the derivation of boundary integral equations for scattering by an infinite two-dimensional rough surface. *Journal of Mathematical Physics*, 39(2):894–912, 1998.

[66] J.-X. Dessa, J. Virieux, and S. Lambotte. Infrasound modeling in a spherical heterogeneous atmosphere. *Geophys. Res. Lett.*, 32(12), 2005.

[67] J-B. Doc, B. Lihoreau, and S. Félix. Higher order pade approximation for the parabolic equation in a varying cross-section waveguide. *Acta Acustica united with Acustica*, 98:691–699, 09 2012.

[68] D. Donohue and J. Kuttler. Propagation modeling over terrain using the parabolic wave equation. *IEEE Transactions on Antennas and Propagation*, 48(2):260–277, 2000.

[69] V. A. Dougalis and N. A. Kampanis. Finite element methods for the parabolic equation with interfaces. *Journal of Computational Acoustics*, 04(01):55–88, 1996.

[70] A. Dowling and J. Williams. *Sound and sources of sound*. Ellis Horwood series in engineering science. E. Horwood, 1983.

[71] D. Dragna, P. Blanc-Benon, and F. Poisson. Time-domain solver in curvilinear coordinates for outdoor sound propagation over complex terrain. *J. Acoust. Soc. Am.*, 133(6):3751–3763, 2013.

[72] D. Dragna, B. Cotté, P. Blanc-Benon, and F. Poisson. Time-domain simulations of outdoor sound propagation with suitable impedance boundary conditions. *AIAA Journal*, 49(7):1420–1428, 2011.

[73] Didier Dragna, Philippe Blanc-Benon, and Franck Poisson. *Effects of topography in time-domain simulations of outdoor sound propagation*. 2012.

[74] D. et al. Drob. An empirical model of the earth's horizontal wind fields: Hwm07. *Journal of Geophysical Research: Space Physics*, 113(A12), 2008.

[75] T. Eibert. Irregular terrain wave propagation by a fourier split-step wide-angle parabolic wave equation technique for linearly bridged knife-edges. *Radio Science*, 37(1):5–1–5–12, 2002.

[76] T. Embleton. Tutorial on sound propagation outdoors. *J. Acoust. Soc. Am.*, 100(1):31–48, 1996.

[77] Damiens F., Millet C., and Lott F. An investigation of infrasound propagation over mountain ranges. *J. Acoust. Soc. Am.*, 143(1):563–574, 2018.

[78] T. et al. Farr. The shuttle radar topography mission. *Reviews of Geophysics*, 45(2), 2007.

[79] R. Fleagle and J. Businger. *An Introduction to Atmospheric Physics*. International Geophysics. Elsevier Science, 1981.

[80] V. Fock. *Electromagnetic diffraction and propagation problems*. New York : Pergamon Press, [1st ed.] edition, 1965.

[81] B. Fornberg. Generation of finite difference formulas on arbitrarily spaced grids. *Mathematics of Computation*, 51(184):699–706, 1988.

[82] O. Gainville, Ph. Blanc-Benon, E. Blanc, R. Roche, C. Millet, F. Le Piver, B. Despres, and P. F. Piserchia. *Misty Picture: A Unique Experiment for the Interpretation of the Infrasound Propagation from Large Explosive Sources*, pages 575–598. Springer Netherlands, 2009.

[83] L-J. Gallin, M. Rénier, E. Gaudard, T. Farges, R. Marchiano, and F. Coulouvrat. One-way approximation for the simulation of weak shock wave propagation in atmospheric flows. *J. Acoust. Soc. Am.*, 135(5):2559–2570, 2014.

[84] M. Garces. On infrasound standards, part 1 time, frequency, and energy scaling. *InfraMatics*, 02:13–35, 01 2013.

[85] K. Gilbert and X. Di. A fast green's function method for one-way sound propagation in the atmosphere. *J. Acoust. Soc. Am.*, 94(4):2343–2352, 1993.

[86] K. Gilbert and M. White. Application of the parabolic equation to sound propagation in a refracting atmosphere. *J. Acoust. Soc. Am.*, 85:630–637, 1989.

[87] O. Godin. An effective quiescent medium for sound propagating through an inhomogeneous, moving fluid. *J. Acoust. Soc. Am.*, 112(4):1269–1275, 2002.

[88] O. Godin. Acoustic-gravity waves in atmospheric and oceanic waveguides. *J. Acoust. Soc. Am.*, 132(2):657–669, 2012.

[89] Oscar Gonzalez and Andrew M. Stuart. *A First Course in Continuum Mechanics*. Cambridge Texts in Applied Mathematics. Cambridge University Press, 2008.

[90] E. Gossard and W. Hooke. *Waves in the atmosphere : atmospheric infrasound and gravity waves, their generation and propagation.* New York : Elsevier Scientific, 1975.

[91] D. Green, R. Waxler, J-M. Lalande, D. Velea, and C. Talmadge. Regional infrasound generated by the Humming Roadrunner ground truth experiment. *Geophys. J. Int.*, 214(3):1847–1864, 2018.

[92] R. Greene. The rational approximation to the acoustic wave equation with bottom interaction. *J. Acoust. Soc. Am.*, 76(6):1764–1773, 1984.

[93] D. Heimann and R. Karle. A linearized euler finite-difference time-domain sound propagation model with terrain-following coordinates. *J. Acoust. Soc. Am.*, 119(6):3813–3821, 2006.

[94] G. Heinzel, A. Rüdiger, and R. Schilling. Spectrum and spectral density estimation by the discrete fourier transform (dft), including a comprehensive list of window functions and some new flat-top windows. *Max-Plank Inst.*, 12, 01 2002.

[95] P. Holm. Wide-angle shift-map PE for a piecewise linear terrain—a finite-difference approach. *IEEE Transactions on Antennas and Propagation*, 55(10):2773–2789, 2007.

[96] L. Hsieh, C-F. Chen, M-C. Yuan, and Y-T. Lin. Azimuthal limitation in 3d pe approximation for underwater acoustic propagation. *J. Comp. Acoustics*, 15(02):221–233, 2007.

[97] K. Huang, K. Solna, and H. Zhao. Coupled parabolic equations for wave propagation. *Methods Appl. Anal.*, 11(3):399–412, 09 2004.

[98] R. Janaswamy. A curvilinear coordinate-based split-step parabolic equation method for propagation predictions over terrain. *IEEE Transactions on Antennas and Propagation*, 46(7):1089–1097, July 1998.

[99] P. Jean. A variational approach for the study of outdoor sound propagation and application to railway noise. *Journal of Sound and Vibration*, 212(2):275 – 294, 1998.

[100] F. Jensen, W. Kuperman, M. Porter, and H. Schmidt. *Computational Ocean Acoustics*. Modern Acoustics and Signal Processing. Springer New York, 2011.

[101] J. Johnson and R. Maurizio. Volcano infrasound: A review. *Journal of Volcanology and Geothermal Research*, 206(3):61–69, 2011.

[102] R. Jones, J. Riley, and T. Georges. HARPA: A versatile three-dimensional Hamiltonian ray-tracing program for acoustic waves in the atmosphere above irregular terrain. Technical report, August 1986.

[103] A. Jursa. Handbook of geophysics and the space environment, 4th edition. 12 1985.

[104] N. Kampanis. Numerical simulation of low-frequency aeroacoustics over irregular terrain using a finite element discretization of the parabolic equation. *J. Comp. Acoustics*, 10:97–111, 2002.

[105] N.A. Kampanis, A.I. Delis, D.C. Antonopoulou, and G. Kozyrakis. A finite element discretization of the standard parabolic equation in generalized boundary fitting coordinates. *Applied Numerical Mathematics*, 67:152 – 166, 2013. NUMAN 2010.

[106] C. Khodr, M. Azarpeyvand, and D.N. Green. Cartesian three-dimensional parabolic equation for propagation above irregular boundaries (under review). *J. Acoust. Soc. Am.*, 2020.

[107] K. Kim and J. Lees. Local Volcano Infrasound and Source Localization Investigated by 3D Simulation. *Seismological Research Letters*, 85(6):1177–1186, 10 2014.

[108] K. Kim and J. M. Lees. Finite-difference time-domain modeling of transient infrasonic wavefields excited by volcanic explosions. *Geophysical Research Letters*, 38(6), 2011.

[109] K. Koch and C. Pilger. Infrasound observations from the site of past underground nuclear explosions in North Korea. *Geophys. J. Int.*, 216(1):182–200, 09 2018.

[110] W. Kuperman, M. Porter, J. Perkins, and R. Evans. Rapid computation of acoustic fields in three-dimensional ocean environments. *J. Acoust. Soc. Am.*, 81(1):125–133, 1991.

[111] J. Kuttler. Differences between the narrow-angle and wide-angle propagators in the split-step fourier solution of the parabolic wave equation. *IEEE Transactions on Antennas and Propagation*, 47(7):1131–1140, 1999.

[112] G. Lacanna, M. Ichihara, M. Iwakuni, M. Takeo, M. Iguchi, and M. Ripepe. Influence of atmospheric structure and topography on infrasonic wave propagation. *Journal of Geophysical Research: Solid Earth*, 119(4):2988–3005, 2014.

[113] G. Lacanna and M. Ripepe. Influence of near-source volcano topography on the acoustic wavefield and implication for source modeling. *Journal of Volcanology and Geothermal Research*, 250:9–18, 01 2013.

[114] H. Langtangen and S. Linge. *Finite Difference Computing with PDEs: A Modern Software Approach*. Springer Publishing Company, Incorporated, 1st edition, 2017.

[115] A. Le Pichon, E. Blanc, and A. Hauchecorne. *Infrasound Monitoring for Atmospheric Studies*. Springer, 2009.

[116] D. Lee, G. Botseas, and W. Siegmann. Examination of three-dimensional effects using a propagation model with azimuth-coupling capability (for3d). *J. Acoust. Soc. Am.*, 91(6):3192–3202, 1992.

[117] D. Lee and S. McDaniel. Ocean acoustic propagation by finite difference methods. International Series in Modern Applied Mathematics and Computer Science. Pergamon, 1988.

[118] D. Lee, A. Pierce, and E-C. Shang. Parabolic equation development in the twentieth century. *J. Comp. Acoustics*, 08(04):527–637, 2000.

[119] K. Lee, W. Seong, and Y. Na. Three-dimensional cartesian parabolic equation model with higher-order cross-terms using operator splitting, rational filtering, and split-step padé algorithm. *J. Acoust. Soc. Am.*, 146(3):2041–2049, 2019.

[120] A Leontovich. On a method of solving the problem of propagation of electromagnetic waves near the surface of the earth. *Izv. Akad. Nauk USSR Ser. Phys*, 8:16–22, 1944.

[121] M. Levy. *Parabolic Equation Methods for Electromagnetic Wave Propagation*. Electromagnetics and Radar Series. Institution of Electrical Engineers, 2000.

[122] K. Li and Q. Wang. Analytical solutions for outdoor sound propagation in the presence of wind. *J. Acoust. Soc. Am.*, 102(4):2040–2049, 1997.

[123] M. Lighthill and M. Newman. On sound generated aerodynamically i. general theory. *Proceedings of the Royal Society of London. Series A. Mathematical and Physical Sciences*, 211(1107):564–587, 1952.

[124] B. Lihoreau, B. Gauvreau, M. Bérengier, P. Blanc-Benon, and I. Calmet. Outdoor sound propagation modeling in realistic environments: Application of coupled parabolic and atmospheric models. *J. Acoust. Soc. Am.*, 120:110–119, 2006.

[125] Y-T. Lin. Three-dimensional boundary fitted parabolic-equation model of underwater sound propagation. *J. Acoust. Soc. Am.*, 146(3):2058–2067, 2019.

[126] Y-T. Lin, J. Collis, and T. Duda. A three-dimensional parabolic equation

model of sound propagation using higher-order operator splitting and padé approximants. *J. Acoust. Soc. Am.*, 132(5):EL364–EL370, 2012.

[127] Y-T. Lin, T. Duda, and A. Newhall. Three-dimensional sound propagation models using the parabolic-equation approximation and the split-step fourier method. *J. Comp. Acoustics*, 21(01):1250018, 2013.

[128] J. Lonzaga, R. Waxler, J. Assink, and C. Talmadge. Modelling waveforms of infrasound arrivals from impulsive sources using weakly non-linear ray theory. *Geophys. J. Int.*, 200(3):1347–1361, 01 2015.

[129] F. Lott. A new theory for downslope windstorms and trapped mountain waves. *Journal of the Atmospheric Sciences*, 73(9):3585–3597, 2016.

[130] W. Luo and H. Schmidt. Three-dimensional propagation and scattering around a conical seamount. *J. Acoust. Soc. Am.*, 125(1):52–65, 2009.

[131] Collins M. A split-step padé solution for the parabolic equation method. *J. Acoust. Soc. Am.*, 93(4):1736–1742, 1993.

[132] O. Marsden, C. Bogey, and C. Bailly. A study of infrasound propagation based on high-order finite difference solutions of the navier-stokes equations. *J. Acoust. Soc. Am.*, 135(3):1083–1095, 2014.

[133] S. McKee, D. Wall, and S. Wilson. An alternating direction implicit scheme for parabolic equations with mixed derivative and convective terms. 126(1):64–76, 1996.

[134] M. McKenna, R. Gibson, B. Walker, J. McKenna, N. Winslow, and Kofford A. Topographic effects on infrasound propagation. *J. Acoust. Soc. Am.*, 131(1):35–46, 2012.

[135] M. Metcalf, J. Reid, and M. Cohen. *Modern Fortran Explained.* Oxford University Press, Inc., New York, NY, USA, 4th edition, 2011.

[136] A. M. Metzler, D. Moran, J. M. Collis, P. A. Martin, and W. L. Siegmann. A scaled mapping parabolic equation for sloping range-dependent environments. *J. Acoust. Soc. Am.*, 135(3):EL172–EL178, 2014.

[137] F. Milanazzo, C. Zala, and G. Brooke. Rational square-root approximations for parabolic equation algorithms. *J. Acoust. Soc. Am.*, 101(2):760–766, 1997.

[138] R. Modrak, S. Arrowsmith, and D. Anderson. A Bayesian framework for infrasound location. *Geophys. J. Int.*, 181(1):399–405, 04 2010.

[139] K. Naugolnykh and L. Ostrovsky. *Nonlinear Wave Processes in Acoustics*. Cambridge Texts in Applied Mathematics. Cambridge University Press, 1998.

[140] A. Nippress, D. Green, O. Marcillo, and S. Arrowsmith. Generating regional infrasound celerity-range models using ground-truth information and the implications for event location. *Geophys. J. Int.*, 197(2):1154–1165, 2014.

[141] D. Norris, R. Gibson, and K. Bongiovanni. *Numerical Methods to Model Infrasonic Propagation Through Realistic Specifications of the Atmosphere*, pages 541–573. Springer Netherlands, Dordrecht, 2009.

[142] S. Oerlemans and J. G. Schepers. Prediction of wind turbine noise and validation against experiment. *International Journal of Aeroacoustics*, 8(6):555–584, 2009.

[143] V. Ostashev, D. Juve, and P. Blanc-Benon. Derivation of a wide-angle parabolic equation for sound waves in inhomogeneous moving media. *Acta Acustica united with Acustica*, 83(3):455–460, 1997.

[144] V. Ostashev, M. Muhlestein, and D. Keith Wilson. Extra-wide-angle parabolic equations in motionless and moving media. *J. Acoust. Soc. Am.*, 145(2):1031–1047, 2019.

[145] V. Ostashev and D. Wilson. *Acoustics in Moving Inhomogeneous Media*. Lon-

don: CRC Press, 2016.

[146] V. Ostashev, K. Wilson, L. Liu, D. Aldridge, Symons N., and Marlin D. Equations for finite-difference, time-domain simulation of sound propagation in moving inhomogeneous media and numerical implementation. *J. Acoust. Soc. Am.*, 117(2):503–517, 2005.

[147] Vladimir E. Ostashev, Erik M. Salomons, Steven F. Clifford, Richard J. Lataitis, D. Keith Wilson, Philippe Blanc-Benon, and Daniel Juvé. Sound propagation in a turbulent atmosphere near the ground: A parabolic equation approach. *The Journal of the Acoustical Society of America*, 109(5):1894–1908, 2001.

[148] D. A. Outing, W. L. Siegmann, M. D. Collins, and E. K. Westwood. Generalization of the rotated parabolic equation to variable slopes. *J. Acoust. Soc. Am.*, 120(6):3534–3538, 2006.

[149] J. S. Papadakis. Exact, nonreflecting boundary conditions for parabolic-type approximations in underwater acoustics. *Journal of Computational Acoustics*, 02(02):83–98, 1994.

[150] J. S. Papadakis and B. Pelloni. A method for the treatment of a sloping sea bottom in the parabolic approximation. *Journal of Computational Acoustics*, 04(01):89–100, 1996.

[151] J. S. Papdakis and E. T. Flouri. A neumann to dirichlet map for the bottom boundary of a stratified sub-bottom region in parabolic approximation. *Journal of Computational Acoustics*, 16(03):409–425, 2008.

[152] S. Parakkal, K. Gilbert, and X. Di. Application of the beilis-tappert parabolic equation method to sound propagation over irregular terrain. *J. Acoust. Soc. Am.*, 131(2):1039–1046, 2012.

[153] S. Parakkal, K. Gilbert, X. Di, and H. Bass. A generalized polar coordinate

method for sound propagation over large-scale irregular terrain. *J. Acoust. Soc. Am.*, 128(5):2573–2580, 2010.

[154] J. Park, I-Y. Che, B. Stump, C. Hayward, F. Dannemann, S-J. Jeong, K. Kwong, S. McComas, H. R. Oldham, M. M. Scales, and V. Wright. Characteristics of infrasound signals from North Korean underground nuclear explosions on 2016 January 6 and September 9. *Geophys. J. Int.*, 214(3):1865–1885, 06 2018.

[155] J. Perkins and R. Baer. An approximation to the three-dimensional parabolic-equation method for acoustic propagation. *J. Acoust. Soc. Am.*, 72(2):515–522, 1982.

[156] P. Petrov and F. Sturm. An explicit analytical solution for sound propagation in a three-dimensional penetrable wedge with small apex angle. *J. Acoust. Soc. Am.*, 139(3):1343–1352, 2016.

[157] A. Pierce. *Acoustics: An Introduction to its Physical Principles and Applications*. Springer, 1981.

[158] A. Pierce. Wave equation for sound in fluids with unsteady inhomogeneous flow. *J. Acoust. Soc. Am.*, 87(6):2292–2299, 1990.

[159] C. Pilger, F. Streicher, L. Ceranna, and K.W. Koch. Application of propagation modeling to verify and discriminate ground-truth infrasound signals at regional distances. volume 2, pages 39–55, 2013.

[160] M. B. Porter, F. B. Jensen, and C. M. Ferla. The problem of energy conservation in one-way models. *J. Acoust. Soc. Am.*, 89(3):1058–1067, 1991.

[161] E. Premat, J. Defrance, M. Priour, and F-E. Aballéa. Coupling bem and gfpe for complex outdoor sound propagation. *Euronoise 2003, Naples*, 01 2003.

[162] E. Premat and Y. Gabillet. A new boundary-element method for predicting

outdoor sound propagation and application to the case of a sound barrier in the presence of downward refraction. *J. Acoust. Soc. Am.*, 108(6):2775–2783, 2000.

[163] W. H. Press, S. A. Teukolsky, W. T. Vetterling, and B. P. Flannery. *Numerical Recipes in FORTRAN (2nd Ed.): The Art of Scientific Computing*. Cambridge University Press, New York, NY, USA, 1992.

[164] K. Rasmussen. On the effect of terrain profile on sound propagation outdoors. *J. Sound Vibration*, 98(1):35–44, 1985.

[165] K. Rasmussen. Sound propagation over screened ground under upwind conditions. *J. Acoust. Soc. Am.*, 100(6):3581–3586, 1996.

[166] R. Raspet, G. Baird, and W. Wu. Normal mode solution for low-frequency sound propagation in a downward refracting atmosphere above a complex impedance plane. *J. Acoust. Soc. Am.*, 91(3):1341–1352, 1992.

[167] S. Riestra and A. Hirschberg. An introduction to acoustics. *Eindhoven: Technische Universiteit Eindhoven*, 2018.

[168] J. Robertson. Sound propagation over a large wedge: A comparison between the geometrical theory of diffraction and the parabolic equation. *J. Acoust. Soc. Am.*, 106(1):113–119, 1999.

[169] Y. Saad. *Iterative Methods for Sparse Linear Systems*. Dordrecht: Kluwer Academic Publisher, 2003.

[170] Y. Saad and M. H. Schultz. Gmres: A generalized minimal residual algorithm for solving nonsymmetric linear systems. *SIAM Journal on Scientific and Statistical Computing*, 7(3):856–869, 1986.

[171] R. Sabatini and P. Cristini. An immersed interface method for the solution of the standard parabolic equation in range-dependent ocean environments. *J.*

Acoust. Soc. Am., 143(4):EL243–EL247, 2018.

[172] R. Sabatini, O. Marsden, C. Bailly, and C. Bogey. A numerical study of nonlinear infrasound propagation in a windy atmosphere. *J. Acoust. Soc. Am.*, 140(1):641–656, 2016.

[173] R. Sabatini, O. Marsden, C. Bailly, and O. Gainville. Three-dimensional direct numerical simulation of infrasound propagation in the earth's atmosphere. *Journal of Fluid Mechanics*, 859:754–789, 2019.

[174] R. Sack and M. West. A parabolic equation for sound propagation in two dimensions over any smooth terrain profile: The generalized terrain parabolic equation (GT-PE). *Applied Acoustics*, 45:113, 1995.

[175] J. D. Sagers and M. S. Ballard. Testing and verification of a scale-model acoustic propagation system. *The Journal of the Acoustical Society of America*, 138(6):3576–3585, 2015.

[176] E. Salomons. Improved green's function parabolic equation method for atmospheric sound propagation. *J. Acoust. Soc. Am.*, 104(1):100–111, 1998.

[177] E. Salomons. *Computational Atmospheric Acoustics*. Dordrecht: Kluwer Academic Publisher, 2001.

[178] E. Salomons, R. Blumrich, and D. Heimann. Eulerian time-domain model for sound propagation over a finite-impedance ground surface. comparison with frequency-domain models. *Acta Acustica united with Acustica*, 88(4):483–492, 2002.

[179] E.M. Salomons. Sound propagation in complex outdoor situations with a non-refracting atmosphere: Model based on analytical solutions for diffraction and reflection. *Acustica*, 83(3):436–454, 1997.

[180] B. Seckler and J. Keller. Asymptotic theory of diffraction in inhomogeneous

media. *The Journal of the Acoustical Society of America*, 31(2):206–216, 1959.

[181] B. Seckler and J. Keller. Geometrical theory of diffraction in inhomogeneous media. *J. Acoust. Soc. Am.*, 31(2):192–205, 1959.

[182] A. Segalini, R. Örlü, and P. H. Alfredsson. Uncertainty analysis of the von kármán constant. *Exp. Fluids*, 54(1460), 2013.

[183] S. Shani-Kadmiel, J. D. Assink, P. S. M. Smets, and L. G. Evers. Seismoacoustic coupled signals from earthquakes in central italy: Epicentral and secondary sources of infrasound. *Geophysical Research Letters*, 45(1):427–435, 2018.

[184] W. Siegmann, G. Kriegsmann, and D. Lee. A wide-angle three-dimensional parabolic wave equation. *J. Acoust. Soc. Am.*, 78(2):659–664, 1985.

[185] W. Siegmann and D. Lee. Aspects of three-dimensional parabolic equation computations. *Computers Math. Applic.*, 11(7):853–862, 1985.

[186] M. Silva, E. Costa, and M. Liniger. Analysis of the effects of irregular terrain on radio wave propagation based on a three-dimensional parabolic equation. *IEEE Transactions on Antennas and Propagation*, 60(4):2138–2143, 2012.

[187] V. Simoncini. Computational methods for linear matrix equations. *SIAM Review*, 58(3):377–441, 2016.

[188] N. Sissenwine, M. Dubin, and H. Wexler. The us standard atmosphere, 1962. *Journal of Geophysical Research*, 67(9):3627–3630, 1962.

[189] K. Smith. A three-dimensional propagation algorithm using finite azimuthal aperture. *J. Acoust. Soc. Am.*, 106(6):3231–3239, 1999.

[190] O.R. Spivack and M. Spivack. Efficient boundary integral solution for acoustic wave scattering by irregular surfaces. *Engineering Analysis with Boundary*

Elements, 83:275–280, 2017.

[191] J. Strikwerda. *Finite Difference Schemes and Partial Differential Equations, Second Edition*. Springer Berlin Heidelberg, 2004.

[192] F. Sturm. Numerical study of broadband sound pulse propagation in three-dimensional oceanic waveguides. *J. Acoust. Soc. Am.*, 117(3):1058–1079, 2005.

[193] F. Sturm. Leading-order cross term correction of three-dimensional parabolic equation models. *J. Acoust. Soc. Am.*, 139(1):263–270, 2016.

[194] F. Sturm and J. A. Fawcett. On the use of higher-order azimuthal schemes in 3-D PE modeling. *J. Acoust. Soc. Am.*, 113(6):3134–3145, 2003.

[195] F. Sturm and N. Kampanis. Accurate treatment of a general sloping interface in a finite-element 3D narrow-angle PE model. *J. Comp. Acoustics*, 15(03):285–318, 2007.

[196] F. Sturm and A. Korakas. Comparisons of laboratory scale measurements of three-dimensional acoustic propagation with solutions by a parabolic equation model. *The Journal of the Acoustical Society of America*, 133(1):108–118, 2013.

[197] L. Sutherland and H. Bass. Atmospheric absorption in the atmosphere up to 160 km. *J. Acoust. Soc. Am.*, 115(3):1012–1032, 2004.

[198] S. Taherzadeh, K. Li, and K. Attenborough. Some practical considerations for predicting outdoor sound propagation in the presence of wind and temperature gradients. *Applied Acoustics*, 54(1):27 – 44, 1998.

[199] F. Tappert, J. Keller, and J. Papadakis. *The parabolic approximation method*, pages 224–287. Springer Berlin Heidelberg, 1977.

[200] H. Tennekes. The logarithmic wind profile. *Journal of the Atmospheric Sci-*

ences, 30(2):234–238, 1973.

[201] D. J. Thomson and N. R. Chapman. A wide-angle split-step algorithm for the parabolic equation. *J. Acoust. Soc. Am.*, 74(6):1848–1854, 1983.

[202] A. Tolstoy. 3-D propagation models and issues. *J. Comp. Acoustics*, 04(03):243–271, 1996.

[203] L.N. Trefethen and L. Halpern. Well-posedness of one-way wave equations and absorbing boundary conditions. *Mathematics of Computation*, 47(176):421–435, 1986.

[204] T. van Renterghem, E.M. Salomons, and D. Botteldooren. Efficient fdtd-pe model for sound propagation in situations with complex obstacles and wind profiles. *Acta Acustica united with Acustica*, 91(4):671–679, 2005.

[205] S.N. Vecherin, K.D. Wilson, and V.E. Ostashev. Incorporating source directionality into outdoor sound propagation calculations. *J. Acoust. Soc. Am.*, 130(6):3608–3622, 2011.

[206] J. Virieux, N. Garnier, E. Blanc, and J.-X. Dessa. Paraxial ray tracing for atmospheric wave propagation. *Geophys. Res. Lett.*, 31(20), 2004.

[207] M. Visbal and D. Gaitonde. On the use of higher-order finite-difference schemes on curvilinear and deforming meshes. 181(1):155–185, 2002.

[208] Sanders W. and Collins M. Nonuniform depth grids in parabolic equation solutions. *J. Acoust. Soc. Am.*, 133(4):1953–1958, 2013.

[209] K. Waagan. Low-frequency long-range atmospheric noise propagation modeling with the pe method. (2014/00260):31, 2014.

[210] K. Waagan. Noise mapping with the pe method – a case study from interior

norway. page 37, 2015.

[211] K. Walker and M. Hedlin. *A Review of Wind-Noise Reduction Methodologies*, pages 141–182. 01 2010.

[212] Q. Wang and K.M. Li. Sound propagation over concave surfaces. *J. Acoust. Soc. Am.*, 106(5):2358–2366, 1999.

[213] R. Waxler. A vertical eigenfunction expansion for the propagation of sound in a downward-refracting atmosphere over a complex impedance plane. *J. Acoust. Soc. Am.*, 112(6):2540–2552, 2002.

[214] R. Waxler. Modal expansions for sound propagation in the nocturnal boundary layer. *J. Acoust. Soc. Am.*, 115(4):1437–1448, 2004.

[215] R. Waxler, J. Assink, and D. Velea. Modal expansions for infrasound propagation and their implications for ground-to-ground propagation. *J. Acoust. Soc. Am.*, 141(2):1290–1307, 2017.

[216] R. Waxler, L.G. Evers, J. Assink, and P. Blom. The stratospheric arrival pair in infrasound propagation. *J. Acoust. Soc. Am.*, 137(4):1846–1856, 2015.

[217] M. West, K. Gilbert, and R.A. Sack. A tutorial on the parabolic equation (PE) model used for long range sound propagation in the atmosphere. *Applied Acoustics*, 37(1):31 – 49, 1992.

[218] Brian T. R. Wetton and Gary H. Brooke. One-way wave equations for seismoacoustic propagation in elastic waveguides. *J. Acoust. Soc. Am.*, 87(2):624–632, 1990.

[219] R. Whitaker, D. Norris, D. Havelock, S. Kuwano, and M. Vorländer. *Infrasound Propagation*, pages 1497–1519. Springer New York, 2008.

[220] M. White. Application of the parabolic equation to the outdoor propagation

of sound. *Applied Acoustics*, 27(3):227 – 238, 1989.

[221] P. White. Earth Global Reference Atmospheric Model (GRAM) Overview and Future Improvements. In *42nd COSPAR Scientific Assembly*, volume 42, pages C4.2–2–18, Jul 2018.

[222] D. K. Wilson and V. E. Ostashev. Statistical moments of the sound field propagating in a random, refractive medium near an impedance boundary. *The Journal of the Acoustical Society of America*, 109(5):1909–1922, 2001.

[223] K. Wilson. The sound-speed gradient and refraction in the near-ground atmosphere. *J. Acoust. Soc. Am.*, 113(2):750–757, 2003.

[224] K. Wilson, V. Ostashev, S. Collier, N. Symons, D. Aldridge, and D. Marlin. Time-domain calculations of sound interactions with outdoor ground surfaces. *Applied Acoustics*, 68:173, 2007.

[225] K. Woolfe, M. D. Collins, D. C. Calvo, and W. L. Siegmann. Seismo-acoustic benchmark problems involving sloping fluid–solid interfaces. *Journal of Computational Acoustics*, 24(04):1650022, 2016.

[226] Li Xie, Jie Ding, and Feng Ding. Gradient based iterative solutions for general linear matrix equations. *Computers and Mathematics with Applications*, 58(7):1441 – 1448, 2009.

[227] C-X. Xu, J. Tang, S-C. Piao, J-Q. Liu, and S-Z. Zhang. Developments of parabolic equation method in the period of 2000–2016. *Chinese Physics B*, 25(12):124315, nov 2016.

[228] D. Yevick and D. Thomson. Complex padé approximants for wide-angle acoustic propagators. *J. Acoust. Soc. Am.*, 108(6):2784–2790, 2000.

[229] D. Yevick and D. J. Thomson. Impedance-matched absorbers for finite-difference parabolic equation algorithms. *J. Acoust. Soc. Am.*, 107(3):1226–

1234, 2000.

[230] Petr Yuldashev, M. Averiyanov, V. Khokhlova, Sébastien Ollivier, and Philippe Blanc-Benon. Nonlinear spherically divergent shock waves propagating in a relaxing medium. *Acoustical Physics*, 54:32–41, 01 2008.

[231] Petr Yuldashev, Sébastien Ollivier, Mikhail Averiyanov, Oleg Sapozhnikov, Vera Khokhlova, and Philippe Blanc-Benon. Nonlinear propagation of spark-generated n-waves in air: Modeling and measurements using acoustical and optical methods. *The Journal of the Acoustical Society of America*, 128(6):3321–3333, 2010.

[232] C. Zelley and C. Constantinou. A three-dimensional parabolic equation applied to VHF/UHF propagation over irregular terrain. *IEEE Transactions on Antennas and Propagation*, 47(10):1586–1596, 1999.

[233] Dong Zhu and Leif Bjørnø. A three-dimensional, two-way, parabolic equation model for acoustic backscattering in a cylindrical coordinate system. *The Journal of the Acoustical Society of America*, 108(3):889–898, 2000.

[234] C. Zwikker and C. Kosten. *Sound absorbing Materials*. Elsevier, New York, 1949.